

Dissertation
submitted to the
Combined Faculty of Natural Sciences and Mathematics
of the Ruperto Carola University Heidelberg, Germany
for the degree of
Doctor of Natural Sciences

Presented by
Julia Sieber-Frank, M. Sc.
born in: Sindelfingen

Oral examination: _____

Characterisation of anti-cancer properties of synthetic flavaglines and preparation of their preclinical evaluation

Referees: Prof. Dr. med. Magnus von Knebel Doeberitz
Dr. Guoliang Cui

Reading
gives us someplace to go
when we have to stay where we are

- Mason Cooley -

The presented Dissertation was started in February 2018 and completed in December 2020 under the supervision of Prof. Dr. Magnus von Knebel Doeberitz at the department of Applied Tumour Biology at the Institute for Pathology, University of Heidelberg (Germany) and the Clinical Cooperation Unit Applied Tumour Biology of the German Cancer Research Centre (DKFZ), Heidelberg (Germany).

Affidavit according to §8 of the doctoral degree regulations of the Combined Faculty of Natural Sciences and Mathematics

1. The thesis I have submitted entitled ‘Characterisation of anti-cancer properties of synthetic flavaglines and preparation of their preclinical evaluation’ is my own work.
2. I have only used the sources indicated and have not made unauthorised use of services of a third party. Where the work of others has been quoted or reproduced, the source is always given.
3. I have not yet presented this thesis or parts thereof to a university as part of an examination or degree.
4. I confirm that the declarations made above are correct.
5. I am aware of the importance of a sworn affidavit and the criminal prosecution in case of a false or incomplete affidavit.

I affirm that the above is the absolute truth to the best of my knowledge and that I have not concealed anything.

Heidelberg, 01.03.2012

(Julia Sieber-Frank)

Contents

List of Figures	ix
List of Tables	x
Abbreviations	xi
Summary	xiv
Zusammenfassung	xvi
1 Introduction	1
1.1 Cancer and cancer hallmarks	1
1.2 Cell cycle arrest and cell death mechanisms	3
1.2.1 Cell cycle arrest	4
1.2.2 Cellular senescence	4
1.2.3 Apoptosis	5
1.2.4 Alternative cell death mechanisms	7
1.3 Glucose metabolism and the Warburg effect	9
1.3.1 Cellular pathways regulating glucose metabolism	12
1.3.2 Application of glucose anti-metabolite 2-deoxyglucose in cancer	13
1.4 Flavaglines as promising anti-cancer compounds	15
1.4.1 Characteristics of natural flavaglines	15
1.4.2 Chemical synthesis of flavaglines as a way to improve their availability and applicability	16
1.5 Colorectal cancer	18
1.6 Human papillomavirus-associated cancers	20
1.7 Treatment resistances in clinical oncology	22
1.8 Rationale and aims of the project	24
2 Material	25
2.1 Chemicals and reagents	25
2.2 Consumables	30
2.3 Kits	32
2.4 Antibodies	33
2.5 Primers	34
2.6 Instruments	35
2.7 Software	38
2.8 Cell lines	39
2.9 Buffers and cell culture special media	41

3	Methods	45
3.1	General methods	45
3.1.1	Maintenance and harvest of cells	45
3.1.2	Cryopreservation of cell lines	45
3.1.3	Anti-cancer agents	46
3.2	Generation of IMD-3-resistant haploid cells	46
3.3	Cellular assays	48
3.3.1	Cell viability assay	48
3.3.1.1	Influence of glucose, FBS and P/S on the efficacy of IMD-3	48
3.3.2	Proliferation assay	49
3.3.3	Real-time cell proliferation monitoring	50
3.3.4	Pulse-chase cytotoxicity assay	50
3.3.5	Senescence-associated β -galactosidase staining	51
3.3.6	Specimen preparation of treated cells on microscope slides for IF staining	52
3.3.7	Generation of treated cell pellets for protein, RNA and DNA analysis	52
3.3.8	Glucose uptake assay	53
3.3.9	Lactate assay	53
3.3.10	Pentose phosphate pathway activity	54
3.3.11	DAC-pretreatment of WT and IMD-3-resistant cells	55
3.3.12	Cell viability assay of 3D spheroid cultures	56
3.3.13	3D Organotypic co-culture model	56
3.3.13.1	Culturing of fibroblasts and keratinocytes for OTCs	57
3.4	RNA techniques	58
3.4.1	RNA isolation	58
3.4.2	Bead chip RNA gene expression analysis	58
3.4.3	RNA transcriptome data analysis	58
3.4.3.1	Ingenuity pathway analysis of differential expression data	59
3.5	DNA techniques	60
3.5.1	DNA isolation	60
3.5.2	DNA methylation analysis	60
3.5.2.1	Bisulfite treatment of DNA	60
3.5.2.2	LINE-1 PCR amplification	60
3.5.2.3	PCR product analysis by gel electrophoresis	61
3.5.2.4	LINE-1 sequencing	61
3.6	Protein techniques	62
3.6.1	Protein isolation	62
3.6.2	Determination of protein concentration by Bradford assay	62
3.6.3	Sodium dodecylsulfate-polyacrylamide gel electrophoresis	62
3.6.4	Western blot	62

3.7	Paraffin processing of tissue and staining procedures	63
3.7.1	Paraffin embedding and cutting of tissue sections	63
3.7.2	Deparaffinisation of tissue slides	63
3.7.3	Haematoxylin and eosin staining	63
3.7.4	Immunohistochemical staining	64
3.7.5	Fluorescence staining	65
3.8	<i>In vivo</i> experiments	66
3.8.1	Animals	66
3.8.2	Xenograft model	66
3.8.3	<i>In vivo</i> screening to determine the optimal treatment dosages and combination in xenograft-bearing mice	66
3.8.4	Efficacy and side effect profiling of optimal treatment dosage in xenograft-bearing mice	67
3.8.5	Application of IMD-3 solubilised in HSA	69
3.8.6	Sample preparation	69
3.9	IMD-3 characterisation	70
3.9.1	UV spectroscopy	70
3.9.2	Electrospray ionisation mass spectrometry (ESI-MS) analysis of IMD-3-treated cell culture samples and mouse tumours	70
3.10	Statistical analysis	71
4	Results	72
4.1	Anti-cancer activity of synthetic flavagline derivatives and their influence on cellular metabolism	72
4.1.1	Synthetic flavagline derivatives reduce cell viability in a broad spectrum of different cancer cell lines	72
4.1.2	Synthetic flavagline derivatives mainly exert anti-tumour effect through proliferation inhibition	79
4.1.3	Synthetic flavagline derivatives inhibit cell proliferation independent of senescence induction	85
4.1.4	Downregulation of GLUT-1 expression and deregulation of glucose metabolism is a common characteristic of IMD-3 treatment	87
4.1.5	Glucose utilisation is not shifted towards the pentose phosphate pathway upon IMD-3 treatment	92
4.1.6	Transcriptome analysis confirms proliferation inhibition, modulation of glucose metabolism and indicates ROS induction upon IMD-3 treatment	93
4.1.7	Anti-cancer activity of IMD-3 could be confirmed in 3D cell culture models	96
4.2	Identification of resistance mechanisms against synthetic flavagline treatment	100

4.2.1	Gene-trap mutagenesis led to the generation of a long-term IMD-3-resistant cell line	100
4.2.2	Anti-proliferative effect of IMD-3 is overcome in resistant cells	101
4.2.3	IMD-3-induced modulation of glucose metabolism is absent in resistant cells, while GLUT-1 expression is preserved	103
4.2.4	Pentose phosphate pathway activity remains unchanged in IMD-3-resistant cells	105
4.2.5	Genetic and epigenetic analysis does not reveal reasons for the acquired resistance	106
4.2.6	Transcriptome analysis reveals decreased glycolytic activity in IMD-3-resistant cells	109
4.3	Evaluation of synthetic flavagline treatment <i>in vivo</i>	113
4.3.1	Evaluation of anti-tumour efficacy <i>in vivo</i> and analysis of treatment-related side effects	113
4.3.1.1	Dose finding experiment reveals no side effects of synthetic flavaglines in a xenograft model	113
4.3.1.2	The selected treatment doses show no detectable anti-tumour or side effects	120
4.3.2	Analysis of possible reasons for discordance between <i>in vitro</i> and <i>in vivo</i> drug efficacy	123
4.3.2.1	<i>In vivo</i> application of IMD-3 solubilised in HSA shows no anti-tumour effect	129
4.3.2.2	Mass spectrometry analysis reveals presence of IMD-3 in xenograft tumours	130
5	Discussion	134
5.1	<i>In vitro</i> characterisation of synthetic flavaglines	134
5.1.1	Molecular phenotype and sensitivity towards synthetic flavagline treatment	136
5.1.2	Inhibition of proliferation and glucose metabolism by synthetic flavagline derivatives	137
5.1.3	Molecular characteristics of synthetic flavagline derivatives in 3D culture models	140
5.2	Assessment of resistance towards synthetic flavaglines	141
5.2.1	Altered glucose metabolism in IMD-3-resistant cells	142
5.2.2	Genetic and epigenetic analysis of IMD-3-resistance	143
5.2.3	Transcriptional alterations in IMD-3-resistant cells	144
5.3	<i>In vivo</i> evaluation of synthetic flavagline activity	146

5.3.1	Dose finding, side effect profiling and anti-tumour activity of synthetic flavaglines in initial xenograft experiments	146
5.3.2	Influence of albumin on IMD-3 efficacy	147
5.3.3	Mass spectrometry analysis of xenograft tumours and analysis of hampered <i>in vivo</i> treatment efficacy	149
5.4	Outlook	152
	References	154
	Supplement	184
	Electronic supplements (on CD)	206
	Acknowledgements	xviii

List of Figures

1	The hallmarks of cancer	2
2	Apoptotic cell death pathways	8
3	Cellular glucose metabolism	11
4	2DG reaction and PET imaging	13
5	Chemical structures of IMD-1 and IMD-3	17
6	Schematic overview of pulse-chase cytotoxicity assay	51
7	Schematic overview of DAC-pretreatment schedule	55
8	<i>In vivo</i> treatment combinations and dosages	67
9	<i>In vivo</i> treatment schedule for dosage optimisation	67
10	<i>In vivo</i> treatment schedule for MRI and PET analysis	68
11	Treatment sensitivity of IDH-WT and -mutant cells	74
12	Treatment sensitivity of CRC cell lines	76
13	Treatment sensitivity of MLH1 knockout cell lines	77
14	Treatment sensitivity of HPV-transformed cancer cell lines	78
15	Apoptosis induction in CaSki cells	80
16	Apoptosis induction in SiHa cells	81
17	Apoptosis induction in UPCI-SCC-90 cells	82
18	Cytotoxicity of synthetic flavaglines in CRC cell lines	83
19	Proliferation inhibition in CRC cell lines	84
20	Senescence induction in cervical cancer cells	86
21	Influence on glucose metabolism of HPV-transformed cell lines	87
22	GLUT-1 expression in HPV-transformed cancer cell lines	88
23	GLUT-1 and cell proliferation staining in CaSki cells	89
24	GLUT-1 and cell proliferation staining in SiHa cells	90
25	GLUT-1 and cell proliferation staining in UPCI-SCC-90 cells	91
26	Pentose phosphate pathway activity of CRC cell lines	92
27	Commonly deregulated pathways upon IMD-3 treatment	94
28	Heat map for selected DEGs in CRC and HPV-positive cell lines	95
29	Treatment sensitivity of cervical cancer cell 3D spheroids	97
30	HE staining of 3D co-culture models	98
31	Fluorescence staining of 3D co-culture models	99
32	HE staining of 3D culture models only containing keratinocytes	100
33	Generation of a long-term IMD-3-resistant cell line	101
34	Real-time cell proliferation monitoring of WT and IMD-3-resistant cells	102
35	Proliferation inhibition in WT and IMD-3-resistant cells	103
36	Influence on glucose uptake velocity of WT and IMD-3-resistant cells	104
37	GLUT-1 expression in WT and IMD-3-resistant cells	104

LIST OF FIGURES

38	Pentose phosphate pathway activity of WT and IMD-3-resistant cells	105
39	NGS screening of IMD-3-resistant HGC176 cells	106
40	DAC-pretreatment influence on IMD-3 sensitivity of WT and resistant cells . . .	108
41	LINE-1 CpG methylation status of DAC-pretreated WT and resistant cells . . .	109
42	Deregulated pathways in IMD-3-resistant cells	110
43	Sensitivity of WT and IMD-3-resistant cells towards 2DG	111
44	Commonly deregulated pathways in WT and IMD-3-resistant cells	112
45	Dose escalation: Tumour growth and survival of 2DG- and IMD-1-treated mice	114
46	Dose escalation: Tumour growth and survival of IMD-3-treated mice	115
47	Dose escalation: HE staining of organs from xenograft-bearing mice	117
48	Dose escalation: HE staining of the digestive tract from xenograft-bearing mice	118
49	Dose escalation: HE, GLUT-1, and Ki-67 staining and QuPath image classifier of xenograft tumours	119
50	Dose escalation: Ki-67 and GLUT-1-positive cells in xenograft tumours	120
51	Tumour growth and survival upon IMD-3 (1.0 mg/kg) and 2DG (100 mg/kg) treatment	121
52	PET/CT and MRI analysis of xenograft-bearing mice	122
53	Influence of long-term storage on synthetic flavagline efficacy	123
54	Schematic description of the difference in treatment preparation for <i>in vivo</i> and <i>in vitro</i> experiments	124
55	Influence of medium composition during treatment preparation on synthetic flavagline efficacy	125
56	Identification of FBS interaction with IMD-3 <i>in vitro</i>	126
57	Interaction of IMD-3 with FBS during treatment preparation enhances efficacy	127
58	Stability and solubility of IMD-3.	128
59	Tumour growth and survival upon treatment with IMD-3 and 2DG solubilised in HSA	129
60	GLUT-1-positive cells in xenograft tumours treated with IMD-3 solubilised in HSA	130
61	ESI-MS measurement of IMD-3 alone and in cell lysates	131
62	Exemplary ESI-MS measurement of IMD-3 in xenograft tumours	133
63	Path to clinical translation of synthetic flavaglines	135
64	Schematic comparison of IMD-3 preparation and application <i>in vivo</i> and <i>in vitro</i>	148
S1	Treatment sensitivity of different cancer entities	193
S2	Glucose uptake velocity in CRC cell lines	194
S3	Deregulated pathways in CRC cell lines	194
S4	Deregulated pathways in HPV-positive cell lines	195
S5	Cytotoxicity release of ³ H-thymidine from WT and IMD-3-resistant cells . . .	196
S6	Positive NGS screening example	196

S7	Deregulated pathways in WT and IMD-3-resistant cells	197
S8	DEGs upon IMD-3 treatment shared between cell lines	197
S9	Dose escalation: Individual tumour growth curves of 2DG- and IMD-1-treated mice	198
S10	Dose escalation: Individual tumour growth curves of IMD-3-treated mice	199
S11	Individual tumour growth curves of IMD-3 (1.0 mg/kg) and 2DG (100 mg/kg) treated mice	200
S12	IMD-3 stability in aqueous solution	201
S13	Individual tumour growth curves upon treatment with IMD-3 (1.0 mg/kg) and 2DG (100 mg/kg) solubilised in HSA	202
S14	ESI-MS measurements of xenograft tumours from mice treated with IMD-3	203
S15	ESI-MS measurements of xenograft tumours from mice treated with IMD-3 solubilised in HSA	205

List of Tables

1	List of used chemicals and reagents	25
2	List of consumables	30
3	List of used kits	32
4	List of used antibodies	33
5	List of primer sequences	34
6	List of used instruments	35
7	List of used software	38
8	List of used cell lines	39
9	List of self-made buffers	41
10	List of special cell culture media	44
11	<i>In vitro</i> treatment concentrations	46
12	DNA digestion and ligation	47
13	Inverse PCR	47
14	Cell numbers: Cell viability	49
15	Cell numbers: Senescence	51
16	Cell numbers: Microscopy slides	52
17	Cell numbers: Protein, RNA, DNA isolation	52
18	Cell number: Glucose uptake	53
19	IPA core analysis settings	59
20	LINE-1 PCR	60
21	Pyrosequencing	61
22	Tissue dehydration programme	64
23	Summary: Treatment sensitivity of different cancer cell entities	73
24	Overview: Deregulated genes and pathways upon IMD-3 treatment	93
25	Overview: Deregulated genes and pathways in treated WT and resistant cells	111
26	Dose escalation: Overview of survival	116
27	Survival of xenograft mice treated with IMD-3 and 2DG	121
28	Survival of xenograft mice treated with IMD-3 and 2DG solubilised in HSA	130
29	ESI-MS results of IMD-3-treated xenograft tumours	132
S1	IC ₅₀ concentrations of synthetic flavaglines	184
S2	Glucose uptake velocity of CaSki cells	185
S3	IPA: z-scores and p-values of deregulated pathways (z-score sorted)	186
S4	IPA: z-scores and p-values of deregulated pathways (p-value sorted)	188
S5	Selected DEGs in CRC and HPV-positive cell lines	189
S6	Glucose uptake velocity of WT and IMD-3-resistant cells	190
S7	Selected DEGs in WT and IMD-3-resistant cell lines	191
S8	IPA: z-scores and p-values of deregulated pathways in WT and resistant cells	192

Abbreviations

β -NAD	β -Nicotinamide adenine dinucleotide hydrate
2DG	2-Deoxy-D-glucose
5-FU	5-Fluorouracil
AKT	AKT serine/threonine kinase 1
APC	Adenomatous polyposis coli
BH	Benjamini-Hochberg
BSA	Bovine serum albumin
CKI	CDK inhibitor
CRC	Colorectal cancer
CT	Computed tomography
DABCO	1,4-Diazabicyclo[2.2.2]octane
DAC	5-Aza-2'-deoxycytidine
DEGs	Differentially expressed genes
DISC	Death-inducing signalling complex
DMEM	Dulbecco's Modified Eagle Medium
DMEM/F12	Dulbecco's Modified Eagle Medium/Nutrient Mixture F-12
DMSO	Dimethyl sulfoxide
dpm	Disintegrations per minute
DR	Death receptor
EdU	5-Ethynyl-2'-deoxyuridine
EGF/EGFR	Epidermal growth factor / Epidermal growth factor receptor
eIF	Eukaryotic translation initiation factor
ESI-MS	Electrospray ionisation mass spectrometry
EtOH	Ethanol
FBS	Fetal bovine serum
FC	Fold change
FDG	2-Deoxy-2-[¹⁸ F]fluoro-D-glucose
G6P	Glucose-6-phosphate
GLS	Glutaminase
GLUT-1	Glucose transporter 1
GPT	Glutamate-pyruvate transaminase
GSH	Glutathione
GT	Gene-trap
HIF-1	Hypoxia-inducible factor 1
HK	Hexokinase
HNPCC	Hereditary nonpolyposis colorectal cancer
HNSCC	Head and neck squamous cell carcinoma

ABBREVIATIONS

HPR	Horseradish peroxidase
HPV	Human papillomavirus
HSA	Human serum albumin
HSF1	Heat shock factor 1
HSPA8	Heat shock protein family A (Hsp70) member 8
ICB	Immune checkpoint blockade
IF	Immunofluorescence
IHC	Immunohistochemistry
IMD-1	IMD-026259
IMD-3	IMD-026260
IMDM	Iscove's Modified Dulbecco's Medium
IPA	Ingenuity Pathway Analysis
LDH	Lactate dehydrogenase
LSC	Liquid scintillation counting
MMR	Mismatch repair
MRI	Magnetic resonance imaging
MSI	Microsatellite instable / instability
MSS	Microsatellite stable / stability
NDUFA3A	NADH:Ubiquinone oxidoreductase complex assembly factor 3
NGS	Next generation sequencing
NRF2	Nuclear factor, erythroid 2 like 2
NSCLC	Non-small cell lung cancer
OTC	Organotypic co-culture
OxPhos	Oxidative phosphorylation
P/S	Penicillin/Streptomycin
PBS	Phosphate-buffered saline
PDK	Pyruvate dehydrogenase kinase
PET	Positron emission tomography
PFK	Phosphofructokinase
PGI	Phosphoglucose isomerase
PI3K	Phosphoinositide 3-kinase
PIK3CA	Phosphatidylinositol-4,5-bisphosphate 3-kinase catalytic subunit alpha
PIK3R1	Phosphoinositide-3-kinase regulatory subunit 1
PIK3R2	Phosphoinositide-3-kinase regulatory subunit 2
PK	Pyruvate kinase
PPP	Pentose phosphate pathway
QuPath	Quantitative Pathology and Bioimage Analysis
R5P	Ribose 5-phosphoshate
RCD	Regulated cell death

RHT	Rohinitib (synthetic flavagline derivative)
ROS	Reactive oxygen species
SDHC	Succinate dehydrogenase complex subunit C
SUV _{max}	Maximum standardised uptake value
TCA cycle	Tricarboxylic acid cycle
TFA	Trifluoroacetic acid
TGF- β 1	Transforming growth factor β 1
TXNIP	Thioredoxin interacting protein
UPR	Unfolded protein response
VEGF	Vascular endothelial growth factor
WB	Western blot
WT	Wild type
X-gal	5-Bromo-4-chloro-3-indolyl- β -D-galactopyranoside

Summary

Cancer is a major healthcare burden worldwide. Despite the high heterogeneity of malignant diseases, several characteristics, described as cancer hallmarks, are common among most tumours. Therapeutic approaches targeting these common features represent a promising path to universally applicable cancer therapy. One of such common cancer hallmarks is metabolic reprogramming, most prominently reflected by the phenomenon of the Warburg effect. The Warburg effect describes an enhanced metabolism of glucose via the glycolytic pathway instead of oxidative phosphorylation, which results in extremely high glucose consumption and glucose dependence in the majority of tumours. Attempts to target high glucose consumption of tumour cells by the glucose anti-metabolite 2-deoxy-D-glucose (2DG) were hampered by toxic side effects observed upon effective 2DG dosages. Previous work of the Department has shown a possibility to overcome these side effects by combining 2DG with flavaglines, a compound group with high anti-neoplastic potential. The successful chemical synthesis of flavaglines opened up a realistic perspective for clinical translation of the promising drug combination, previously inhibited by the limitations of the complicated extraction processes of natural flavaglines.

The present thesis aims to analyse the mechanisms of action of synthetic flavaglines and to perform first steps towards their preclinical evaluation. Specifically, the *in vitro* and *in vivo* characteristics of two novel synthetic flavagline compounds, IMD-1 and IMD-3, were analysed as well as mechanisms of potential therapy resistance.

Investigation of synthetic flavagline efficacy in cancer cell lines from different tumour tissues revealed great growth-inhibitory efficacy of IMD-3 treatment in all analysed cancer cell lines. In the majority of the analysed cell lines, the effect could be further enhanced by the combination of IMD-3 with 2DG. Synthetic flavaglines showed low unspecific cytotoxicity and mainly mediated their anti-cancer activity through proliferation inhibition and apoptosis induction. Furthermore, strong inhibition of glucose uptake, downregulation of glucose transporter 1 (GLUT-1) expression as well as inhibition of pentose phosphate pathway (PPP) activity could be identified as a common characteristic of IMD-3 treatment. Systematic analysis of treatment-related effects on the transcript level showed induction of cell cycle arrest and inhibition of glucose metabolism, confirming the *in vitro* observations. To analyse the effect of flavaglines and 2DG in 3D tissue context, tumour spheroids and a 3D co-culture model of tumour cells and normal keratinocytes were used. 3D culture models generally confirmed the mechanistic findings observed in 2D culture, however indicated a different efficacy range with higher drug concentrations or longer drug exposures required for achieving a similar growth-inhibitory effect as in 2D culture. The co-culture experiments also indicated compound doses allowing selective targeting of tumour cells while sparing normal tissue.

Generation of a haploid cell line showing long-term resistance towards IMD-3 treatment allowed the investigation of mechanisms responsible for synthetic flavagline resistance. Strikingly, in contrast to their sensitive counterpart, resistant cells showed no GLUT-1 downregulation upon IMD-3 treatment, whereas PPP activity was increased, indicating a shift in glucose metabolism of treatment-resistant cells. The transcriptome analysis of IMD-3-resistant cells, showing decreased glycolytic activity compared to sensitive cells, pointed at the possibility of using markers of glycolytic activity for prediction of therapy success.

For the *in vivo* evaluation of the anti-tumour activity of synthetic flavaglines a two-step experimental approach using a xenograft model (HCT116 cells in Rag2^{-/-}Il2rg^{-/-} mice) was followed. After an initial dose finding experiment, a second experiment with larger animal groups did not yield significant effects of flavaglines alone or in combination with 2DG regarding tumour growth and survival of animals. Positron Emission Tomography (PET) demonstrated no change in glucose uptake by tumour cells in any of the treatment groups. The analysis of possible reasons for the observed discordance between *in vitro* and *in vivo* efficacy data indicated modifications of the drug preparation for *in vivo* delivery as a potential reason. Although adapted preparation protocols for the flavagline solution allowed successful delivery of the substance to the tumour tissue, as proven by mass spectrometry, no significant effects on tumour growth and survival could be demonstrated in frame of the thesis. Future experiments shall quantify the substance concentration in tumour tissue and study the role of application routes on the drug delivery.

Taken together, the present thesis has identified downregulation of the glucose transporter GLUT-1 and inhibition of glucose uptake as major mechanisms of action of the examined synthetic flavagline derivatives. This observation together with *in vitro* data, demonstrating a significant and tumour cell-selective growth-inhibitory effect of flavaglines combined with 2DG, indicate the significant clinical potential of this substance group for cancer treatment. First *in vivo* data obtained in a murine xenograft model demonstrate that optimising pharmacokinetics, including drug delivery and application schemes, represents a major challenge for further preclinical development of flavaglines. Future studies shall therefore focus on optimising these steps in order to successfully translate the highly promising anti-tumour effects of synthetic flavaglines into the setting of living organisms.

Zusammenfassung

Krebs stellt weltweit eine große Belastung für das Gesundheitswesen dar. Trotz der hohen Heterogenität von Tumorerkrankungen sind einige Eigenschaften den meisten Tumoren gemeinsam. Therapeutische Ansätze, die auf diese gemeinsamen Eigenschaften abzielen, stellen daher einen vielversprechenden Weg zu universell einsetzbaren Krebstherapien dar. Eine dieser gemeinsamen Eigenschaften ist die metabolische Reprogrammierung, die sich am deutlichsten im Phänomen des Warburg-Effekts widerspiegelt. Der Warburg-Effekt beschreibt eine verstärkte Verstoffwechslung von Glucose über die Glykolyse anstelle der oxidativen Phosphorylierung, was in den meisten Tumoren zu einem hohen Glucoseverbrauch und einer Abhängigkeit von Glucose führt. Versuche den hohen Glucoseverbrauch von Tumorzellen durch den Glucose-Antimetaboliten 2-Desoxy-D-Glucose (2DG) auszunutzen, wurden durch toxische Nebenwirkungen erschwert, die bei wirksamen 2DG-Dosierungen auftraten. Frühere Arbeiten der Abteilung zeigten eine Möglichkeit diese Nebenwirkungen durch die Kombination von 2DG mit Flavaglinen, einer Substanzgruppe mit hohem antineoplastischem Potenzial, zu überwinden. Die erfolgreiche chemische Synthese von Flavaglinen eröffnet eine realistische Möglichkeit für die klinische Umsetzung dieser vielversprechenden Wirkstoffkombination, die zuvor durch die komplizierten Extraktionsprozesse natürlicher Flavaglinoide verhindert wurde.

Ziel der vorliegenden Arbeit ist es die Wirkmechanismen von synthetischen Flavaglinen zu analysieren und erste Schritte zu deren präklinischen Evaluierung durchzuführen. Konkret wurden die *in vitro*- und *in vivo*-Eigenschaften von zwei neuen synthetischen Flavaglinen, IMD-1 und IMD-3, sowie Mechanismen einer möglichen Therapieresistenz analysiert.

Die Untersuchung der Wirksamkeit der synthetischen Flavaglinoide in Krebszelllinien aus verschiedenen Tumorgeweben zeigte eine ausgeprägte wachstumshemmende Wirkung der IMD-3-Behandlung in allen analysierten Krebszelllinien. In der Mehrzahl der analysierten Zelllinien konnte der Effekt durch die Kombination von IMD-3 mit 2DG verstärkt werden. Dabei zeigten synthetische Flavaglinoide eine geringe unspezifische Zytotoxizität und vermittelten ihre Anti-Krebs-Aktivität hauptsächlich durch Proliferationshemmung und Apoptoseinduktion. Darüber hinaus konnte eine starke Hemmung der Glucoseaufnahme, eine Herabregulation der Expression des Glucosetransporters 1 (GLUT-1) sowie die Hemmung der Aktivität des Pentosephosphatweges (PPP) als gemeinsame Eigenschaften der IMD-3-Behandlung identifiziert werden. Die systematische Analyse der Behandlungseffekte auf Transkript-Ebene zeigte die Induktion des Zellzyklusstillstands und die Hemmung des Glucosestoffwechsels, was die *in vitro* Beobachtungen bestätigte. Um die Wirkung von Flavaglinen und 2DG im 3D-Kontext zu analysieren, wurden Tumor-Sphäroide und ein 3D-Co-Kulturmodell aus Tumorzellen und normalen Keratinozyten verwendet. Die 3D-Kulturmodelle bestätigten die in der 2D-Kultur beobachteten Mechanismen, wiesen jedoch auf einen anderen Wirksamkeitsbereich hin, wobei höhere Wirkstoffkonzentrationen oder längere Wirkstoffexposition erforderlich sind, um einen

ähnlichen wachstumshemmenden Effekt wie in der 2D-Kultur zu erzielen. Die Co-Kultur-Experimente zeigten auch ein selektives Angreifen von Tumorzellen bei gleichzeitiger Schonung des Normalgewebes für bestimmte Wirkstoffkonzentrationen.

Die Erzeugung einer haploiden Zelllinie, die eine stabile Resistenz gegenüber der Behandlung mit IMD-3 aufweist, ermöglichte die Untersuchung der Mechanismen, die zur Resistenz gegenüber synthetischen Flavaglinen führen. Dabei zeigte sich, dass die resistenten Zellen im Gegensatz zu ihrem sensitiven Pendant keine GLUT-1-Herabregulation nach der IMD-3-Behandlung aufweisen und eine erhöhte PPP-Aktivität besitzen, was auf eine Verschiebung des Glucosestoffwechsels in den behandlungsresistenten Zellen hinweist. Die Transkriptomanalyse der IMD-3-resistenten Zellen zeigte eine verringerte glykolytische Aktivität im Vergleich zu den sensitiven Zellen und deutete auf die Möglichkeit hin, Marker der glykolytischen Aktivität zur Vorhersage des Therapieerfolgs zu verwenden.

Für die *in vivo*-Evaluierung der Anti-Tumor-Aktivität der synthetischen Flavagline wurde ein zweistufiger experimenteller Ansatz unter Verwendung eines Xenograft-Modells (HCT116-Zellen in Rag2^{-/-}Il2rg^{-/-}-Mäusen) verfolgt. Nach einem ersten Dosisfindungsversuch, von Flavaglinen allein oder in Kombination mit 2DG, ergaben sich in einem zweiten Versuch mit größeren Tiergruppen keine signifikanten Effekte auf das Tumorwachstum und Überleben der Tiere. Die Positronen-Emissions-Tomographie (PET) zeigte in keiner der Behandlungsgruppen eine Veränderung der Glucose-Aufnahme in die Tumorzellen. Die Analyse möglicher Gründe für die beobachtete Diskrepanz zwischen den *in vitro*- und *in vivo*-Wirksamkeitsdaten wies auf eine Modifikation der Wirkstoffzubereitung für die *in vivo*-Verabreichung als möglichen Grund hin. Obwohl die Substanz, nach der Verabreichung der angepassten Flavaglin-Lösung, durch Massenspektrometrie im Tumorgewebe nachgewiesen werden konnte, konnten im Rahmen der Arbeit keine signifikanten Effekte auf das Tumorwachstum und Überleben nachgewiesen werden. Zukünftige Experimente sollten daher die Substanzkonzentration im Tumorgewebe quantifizieren und die Rolle der Applikationswege auf die Wirkstoffverteilung untersuchen.

Zusammenfassend wurden in der vorliegenden Arbeit die Herabregulation des Glucosetransporters GLUT-1 und die Hemmung der Glucoseaufnahme als wesentliche Wirkmechanismen der untersuchten synthetischen Flavagline identifiziert. Zusammen mit den *in vitro*-Daten, die eine signifikante und tumorzellselektive wachstumshemmende Wirkung von Flavaglinen in Kombination mit 2DG zeigen, weisen diese Beobachtung auf ein bedeutendes klinisches Potenzial dieser Substanzgruppe für die Krebstherapie hin. Die ersten *in vivo*-Daten, die in einem murinen Xenograft-Modell gewonnen wurden, zeigen, dass die Optimierung der Pharmakokinetik, einschließlich der Verabreichungs- und Applikationsschemata, eine große Herausforderung für die weitere präklinische Entwicklung von Flavaglinen darstellt. Zukünftige Studien sollten sich daher auf die Optimierung dieser Schritte konzentrieren, um die vielversprechenden Anti-Tumor-Effekte der synthetischen Flavagline erfolgreich in eine klinische Anwendung zu übertragen.

1 Introduction

1.1 Cancer and cancer hallmarks

Cancer is currently the worldwide second leading cause of annual deaths after cardiovascular diseases and accounts for 9.6 million deaths in 2018 [1, 2]. Due to improved diagnostics and prevention of cardiovascular diseases, cancer is predicted to become the primary cause of death, leading to an estimated number of 27 million cases and 16 million deaths in 2040 [3]. Although factors enhancing cancer risk, such as tobacco, alcohol consumption, obesity, UV radiation or infections, are similar worldwide, the incidence of cancer subtypes varies greatly between geographic regions and sexes, requiring specific preventive programmes [4, 5]. Prognosis of several cancer types, such as colorectal cancer (CRC), has improved over the years due to early detection methods and better treatment options, however still 18 % of women and 21 % of men develop cancer throughout their lives [3]. Conventional treatment options, such as chemo- and radiotherapy, are associated with severe side effects strongly influencing the life quality of patients due to non-specific targeting of highly proliferating cells affecting healthy tissue [6]. Therefore, research focused on the development of novel therapies specifically targeting cancer cell characteristics.

Cancer is a genetic disease caused by the accumulation of mutations leading to abnormal cell growth. Those mutations are caused by a complex interplay between the genetic predisposition of a person and environmental influences [3]. As a consequence, mutations found in each cancer are unique to each patient. However, over the years it has become evident that the underlying mechanisms responsible for malignant transformation are universal for all cancer types, leading to the definition of common cancer hallmarks (Fig. 1) [7]. The most obvious trait shared between cancer cells is their ability to sustain cell proliferation, which is usually highly regulated in normal tissue. Gain of function mutations or deregulation of negative-feedback loops lead to the activation of oncogenes, such as RAS, ensuring continuous growth-promoting signalling [7,8]. Also, upregulation of cellular receptors, such as epidermal growth factor receptor (EGFR), can induce enhanced signalling of oncogenic pathways driving tumour growth [9]. Besides activation of proliferative signals, cancer cells commonly acquire resistance against growth-inhibiting signals mediated by tumour suppressors, such as p53 or RB [7]. In normal tissue p53 and RB prohibit cell cycle progression and induce apoptosis as a result of intra- or extracellular signals [8]. Thus, inactivating mutations in tumour suppressor genes are found in the majority of cancers, with p53 representing the most frequently mutated gene [5]. Furthermore, genetic and epigenetic alterations in cancer cells can overcome other regulatory mechanisms, such as limited replicative potential and apoptosis induction [7]. Usually, replicative shortening of telomeres limits the life span of cells, which undergo replicative senescence or cell death due to telomere crisis. However, aberrant telomerase activity is detected in the majority of immortalised cells counteracting telomere shortening [8, 10, 11]. Telomere crisis can also

promote malignant transformation due to increased genome instability in the absence of functional tumour suppressors, such as p53 [8, 12]. Inactivation of p53 also enables the cancer cells to circumvent apoptosis induction [13], in parallel to deregulation of pro- and anti-apoptotic proteins belonging to the Bcl-2 family (see 1.2.3) [14]. The interplay of these molecular changes enables aberrant cell growth and tumour manifestation.

To sustain high proliferation, cancer cells require sufficient supply with oxygen and nutrients. Therefore, induction of angiogenesis is essential for the survival and outgrowth of cancer [15, 16]. Flipping the "angiogenic switch" through activation of growth factors, such as vascular endothelial growth factor (VEGF), enables the exponential outgrowth of dormant lesions, the growth of which is hampered at a size of 1-2 mm due to lacking vascularisation [17, 18]. Angiogenesis is also essential for invasive tumour growth and formation of distant metastases [17], which represent another major cancer hallmark [7].

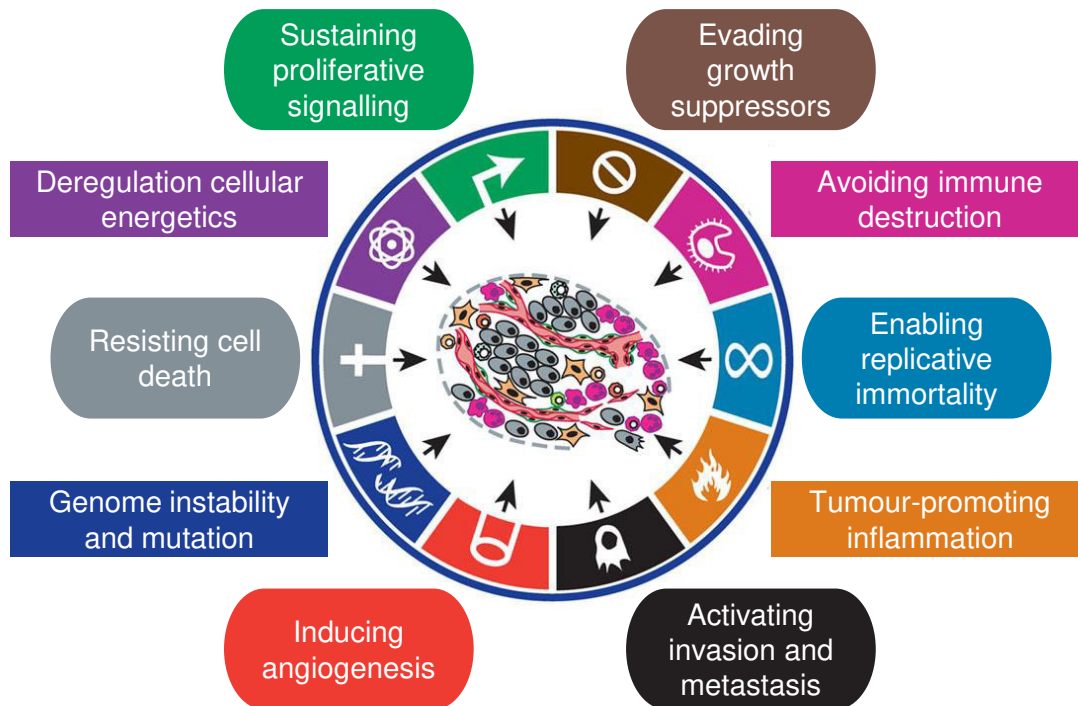


Figure 1: Cancer hallmarks enabling transformation and maintenance of the malignant phenotype. The first six identified cancer hallmarks (round) encompass ‘sustaining of proliferative signals’, ‘evading growth suppression’, ‘replicative immortality’, ‘angiogenesis induction’, ‘cell death resistance’ and ‘invasion and metastasis’. Further research identified four additional characteristics, of which ‘deregulation of cellular metabolism’ and ‘evasion of immune destruction’ display two novel cancer hallmarks, whereas ‘genome instability and mutation’ and ‘tumour-promoting inflammation’ were termed ‘enabling characteristics’ as they support the acquisition of all cancer hallmarks [7, 8]. Image was adapted from Hanah and Weinberg, 2011 [8].

Continuous research on the topic of common cancer features revealed novel characteristics shared between cancer cells, which contribute to tumour development (Fig. 1). Malignant transformation is driven by mutations, however normally DNA replication is highly regulated to avoid spontaneous mutations. Therefore, deregulation of the cellular control systems, including DNA repair, is essential for the acquisition of genome instability and mutations [8]. At the same time, high mutational load of cancer cells is accompanied by the generation of tumour antigens, which can be recognised by the immune system leading to the eradication of transformed cells [19]. To overcome immune surveillance and enable tumour manifestation, tumours often exploit immune evasion mechanisms [8]. One of the most prominent examples of cancer immune evasion is induction of T-cell exhaustion through PD-1/PD-L1 interaction by overexpression of PD-L1 in cancer cells [20]. Besides the anti-tumour activity of the immune system, persistent inflammation caused by tumour-infiltrating immune cells favours neoplastic transformation and tumour outgrowth [8, 21]. Another essential alteration found among different cancer types is reprogramming of cellular metabolism to fuel enhanced cell growth and proliferation, including enhanced glucose uptake, glutaminolysis and fatty acid synthesis [8, 22].

Detection of these cancer hallmarks has led to the development of novel therapeutic approaches targeting these cancer specific characteristics. For instance, targeting immune escape using monoclonal anti-PD-1 antibodies has achieved tremendous therapeutic effect in different cancer entities, leading to a response rate of 87 % in Hodgkin's lymphoma [23] and 53 % in patients with mismatch-repair-deficient cancers [24, 25]. Furthermore, angiogenesis inhibitors have shown great efficacy in mono- and combinatory therapy treating renal-cell cancer, CRC and non-small cell lung cancer (NSCLC) [26–28].

Another therapeutic approach, which has been evaluated in different experimental settings, is targeting altered cellular metabolism. However, therapeutic approaches targeting altered glucose metabolism in cancer cells have so far shown limited anti-cancer efficacy and remain challenging [29–32]. Therefore, novel approaches exploiting new therapeutic compounds and compound combinations, targeting altered glucose metabolism in cancer cells, are highly warranted.

1.2 Cell cycle arrest and cell death mechanisms

Common characteristics shared between cancer cells include unlimited growth and proliferation besides evasion of cell death to enable cancer progression [7, 8]. Thus, cancer therapy approaches aim to inhibit cell proliferation and induce cell death to hamper disease progression and induce cancer remission. This can be achieved through the induction of several cellular mechanisms, which control cell proliferation and cell death, including cell cycle arrest, apoptosis, necrosis or senescence.

1.2.1 Cell cycle arrest

Cell proliferation displays a tightly regulated process with the aim to prevent transfer of cellular damage to daughter cells. Three checkpoints during the cell cycle allow the cell to assess whether the circumstances for DNA replication and cell division are favourable [33].

In general, the cell cycle is divided into four phases with two gap phases, G_1 and G_2 , separating the S phase, during which DNA replication is performed, from chromosome separation and cell division during M phase [33]. Checkpoints regulate cell cycle entry at the end of G_1 phase, the entering of mitosis at G_2/M phase transition and chromosome separation at metaphase-to-anaphase transition [33]. Cell cycle progression at those checkpoints is regulated through assembly of cyclin-CDK complexes consisting of one cyclin-dependent kinase (CDK), activated by phosphorylation through CDK-activating kinases (CAK), and one cyclin protein [33]. Detection of DNA damage can prohibit cell cycle progression at the G_1/S or G_2/M checkpoint through inhibition of cyclin-CDK complex activity by binding of CDK inhibitor proteins (CKIs), such as p16 or p21, or phosphorylation by Wee1 kinase [33]. DNA damage triggers phosphorylation and activation of p53, which induces p21 expression leading to cell cycle arrest. Another pathway involves phosphorylation of CDC25, prohibiting downstream activation of M phase-CDKs and, thus, blocking M phase entry [33]. Defects occurring during chromosome separation lead to the inactivation of the anaphase-promoting complex (APC/C), which usually promotes anaphase transition [33].

In general, induction of cell cycle arrest allows for the repair of the detected damage before continuing the cell cycle. However, if normal cells experience too severe damage or abnormal signalling, apoptosis is triggered to eliminate the damaged cells. As a consequence, several regulators of cell cycle and cell cycle arrest, such as p53, RB, RAS, MYC and p16, are frequently mutated in cancer cells, allowing them to acquire mutations while maintaining continuous growth and proliferation [5, 33].

1.2.2 Cellular senescence

Cellular senescence describes a permanent cell cycle arrest with cells losing their ability to proliferate but remaining viable and metabolically active [34]. Several morphological and molecular characteristics are associated with the senescent phenotype, including flattened and enlarged cytoplasm, enlarged nuclei, altered chromatin structure, lysosome accumulation, aberrant β -galactosidase activity and stable expression of CKIs, such as p16 [34–37]. Detection of aberrant lysosomal activity of β -galactosidase at pH 6 using 5-Bromo-4-chloro-3-indolyl- β -D-galactopyranoside (X-gal) is a commonly used marker to identify senescent cells [37].

Replicative senescence was first detected in fibroblasts due to telomere shortening and loss of the protective protein cap at chromosome ends during DNA replication [33, 38, 39]. Telomeres are repetitive DNA sequences at the chromosome end synthesised by telomerases, which also mediate the formation of a protective protein cap [33]. However, due to telomerase de-

iciency in most somatic cells, telomeres are shortened during DNA replication, limiting the number of possible cell divisions before cellular senescence is induced due to DNA damage signalling [33]. Senescence can also be induced through other stress stimuli, including continuous cytokine, mitogen or growth factor stimulation, oncogene activation (e.g. RAS), loss of tumour suppressors (e.g. PTEN), chemotherapeutic drugs, radiation therapy and DNA damage independent from telomere shortening [36, 40, 41]. Upon those stimuli, senescence is mediated by the stable activation of CKIs, such as p21 and p16, through the p53/p21 or p16/RB pathway [35, 36]. Thus, senescence-mediated cell cycle arrest protects cells from possible malignant transformation upon severe damage [35, 36, 42].

Although senescent cells do not proliferate, they remain metabolically active influencing the surrounding microenvironment and neighbouring cells [36]. The so-called senescence-associated secretory phenotype (SASP) is characterised by the secretion of chemokines, cytokines, growth factors and proteases, and usually promotes inflammation and subsequent clearance of senescent cells, thus having tumour suppressive effect [36, 43]. However, if senescent cells are not cleared efficiently, the SASP can become a tumour promoting factor as it stimulates proliferation of neighbouring cells and enhances migration, invasion and angiogenesis [36, 43, 44]. This effect plays an important role in cancer therapy, as a broad spectrum of current therapeutics was found to induce senescence in cancer cells, including doxorubicin, irinotecan, cisplatin, 5-fluorouracil (5-FU) and several others [45]. Furthermore, senescence was long thought to be an irreversible process, however cells were found to escape their arrested state by acquisition of a more malignant phenotype [45]. Thus, therapy-induced senescence (TIS) could be responsible for tumour recurrence and elimination of senescent cells could enhance therapeutic effect [45]. Current research focuses on the elimination of senescent cells using senolytic drugs, which induce apoptosis in senescent cells [35, 43, 45]. For instance, elimination of senescent cells following doxorubicin treatment was found to reduce inflammation, tumour recurrence and treatment toxicity *in vivo* [46]. Furthermore, Rapamycin, an mTOR kinase inhibitor, was found to inhibit the SASP, reducing its tumour promoting features [43, 45]. Thus, senescence and the SASP play a crucial role in tumour suppression as well as in tumour promotion and understanding the influence of TIS is essential to develop novel therapeutic combination therapies to eliminate senescent cells and improve disease outcome.

1.2.3 Apoptosis

Cellular defects, such as DNA damage, lead to the induction of cellular safety mechanisms, including cell cycle arrest (see 1.2.1), cellular senescence (see 1.2.2) or regulated cell death (RCD), in case the damage cannot be repaired [33, 47]. Apoptosis displays the most common RCD pathway to eliminate unwanted and defect cells [33, 47]. It can be induced by external and internal factors leading to a coordinated destruction of the cell characterised by shrinking, collapse of the cytoskeleton, DNA fragmentation and formation of apoptotic bodies, which are cleared by macrophages or neighbouring cells [33, 47].

The major mediators of apoptotic cell death are caspases, a family of cysteine-dependent aspartate-specific proteases hydrolysing their substrates at aspartate residues, which are activated through proteolytic cleavage [48, 49]. Initiator caspases (caspase-2, -8, -9, -10) are activated upon death stimuli and lead to the downstream activation of effector caspases (caspase-3, -6, -7), which mediate apoptotic cell destruction [48, 50]. Effector caspases disrupt the cellular structure by cleavage of actin and lamin, and initiate DNA fragmentation through inactivation of DNA repair enzymes, e.g. poly(ADP-ribose)-polymerases (PARPs), or release of deoxyribonucleases, such as DFF40 by cleavage of the inhibitory domain DFF45. Furthermore, they activate p53 through cleavage of its inhibitor MDM2, increase intracellular reactive oxygen species (ROS) by disrupting the electron transport chain (ETC) and induce cellular blebbing [48, 49, 51, 52]. Caspase activity can be modulated in different ways, either through caspase inhibitors (cFLIP_L) competing with caspase-8 binding to the death-inducing-signalling-complex (DISC) [33] or inhibitors of apoptosis (IAPs), such as XIAP or cIAP1/2, prohibiting effector caspase-3, -7 and -9 activity (Fig. 2) [48, 53].

Extrinsic activation of apoptosis requires the binding of tumour necrosis factor (TNF) ligands (FAS-L, TNF α , TRAIL, TWEAK) to death receptors (DRs) belonging to the TNF receptor family, including FAS, TNFR1, TRAIL-R1 and -R2, and APO-3 [51, 54–56]. Upon ligand binding, signalling through the intracellular death domain leads to the recruitment of adaptor proteins and DISC assembly [33, 51, 57]. Depending on the activated receptor, DISC may consist of different adaptor proteins, which initiate downstream signalling cascades mediating cell death or, in case of TNFR1, pro-survival signals [51]. Ligand binding to the FAS receptor causes its trimerisation and intracellular association of FADD and procaspase-8. Subsequent oligomerisation of procaspase-8 leads to its autoproteolytic cleavage and activation, initiating downstream activation of effector caspases and cleavage of anti-apoptotic kinases, such as AKT, RIPK1 and FAK (Fig. 2) [51]. Similarly, activation of TNFR1 can lead to caspase-8 mediated apoptosis, if protein synthesis is hampered, or can induce caspase-2 dependent apoptosis through binding of adaptor proteins RIPK1 and CRADD [51, 56, 58].

Activity of the extrinsic apoptosis pathway can be modulated through modification of caspase activity or decoy receptors, which compete for ligand binding but lack the internal death domain required for signal transduction [51, 59].

In contrast to the extrinsic pathway, intrinsic or mitochondrial apoptosis is induced through DNA damage, cellular injury, lack of nutrients or oxygen and missing survival signals [14, 33]. The intrinsic apoptosis pathway is mainly regulated by pro- and anti-apoptotic proteins belonging to the Bcl-2 family [14]. Usually, anti-apoptotic proteins, such as BCL-2, MCL-1, and BCL-xL, bind the pro-apoptotic proteins BAX and BAK to prevent apoptosis. Induction of intrinsic apoptosis leads to the production and activation of BH3-only proteins [14, 33]. While missing survival signals induce BIM, p53 activation upon DNA damage induces PUMA and

NOXA [33]. BH3-only proteins bind to the anti-apoptotic Bcl-2 proteins and trigger the release of pro-apoptotic proteins BAK and BAX [14, 33, 60]. Released BAX translocates from the cytosol to the outer mitochondrial membrane, where oligomerisation of BAX and BAK causes mitochondrial outer membrane permeabilisation (MOMP) releasing cytochrome c, anti-IAP proteins (DIABLO, HTRA2), endonuclease G and apoptosis inducing factors (AIFs) into the cytosol [33, 57, 60]. Released cytochrome c associates with caspase-9 and APAF-1 forming the apoptosome complex, which subsequently activates the caspase cascade, including effector caspase-3 and -7 [53, 57] (Fig. 2). Interestingly, intrinsic apoptosis can also be triggered through the extrinsic pathway by caspase-8 mediated cleavage of the BH3-only protein BID to tBID, which subsequently inhibits anti-apoptotic Bcl-2 proteins [14, 33].

Overall, apoptosis displays a tightly regulated process ensuring coordinated destruction of damaged cells [14]. Thus, deregulation of apoptosis signalling is crucial for the survival of cancer cells and the manifestation of tumours, as it allows accumulation of mutations by preventing cellular destruction [7]. Several current treatment approaches focus on the reactivation of apoptosis in cancer cells either through stimulation of DRs using TNF α or TRAIL, or through activation of intrinsic apoptosis by blocking of anti-apoptotic Bcl-2 protein or IAP activity [14, 57, 61, 62]. Application of TRAIL in combination with radiotherapy or BH3 mimetics, such as ABT-737, have already shown promising results in preclinical research [63, 64].

1.2.4 Alternative cell death mechanisms

While apoptosis is the most common form of RCD, alternative mechanisms are in place to eliminate damaged cells and ensure the survival of the organism.

Acute injury causing severe cellular damage, such as extreme heat, sudden nutrient or oxygen shortage, induces uncontrolled, accidental cell death, referred to as necrosis [33, 65]. Necrotic cell death is characterised by the swelling and bursting of cells causing an inflammatory response, while lacking apoptotic characteristics, such as defined DNA fragmentation patterns [33, 65]. About 15 years ago another RCD pathway was identified exhibiting the same features as unregulated necrosis but being controlled through DR signalling, thus being named necroptosis [66]. Although necroptosis is induced through DR signalling, it is clearly distinct from apoptosis, as it lacks apoptotic characteristics, such as caspase and Bcl-2 family activity, membrane blebbing, defined DNA fragmentation and cytochrome c release [67, 68]. Activation of the protein kinases RIPK1 and, especially, RIPK3 is essential for necroptotic cell death [69, 70]. Necroptosis induction occurs upon activation of DR signalling leading to DISC assembly and subsequent ripoptosome formation in the absence of cIAPs and caspase-8 activity (Fig. 2) [71].

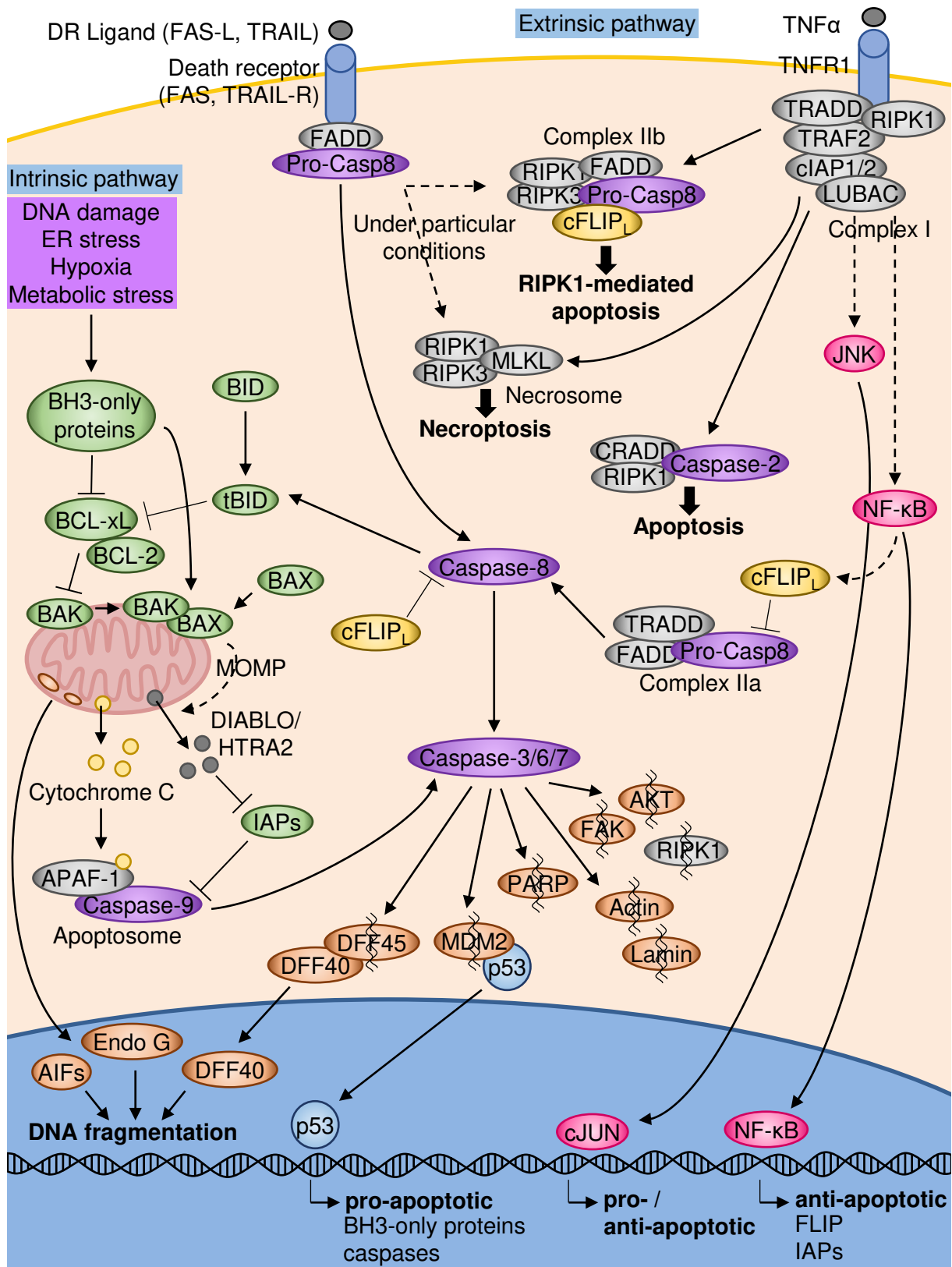


Figure 2: Overview of apoptotic cell death pathways. Extrinsic apoptosis is activated through DR signalling. Upon ligand binding intracellular signalling cascades are activated leading to caspase cleavage and subsequent apoptosis induction. Depending on the activated receptor and subsequent signalling cascade, DRs can also mediate survival signals or induce necroptosis. Intracellular stress signals, such as DNA damage, can activate the intrinsic apoptosis pathway leading to mitochondrial outer membrane permeabilisation (MOMP) releasing pro-apoptotic

Figure 2: proteins. Cytochrome C release causes apoptosome formation leading caspase cascade activation. p53, cJUN and NF- κ B can induce the transcription of pro- and anti-apoptotic genes. Caspases are highlighted in violet, while Bcl-2 proteins are shown in green. Image was based on [51, 53, 56, 57, 71].

Another pathway, the role of which in cell death is controversially discussed, is autophagy [69, 72, 73]. Usually, autophagy describes a cellular stress response to starvation, hypoxia or pathogen infections, as well as a quality control mechanism to eliminate damaged organelles and proteins [73–75]. Autophagosomes are double-membrane structures, which engulf cellular organelles and cytosol before fusing their outer membrane with lysosomes, causing degradation of their content, to regain amino acids and ensure cell survival [69, 75]. Although cell death with enhanced autophagosome formation was detected, it remains unclear if autophagy itself mediates cell death or if cell death is accompanied by autophagy [69]. Usually, autophagy inhibition does not prohibit cell death indicating its pro-survival activity, however autophagy can mediate cell death in cancer cells lacking apoptotic Bcl-2 proteins [34, 69, 76].

Throughout the years several other terms were introduced to describe cell death pathways, however the majority displays features of apoptosis or necrosis and, hence, cannot be described as distinct cell death mechanisms [34, 69, 76]. Thus, apoptosis and necrosis remain the most prominent examples of cell death, however continuous research has broadened the view of mechanisms responsible for cell death and increased the understanding of how organisms maintain cellular homeostasis [34].

1.3 Glucose metabolism and the Warburg effect

Glucose is one of the main sources for the cell to generate energy and precursor molecules for synthesis of cellular building blocks, such as nucleic acids [33]. In normal cells, incorporated glucose is metabolised through glycolysis leading to the generation of two molecules of pyruvate while yielding two molecules of ATP and NADH per molecule glucose (Fig. 3). Subsequently, pyruvate is transported into the mitochondria and converted to acetyl-CoA before entering the tricarboxylic acid (TCA) cycle generating activated carrier molecules NADH, FADH₂ and GTP, and important intermediates fuelling amino acid, fatty acid and nucleotide synthesis [33]. Generated NADH and FADH₂ are used to transfer electrons to the ETC in the inner mitochondrial membrane leading to the generation of up to 36 ATP molecules and CO₂ [33, 77]. While oxidative phosphorylation (OxPhos) requires the consumption of oxygen, glycolysis can proceed under anaerobic conditions. Anaerobic glycolysis maintains ATP production while recovering NAD⁺ from NADH through conversion of pyruvate to lactate by lactate dehydrogenase (LDH), ensuring continuous glycolysis [33].

Another pathway of glucose utilisation parallel to glycolysis, is pentose phosphate pathway (PPP) utilising the first glycolytic intermediate, glucose-6-phosphate (G6P), to generate pentoses, such as ribose 5-phosphoshate (R5P), required for nucleic acid synthesis (Fig. 3) [78]. Furthermore, the PPP is the major source for NADPH required to maintain cellular redox balance and fatty acid synthesis [78]. Thus, glucose metabolisation is essential to maintain cellular function, growth and proliferation.

Already in the 1920s, Otto Warburg described the switch of glucose metabolism from OxPhos towards glycolysis, even in the presence of oxygen, and increased glucose uptake in cancer cells, leading to the later designation of this phenomenon as ‘Warburg effect’ or aerobic glycolysis [79–81]. Although decline of cellular ATP production due to aerobic glycolysis seems to be detrimental, this metabolic phenotype is detected in the majority of human cancers, indicating that aerobic glycolysis has beneficial effects for cancer cell growth and proliferation [82]. ATP levels are not the limiting factor in proliferating cells and 10 - 100 times faster metabolisation of glucose to lactate through aerobic glycolysis compared to OxPhos generates the same amount of ATP in the same time upon glucose availability [77, 83]. At the same time, cancer cells strongly depend on rapid synthesis of macromolecules to enable fast growth and proliferation. Therefore, complete metabolisation of glucose through OxPhos into CO₂ and ATP would limit rapid biomass generation [77]. Aerobic glycolysis allows the cells to redirect glycolytic intermediates for synthesis of lipids, amino acids and pyrimidines or glycosylation of lipids and proteins (Fig. 3), while self-sustaining glycolysis through generation of required ATP and NAD⁺ [33]. Additionally, redirecting G6P towards the PPP enhances generation of NADPH and R5P required for maintaining cellular redox capacity and nucleotide synthesis [78]. To match their metabolic and anabolic demands cancer cells require substantially higher amounts of glucose. The increased need for glucose is often reflected in the upregulation of glucose transporters, such as GLUT-1, the most abundant glucose transporter [84], and GLUT-3, leading to an up to 200-fold increased lactate production [22, 79, 85]. Thus, a switch to aerobic glycolysis delivers a significant growth advantage for cancer cells providing required macromolecules.

Furthermore, rewiring of glucose metabolism allows tumours to survive the initial development phase with lack of sufficient vascularisation [22], while increased lactate secretion and resulting acidification of the microenvironment enables invasive growth of cancer cells [86]. Moreover, secreted lactate can be incorporated by adjacent tumour cells to fuel the TCA cycle and OxPhos [87]. It is important to note that, although increased aerobic glycolysis inhibits OxPhos through the ‘Crabtree effect’ [88, 89], cancer cells still require precursor molecules from the TCA cycle for growth and proliferation [30, 90]. Thus, parallel to increased glucose consumption, many tumour cells depend on glutamine metabolism to fuel the TCA cycle [90, 91].

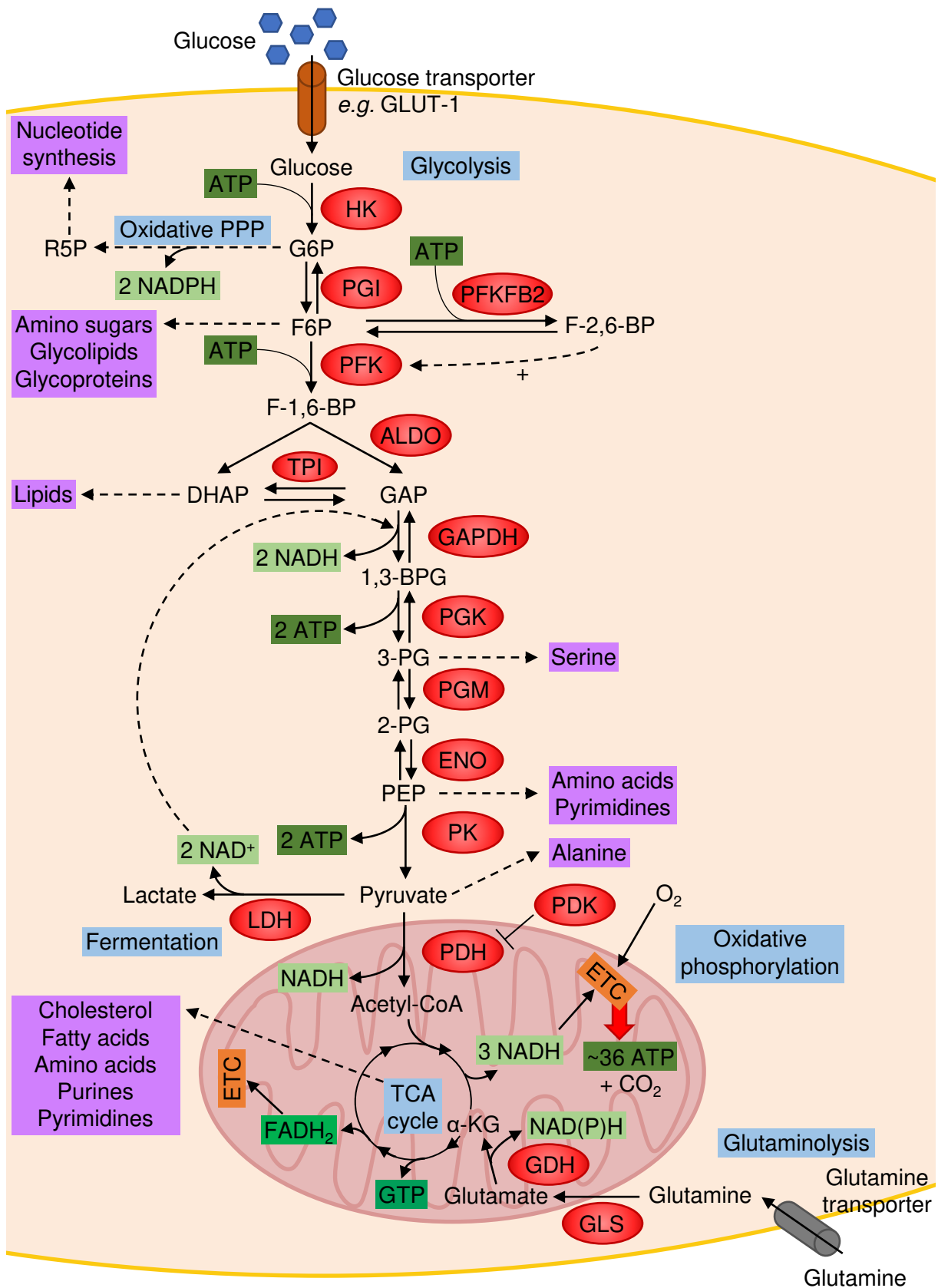


Figure 3: Overview of cellular glucose metabolism. Glucose is transported into the cells via glucose transporters (e.g. GLUT-1) and further metabolised through glycolysis resulting in a net gain of 2 ATP and 2 NADH for each molecule of glucose. In the presence of oxygen, pyruvate is oxidised in the TCA cycle enabling ATP generation through OxPhos. The TCA cycle can also be fuelled through glutaminolysis converting glutamine into α -KG.

Figure 3: In the absence of oxygen, pyruvate is converted to lactate to regain NAD^+ and sustain glycolysis. Precursor molecules generated during glucose metabolism can be used in other metabolic pathways. G6P: Glucose-6-phosphate, F6P: Fructose-6-phosphate, F-1,6-BP: Fructose-1,6-bisphosphate, F-2,6-BP: Fructose-2,6-bisphosphate, DHAP: Dihydroxyacetone phosphate, GAP: Glyceraldehyde-3-phosphate, 1,3-BPG: 1,3-bisphosphoglycerate; 3-PG: 3-Phosphoglycerate, 2-PG: 2-Phosphoglycerate, PEP: Phosphoenolpyruvate, α -KG: α -Ketoglutarate, HK: Hexokinase, PGI: Phosphoglucose isomerase, PFK: Phosphofructokinase, ALDO: Fructose-bisphosphate aldolase, TPI: Triosephosphate isomerase, GAPDH: Glyceraldehyde 3-phosphate dehydrogenase, PGK: Phosphoglycerate kinase, PGM: Phosphoglycerate mutase, ENO: Enolase, PK: Pyruvate kinase, PDH: Pyruvate dehydrogenase, PDK: Pyruvate dehydrogenase kinase, LDH: Lactate dehydrogenase, PFKFB: 6-Phosphofructo-2-kinase/fructose-2,6-bisphosphatase, GLS: Glutaminase, GDH: Glutamate dehydrogenase, ETC: Electron transport chain. Image was based on [33, 92, 93].

1.3.1 Cellular pathways regulating glucose metabolism

Rewiring of cellular metabolism is a complex interplay of different factors providing growth advantages and promoting tumour manifestation. The most prominent regulator of cell growth and glucose metabolism is the PI3K/AKT/mTOR pathway, which is activated in the majority of cancers [77, 92]. PI3K/AKT/mTOR signalling is activated upon growth factor stimulation, including EGFR, which expression is enhanced in 90 % of human carcinomas [84, 94, 95]. Furthermore, loss of function in tumour suppressors, such as PTEN, activating mutations in the PI3K subunit *PIK3CA* or downstream activation of AKT can promote PI3K/AKT/mTOR signalling [84, 92]. Enhanced pathway activity stimulates glucose metabolism through increased synthesis, plasma membrane incorporation and stabilisation of glucose transporters, such as GLUT-1 [92, 96, 97]. AKT activation promotes aerobic glycolysis through enhancement of hexokinase 2 (HK2) activity and indirect activation of phosphofructokinase 1 (PFK1), which catalyses the rate-limiting step in glycolysis [92]. Furthermore, AKT inhibits thioredoxin-interacting protein (TXNIP) activity, a negative regulator of glucose metabolism that usually reduces membranous GLUT-1 through internalisation (Fig. 3) [92]. Enhanced AKT signalling also increases PPP activity, promotes pyruvate to lactate conversion and enhances lipid synthesis [92]. Downstream of AKT, mTOR activation upregulates hypoxia-inducible factor 1 (HIF-1) expression. HIF-1, the major regulator of hypoxia [98], blocks pyruvate entry into the TCA cycle through upregulation of pyruvate dehydrogenase kinase (PDK) (Fig. 3) [92, 99, 100] and directly enhances expression of glycolytic proteins and glucose receptors, such as GLUT-1 [101, 102].

Taken together, enhanced PI3K/AKT/mTOR signalling modulates different aspects of glucose metabolism promoting the Warburg effect in cancer cells. Besides PI3K/AKT/mTOR activity, also other factors contribute to increased aerobic glycolysis, including microRNAs [99], loss of p53 [103, 104], isoform switches in glycolytic enzymes, such as pyruvate kinase (PK) [105], or enhanced PFK expression [106].

1.3.2 Application of glucose anti-metabolite 2-deoxyglucose in cancer

Aerobic glycolysis in cancer cells is accompanied by increased glucose uptake, distinguishing tumour cells from the surrounding normal tissue. This characteristic is already exploited in the clinic to visualise tumours using positron emission tomography (PET), allowing the non-invasive visualisation of many cancer lesions with a specificity and sensitivity of 90 % [82]. PET can be carried out by application of 2-deoxy-2-[^{18}F]fluoro-D-glucose (FDG), fluorine-labelled 2-deoxy-D-glucose (2DG) [107, 108]. Similar to glucose, its analogue 2DG is incorporated into the cell through glucose transporters and phosphorylated by hexokinases (HK) in the first step of glycolysis (Fig. 4A) [82, 99, 109]. However, due to the missing hydroxyl group at the C-2 position, downstream metabolisation of 2DG-6-phosphate (2DG-6P) by phosphoglucose isomerase (PGI) is prohibited and 2DG-6P accumulates in the tumour cells (Fig. 4A) [82]. This characteristic is exploited in PET imaging to visualise primary tumours and metastases, and to monitor treatment responses (Fig. 4B) [110].

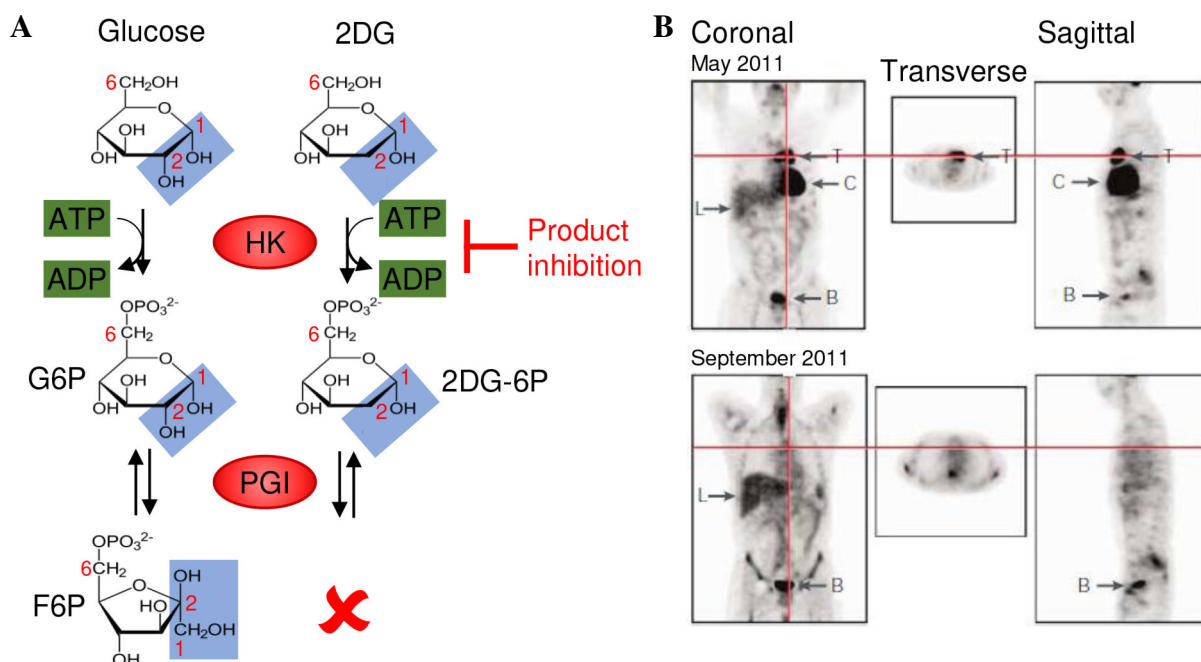


Figure 4: First steps of glucose or 2DG metabolisation through glycolysis (A) and application of FDG as PET tracer. (A) Metabolisation of glucose and 2DG in the first steps of glycolysis. Image was based on Hong and Hagen, 2015 [111]. (B) PET imaging of a lymphoma patient using FDG before (top) and after (bottom) chemotherapy. T: Tumour, L: Liver, C: Cardiac, B: Bladder. Image was taken from Gambhir, 2002 [108].

Besides its application as PET tracer, 2DG exhibits anti-cancer properties through inhibition of the glycolytic enzymes HK and PGI [104, 111, 112]. 2DG further reduces glucose metabolism through upregulation of TXNIP [111]. In prostate cancer cells, application of 2DG has been shown to reduce the glycolytic rate leading to decreased levels of NADH and ATP required for cell growth and proliferation [104]. Furthermore, altered protein glycosylation caused by 2DG

triggers ER stress due to misfolded proteins inducing the unfolded protein response (UPR), which subsequently induces apoptosis [113–115]. Interestingly, cancer cells were found to exhibit a higher sensitivity towards 2DG treatment compared to normal cells due to increased levels of ROS [116].

Anti-cancer efficacy of 2DG was found to be enhanced under hypoxic conditions, as cancer cells cannot circumvent glycolysis inhibition by increasing of OxPhos as possible under normoxic conditions [104, 117]. This effect might allow targeting of slowly proliferating cells in hypoxic areas of the tumour, which are usually less sensitive to chemotherapy [117]. Indeed, 2DG has been shown to enhance the efficacy of chemotherapeutic agents in different cancer entities [118–125], while showing little effect on normal cells [126] and reducing radiation-induced damage in normal tissue [127, 128].

Despite successful preclinical evaluation of 2DG, clinical studies assessing the efficacy of 2DG have shown limited success. Intravenous application of 2DG led to a partial response in cancer patients, however transient toxic side effects were observed upon application, including hyperglycaemia and diaphoresis among others [129]. Reduced dosages of 2DG, although better tolerated, showed limited clinical efficacy and did not slow down disease progression in patients with advanced solid tumours, also if applied in combination with other agents [31, 32]. Combination of 2DG with radiotherapy was tolerated by patients with gliomas, but improvement of the condition was only observed in 25 % of patients and treatment was accompanied by side effects, such as nausea, vomiting and hyperglycaemia [130]. Although a moderate increase in survival was detected in glioma patients, treatment tolerance varied greatly between patients leading to the early termination of the study for two patients [127].

Although 2DG application was successful in different preclinical settings, its clinical application is hampered due to associated side effects and minor treatment responses [29]. These might be related to the competition between 2DG and glucose, which is present at much higher concentrations. Glucose has a fasting blood concentration of approximately 1 g/l [131] and therefore might limit the effectiveness of 2DG treatment [132]. In addition, high dosages of 2DG have been shown to induce expression of the ABC transporter P-gp *in vitro* [133], possibly contributing to treatment resistance. Thus, to exploit the characteristics of 2DG in clinical application, novel combination approaches are required to increase its efficacy and reduce treatment associated side effects.

1.4 Flavaglines as promising anti-cancer compounds

1.4.1 Characteristics of natural flavaglines

Historically, the use of plants in medicine was essential for the treatment of diseases and led to the discovery of pharmacologically active compounds, such as morphine or salicin, a precursor of salicylic acid (Aspirin) [134]. Nowadays, derivatives of natural compounds still represent a promising direction in modern pharmacology and oncology, which is underlined by the approval of 14 natural derivatives for oncologic treatment between 2007 and 2013 [135].

The plant genus *Aglaia*, consisting of approximately 120 species, belongs to the family of *Meliaceae* and is mainly distributed in tropical and sub-tropical rainforests of the Pacific region and Southeast Asia [136–138]. It has been commonly applied in traditional medicine to treat fever, inflammation, contused wounds, cough or diarrhoea [138]. Isolation of secondary metabolites led to the discovery of three structurally related aromatic compound groups exclusive to the *Aglaia* plant genus: thapsakins, thapoxepines and flavaglines [138, 139]. Thapsakins are characterised by a cyclopenta[bc]benzopyran structure, while thapoxepines share a benzo[b]oxepines skeleton and flavaglines a cyclopenta[b]benzofuran skeleton [136, 138, 139]. The isolated compounds exhibited a great variety of biological effects, including anti-inflammatory, anti-fungal, insecticidal, molluscicidal, anti-viral and anti-bacterial activity [140]. Compared to thapsakins and thapoxepines, flavaglines, also called rocaglates, were found to exhibit pronounced cytotoxic activity in cancer cells [139].

The first flavagline, named rocaglamide (RocA), was isolated in 1982 by King *et al.* and exhibited anti-tumour activity against human epidermoid carcinoma cells *in vitro* and against lymphocytic leukaemia in mice [141]. Thus, RocA raised pharmacological interest in flavaglines, leading to the isolation and characterisation of more than 100 natural flavagline derivatives [138, 142]. Characterisation of different compounds revealed a variety of biological properties, including cytotoxicity, induction of cell cycle arrest, proliferation inhibition and protein synthesis inhibition in different human cancer cell lines *in vitro* and tumour growth inhibition *in vivo* [140, 143, 144]. One of the early detected characteristics of flavaglines is inhibition of protein synthesis [144], which is nowadays considered to be essential for their anti-tumour activity [135, 145].

Translation initiation displays the rate limiting step of eukaryotic protein synthesis and requires the presence of eukaryotic translation initiation factors (eIFs) to mediate 5'-capped mRNA translation [146, 147]. Translation initiation requires unwinding of the mRNA 5'-end by the helicase eIF4A to allow ribosome binding [147]. This process is highly regulated by other eIFs, including phosphorylation of eIF4E, which enables formation of the helicase complex and subsequent unwinding of the secondary mRNA structure [147]. Some flavagline derivatives were found to inhibit eIF4E phosphorylation and, as a consequence, prevent *de novo* synthesis of

the short-lived anti-apoptotic protein cFLIP, thereby sensitising tumour cells towards apoptosis-inducing agents [145, 148]. Interestingly, flavagline treatment only sensitised cancer cells towards apoptosis and did not affect normal T cells [145, 148], which makes flavaglines promising candidates for application in cancer therapy. Other flavagline derivatives were found to inhibit translation through enhancing helicase eIF4A-RNA binding [149–152].

Overall, flavagline derivatives induce cell cycle arrest and apoptosis in different cancer entities [143, 153, 154]. Although direct apoptosis induction seems to be only a minor part of their effect [153], flavaglines efficiently sensitise cancer cells towards apoptosis-inducing agents, such as TRAIL, FAS-L, cisplatin and TNF α , *in vitro* [145, 148, 155, 156]. *In vivo* studies of natural flavaglines, e.g. silvestrol, demonstrated promising anti-tumour activity through apoptosis induction and proliferation inhibition in xenograft models [149]. However, while prolonging survival of ALL xenograft mice [157], no anti-tumour activity was detected in other lymphoma mouse models [158].

Despite promising characteristics, such as high susceptibility of cancer cells towards flavagline treatment in comparison to normal cells *in vitro* [145, 148, 153, 159, 160] and their low toxicity in normal tissue demonstrated *in vivo* [149], further preclinical and clinical evaluation of flavaglines was hampered. The complicated extraction process of flavaglines and their relatively low abundance in the plant material impede the generation of large quantities of compounds required for clinical evaluation [138, 139]. Therefore, approaches to overcome these obstacles are of high importance to enable preclinical and clinical evaluation of flavaglines.

1.4.2 Chemical synthesis of flavaglines as a way to improve their availability and applicability

The obstacles in the production of natural flavaglines encouraged the development of several synthetic flavagline derivatives [137]. Chemical synthesis of flavaglines has several advantages over the extraction of natural compounds, including large scale compound synthesis, constant quality of the synthesised compound and the possibility to optimise their characteristics through adaptations of their chemical structure [137–139].

Due to the structural complexity of flavaglines, complete synthesis remains challenging [139] and first total synthesis of RocA was reported approximately 10 years after its first isolation in 1982 [135, 138, 161]. Since then, several different strategies have been developed to synthesise the flavagline skeleton and identify and optimise the structure-activity relationship, leading to the development of novel flavagline derivatives [135, 137, 162, 163].

Synthetic flavagline derivatives have been shown to target tumour cells by interacting with eIF4A helicase [151, 164–167], one of the major targets of natural flavaglines. They also showed specificity for cancer cells and synergised with chemotherapeutics [166–169], while counteracting the toxic effects of chemotherapeutics on normal cells [170, 171]. The synthetic

flavagline, Zotatfin, is currently investigated in a phase-I/II clinical trial against advanced solid tumours [172] and has recently regained attention due to its anti-viral activity against SARS-CoV-2 *in vitro* [173].

In parallel to unravelling biological features also found in natural flavaglines, research on synthetic flavaglines led to the discovery of a novel mechanism linking translation inhibition and cellular metabolism [174]. Santagata *et al.* revealed that translation inhibition reduces expression of genes regulated by heat shock factor 1 (HSF1) transcription factor. It was also demonstrated that the synthetic flavagline RHT prohibits HSF1 promoter binding, leading to enhanced expression of TXNIP and decreased glucose uptake in cancer cells [174]. Similar to other flavaglines, normal cells were less sensitive towards RHT treatment and little toxicity was detected *in vivo*, while leukaemia xenograft growth was inhibited [174]. The ability of flavaglines to influence cellular metabolism was recently supported by the findings of Chan *et al.* showing downregulation of glucose metabolism in pancreatic cancer *in vitro* and *in vivo* upon CR-1-31-B treatment [165].

Although synthetic flavaglines have shown promising anti-tumour activity in *in vitro* and *in vivo* studies with high selectivity for cancer cells, further research is required to better understand their mechanisms of actions, unravel pathways that may lead to therapy resistance, improve their pharmacological and toxicological characteristics, increase the therapeutic window and establish suitable dosage and treatment schedules [138].

The present thesis focuses on the characterisation of two novel synthetic flavagline derivatives, which were synthesised and kindly provided by IMAX Discovery GmbH (Konstanz, Germany). The two substances differ in the structure of their amine: IMD-026259 (hereafter IMD-1) contains a pyrrolidine ring (Fig. 5A), while IMD-026260 (hereafter IMD-3) contains a methylamino group (Fig. 5B).

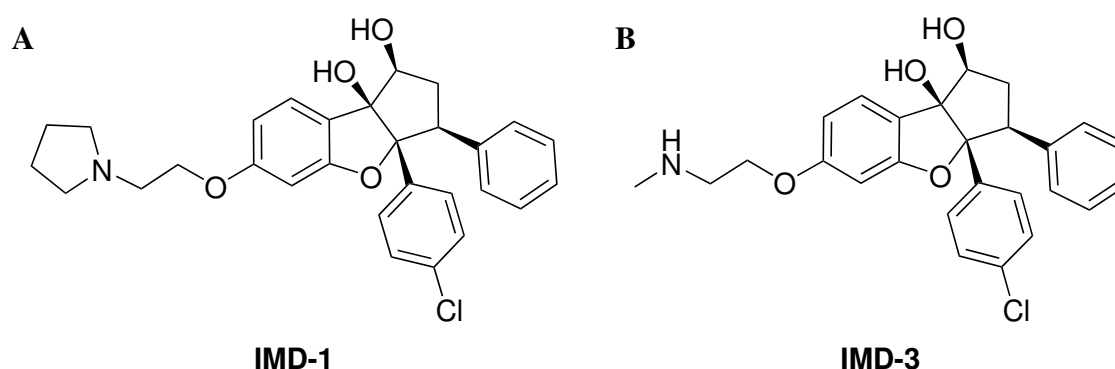


Figure 5: Chemical structures of flavagline derivatives IMD-1 (IMD-026259) (A) and IMD-3 (IMD-026260) (B).

Both substances were previously found to inhibit hypoxia-induced HIF-1-dependent gene expression in 293T and Jurkat cells at concentrations higher than 50 nM [175]. Both IMD substances decreased expression of the HIF-1 target gene PDK1 [175], which is usually upreg-

ulated in response to hypoxia and blocks pyruvate entry into the TCA cycle [92]. They also reduced HIF-1 α protein levels, a subunit of HIF-1, without inhibiting protein translation universally [175]. Furthermore, *in vitro* and *in vivo* application of IMD-3 inhibited angiogenesis [175], which is directly regulated by HIF-1 [98].

Due to the importance of HIF-1 signalling for maintaining altered cancer cell metabolism, combination of IMD-substances with other inhibitors of cancer cell metabolism, such as 2DG, could represent a promising strategy to enhance the anti-tumour activity of IMD substances and reduce required dosages, while exploiting high glucose dependence of cancer cells.

1.5 Colorectal cancer

Among both sexes, CRC displays the third most common cancer type worldwide with an incidence of 1.8 million new cases in 2018. It is the second most prevalent cancer in women (9.5 % of all sites) and third most prevalent cancer in men (10.9 % of all sites). In 2018, CRC accounted for 9.2 % of cancer-related deaths in both sexes having the second highest mortality after lung cancer (18.4 %). While in women CRC is the third most common cause of cancer-related death (9.5 %) following breast and lung cancer, in men CRC is responsible for 9.0 % of cancer-related deaths, ranking forth after lung, liver and stomach cancer [2].

Although CRC was relatively rare in the 1950s [176], its incidence rose in the last years especially in countries with a rising or high Human Development Index [2]. Hence, CRC displays a socio-economic disease and its incidence is strongly influenced by ageing of the population and life style changes, including diet, obesity and physical activity [2]. While increased physical activity has a protective effect on colon cancer incidence, increased red and processed meat consumptions are negatively correlated [2, 176]. Thus, CRC incidence varies greatly between regions, being most prevalent in Europe, Australia/New Zealand, North America and Eastern Asia, while having the lowest incidence in South Asia and Africa [2]. In contrast to CRC incidence, CRC-related mortality decreases in developed countries due to better screening programmes and treatment options, as patient survival strongly correlates with the CRC stage at diagnosis [2, 176, 177]. While patients with distant metastases only have a 5-year survival rate of 10 %, earlier detection improves survival of patients with regional disease to 70 % and detection at a localised stage enhances survival to 90 % [176–178].

The majority of patients diagnosed with sporadic CRC is older than 50 years, with 80 % of colon and 75 % of rectal cancer patients being over 60 years [176]. 95 % of sporadic CRCs arise through polyp formation, which can already be detected at an early stage by colonoscopy [176, 177, 179, 180]. Thus, preventive CRC screenings starting at an age of 50 reduce overall CRC incidence and mortality [181, 182]. However, CRC incidence rises in adults under age of 50 years, requiring adaption of screening programmes [183, 184]. While the majority of CRCs arises sporadically [185], 15 - 20 % of patients show increased CRC risk due to familial history often associated with earlier disease onset and thus also require different diagnostic methods starting at an early age [177, 186, 187].

Hereditary CRC syndromes cause about 5-10% of all CRCs [187]. The two most common hereditary syndromes are hereditary nonpolyposis colorectal cancer (HNPCC), also called Lynch syndrome, and familial adenomatous polyposis (FAP) [177].

FAP is inherited via a germline mutation in the adenomatous polyposis coli (*APC*) gene and associated with approximately 100% CRC risk until the age of 40 without clinical intervention [177, 179]. In contrast to FAP patients predisposed to developing hundreds to thousands of colonic polyps [188], HNPCC patients have only slightly increased risk of polyp formation compared to the general population [189, 190]. However, HNPCC carriers have a lifetime risk of approximately 50% to develop CRC or endometrial cancer (EC) [191, 192]. Besides increased risk for CRC and EC, mutation carriers have an overall increased risk to develop cancer in other organs, including the small intestine, stomach and ovaries [185].

A hallmark of HNPCC is manifestation of tumours showing a specific molecular phenotype, called microsatellite instability (MSI). This phenotype, observed in 15% of all CRC cases, arises upon deficiency in the DNA mismatch repair (MMR) system due to biallelic inactivation of one of the MMR genes (*MLH1*, *MSH2*, *MSH6*, *PMS2*) [185, 193]. Sporadic MSI tumours (12% of all cases) arise due to promoter methylation and subsequent silencing of the *MLH1* gene [185]. In case of hereditary MSI tumours, one of the alleles is affected in the germline and the second one is inactivated by a somatic hit (Knudson's Two Hit Theory) [194]. In both, sporadic and hereditary MSI tumours, MMR deficiency causes accumulation of insertion/deletion mutations during DNA replication, especially at repetitive DNA sequences (microsatellites), resulting in a frameshift. When these mutations hit microsatellites residing within tumour-suppressor genes, they may lead to loss of tumour suppressor function and contribute to tumour development [195–197]. At the same time, these mutations lead to the generation of frameshift neoantigens, rendering MSI tumours highly immunogenic and resulting in the commonly observed dense immune infiltration of MSI tumour [198, 199]. The high immune-selective pressure causes outgrowth of cell clones with acquired immune escape mechanisms, such as loss of antigen presentation, either through β 2-microglobulin mutation, a part of HLA class I molecules, or mutation of HLA class II regulators, *RFX5* and *CIITA* [200]. The major role of immunoediting during MSI tumour evolution was recently underlined by the molecular evidence indicating elimination of mutations associated with high immunogenicity, unless they bring a substantial growth advantage outweighing the disadvantage of immune visibility [201].

Besides its influence on the tumour development, the MSI phenotype also impacts clinical treatment outcome. Overall, MSI patients have substantially improved survival rate compared to patient with equally staged microsatellite stable (MSS) tumours [185]. However, MSI cancer patients seem to have limited benefit from 5-FU treatment with some studies reporting detrimental effects in MSI cancer patients upon therapy [202, 203]. In contrast, MSI cancer patients benefit from irinotecan-based chemotherapy, which could be ascribed to impaired DNA damage repair and resulting synthetic lethality [204]. Targeted therapy approaches, using VEGF, EGF

or kinase inhibitors, have shown beneficial effects on life quality and survival of metastatic CRC patients, however the therapeutic outcome strongly depends on the mutation status of the patient [181, 205–207]. Importantly, due to their high immunogenicity, cancers with MSI phenotype show great response to immune checkpoint blockade (ICB) therapy irrespective of their organ of origin [24, 25]. This led to first FDA approval of cancer therapy based on a biomarker alone [208]. Still, a certain proportion of MSI and a substantial proportion of MSS CRC remain resistant to currently applied therapeutic approaches [209], underlining the need for alternative treatment approaches.

In the last years, aerobic glycolysis and GLUT-1 overexpression were associated with CRC development and treatment resistances [89]. Additionally, APC mutations were found to enhance glucose consumption and lactate secretion by increasing the expression of glycolytic enzymes PKM2 and LDHA [210]. Inhibition of LDHA was found to decrease glucose uptake and ATP production, leading to reduced CRC cell growth *in vitro* [211]. Also, mutations of *PIK3CA*, a subunit of PI3K modulating the Warburg effect in cancer cells (see 1.3), were identified in one third of CRCs [179]. Analysis of metabolic genes in CRC tissue samples revealed increased glycolysis and PPP activity, while showing downregulation of TCA cycle genes due to MYC deregulation [212]. Thus, targeting aerobic glycolysis in CRC might display a novel treatment approach and could counteract treatment resistance.

1.6 Human papillomavirus-associated cancers

In 2018 pathogen infections caused over 2 million cancers worldwide with *Helicobacter pylori* being the most prevalent, leading to approximately 0.8 million new cases, followed by human papillomavirus (HPV) infections, accounting for ca. 0.7 million cases [213]. Almost 100 % of cervical cancers are associated with HPV infections having the fourth highest incidence (6.6 % of all sites) and mortality (7.5 % of cancer-related deaths) in women worldwide [2, 214]. Cervical cancers represent 80 % of all HPV-associated cancers, which include anogenital and oropharyngeal cancers [215]. Female patients bear approximately 90 % of HPV-attributed cancer burden [213]. HPV-associated cancer strongly correlates with low country income levels, showing the highest incidence in sub-Saharan Africa, Southeast Asia, Central and East Europe, South America and India [213]. Low and high income levels also influence the distribution of HPV-cancer types with higher income countries exhibiting a greater proportion of affected men as well as head and neck squamous cell carcinomas (HNSCC) and anogenital cancers [2]. Improved cervical screening methods to detect pre-cancerous lesions and preventive vaccinations against high-risk HPV types have reduced incidence and mortality of cervical cancer in high income countries [213]. However, worldwide reduction of cervical cancer burden requires more effective vaccination strategies, which are hampered by financial and political barriers in low-income countries [2, 213].

Overall, more than 200 different HPV types are known, of which only a small subset of high-risk HPVs is associated with cancer development [214, 216]. High-risk HPV types 16 and 18 account for approximately 72 % of HPV-related cancers, while another 17 % are caused by HPV 31, 33, 45, 52 and 58 [213]. The majority of HPV infections is cleared by the immune system [217, 218]. However persistent infections with low-risk HPV types can lead to the formation of benign lesions (e.g. warts), while high-risk HPVs can cause malignant lesions over time [218, 219].

HPVs are double-stranded DNA viruses, which infect the dividing basal epithelial cells of the skin and mucosa through minor injuries in the epithelium. Replication of the viral episomes requires expression of the early phase viral proteins E1 - E7 and depends on the host replication machinery [218–221]. Re-initiation of S phase by the viral proteins E6 and E7 increases the number of replicated viral genomes in the cell. Subsequently, virus assembly and shedding occur in the upper epithelial layer upon late phase L1 and L2 capsid protein expression [219, 220, 222]. During the permissive state, expression of viral proteins is tightly regulated, leading to generation of more virus carrying cells and virus release [218]. Virus replicating cells exhibit distinct cellular changes including a thickened cytoplasmic rim, perinuclear vascularisation and nuclear hyperchromasia, which characterise cervical intraepithelial neoplasia grade I (CIN I) lesions [218]. Only a small subset of permissive lesions develops into pre-cancerous CIN II or III lesions or invasive cancer [218]. Cell proliferation and immortalisation is caused by the overexpression of the viral oncogenes E6 and E7 upon loss of E2, which controls viral gene expression [214, 223]. E6 and E7 inhibit the activity of the tumour suppressors p53 and RB, leading to aberrant S phase gene expression, DNA replication, chromosomal instability and apoptosis evasion [214, 224].

The standard therapy for HPV-induced neoplasias and cancers encompasses surgery to remove affected tissue and additional (neo-)adjuvant chemo- and/or radiotherapy in case of cancer [218]. However, these treatments are accompanied by several complications including damage of normal healthy tissue, cosmetic impairments, anal and sexual dysfunction or premature delivery [225–228]. Furthermore, patients need to undergo repetitive surgeries due to disease recurrence, which is observed in 10 - 40 % of patients with high-grade anogenital lesions [229]. Currently, HPV status does not influence treatment decisions, however distinguishing between HPV-positive and HPV-negative cancers is of high clinical relevance, as patients with HPV-positive oropharyngeal squamous cell carcinomas exhibit a better prognosis and may require treatment de-escalation in order to prevent treatment-associated long-term morbidity [218, 230, 231].

HPV-transformed tumours were found to frequently exhibit upregulation of PI3K/AKT/mTOR signalling [232, 233], a major regulator of the Warburg effect (see 1.3) [77], and enhanced levels of GLUT-1 expression were detected in HPV-positive HNSCCs [234]. Furthermore,

viral oncogenes were found to promote the Warburg effect through HIF-1 α induction and subsequent upregulation of glycolytic enzymes and regulators, such as HK2, PKM2, PDK1 or LDH [216,235–239]. Initial studies targeting mTOR in HPV-positive HNSCCs increased long-term survival *in vivo* [236], while inhibition of PI3K/mTOR signalling enhanced sensitivity of HNSCCs towards radiotherapy [240]. Thus, targeting the Warburg effect in HPV-positive cancer might display a novel treatment option reducing side effects associated with chemotherapy or ablative surgery.

1.7 Treatment resistances in clinical oncology

The development of novel targeted therapy approaches significantly improved clinical outcome for cancer patients [241, 242]. However, intrinsic and acquired drug resistances and lack of reliable prognostic markers to predict treatment responses, display a major obstacle in cancer therapy [241, 243].

Overall, direct mutation of genes encoding the target protein, downstream alterations in the targeted pathway or activation of parallel pathways, modification of drug efflux and metabolism, evasion of growth arrest or death signalling, cancer immunoediting and changes in the tumour microenvironment can contribute to resistance development [241, 244]. For example, therapeutic approaches targeting EGFR, a commonly overexpressed molecule in carcinomas [94], can become ineffective in tumours with mutations downstream of the EGFR in the MAPK signalling pathway, leading to constitutive activation of the pathway irrespectively of external signalling [206, 207, 245]. Even among MSI cancer patients treated with ICB, representing a major breakthrough in cancer therapy, a substantial proportion does not respond to therapy. Currently, mechanisms of resistance to ICB are rigorously researched and studies indicate alterations in neoantigen expression, processing or presentation on MHC molecules, microenvironmental changes impairing T cell function and lack of memory T cells as possible resistance mechanisms [242, 246, 247].

Furthermore, tumour heterogeneity plays an important role in resistance development, as the selective pressure potentially introduced by drug application can lead to outgrowth of resistant cell clones [241, 244]. The small population of stem-like cancer cells can survive initial drug treatment due to their quiescent state and thus can acquire mutations over time establishing drug resistance [241]. Adaptations leading to drug resistance are not restricted to the acquisition of genetic mutations, but can also be mediated by epigenetic changes, including DNA methylation or histone modification by acetylation, phosphorylation or methylation [248]. Epigenetic changes allow faster adaptation towards drug exposure compared to genetic mutations, as they can occur more rapidly and also persist upon drug removal [241, 249, 250].

Adaptation of metabolic pathways, including fatty acid synthesis, TCA cycle and glucose metabolism among others, also plays a crucial role in resistance development of tumours [89,251]. For instance, alterations in pyrimidine metabolism were found to mediate resistance towards decitabine and 5-azacytidine therapy in myeloid malignancies [252].

Furthermore, different pathways of glucose metabolism were found to be involved in mechanisms of therapy resistance. Besides increased PPP activity contributing to treatment resistance [253,254], enhanced aerobic glycolysis was found to mediate chemoresistance in different tumour entities [89] and targeting this characteristic has been shown to be capable of restoring sensitivity towards the treatment. For instance, 2DG was found to re-sensitise glucocorticoid-resistant primary leukaemia cells towards glucocorticoid treatment [255] or applied in combination with kinase inhibitors prevent HIF-1 α -induced resistance in cervical cancer cells arising upon single treatment with kinase inhibitors [235].

There is a great diversity of resistance mechanisms depending on the cancer entity, the applied treatment, as well as the mutational landscape of each individual tumour [256]. Although research contributed substantially to elucidation of the mechanisms underlying treatment resistance in cancer, resistance still displays a major obstacle in successful cancer therapy. Thus, it is important to understand possible treatment resistance mechanisms parallel to the development of novel drugs in order to enhance the understanding of the molecular mechanisms of action, develop suitable strategies to circumvent arising treatment resistances and identify biomarkers capable of reliably predict therapy success in the clinic.

1.8 Rationale and aims of the project

Although initiating events leading to cancer development differ between various cancer types, common traits that are required to sustain abnormal growth and survival are shared across cancers. These shared cancer hallmarks represent promising targets for designing tumour therapeutic approaches. One of the most common cancer hallmarks is an increased glucose demand due to Warburg effect. This hallmark is already exploited in clinical tumour diagnostics for tumour visualization using a labelled glucose analogue, ^{18}F -2DG. However, therapeutic application of 2DG has so far only shown limited anti-tumour effects.

Recently, combination of 2DG with flavaglines, compounds found in extracts from the plant genus *Aglaia*, has shown potent anti-cancer efficacy. The successful chemical synthesis of flavaglines allowed their standardised high through-put production enabling clinical translation for tumour therapy. The present PhD thesis aims at characterising the *in vitro* and *in vivo* anti-cancer effects of novel synthetic flavagline derivatives and preparing the ground for their preclinical and clinical evaluation.

To establish a better understanding of the mechanisms underlying the biological effects of synthetic flavaglines, their cytotoxicity, influence on cell proliferation, apoptosis, and cellular senescence shall be evaluated *in vitro*. Furthermore, influence of synthetic flavaglines on glucose metabolism shall be examined by investigating glucose uptake, glycolysis and pentose phosphate pathway activity in cancer cells.

To unravel potential resistance mechanisms towards synthetic flavaglines, a treatment-resistant cell line shall be generated using gene-trap mutagenesis approach and the differences between wild type and gene-trapped cells shall be evaluated. For this, the above-mentioned characteristics shall be investigated focusing on cell death mechanisms triggered by flavaglines and alterations in glucose metabolism upon synthetic flavagline treatment.

Besides the *in vitro* characterisation of synthetic flavaglines, first steps shall be performed for the assessment of their anti-cancer potential *in vivo*. For this, the efficacy of synthetic flavaglines shall be evaluated using a murine xenograft model aiming at finding the optimal dosage of synthetic flavagline and 2DG treatment alone and in combination and analysing potential side effects induced by the treatment.

Overall, the present PhD thesis aims to (I) characterise the anti-cancer activity of synthetic flavaglines alone and in combination with 2DG with a particular focus on cell death mechanisms and glucose metabolism, (II) elucidate cellular mechanisms responsible for resistance towards synthetic flavaglines and clarify the crucial mechanisms of action underlying the anti-cancer activity and (III) perform first *in vivo* evaluation of synthetic flavagline treatment in a xenograft mouse model.

2 Material

2.1 Chemicals and reagents

Table 1: List of used chemicals and reagents.

Reagent	Supplier (City, Country)
β -Mercaptoethanol for synthesis	Merck KGaA (Darmstadt, Germany)
β -Nicotinamide adenine dinucleotide hydrate (β -NAD)	Sigma-Aldrich (St. Louis, USA)
1,4-Diazabicyclo[2.2.2]octane (DABCO)	Carl Roth (Karlsruhe, Germany)
2-Deoxy-2- ^{18}F fluoro-D-glucose (FDG)	Small Animal Imaging Center (DKFZ) (Heidelberg, Germany)
2-Deoxy-D-glucose	Sigma-Aldrich (St. Louis, USA)
2-Deoxy-D-glucose (99 %)	ACROS Organics (Geel, Belgium)
2-Phospho-L-ascorbic acid-trisodium salt ($\geq 95\%$)	Sigma-Aldrich (St. Louis, USA)
4',6-Diamidino-2-phenylindole dihydrochloride (DAPI)	Sigma-Aldrich (St. Louis, USA)
5-Aza-2'-deoxycytidine (DAC)	Sigma-Aldrich (St. Louis, USA)
AccuPrime Polymerase	Thermo Fisher Scientific (Waltham, USA)
Acetone	Honeywell International Inc. (Charlotte, USA)
Acetonitrile	Sigma-Aldrich (St. Louis, USA)
Adenine (suitable for cell culture)	Sigma-Aldrich (St. Louis, USA)
Agarose	Biozym Scientific GmbH (Oldendorf, Germany)
Ammonium sulfate ($(\text{NH}_4)_2\text{SO}_4$)	AppliChem (Darmstadt, Germany)
Aprotinin	Carl Roth (Karlsruhe, Germany)
<i>Aqua ad injectabilia</i> (Ampuwa [®])	Fresenius Kabi Deutschland GmbH (Bad Homburg, Germany)
Aquatex	Merck (Darmstadt, Germany)
bi-Distilled Water (MilliQ)	Merck Millipore (Darmstadt, Germany)
Boric acid	neoFroxx GmbH (Einhausen, Germany)
Bovine serum albumin (BSA), Fraction V	Sigma-Aldrich (St. Louis, USA)
Bovine serum albumin solution (20 mg/ml)	Sigma-Aldrich (St. Louis, USA)

Reagent	Supplier (City, Country)
Bradford reagent (Protein Dye Reagent Concentrate)	Bio-Rad Laboratories GmbH (Munich, Germany)
Buffer solution pH 10 TITRINORM®	VWR International S.A.S. (Fontenay-sous-Bois, France)
Buffer solution pH 4 TITRINORM®	VWR International S.A.S. (Fontenay-sous-Bois, France)
Buffer solution pH 7 TITRINORM®	VWR International S.A.S. (Fontenay-sous-Bois, France)
Buffer substance Dulbecco's	Serva Electrophoresis GmbH (Heidelberg, Germany)
Calcium chloride dihydrate (CaCl ₂ • 2 H ₂ O)	Merck KGaA (Darmstadt, Germany)
Cholera toxin from <i>Vibrio cholerae</i>	Sigma-Aldrich (St. Louis, USA)
cis-Diamineplatinum(II) dichloride	Sigma-Aldrich (St. Louis, USA)
Citric acid monohydrate	Merck (Darmstadt, Germany)
Deoxy-D-glucose, 2-[1- ³ H] (1 mCi/ml)	American Radiolabeled Chemicals Inc. (St. Louis, USA)
Dimethyl sulfoxide (DMSO)	Serva Electrophoresis GmbH (Heidelberg, Germany)
di-Sodium hydrogen phosphate dihydrate (Na ₂ HPO ₄ • 2 H ₂ O)	Carl Roth (Karlsruhe, Germany)
DL-Norleucin	Sigma-Aldrich (St. Louis, USA)
DNA Ladder, 100 bp	Invitrogen GmbH (Darmstadt, Germany)
Dulbecco's Modified Eagle Medium (DMEM); 1.0 g/l glucose	Life Technologies (Carlsbad, USA)
Dulbecco's Modified Eagle Medium (DMEM); 4.5 g/l glucose	Life Technologies (Carlsbad, USA)
Dulbecco's Modified Eagle Medium (DMEM); No glucose	Life Technologies (Carlsbad, USA)
Dulbecco's Modified Eagle Medium / Nutrient Mixture F-12 (DMEM / F12)	Life Technologies (Carlsbad, USA)
Dulbecco's PBS (without Ca & Mg)	Life Technologies (Carlsbad, USA)
Ethylenediaminetetraacetic acid (EDTA)	Sigma-Aldrich (St. Louis, USA)
EGF, human recombinant (<i>E. coli</i>)	PromoCell GmbH (Heidelberg, Germany)
Eosin	Waldeck GmbH & Co. KG (Münster, Germany)

Reagent	Supplier (City, Country)
Ethanol (96 %)	Zentrallager INF 367 (Heidelberg, Germany)
Ethanol (99 %)	Zentrallager INF 367 (Heidelberg, Germany)
Ethanol absolute (≥ 99.8 %)	VWR International S.A.S. (Fontenay-sous-Bois, France)
Fetal Bovine Serum (FBS)	Life Technologies (Carlsbad, USA)
Fibrinogen from bovine plasma	Sigma-Aldrich (St. Louis, USA)
Formalin (37 %)	Bernd Kraft GmbH (Duisburg, Germany)
Gentamicin (50 mg/ml)	Thermo Fisher Scientific (Waltham, USA)
Glacial acetic acid AnalaR [®]	VWR International S.A.S.
NORMAPUR [®] (100 %)	(Fontenay-sous-Bois, France)
Glucose, D-[³ H-(U)] (1 mCi/ml)	American Radiolabeled Chemicals Inc. (St. Louis, USA)
Glutamate-Pyruvate Transaminase (GPT) from pig heart	Roche Diagnostics GmbH (Mannheim, Germany)
Glutamic acid	Sigma-Aldrich (St. Louis, USA)
Glycerol	Carl Roth (Karlsruhe, Germany)
Histofluid	Paul Marienfeld GmbH (Lauda-Königshofen, Germany)
Human serum albumin (≥ 99 %) (HSA)	Sigma-Aldrich (St. Louis, USA)
Human [®] Albumin 200 g/l Baxalta, Solution for Infusion	Takeda GmbH (Konstanz, Germany)
Hydrochloric acid (≥ 37 %) (HCl)	Honeywell International Inc. (Charlotte, USA)
Hydrocortisone (γ -irradiated, powder, BioXtra, suitable for cell culture)	Sigma-Aldrich (St. Louis, USA)
Hydrogen peroxide solution (30 % w/w)	Sigma-Aldrich (St. Louis, USA)
IMD-026259 (IMD-1)	IMAX Discovery GmbH (Konstanz, Germany)
IMD-026260 (IMD-3)	IMAX Discovery GmbH (Konstanz, Germany)
Insulin from bovine pancreas	Sigma-Aldrich (St. Louis, USA)
Iscove's Modified Dulbecco's Medium (IMDM)	Life Technologies (Carlsbad, USA)

Reagent	Supplier (City, Country)
Isopropyl alcohol	Sigma-Aldrich (St. Louis, USA)
Laemmli-buffer	Bio-Rad Laboratories GmbH (Munich, Germany)
L-Glutamine (200 mM)	PAA Laboratories GmbH (Pasching, Austria)
L-Lactic dehydrogenase (LDH) from bovine heart	Sigma-Aldrich (St. Louis, USA)
Magnesium chloride hexahydrate (MgCl ₂ • 6 H ₂ O)	Fluka Chemie GmbH (Buchs, Switzerland)
Mayer's Haematoxylin	PanReac AppliChem ITW Reagents (Darmstadt, Germany)
MEM Non-Essential Amino Acids Solution (100 x) (MEM-NEAA)	Life Technologies (Carlsbad, USA)
Methanol	VWR International S.A.S. (Fontenay-sous-Bois, France)
Methyl cellulose	Sigma-Aldrich (St. Louis, USA)
Midori Green Advance DNA Stain	Nippon Genetics Europe GmbH (Düren, Germany)
Milk, powdered	Carl Roth (Karlsruhe, Germany)
Monopotassium phosphate (KH ₂ PO ₄)	GERBU Biotechnik GmbH (Gaiberg, Germany)
Mowiol 4-88	Carl Roth (Karlsruhe, Germany)
MseI restriction enzyme	New England Biolabs GmbH (Ipswich, USA)
Normal horse serum	Vector Laboratories (Burlingame, USA)
Orange DNA Loading Dye, 6 x	Thermo Fisher Scientific (Waltham, USA)
Paraffin, Histo-Comp [®]	Vogel GmbH & Co. KG (Fernwald, Germany)
Penicillin/Streptomycin (P/S) (10000 U/ml; 10000 µg/ml)	Life Technologies (Carlsbad, USA)
Perchloric acid (HClO ₄) 70 %	Sigma-Aldrich (St. Louis, USA)
Phenol red	Life Technologies (Carlsbad, USA)
Potassium chloride (KCl)	Merck KGaA (Darmstadt, Germany)
Potassium hydroxide (KOH)	Honeywell Specialty Chemicals GmbH (Seelze, Germany)

Reagent	Supplier (City, Country)
Precision Plus Protein Standards All Blue	Bio-Rad Laboratories GmbH (Munich, Germany)
Protease-Inhibitor	Sigma-Aldrich (St. Louis, USA)
PyroMark Annealing Buffer	Qiagen (Hilden, Germany)
PyroMark Binding Buffer	Qiagen (Hilden, Germany)
PyroMark Denaturation Solution	Qiagen (Hilden, Germany)
PyroMark Gold Q24 Reagents	Qiagen (Hilden, Germany)
PyroMark Wash Buffer, 10 x	Qiagen (Hilden, Germany)
Restore TM Western Blot Stripping Buffer	Thermo Fisher Scientific (Rockford, USA)
RIPA Buffer	Sigma-Aldrich (St. Louis, USA)
RPMI 1640 Medium	Life Technologies (Carlsbad, USA)
Sepharose beads (Streptavidin Sepharose High Performance)	GE Healthcare Europe GmbH (Freiburg, Germany)
Sodium azide (NaN ₃)	Sigma-Aldrich (St. Louis, USA)
Sodium chloride (NaCl)	Fisher Scientific (Loughborough, UK)
Sodium hydroxide (NaOH)	Sigma-Aldrich (St. Louis, USA)
Sodium pyruvate solution (100 mM)	Sigma-Aldrich (St. Louis, USA)
Special Fixative for Anatomical Specimens	Morphisto GmbH (Frankfurt am Main, Germany)
T4 DNA Ligase	New England Biolabs GmbH (Ipswich, USA)
TGF- β 1, recombinant human protein	Life Technologies (Carlsbad, USA)
TGS Running Buffer (10 x)	Bio-Rad Laboratories GmbH (Munich, Germany)
Thymidine	Sigma-Aldrich (St. Louis, USA)
Thymidine, [methyl- ³ H] (1 mCi/ml)	Hartmann Analytic GmbH (Braunschweig, Germany)
Trifluoroacetic acid (TFA)	Sigma-Aldrich (St. Louis, USA)
TRIS	Carl Roth (Karlsruhe, Germany)
Tris-HCl	AppliChem (Darmstadt, Germany)
Triton X-100	Merck KGaA (Darmstadt, Germany)
Trypan Blue Solution 0.5 % (w/v)	Sigma-Aldrich (St. Louis, USA)
Trypsin EDTA (0.05 %)	Life Technologies (Carlsbad, USA)
Tween 20	Carl Roth (Karlsruhe, Germany)

Reagent	Supplier (City, Country)
Ultima Gold™ LSC Cocktail	Perkin Elmer (Waltham, USA)
Water, DNase and RNase-free	MP Biomedicals (Solon, USA)
Western Lightning Plus ECL	Perkin Elmer (Waltham, USA)
Xylene	Fisher Scientific GmbH (Schwerte, Germany)

2.2 Consumables

Table 2: List of consumables.

Consumables	Supplier (City, Country)
4 - 20% Mini-PROTEAN® TGX™ Precast Protein Gels, 10-well, 50 µl	Bio-Rad Laboratories GmbH (Munich, Germany)
Amersham™ Hybond™ 0.45 PVDF Blotting Membrane	GE Healthcare Life Sciences (Chicago, USA)
Cell culture dish (10, 15 cm)	Corning Incorporated (Corning, USA)
Cell culture flask (CELLSTAR: 25, 75, 175 cm ²)	Greiner Bio-One (Frickenhausen, Germany)
Cell culture plate (CELLSTAR: 6-, 96-well, F-bottom)	Greiner Bio-One (Frickenhausen, Germany)
Cell suspension plate (96-well, U-bottom)	Greiner Bio-One (Frickenhausen, Germany)
ClipTip™ Pipette Tips	Thermo Fisher Scientific (Waltham, USA)
Combitips advanced (5 ml)	Eppendorf AG (Hamburg, Germany)
Cryo tubes (Cryo.S™)	Greiner Bio-One (Frickenhausen, Germany)
Dako Pen	Dako North America (Carpinteria, USA)
Disposable cuvettes made of PS, semi-micro (E-1642)	neoLab Migge GmbH (Heidelberg, Germany)
E-Plate VIEW 96-well, sterile, F-bottom	ACEA Biosciences Ind. (San Diego, USA)
Falcon tube (15, 50 ml)	Greiner Bio-One (Frickenhausen, Germany)
Luna™ Cell Counting Slides	Logos Biosystems Inc. (Anyang-si, South Korea)
Micolance™ 3 needle (25G x 1" - Nr. 18)	Becton, Dickinson and Company (Franklin Lakes, USA)

Consumables	Supplier (City, Country)
Micolance™ 3 needle (27G x 3/4" - Nr. 20)	Becton, Dickinson and Company (Franklin Lakes, USA)
Microplate BRAND® (96-well, white)	BRAND GMBH + CO KG (Wertheim, Germany)
Microscope cover slips	Paul Marienfeld GmbH (Lauda-Königshofen, Germany)
Microscope slides	Paul Marienfeld GmbH (Lauda-Königshofen, Germany)
Microscope slides (Superfrost® Plus)	Gerhard Menzel GmbH (Braunschweig, Germany)
Parafilm "M" Laboratory Film	Bemis Corporate (Neenah, USA)
PCR plates, 24-well, transparent, no skirt (0.2 ml)	BRAND GMBH + CO KG (Wertheim, Germany)
PCR reaction tubes (0.2 ml)	Greiner Bio-One (Frickenhausen, Germany)
Petri dish (10 cm)	Corning Incorporated (Corning, USA)
Pipette filter tips (DeckWorks: 10, 20, 200, 1000 µl)	Corning Incorporated (Corning, USA)
Pipette tips (10, 200, 1000 µl)	Greiner Bio-One (Frickenhausen, Germany)
Pipette tips MultiFlex® (1 - 200 µl)	Carl Roth (Karlsruhe, Germany)
PyroMark Q24 Cartridge, Method 005	Qiagen (Hilden, Germany)
PyroMark Q24 Plate	Qiagen (Hilden, Germany)
PyroMark Q24 Vacuum Prep Troughs	Qiagen (Hilden, Germany)
PyroMark Vacuum Prep Filter Probe	Qiagen (Hilden, Germany)
QuadriPERM® cell culture vessel	Sarstedt (Nümbrecht, Germany)
Reaction tube (1.5, 2.0, 5 ml)	Eppendorf AG (Hamburg, Germany)
Reinraumtuch Bemcot M3-II (M3 Scaffold)	Reinraum-Produkte GmbH (Braunschweig, Germany)
Scintillation counting vial (20 ml)	Sarstedt (Nümbrecht, Germany)
Serological pipette (2 ml)	Corning Incorporated (Corning, USA)
Serological pipette (5, 10, 25, 50 ml)	Sarstedt (Nümbrecht, Germany)
Sterile filter (0.22 µm)	Merck Millipore (Darmstadt, Germany)
Syringe (5, 10, 20, 50 ml)	Becton, Dickinson and Company (Franklin Lakes, USA)
Syringe Injekt®-F (1 ml)	B.Braun Melsungen AG (Melsungen, Germany)

Consumables	Supplier (City, Country)
ThinCert™ insert for 12-well, 0.4 µm, translucent	Greiner Bio-One (Frickenhausen, Germany)
ThinCert™ plate 12-well, deep well	Greiner Bio-One (Frickenhausen, Germany)
Tissue embedding cassettes	Kartell Spa (Noviglio, Italy)
Tissue foam biopsy pads (Surgipath®)	Leica Biosystems (Nußloch, Germany)
Whatman® filter papers	Whatman International Ltd (Maidstone, UK)

2.3 Kits

Table 3: List of used kits.

Kit	Supplier (City, Country)
CellTiter 96® AQueous One Solution	Promega (Madison, USA)
CellTiter-Glo® 3D Cell Viability Assay	Promega (Madison, USA)
CINtec® p16 ^{INK4a} Histology Kit	Roche Diagnostics GmbH (Mannheim, Germany)
DNase I Amplification Grade	Life Technologies (Carlsbad, USA)
DNeasy Blood and Tissue	Qiagen (Hilden, Germany)
dNTP set (100 mM), 4 x 250 µl	Invitrogen GmbH (Darmstadt, Germany)
EdU Cell Proliferation Kit	baseclick GmbH (Neuried, Germany)
Hot MOLPol DNA Polymerase kit	Molegene (Butzbach, Germany)
Liquid DAB+ Substrate Chromogen System	Dako North America (Carpinteria, USA)
Methylamp™ DNA Modification Kit	Epigentek Group Inc. (Farmingdale, USA)
QIAamp DNA Mini Kit	Qiagen (Hilden, Germany)
QIAquick PCR Purification Kit	Qiagen (Hilden, Germany)
RNeasy Mini Kit	Qiagen (Hilden, Germany)
Senescence β-Galactosidase Staining Kit	Cell Signaling Technology
Vectastain® Elite® ABC kit, peroxidase (Mouse IgG)	Vector Laboratories (Burlingame, USA)
Venor® GeM Classic	Minerva Biolabs (Berlin, Germany)

2.4 Antibodies

Table 4: List of used primary and secondary antibodies.

Antibody	Supplier (City, Country)	Additional information	Source	Dilution
α -Tubulin	Sigma-Aldrich (Steinheim, Germany)	monoclonal, T9026	mouse	1:2000 (WB)
Caspase-3, cleaved	Cell Signaling Technology Inc. (Danvers, USA)	polyclonal, Asp175, #9661	rabbit	1:200 (IF)
Cytokeratin 18, caspase-cleaved	Roche Diagnostics GmbH (Mannheim, Germany)	monoclonal, M30 CytoDeath, 12 140 349 001	mouse	1:40 (IF)
Cytokeratin 7	Dr. Kutz Langbein (DKFZ, Heidelberg)	-	guinea pig	1:1000 (IF)
Cytokeratin 14	Leica Biosystems (Newcastle, UK)	monoclonal, NCL-L-LL002	mouse	1:100 (IF)
GLUT-1	Thermo Fisher Scientific (Rockford, USA)	polyclonal, RB-9052	rabbit	1:500 (IHC/WB) 1:200 (IF)
Ki-67	Cell Signaling Technology Inc. (Danvers, USA)	monoclonal, D2H10, #9027	rabbit	1:800 (IHC)
Secondary antibodies				
Anti-guinea pig IgG-Alexa488	Jackson ImmunoResearch Laboratories, Inc. (West Grove, USA)	706-546-148	donkey	1:800 (IF)
Anti-mouse IgG-Alexa488	Jackson ImmunoResearch Laboratories, Inc. (West Grove, USA)	715-546-151	donkey	1:800 (IF)
Anti-rabbit IgG-Alexa488	Thermo Fisher Scientific (Rockford, USA)	A21206	donkey	1:800 (IF)
Anti-mouse IgG-Cy3	Jackson ImmunoResearch Laboratories, Inc. (West Grove, USA)	715-166-151	donkey	1:1000 (IF)

Antibody	Supplier (City, Country)	Additional information	Source	Dilution
Anti-rabbit IgG-Cy3	Jackson ImmunoResearch Laboratories, Inc. (West Grove, USA)	711-166-152	donkey	1:1000 (IF)
Anti-mouse / rabbit IgG, biotinylated	Vector Laboratories (Burlingame, USA)	BA-1400	horse	1:50 (IHC)
Anti-mouse IgG, HRP-linked	Cell Signaling Technology Inc. (Danvers, USA)	#7076	horse	1:5000 (WB)
Anti-rabbit IgG, HRP-linked	Cell Signaling Technology Inc. (Danvers, USA)	#7074	goat	1:2000 (WB)

2.5 Primers

Table 5: List of primer sequences. HGP primers were used for the generation of IMD-3-resistant cells performed by Haplogen GmbH (Vienna, Austria). LINE-1 primers were ordered at Microsynth (Balgach, Schweiz).

Name	Direction	Sequence
HGP0273-fw	forward	5' CAAGCAGAAGACGGCATAACGAGAT ACGAATTC GTGACTGGAGTTCAGACGTGTGCTCTTCCGATC gttctgtgtgtctctctG 3'
HGP0269-rev	reverse	5' AATGATACGGCGACCACCGAGATCTACAC TAATC TTA ACACTCTTTCCCTACACGACGCTCTTCCGATCT atctgatggttctctagcttggc 3'
HPG0038-seq	sequencing	5' CTAGCTTGCCAAACCTACAGGTGGGGTCTTTCA 3'
LINE1-fw_01	forward	5' TTTTGAGTTAGGTGTGGGATATA 3'
LINE1-rev-biot_01	reverse	5' AAAATCAAAAAATTCCCTTTC 3' (5' biotinylated)
LINE1-pyrseq_01	sequencing	5' AGTTAGGTGTGGGATATAGT 3'

2.6 Instruments

Table 6: List of used instruments.

Instrument	Supplier (City, Country)
Analytic scale (SBC 32)	Sartorius (Göttingen, Germany)
ApexQe FT-ICR Instrument	Bruker Corporation (Billerica, USA)
AREX Digital Hot Plate Stirrer	VELP Scientifica Srl (Usmate Velate, Italy)
BioWizard Silver Line Safety Cabinet	Kojair (Mänttä-Vilppula, Finland)
Bruker BioSpec 3 Tesla MRI	Bruker Corporation (Billerica, USA)
Caliper, digital	Conrad Electronic GmbH (Hirschau, Germany)
Camera ColorView Soft Imaging System	Olympus (Tokyo, Japan)
Centrifuge (5417 R)	Eppendorf AG (Hamburg, Germany)
Centrifuge (5424)	Eppendorf AG (Hamburg, Germany)
Centrifuge (5810 R)	Eppendorf AG (Hamburg, Germany)
Centrifuge (Biofuge fresco)	Heraeus Holding (Hanau, Germany)
Centrifuge (Heraeus Fresco 21)	Thermo Fisher Scientific (Waltham, USA)
ChemiDoc Imaging System	Bio-Rad Laboratories GmbH (Munich, Germany)
Electronic multichannel pipette	Thermo Fisher Scientific (Waltham, USA)
E1-ClipTip™ (2-125 µl, 1-30 µl)	
Electrophoresis chamber SubCell GT	Bio-Rad Laboratories GmbH (Munich, Germany)
Electrophoresis power supply	Consort bvba (Turnhout, Belgium)
Gamma cell ¹³⁷ Cs source	Atomic Energy (Chalk River, Canada)
Haemocytometer (Neubauer improved)	Hecht Assistant (Sondeheim, Germany)
Heating plate (MR HeiTec)	Heidolph Instruments GmbH & Co. KG (Schwabach, Germany)
Incubator (no CO ₂)	Heraeus Holding (Hanau, Germany)
Incubator (with CO ₂)	Memmert (Schwabach, Germany)
Incubator (with CO ₂) with RTCA station	Binder GmbH (Tuttlingen, Germany)
Inveon™ µCT/µPET/µSPECT scanner	Siemens Medical Solutions (Knoxville, USA)

Instrument	Supplier (City, Country)
Liquid Scintillation Analyser (TRI-CARB 2900 TR)	Packard Instrument Company (Meriden, USA)
LUNA TM -fl Dual Fluorescence Cell Counter	Logos Biosystems Inc. (Anyang-si, South Korea)
Magnetic stirrer (MR 2002)	Heidolph Instruments GmbH & Co. KG (Schwabach, Germany)
Microscope Fluorescence Olympus AX70	Olympus (Tokyo, Japan)
Microscope Olympus BX43	Olympus (Tokyo, Japan)
Microscope Olympus CK40	Olympus (Tokyo, Japan)
Microscope Olympus IX70	Olympus (Tokyo, Japan)
Microtome (RM2245)	Leica Biosystems (Nußloch, Germany)
Microwave	Siemens (Munich, Germany)
Mini-Trans-Blot Cell	Bio-Rad Laboratories GmbH (Munich, Germany)
Mini-Centrifuge (3-1810)	NeoLab (Heidelberg, Germany)
Multipette plus	Eppendorf AG (Hamburg, Germany)
Nalgene TM Mr. Frosty [®] Cryo 1 °C Freezing Container	Thermo Fisher Scientific (Waltham, USA)
NanoDrop 1000 Spectrophotometer	Thermo Fisher Scientific (Waltham, USA)
Orbital shaker, MixMate 5353 PCR96	Eppendorf AG (Hamburg, Germany)
PCR cabinet (48315)	Kojair Tech Oy (Vilppula, Finland)
pH meter (PB-11)	Sartorius AG (Göttingen, Germany)
Pipette aid (accu-jet [®] pro)	BRAND GMBH + CO KG (Wertheim, Germany)
Pipettes (P10, P20, P200, P1000)	Gilson (Limburg-Offheim, Germany)
PyroMark Q24 Plate Holder	Qiagen (Hilden, Germany)
PyroMark Q24 Vacuum Workstation	Qiagen (Hilden, Germany)
Pyrosequencer PyroMark Q24	Qiagen (Hilden, Germany)
Quartz cuvette	Hellma GmbH & Co. KG (Müllheim, Germany)
Scale (BP 310 S)	Sartorius (Göttingen, Germany)
Scale (HT-500)	A&D Company (San Jose, USA)
Scale (Mettler PM4800 DeltaRange)	Mettler-Toledo GmbH (Gießen, Germany)

Instrument	Supplier (City, Country)
Semi-dry blotter	cti GmbH (Idstein, Germany)
Shaker (RS-OS 5)	Phoenix Instruments GmbH (Garbsen, Germany)
Shaker (Unimax 2010)	Heidolph Instruments GmbH & Co. KG (Schwabach, Germany)
Slide scanner NanoZoomer S210	Hamamatsu Photonics K.K. (Hamamatsu, Japan)
Sonopuls HD 2070	Bandelin electronics (Berlin, Germany)
Tecan GENios plate reader	Tecan Group AG (Männedorf, Switzerland)
Thermocycler peqlab peqstar 2 x gradient	PEQLAB Biotechnologie GmbH (Erlangen, Germany)
Thermomixer comfort	Eppendorf AG (Hamburg, Germany)
Tissue-Tek VIP™ 5 Jr. Vacuum Infiltration Processor	Sakura Finetek Japan Co., Ltd. (Tokyo, Japan)
Tissue-Tek® TEC™ 6 Embedding Console System	Sakura Finetek Japan Co., Ltd. (Tokyo, Japan)
Tube roller (RM 5)	Ingenieurbüro CAT, M. Zipperer GmbH (Ballrechten-Dottingen, Germany)
Tube roller (SU1400)	SunLab Instruments (Mannheim, Germany)
Ultrospec 7000 UV-VIS spectrophotometer	GE Healthcare Life Sciences (Chicago, USA)
Vacuum pump (WOB-L Pump 2511)	Welch-Ilmvac (Niles, USA)
Vortex (REAX 2000)	Heidolph Instruments GmbH & Co. KG (Schwabach, Germany)
Vortex (VF2)	IKA-Works (Wilmington, USA)
Waterbath (HI1201)	Leica Biosystems (Nußloch, Germany)
Waterbath (SUB6)	Grant Instruments (Cambridge, UK)
Waterbath (SW20)	Julabo Labortechnik (Seelbach, Germany)
Waterbath (WBT22)	Carl Roth (Karlsruhe, Germany)
xCelligence® RTCA SP instrument	ACEA Biosciences Inc. (San Diego, USA)

2.7 Software

Table 7: List of used software.

Software	Supplier (City, Country)
AnalySIS	Soft Imaging System GmbH (Münster, Germany)
Cell [^] D Imaging Software for Life Science Microscopy	Olympus Soft Imaging Solutions (Tokyo, Japan)
Cell [^] F Imaging Software for Life Science Microscopy	Olympus Soft Imaging Solutions (Tokyo, Japan)
GraphPad Prism 9.0.0	GraphPad Software Inc. (La Jolla, USA)
ImageLab 5.2.1	Bio-Rad Laboratories GmbH (Munich, Germany)
Ingenuity Pathway Analysis	Qiagen (Hilden, Germany)
Inveon TM Research Workspace (IRW) software 2.2	Siemens Medical Solutions (Knoxville, USA)
Magellan Software	Tecan Group AG (Männedorf, Switzerland)
NanoDrop 1000 3.8.1	Thermo Fisher Scientific (Waltham, USA)
ParaVision software 360 V1.1	Bruker Corporation (Billerica, USA)
ParaVision software 6.0.1.	Bruker Corporation (Billerica, USA)
PyroMark Q24 software, version 2.0.6, build 20	Qiagen (Hilden, Germany)
Quantitative Pathology and Bioimage Analysis (QuPath)	University of Edinburgh (Edinburgh, UK) [257]
R Studio Version 1.2.5033	R Studio (Boston, USA)
R-3.6.3	Bioconductor, Vienna University of Economics and Business (Vienna, Austria); "https://www.r-project.org"
RTCA Software 2.0	ACEA Biosciences Ind. (San Diego, USA)

2.8 Cell lines

The head and neck cancer cell lines UM-SCC-47 [258] and UM-SCC-104 [259] were developed and kindly provided by Professor Dr. Thomas E. Carey (University of Michigan). HGC176 (IMD-3-resistant) and HGC178 (WT) cell lines were generated by Haplogen GmbH (Vienna, Austria). The Hap1 WT cell line and respective MLH1 knockout clones 11, 29, 30, 44 were kindly provided by Dr. Hans Hombauer (DKFZ, Heidelberg).

The HT29 cell line was obtained from the Tumourbank of the DKFZ (Heidelberg, Germany), while the other cell lines were obtained from the European Collection of Authenticated Cell Cultures (ECACC; Salisbury, UK).

Table 8: List of used cell lines.

Cell line	Origin	Medium
HL-60	Acute myeloid leukaemia	RPMI 1640 + FBS 10% + P/S 1 %
U251	Astrocytoma	DMEM + FBS 10 % + P/S 1 %
C33A	Cervical squamous cell carcinoma (MSI)	DMEM + FBS 10 % + P/S 1 %
HGC176 (IMD-3-resistant)	Chronic myeloid leukaemia	IMEM + FBS 10 % + P/S 1 %
HGC178 (WT)	Chronic myeloid leukaemia	IMEM + FBS 10 % + P/S 1 %
Hap1 (WT)	Chronic myeloid leukaemia	IMEM + FBS 10 % + P/S 1 %
Hap1 Δ MLH1 clone 11	Chronic myeloid leukaemia	IMEM + FBS 10 % + P/S 1 %
Hap1 Δ MLH1 clone 29	Chronic myeloid leukaemia	IMEM + FBS 10 % + P/S 1 %
Hap1 Δ MLH1 clone 30	Chronic myeloid leukaemia	IMEM + FBS 10 % + P/S 1 %
Hap1 Δ MLH1 clone 44	Chronic myeloid leukaemia	IMEM + FBS 10 % + P/S 1 %
HT29	Colon adenocarcinoma (MSS)	DMEM + FBS 10 % + P/S 1 %
Colo205	Colon adenocarcinoma (MSS)	RPMI 1640 + FBS 10% + P/S 1 %
SW620	Colon adenocarcinoma (MSS)	RPMI 1640 + FBS 10% + P/S 1 %
DLD-1	Colon adenocarcinoma (MSI)	RPMI 1640 + FBS 10% + P/S 1 %
HCT15	Colon adenocarcinoma (MSI)	RPMI 1640 + FBS 10% + P/S 1 %
HCT116	Colon carcinoma (MSI)	DMEM + FBS 10 % + P/S 1 %

Cell line	Origin	Medium
KM12	Colon carcinoma (MSI)	RPMI 1640 + FBS 10% + P/S 1 %
HT-1080	Fibrosarcoma	DMEM + FBS 10 % + P/S 1 %
CaSki	HPV-related cervical squamous cell carcinoma	DMEM + FBS 10 % + P/S 1 %
SW756	HPV-related cervical squamous cell carcinoma	DMEM + FBS 10 % + P/S 1 %
SiHa	HPV-related cervical squamous cell carcinoma	DMEM + FBS 10 % + P/S 1 %
HeLa	HPV-related endocervical adenocarcinoma	DMEM + FBS 10 % + P/S 1 %
UM-SCC-47	HPV-related head and neck squamous cell carcinoma	RPMI 1640 + FBS 10% + P/S 1 % + MEM-NEAA 1%
UM-SCC-104	HPV-related head and neck squamous cell carcinoma	RPMI 1640 + FBS 10% + Gentamicin 0.05 % + MEM-NEAA 1%
UPCI-SCC-90	HPV-related head and neck squamous cell carcinoma	RPMI 1640 + FBS 10% + P/S 1 % + MEM-NEAA 1%
UPCI-SCC-152	HPV-related head and neck squamous cell carcinoma	RPMI 1640 + FBS 10% + Gentamicin 0.05 % + MEM-NEAA 1%
MCF7	Invasive ductal carcinoma	DMEM + FBS 10 % + P/S 1 %
T-47D	Invasive ductal carcinoma	DMEM + FBS 10 % + P/S 1 %
SW872	Liposarcoma	DMEM + FBS 10 % + P/S 1 %
RPMI-8226	Multiple Myeloma	RPMI 1640 + FBS 10% + P/S 1 %
A549	Non small cell lung carcinoma	DMEM + FBS 10 % + P/S 1 %
Dan-G	Pancreatic adenocarcinoma	RPMI 1640 + FBS 10% + P/S 1 %
MIA PaCa-2	Pancreatic ductal adenocarcinoma	DMEM + FBS 10 % + P/S 1 %
SW1353	Primary central chondrosarcoma	DMEM + FBS 10 % + P/S 1 %
DU-145	Prostate carcinoma	DMEM + FBS 10 % + P/S 1 %
PC-3	Prostate carcinoma	DMEM + FBS 10 % + P/S 1 %

2.9 Buffers and cell culture special media

Table 9: List of self-made buffers.

Buffer	Composition
Ammonium sulfate (3.2 M)	10.5712 g $(\text{NH}_4)_2\text{SO}_4$ 25 ml water
β -NAD solution	75 mg β -NAD 4 ml water
BSA solution (3 %)	3 g BSA, fraction V 99 ml PBS ⁺ 1 ml sodium azide solution 10 % clear by filtration
Buffer I	36.33 g TRIS 600 ml water adjust pH to 10.4 200 ml methanol fill up to 1 l with water
Buffer II	3.03 g TRIS 600 ml water adjust pH to 10.4 200 ml methanol fill up to 1 l with water
Buffer III	5.25 g DL-norleucin 3.03 g TRIS 600 ml water adjust pH to 9.4 200 ml methanol fill up to 1 l with water
Ca/Mg solution (1000 x)	13.2 g $\text{CaCl}_2 \cdot 2 \text{H}_2\text{O}$ 10 g $\text{MgCl}_2 \cdot 6 \text{H}_2\text{O}$ 100 ml water
Citrate buffer (100 mM, 10 x)	21.0 g citric acid monohydrate 800 ml water adjust pH to 6.0 fill up to 1 l with water

2 MATERIAL

Buffer	Composition
DAPI staining solution (100 x)	200 µg DAPI 1 ml water store at -20 °C
Eosin (0.5 %)	2 g Eosin 400 ml water 800 glacial acetic acid
Formalin, buffered (10 %)	18.1 g KH ₂ PO ₄ 28.48 g Na ₂ HPO ₄ • 2 H ₂ O 540 ml formalin 37 % 1.2 l water adjust pH to 7.4 fill up to 2 l with water
Glutamate buffer	5.675 g glutamic acid 38 ml 1 M NaOH adjust pH to 8.9 fill up to 50 ml with water
Laemmli buffer (4 x)	900 µl Laemmli-buffer 100 µl β-mercaptoethanol for synthesis
Milk (5 %)	5 g milk powder 100 ml TBS-T
Mowiol mounting medium	6.0 g glycerol 2.4 g Mowiol 4-88 stir 1 h at room temperature, then add 6.0 ml water stir 1 h at room temperature, then add 12.0 ml 0.2 M Tris-HCl (pH 8.5) incubate for 2 h at 50 °C, stir occasionally 25 mg DABCO per ml solution
PBS for IF (10 x)	95.5 g Buffer substance Dulbecco's (Serva) 1 l water
PBS ⁺	100 ml PBS for IF (10 x) 900 ml water 1 ml Ca/Mg solution (1000 x) final concentration: 0.9 mM CaCl ₂ , 0.49 mM MgCl ₂

Buffer	Composition
PBS for IHC (10 x)	80 g NaCl 2 g KCl 2.4 g KH ₂ PO ₄ 17.8 g Na ₂ HPO ₄ • 2 H ₂ O 800 ml water adjust pH to 7.2 fill up to 1 l with water and autoclave
PBS-T for IHC (1 x)	dilute PBS for IHC (10 x) 1:10 with water add 1 ml Tween 20
Perchloric acid (0.6 M)	5.172 ml 70 % HClO ₄ fill up to 100 ml with water
Potassium hydroxide (3 N)	16.833 g KOH 100 ml water
Sodium hydroxide solution (1 M)	4 g NaOH 100 ml water
Sodium azide solution (10 %)	2 g sodium azide 20 ml water
TBE (10 x)	121.14 g TRIS 55.03 g boric acid 3.73 g EDTA 800 ml water adjust pH to 8.3 fill up to 1 l with water
TBS (10 x)	24.2 g TRIS 80 g NaCl 1 l water adjust pH to 7.6
TBS-T (1 x)	100 ml TBS 10x 900 ml water 1 ml Tween 20
Tris-HCl (0.2 M)	31.52 g 1 l water
Triton X-100 solution (0.02 %)	100 ml PBS ⁺ 20 µl Triton X-100

Table 10: List of special cell culture media.

Medium	Composition
EDTA (0.05 %)	0.25 g EDTA 500 ml Dulbecco's PBS (without Ca & Mg) 0.25 ml Phenol red adjust pH to 7.4
FAD _{complete}	450 ml DMEM 450 ml DMEM/F12 100 ml FBS 10 ml P/S 1 ml hydrocortisone (400 µg/l) 1 ml cholera toxin (8.33 µg/l) 1.7 ml insulin (5 mg/l) 100 µl recombinant human EGF (1 ng/l) 1 ml adenine (24 mg/l)
Methyl cellulose (100 %)	2.4 g methyl cellulose 100 ml hot (60 °C) cell culture medium (no supplements) stir 20 min at room temperature (RT) (max. rotation) add 100 ml warm (RT) cell culture medium (no supplements) add supplements (10 % FBS, 1 % P/S, 1 % Glutamine) stir over night at 4 °C pour to 50 ml falcon tubes and centrifuge 3 h, 4,000 rpm transfer to new falcons but leave "pellet" of 15-20 ml store at -20 °C
rFAD	450 ml DMEM 450 ml DMEM/F12 100 ml FBS 10 ml P/S 1 ml hydrocortisone (400 µg/l) 1 ml cholera toxin (8.33 µg/l)
rFAD ⁺	500 ml rFAD add directly before usage: 250 µl ascorbic acid (50 µg/ml) 2.5 ml aprotinin (250 U/ml)
Trypsin (0.4 %)	16 ml trypsin 2.5 % 84 ml Dulbecco's PBS (without Ca & Mg)

3 Methods

3.1 General methods

3.1.1 Maintenance and harvest of cells

Cells were cultured in their respective medium (see 2.8) at 37 °C in a 5 % CO₂ atmosphere and 85 - 95 % humidity. All experiments were performed under sterile conditions. Cells were passaged 2 - 3 times per week depending on their proliferation rate. After washing with phosphate-buffered saline (PBS), cells were trypsinised at 37 °C until all cells detached and the reaction was stopped by addition of cell culture medium. The cell culture flask was washed with PBS before splitting the cells into the same flasks. The flasks were reused up to 10 times. All experiments were conducted in new cell culture flasks or plates.

For all experiments, the harvested cells were centrifuged at 1,200 rpm (290 g) for 10 min and resuspended in the respective cell culture medium. The cells were counted using a LUNATM-fl dual fluorescence cell counter. A 10 µl aliquot of cells was mixed with 10 µl trypan blue. 10 µl of the mixture were transferred to the cell counting slide for counting.

Cells were regularly checked for mycoplasma contamination by PCR using the Venor[®] GeM Classic kit according to the manufacturer's protocol. Cells were cultured to a maximum of 30 passages after thawing. Cell lines were authenticated using Multiplex Cell Authentication by Multiplexion (Heidelberg, Germany) as described recently [260]. The SNP profiles matched known profiles.

3.1.2 Cryopreservation of cell lines

For cryopreservation, cells were expanded in T175 cell culture flasks and cultured up to 90 % confluence. Cells were harvested as described in 3.1.1 and resuspended in 1 ml cold fetal bovine serum (FBS) containing 10 % dimethyl sulfoxide (DMSO) for each cryo vial. Depending on their proliferation rate, 1/4 to 1/2 of the cells was transferred to one cryo vial. All cryo vials were placed into a Mr. Frosty[®] freezing container and frozen at - 80 °C for 24 - 48 h. Afterwards, they were transferred to liquid nitrogen for long term storage.

To take the cells back into culture, the vials were placed briefly in a 37 °C water bath to thaw. Immediately after thawing, the cells were transferred to a falcon tube containing 10 ml of the respective cell culture medium. The cells were centrifuged at 1,200 rpm (290 g) for 10 min and resuspended in 1 ml cell culture medium. The cells were transferred to a new cell culture flask containing cell culture medium and placed into an incubator with 37 °C, 5 % CO₂ atmosphere and 85 - 95 % humidity. Cells were cultured at least 1 week before using them for experiments.

3.1.3 Anti-cancer agents

Both synthetic flavagline derivatives, IMD-026259 (IMD-1) and IMD-026260 (IMD-3), were kindly provided by IMAX Discovery GmbH (Konstanz, Germany) and solubilised in DMSO. 2DG was purchased from Sigma-Aldrich for *in vitro* experiments and stock solutions were prepared in cell culture medium. Cisplatin was purchased from Sigma-Aldrich and solubilised in 0.9 % sodium chloride solution. 5-Aza-2'-deoxycytidine (DAC) was purchased from Sigma-Aldrich and dissolved in DMSO. If required solutions were sterilised using a 0.22 µm filter.

All stock solutions were stored in small aliquots at -20 °C to avoid repetitive freezing and thawing cycles. Prior to application, treatment stocks were diluted for *in vitro* experiments in the required cell culture medium to obtain a 10 x or 1 x treatment stock. For IMD-1 and IMD-3 always a 100 µM solution was created directly from the DMSO stock, which was used for the subsequent dilution series in cell culture medium to obtain a minimal DMSO concentration. DAC stock was diluted in DMSO resulting in a 2000 x treatment stock, to expose cells maximal to a DMSO concentration of 0.5 %. Standard concentrations are listed in table 11.

Table 11: *In vitro* treatment concentrations of 2DG, cisplatin, DAC and IMD substances. Standard concentrations were applied in all experiments if not stated otherwise.

Treatment	Stock concentration (Solvent)	Applied concentration
2DG	400 mM (Medium, no supplements)	1 mM
Cisplatin	2.5 mM (0.9 % NaCl)	75 µM
DAC	200 mM (DMSO)	0.01, 0.1, 0.5 µM
IMD-1 (IMD-026259)	20.3 mM (DMSO)	100 nM
IMD-3 (IMD-026260)	22.2 mM (DMSO)	100 nM

3.2 Generation of IMD-3-resistant haploid cells

Generation of IMD-3-resistant cells was performed by Haplogen GmbH (Vienna, Austria). First retroviruses carrying the GeneTrap vector were generated in 293T cells. 9×10^6 293T cells were cultured in 15 cm dishes (15 x) in 15 ml DMEM (20 % FBS, 1 % P/S) for 24 h before transfection with Turbofectin. 16 x transfection master mix was prepared in 8 ml OptiMEM containing pCMV-VSV-G, pAdvantage, Gag-Pol and the GeneTrap vector, which consists of splice acceptors, reporter gene (GFP), termination sequence and DNA barcode [261]. 720 µl Turbofectin was added and the solution was mixed immediately. The mixture was incubated at room temperature for 20 min. Medium of 293T cells was changed to fresh DMEM (20 % FBS, 1 % P/S) and another 8 ml of OptiMEM was added to the transfection mix. The transfection mix (1 ml/dish) was added dropwise to the cells. On the next day, cells were checked for GFP expression under the microscope and 15 ml fresh medium was added. In parallel, 1×10^6 Hap1 cells were seeded into 15 cm dishes (6x) in IMDM (10 % FBS, 1 % P/S). On day the next day, viral supernatant was collected from 293T cells and 15 ml fresh medium was added to the cells for a second round of virus production which was harvested after another 24 h.

Viral supernatant was centrifuged (1,600 rpm, 10 min) to remove cellular debris. The supernatant was transferred to Beckman polycarbonate tubes for ultracentrifugation (23,000 rpm, 90 min, 4 °C) to concentrate the virus. Viral concentrate was resuspended in 500 µl PBS and incubated 2 - 3 h at room temperature or over night at 4 °C. Before infection, pellet was dissolved by slightly shaking the viral supernatant. Medium was removed from Hap1 cells and fresh medium with protamine sulfate (8 µg/ml) was added. Viral supernatant was added dropwise to the cells and was incubated over night. 2 - 3 days after the last infection, the cells were checked for successful GeneTrap vector insertion (GFP positive) by FACS.

Gene-trap (GT) mutagenised cells were selected for IMD-3 resistance by exposing them for approximately 4 weeks to 20 nM IMD-3 with constant renewal of medium and treatment. Surviving cells were treated with 40 nM IMD-3 for another week resulting in the stable IMD-3-resistant cell line HGC176. GT cells were pooled and DNA was isolated using the QIAamp DNA Mini Kit. DNA was eluted in water and concentration was measured using QuBit. Subsequently, DNA digestion using MseI was performed over night at 37 °C (Tab. 12) following DNA purification using QIAquick DNA purification kit. DNA concentration was determined and 1 µg of digested DNA was religated (Tab. 12). Again, DNA was purified and 20 µl DNA was subjected to inverse PCR (iPCR) (tab. 13) using the primers HGP0273-fw and HGP0269-rev (see 2.5). 20 µl PCR products was run on a 2% agarose gel to confirm amplification. Samples were subjected to next generation sequencing using the sequencing primer HGP0038-seq (see 2.5) to identify the integration site of the GeneTrap cassette.

Table 12: Protocols for DNA digestion (left) and ligation (right).

DNA digestion		Ligation	
DNA	4 µg	DNA	1 µg
10 x buffer 4	5 µl	10 x ligase buffer	5 µl
BSA	0.5 µl	T4 DNA ligase	1 µl
Restriction enzyme MseI	2.5 µl		

Table 13: Inverse PCR mixture (left) and applied iPCR programme (right).

iPCR mix		iPCR programme		
DNA	20 µl	94 °C	2 min	1 x
10 x AccuPrime Buffer II	5 µl	94 °C	30 sec	} 35 x
sPrimer (10 µM)	1 µl	55 °C	30 sec	
aPrimer (10 µM)	1 µl	68 °C	1 min 45 sec	
AccuPrime Polymerase	0.3 µl	68 °C	7 min	1 x
		12 °C	hold	

3.3 Cellular assays

Cells were harvested (see 3.1.1) and seeded for the different *in vitro* assay. All assays were performed at 37 °C, 5 % CO₂ atmosphere and 85 - 95 % humidity, if not stated otherwise. For each assay the optimal cell number was determined beforehand to ensure 90 - 95 % confluence in the vehicle-treated control at the end of the experiment. Therefore, the cells were cultured under the same conditions as required during the experiment to determine the optimal cell number. Control cells and background medium wells always received the same amount of solvent without treatment as the drug-treated cells.

3.3.1 Cell viability assay

For each treatment condition, cells were seeded in triplicates into a 96-well plate. Cell numbers and medium volume are listed in table 14. Three wells only containing cell culture medium were prepared for the background measurement. No cells were seeded into the outer wells, which were filled with 250 µl PBS. After 24 h, the treatment was started by diluting the treatment 1:10 into the wells. For cells seeded in 200 µl medium instead of 100 µl (Tab. 14), a complete medium change was performed to start the treatment. Cells were incubated for 48 h before adding 20 µl CellTiter 96[®] AQueous One Solution per 100 µl medium to the cells. The cells were incubated with the dye for at least 1 h at 37 °C, before measuring the absorption at 485 nm using a plate reader.

Suspension cell lines were seeded in round bottom 96-well plates and treated as described above. After incubation with the CellTiter 96[®] AQueous One Solution, the plates were centrifuged at 1,200 rpm (290 g) for 10 min and the medium was transferred to a flat-bottom 96-well plate to measure its absorption.

3.3.1.1 Influence of glucose, FBS and P/S on the efficacy of IMD-3

To assess the influence of glucose, FBS and P/S on the efficacy of IMD-3, the cell viability assay was performed as described in 3.3.1. DMEM (without glucose, FBS and P/S: deprived medium) or water *ad injectabilia* were supplemented with different concentrations of glucose, FBS and P/S and used to prepare a 100 µM solution from the IMD-3 DMSO stock (Tab. 11). Subsequently, a dilution series was performed in the respective medium to yield 10 x treatment stocks. The DMSO concentration was kept for all experiments as low as possible. For each treatment condition, control cells received the same amount of solvent.

To evaluate the effect of a constant DMSO concentration per well (0.5 %) on IMD-3 efficacy, the 100 µM stock solution was prepared in DMSO. The subsequent dilutions in cell culture medium were supplemented with DMSO to obtain a final concentration of 5 % DMSO in the 10 x treatment stock.

Table 14: Cell number and medium volume per well for 96-well plate assays.

Cell line	Cell number	Medium volume [μl]	Cell line	Cell number	Medium volume [μl]
A549	3,000	100	HT29	7,000	100
C33A	3,000	100	KM12	16,000	200
CaSki	7,500	100	MC38	4,000	100
Colo205	20,000	100	MCF7	5,500	100
Dan-G	7,000	100	MIA PaCa-2	10,000	100
DLD-1	8,000	100	PC-3	3,000	100
DU-145	7,000	100	RPMI-8226	40,000	100
Hap1 ΔMLH1 clone 11	4,000	100	SiHa	3,500	100
Hap1 ΔMLH1 clone 29	4,000	100	SW1353	2,500	100
Hap1 ΔMLH1 clone 30	4,000	100	SW620	12,000	100
Hap1 ΔMLH1 clone 44	4,000	100	SW756	15,000	100
Hap1	4,000	100	SW872	4,000	100
HCT116	6,000	100	T-47D	9,000	100
HCT15	9,000	100	TC-1	3,000	100
HeLa	4,000	100	U251	4,500	100
HGC176 (IMD-3-resistant)	6,500	100	UM-SCC-104	15,000	200
HGC178 (WT)	6,500	100	UM-SCC-47	4,000	200
HL-60	40,000	100	UPCI-SCC-152	25,000	200
HT-1080	3,000	100	UPCI-SCC-90	25,000	200

3.3.2 Proliferation assay

Cell proliferation was determined using methyl-³H-thymidine incorporation. Cells were seeded into 96-well plates (Tab. 14) and empty wells were filled with 250 μl PBS. After 24 h, 5 μl methyl-³H-thymidine (2.775 TBq/mmol) was added to each well to achieve a final concentration of 0.01 μCi/ml. Afterwards, treatment was added by diluting 10 x stocks into the wells. After 48 h, the medium was removed carefully and the cells were washed with 200 μl cell culture medium (no supplements) containing 1 mM non-labelled thymidine. The medium was removed and the cells were lysed in 200 μl 0.5 M NaOH for 1 h at room temperature. Cell lysates were transferred to scintillation vials and the wells were washed again with 200 μl 0.5 M NaOH. The wash was added to the respective scintillation vial, mixed with 10 ml Ultima GoldTM scintillation cocktail and subjected to liquid scintillation counting (LSC).

3.3.3 Real-time cell proliferation monitoring

Real-time monitoring of cell proliferation was performed by impedance measurement using the xCelligence[®] RTCA SP instrument from ACEA Biosciences. The instrument was placed into a humid incubator with 37 °C and 5 % CO₂ atmosphere. HGC176 and HGC178 cells were seeded into a 96-well E-plate with at least four vertical replicates per condition, including medium wells for the background measurement. The spaces between the wells were filled with 150 µl PBS. Background wells were filled with 150 µl medium. All wells later containing cells was filled with 75 µl medium. The plate was placed into the RTCA station and incubated 30 min at 37 °C before performing a background measurement. In the meantime, cells were prepared for seeding by resuspending 4,500 cells in 75 µl medium per well. After the background measurement, 75 µl cell suspension was added per well. The plate was placed back into the station and the cells were allowed to descend for 30 min before starting the long-term measurement.

After 24 h, the treatment was started by diluting 10 x treatment stocks into the wells. The last impedance measurement before treatment addition was used for normalisation of the cell index. Medium and treatment was changed every 48 h by removing the old medium carefully with a pipette. Cell proliferation was monitored over 2 weeks.

3.3.4 Pulse-chase cytotoxicity assay

Cells were split into T25 flasks and grown for 72 h, adding 10 µCi/ml methyl-³H-thymidine (2.775 TBq/mmol) for the last 12 h. Afterwards, the cells were harvested and seeded in triplicates into a 96-well plate (Tab. 14). Before trypsinisation, an additional washing step with PBS was added to remove non-incorporated tracer. For each time point (12, 24, 48 h) one 96-well plate was seeded and empty wells were filled with 250 µl PBS. To measure the incorporated label at the starting point of the treatment (0 h), the cells were seeded in 8 replicates in a separate plate (Fig. 6).

After growing the cells for 24 h, the treatment was started by diluting 10 x treatment stocks into the wells. In parallel, the 0 h plate was harvested. The other plates were harvested after 12, 24 and 48 h and the amount of radioactive label in the medium and cell lysate was determined using LSC.

To harvest the cells, the medium of each well was transferred into a scintillation vial. The cells were washed carefully with 200 µl cell culture medium (no supplements) containing 1 mM non-labelled thymidine. It is important to avoid detaching of the cells in the washing step. The wash was added to the scintillation vial and mixed with 10 ml Ultima Gold[™] scintillation cocktail. The cells were lysed with 200 µl 0.5 M NaOH of 1 h at room temperature and the lysate was transferred into a new scintillation vial. The wells were washed with 200 µl 0.5 M NaOH, which was added to the vial containing cell lysate and mixed with 10 ml scintillation cocktail. Medium and cell lysate were subjected to LSC measurement.

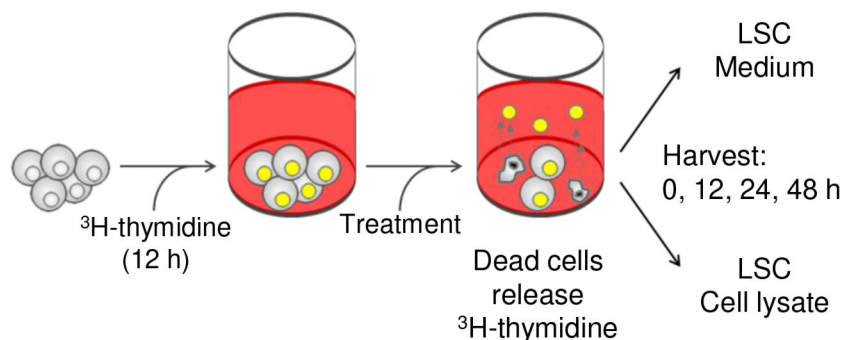


Figure 6: Schematic overview of pulse-chase cytotoxicity assay procedure. Cells were labelled with methyl- ^3H -thymidine for 12 h. Afterwards cells were treated with synthetic flavaglines for 0, 12, 24 and 48 h. Radioactive tracer was released from dying cells into the cell culture medium. At the end of each treatment period, medium was collected separately from the cellular lysate and both were subjected to LSC.

3.3.5 Senescence-associated β -galactosidase staining

To perform a senescence-associated β -galactosidase staining, cells were harvested and seeded in 2 ml medium into 6-well plates (Tab. 15). As a positive control for senescence induction, harvested cells were irradiated with 10 Gy for 90 sec before seeding. Cells were cultured for 5 days with regular medium changes to allow the manifestation of the senescent phenotype in the positive control. The cells were treated for 48 h before performing X-gal staining using the Senescence β -Galactosidase Staining kit according to the manufacturer's instructions. The cells were incubated with the staining solution until a blue staining was observed in the positive control. The cells were overlaid with 70 % glycerol, after removing the staining solution, and stored at 4 °C until imaging.

Table 15: Number of non-irradiated and irradiated cells seeded per well for senescence-associated β -galactosidase staining.

Cell line	Cell number non-irradiated	Cell number irradiated
CaSki	10,000	80,000
SiHa	7,000	56,000
UPCI-SCC-90	100,000	400,000

3.3.6 Specimen preparation of treated cells on microscope slides for IF staining

Four microscope slides were placed into a quadriPERM[®] cell culture vessel and cells were seeded in 4.5 ml medium on each slide (Tab. 16). The cells were allowed to grow for 48 h before the treatment was started. After 42 h, the nucleoside analogue EdU (10 μ M) was added to the cells for 4 h before removing the medium and fixing the cells with cold 80 % methanol (4 °C), 5 min. The slides were shortly dried at room temperature before adding cold acetone (-20 °C), 2 min. Air dried slides were stored at -20 °C until immunofluorescence staining (see 3.7.5).

Table 16: Cell numbers seeded in 4.5 ml medium on a glass slide.

Cell line	Cell number / glass slide
CaSki	300,000
SiHa	200,000
UPCI-SCC-90	800,000

3.3.7 Generation of treated cell pellets for protein, RNA and DNA analysis

To isolate RNA, DNA or protein from treated cells, cells were seeded in triplicates into T75 flasks with 10 ml culture medium and incubated for 72 h (Tab. 17). A complete medium change was performed to start the treatment. After 48 h, cells were harvested and transferred to a falcon tube. The flasks were washed with medium, which was added to the falcon. Cells were counted to obtain the total number of cells. Cells were centrifuged (1,200 rpm (290 g), 10 min) and resuspended in 2 ml PBS. The cell suspension was split for RNA (700 μ l), DNA (700 μ l) and protein (600 μ l) isolation. For protein isolation, triplicates of one treatment condition were pooled. Samples for RNA or DNA isolation were centrifuged once at 1,200 rpm (290 g) for 10 min, while protein samples were centrifuged twice, adding an extra washing step with 1 ml PBS. The supernatant was removed and cell pellets were stored at -20 °C until further processing (RNA: 3.4.1, DNA: 3.5.1, Protein: 3.6.1).

Table 17: Cell numbers seeded in 10 ml medium in a T75 flask.

Cell line	Cell number / T75
HCT116	200,000
HT29	200,000
HGC176 (IMD-3-resistant)	200,000
HGC178 (WT)	200,000
CaSki	500,000
HeLa	100,000
SiHa	250,000
UPCI-SCC-90	2,000,000

3.3.8 Glucose uptake assay

To determine the glucose uptake, cells were seeded in triplicates on 6-well plates with 2 ml medium for each glucose concentration (Tab. 18) and grown for 48 h. The cells were treated for 24 h before adding ^3H -2DG (0.74 TBq/mmol) to monitor glucose uptake. DMEM without glucose and DMEM with 1 g/l glucose were used to obtain different glucose concentrations (1.0, 0.25, 0.0625, 0.0 g/l). 0.5 $\mu\text{Ci/ml}$ of ^3H -2DG was added to each medium. A small aliquot of each medium was taken for background measurement. All treatment conditions were prepared for all four glucose concentrations. The medium was removed and the cells were washed twice with 2 ml PBS. The medium containing different glucose concentration, tracer and treatment was added to the cells and incubated for 15 min at 37 °C. Afterwards, the medium was removed and the cells were washed 3 times with 2 ml PBS to remove not incorporated tracer. The cells were harvested and pelleted (1,200 rpm (290 g), 10 min). The supernatant was removed and the pellet was resuspended in 1 ml PBS. After centrifugation (1,200 rpm, 10 min), the cell pellets were lysed in 0.2 M NaOH over night at 4 °C.

For normalisation, the protein concentration of the cell lysates was determined using Bradford assay (see 3.6.2). Then, lysates were mixed with 10 ml Ultima GoldTM scintillation cocktail and subjected to LSC.

Table 18: Cell numbers per well seeded in 2 ml medium into a 6-well plate.

Cell line	Cell number / well
HCT116	120,000
HT29	120,000
HGC176 (IMD-3-resistant)	100,000
HGC178 (WT)	100,000
CaSki	150,000

3.3.9 Lactate assay

Secretion of lactate was monitored by seeding SiHa cells (20,000 cells/well in 1 ml) in triplicates into a 24-well plate and growing them for 48 h. Treatment was started by dilution of 10 x treatment stocks into the wells. After 18 h, the medium was carefully removed, the cells were washed once with PBS and fresh medium containing treatment was added for 6 h. Afterwards, medium was collected and cells were washed twice with PBS. The cells were lysed in 150 μl 0.2 M NaOH over night at 4 °C. Cell lysate was used for protein determination by Bradford assay (see 3.6.2).

To determine secreted lactate concentration, 250 μl of the collected medium were mixed with 400 μl 0.6 M perchloric acid and incubated for 10 min on ice. Fresh medium was used as background measurement. Samples were centrifuged at 13,000 rpm (16,060 g) for 10 min at 2 °C and

supernatant was transferred to a new tube. Supernatant was mixed with 121 μl 3 N KOH and centrifuged for 10 min at room temperature with 13,000 rpm (16,060 g). 200 μl of obtained supernatant was mixed with 334 μl glutamate buffer, 50 μl β -NAD solution, 25 ml GPT (100 U/ml in 1.8 M $(\text{NH}_4)_2\text{SO}_4$) and 980 ml water in a cuvette and incubated for 10 min. Buffer preparations are listed in table 9. Absorption was measured at 339 nm (A_1) before adding 100 μl L-LDH (500 U/ml in 3.2 M $(\text{NH}_4)_2\text{SO}_4$). Samples were mixed thoroughly and, after 30 min incubation, the absorption (A_2) was measured until the reaction reached a plateau. Each sample was analysed in duplicates. Lactate concentration of the samples was calculated using the Lambert-Beer law and normalised to the protein concentration.

$$c_{\text{Lactate}} = \frac{\Delta A * M_{\text{Lactate}}}{\epsilon * d} * \frac{V_{\text{total}}}{V_{\text{sample}}} \left[\frac{\text{g}}{\text{l}} \right]$$

$$c_{\text{Lactate}} \left[\frac{\text{g}}{\text{l}} \right] = \Delta A * 0.122$$

$$\Delta A = A_2 - A_1, M_{\text{Lactate}} = 90.08 \frac{\text{g}}{\text{mol}}, \epsilon(\text{NADH}) = 6220 \frac{\text{l}}{\text{mol} * \text{cm}},$$

$$d = 1 \text{ cm}, V_{\text{total}} = 1.689 \text{ ml}, V_{\text{sample}} = 0.2 \text{ ml}$$

3.3.10 Pentose phosphate pathway activity

Parallel to glycolysis, glucose can also be metabolised through pentose phosphate pathway (PPP) generating pentoses, including ribose-5-phosphate, a precursor molecule for nucleotide synthesis. Synthesized nucleotides serve as building blocks for DNA and RNA. To measure glucose flux into the PPP, the tritium incorporation into RNA was measured after incubating the cells with ^3H -labelled glucose.

Cells were seeded in triplicates into 6-well plates with 2 ml medium and grown for 48 h (Tab. 18). The treatment was started by performing a complete medium change, while simultaneously adding D- ^3H -[U]-glucose (5 μCi /well, 1.48 TBq/mmol) to the cells. To ensure equal distribution of the tracer, the tracer was added to the cell culture medium before preparing the treatment solutions. After 24 h treatment, the cells were washed twice with 2 ml PBS and harvested using 0.5 ml trypsin. 1.2 ml culture medium (no supplements) was added and the cells were transferred to a 2 ml tube. 1 ml PBS was added to the wells for washing. Cells were pelleted at 1,200 rpm (290 g) for 10 min. After removing the supernatant, the cell pellets were resuspended in PBS used for washing the wells. Again, cells were centrifuged (1,200 rpm, 10 min) and cell pellets were stored at -20°C or directly used for RNA isolation (see 3.4.1).

After determining the RNA concentration, RNA was subjected to LSC after mixing with 10 ml Ultima GoldTM scintillation cocktail. Obtained dpm values were normalised to the RNA concentration of the sample. RNase free water, used for RNA elution, was measured as background.

3.3.11 DAC-pretreatment of WT and IMD-3-resistant cells

HGC176 and HGC178 cells were seeded in triplicates into T25 flasks (0.01×10^6 , 5 ml) and incubated for 48 h. 200 mM DAC stock (DMSO) was used to prepare 2000 x treatment stocks in DMSO to obtain final treatment concentrations of 0.01, 0.1, and 0.5 μM . Controls were treated with the respective amount of DMSO. Treatment stocks were diluted 1:1000 into fresh cell culture medium. Half of the old medium was removed from the cells, leaving 2.5 ml. 2.5 ml fresh medium with 2 x DAC concentration was added to the cells. During the treatment period, DAC treatment was renewed daily. Cells were pretreated with high DAC concentrations (0.5, 0.1 μM) for five consecutive days, before harvesting and seeding into a 96-well plate (Fig. 7A). The low DAC concentration (0.01 μM) was applied over 5 consecutive days, before harvesting the cells and re-seeding them into new T25 flasks (0.01×10^6 , 5 ml). After 48 h, the re-seeded cells were treated for another 5 days with 0.01 μM DAC before seeding into a 96-well plate (Fig. 7B).

After completion of DAC-pretreatment, cells were harvested and each flask was seeded in triplicates into a 96-well plate (6,500 cells/well in 100 μl). For each pretreatment condition, cells were seeded for subsequent IMD-3 treatment and a vehicle-treated control (total of 6 wells per flask). Leftover cells of each condition were pooled and centrifuged at 1,200 rpm (290 g) for 10 min. Afterwards, the pellet was washed with 1 ml PBS and centrifuged. The pellet was stored at -20°C for DNA isolation and methylation analysis (see 3.5.2). After 24 h in the 96-well plate, the cells were treated with 100 nM IMD-3 by diluting a 10 x treatment stock into the wells. After 48 h, the cell viability was measured as described in 3.3.1.

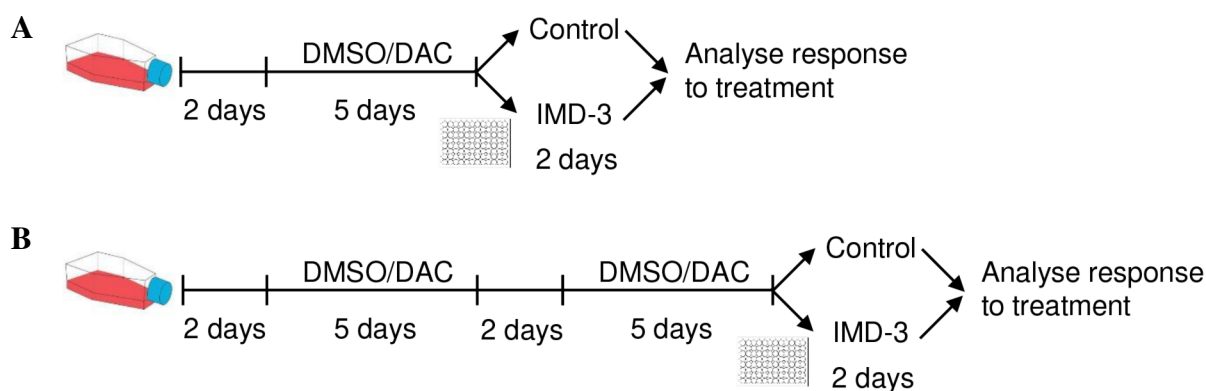


Figure 7: Schematic overview of DAC-pretreatment schedule. (A) High DAC concentrations (0.1, 0.5 μM) were applied for 5 consecutive days before cells were harvested and seeded into a 96-well plate. After 24 h, the cells were treated with IMD-3 for 48 h and cell viability was assessed using MTS-assay. (B) Low DAC concentration (0.01 μM) was applied for 5 consecutive days before cells were re-seeded into new T25 flasks and received another 5 days of DAC pretreatment. Cells were harvested and seeded into a 96-well plate. After 24 h, the cells were treated with IMD-3 for 48 h and cell viability was assessed using MTS-assay.

3.3.12 Cell viability assay of 3D spheroid cultures

Cells were seeded in 200 µl methyl cellulose (5 replicates/condition) into a round bottom 96-well plate and spheroids were allowed to form. 50,000 CaSki cells were seeded in 20 % methyl cellulose and spheroid formation was performed over 3 days. 10,000 SiHa cells were seeded in 30 % methyl cellulose and grown over 5 days, with a half medium change after 2 days. 1 x treatment stocks were prepared in methyl cellulose and a complete medium change was performed to apply the treatment. The cells were either treated for 96 h with refreshing the treatment after 48 h, or over 12 days refreshing the treatment 3 times a week (Mo, We, Fr).

Before performing the cell viability assay, methyl cellulose was removed and 100 µl normal cell culture medium was added. The spheroids were carefully transferred in 75 µl of medium into a white 96-well plate. The viability of the cells was measured using the CellTiter-Glo[®] 3D Cell Viability Assay according to the manufacturer's protocol and luminescence was detected with a plate reader.

3.3.13 3D Organotypic co-culture model

To analyse the influence of the treatment on normal keratinocytes and tumour cells (SiHa), 3D organotypic co-culture (OTC) models were prepared. The M3 scaffold was boiled in the microwave in MilliQ water, rinsed with fresh water and placed in two layers between Whatman paper to dry under pressure. Circles with 11 mm diameter were punched and autoclaved. The scaffolds were placed into the inserts (ThinCertTM), which were put in a 12-well plate. In parallel, a clotting test with 50 µl fibrinogen (8 mg/ml) and 50 µl thrombin (10 I.E./ml) was performed. The fibroblasts were trypsinised, counted and taken up in FBS (250,000 cells/culture in 100 µl FBS). For solution A, FBS containing cells was mixed with thrombin (1:2; 100 µl/culture + 100 µl). For solution B, fibrinogen and PBS (1:2; 100 µl/culture + 100 µl) were mixed. 200 µl of solution A was pipetted drop wise onto the scaffold, before adding 200 µl of solution B. Both solutions were mixed carefully and bubbles were removed. The clotting was performed for 1 - 2 h at 37 °C. Afterwards, 2 ml DMEM medium (10 % FBS, 1 % P/S, 1 ng/ml TGF-β1, 50 µg/ml ascorbic acid) was added below and on top of the cells. The cultures were incubated at 37 °C for several days (optimal 2 - 5 days).

One day before seeding the keratinocytes/tumour cell mixture, the medium was removed from the fibroblast cultures and replaced by 2 ml rFAD medium (including 50 µg/ml ascorbic acid and 500 U/ml aprotinin) (see 2.9). Ascorbic acid and aprotinin are always added directly before usage. On the next day, keratinocytes (see 3.3.13.1) and tumour cells (see 3.1.1) were harvested and counted. For each culture, 250,000 keratinocytes (99 %) were mixed with 2,500 tumour cells (1 %) and pelleted (1,200 rpm, 5 min). 200 µl rFAD (including 50 µg/ml ascorbic acid and 500 U/ml aprotinin) per culture were used to resuspend the cells before seeding them onto the fibrin gel. After 24 h incubation, the keratinocytes/tumour cells were carefully washed by pipetting the medium on the culture up and down. The medium on top of the culture was

removed. The inserts were transferred into a deep-well plate (ThinCert™, 12-well) and 4.5 ml rFAD⁺ medium (see 2.9) was added underneath the culture to allow air-exposed culture (day 0). rFAD⁺ medium of the cultures was changed 3 times a week (Mo, We, Fr) and the treatment was started at day 12 - 13.

The cultures were treated for 7 days, refreshing the treatment with each regular medium change. 4 h prior to fixation, the nucleoside analogue EdU (10 μM) was added to the medium. The cultures were removed carefully from the inserts and fixed in 10 ml Special Fixative for Anatomical Specimens. Afterwards, the cultures were embedded into paraffin for histological analysis (see 3.7.1). Upon immunofluorescence staining (see 3.7.5), fibres of M3 scaffold can stain red as well, due to their interaction with the EdU staining agent.

3.3.13.1 Culturing of fibroblasts and keratinocytes for OTCs

Human fibroblasts (2×10^6) were thawed in a 10 mm cell culture dish with DMEM (10 % FBS, 1 % P/S). Before splitting, the cells should be at least cultured for 1 week to avoid too early passaging of the cells. To harvest the fibroblasts, the cells were washed with PBS and incubated with trypsin (0.1 %) for 3 - 5 min at 37 °C. The reaction was stopped with medium and the fibroblasts were split 1:3 to 1:5.

Keratinocytes were cultured on a feeder layer of radiated fibroblasts. Trypsinised fibroblasts were resuspended in FAD_{complete} medium (see 2.9), radiated with 70 Gy, and 0.75×10^6 cells were seeded in FAD_{complete} onto a 15 mm cell culture dish. Radiated fibroblasts were seeded one day in advance before adding 2×10^6 keratinocytes per 15 mm dish. The first medium change was performed after 2 days of cultivation and was changed each 2 - 3 days afterwards. The keratinocytes were split at 80 - 90 % confluence by removing the medium and washing the cells with 10 ml 0.05 % EDTA. After removing the EDTA, 10 ml fresh 0.05 % EDTA was added and the cells were incubated for 3 min at 37 °C. The cells were washed carefully with the EDTA solution to remove the feeder layer, before aspirating the EDTA solution. Fresh 0.05 % EDTA was added and the cells were incubated at 37 °C for 3 - 5 min before aspirating the solution. The cells were trypsinised as short as possible (2 - max. 5 min) using 0.4 % trypsin at 37 °C. The detached cells were separated carefully by washing the dish with the trypsin before adding 15 ml FAD_{complete} medium. Keratinocytes were either passaged 1:4 or used for OTC generation (see 3.3.13).

3.4 RNA techniques

3.4.1 RNA isolation

RNA isolation from the treated cell pellets (see 3.3.7) was performed using the RNeasy Mini kit according to the manufacturer's protocol. Additionally, an on-column DNase I digestion was performed to remove single and double stranded DNA. RNA was eluted using RNase free water and the concentration was determined using a NanoDrop 1000 spectrophotometer.

3.4.2 Bead chip RNA gene expression analysis

Isolated RNA (see 3.4.1) was diluted in RNase free water to obtain a final concentration of 100 ng/ μ l in a total volume of 10 μ l. The expression analysis was performed at the Microarray Unit of the Genomics and Proteomics Core Facility of the German Cancer Research Centre (DKFZ, Heidelberg) using an Illumina HumanHT-12 v4 chip.

3.4.3 RNA transcriptome data analysis

The obtained data of the RNA gene expression analysis (see 3.4.2) were analysed using R 3.6.1 and Bioconductor 3.9, following the procedure described in the "beadarray" package documentation vignette [262, 263]. Using the "beadarray" package [262], IDAT files provided from DKFZ Genomics and Proteomics Core Facility were used to import the raw experiment data and sample information. Following the 'neqc'-method in the 'limma' package [263] was applied to quantile normalise and \log_2 -transform the expression data. Subsequently, Illumina probe IDs were annotated using the 'illuminaHumanv4.db' annotation package. In the resulting data set, non-matching and known bad quality probes were removed as described in the annotation package. 'limma' functions `lmFit()` and `eBayes()` [263] were used to fit linear models and calculate empirical Bayes statistics to obtain differentially expressed genes (DEGs) between conditions. For each probe \log_2 -fold changes (FC) and p-values were obtained, which were corrected for multiple testing using the Benjamini-Hochberg (BH) correction [264]. Lists of DEGs were exported in CSV format containing \log_2 -FC, BH-corrected p-values, common gene symbol and name, EntrezID, and Illumina's probe identifier for each retained probe. Identification of DEGs was performed jointly with Simon Kalteis.

The obtained lists of DEGs were filtered using R 3.6.3 and the packages 'tidyverse', 'readxl', 'writexl' and 'dplyr' [265–267]. Genes were considered significantly deregulated if they exhibit a BH-corrected p-value ≤ 0.05 and \log_2 -FC ≥ 1 (upregulated) or \log_2 -FC ≤ -1 (downregulated) and later analysis focused on these genes. Due to the structure of the Illumina chip several probes belong to the same gene, assigning several different expression values and BH-corrected p-values to one gene. Genes occurring only once in the data set were retained. For genes with multiple occurrences, non-significant and unregulated entries were dropped

(BH-corrected p-values > 0.05 , or $1 > \log_2FC > -1$), as later analysis will focus on significantly DEGs, and \log_2FC of the remaining entries were averaged and the most conservative (highest) BH-corrected p-value was assigned to the gene. The resulting gene list was exported in XLSX format and used for further analysis. Comparison of gene lists between cell lines was performed to identify all significantly DEGs, which were regulated in the same direction in all tested cell lines. The overlapping genes were visualised with the ‘VennDiagram’ package [268].

3.4.3.1 Ingenuity pathway analysis of differential expression data

To determine which cellular pathways were influenced by the treatment with synthetic flavagline derivatives, a pathway analysis was performed using the Ingenuity Pathway Analysis (IPA) software (Qiagen). The lists of DEGs (see 3.4.3) were loaded into IPA and Illumina’s identifier was used to annotate the expression values and the BH-corrected p-value to the genes. Applied cut offs for the analysis were: BH-corrected p-value ≤ 0.05 , $\log_2FC \geq 1$ for upregulated genes, $\log_2FC \leq -1$ for downregulated genes. A Core Analysis was performed (settings: Tab. 19) and the resulting table of affected canonical pathways was exported. Comparison analysis was performed to compare the affected canonical pathways between the cell lines. The resulting lists were exported in txt format and used to visualise the IPA results. All results obtained from IPA were visualised using R 3.6.3 and the packages ‘tidyverse’, ‘readxl’, ‘writexl’, ‘dplyr’, ‘gplots’, ‘RColorBrewer’, ‘ggplot2’ and ‘scales’ [265–267, 269–273].

Table 19: Settings applied for IPA Core Analysis.

Core Analysis	Settings
General settings:	Direct and indirect relationships
Networks:	Interaction and casual
Node type:	All
Data source:	All
Confidence:	Experimentally observed
Species:	Human
Tissue and cell lines:	All
Mutations:	All

3.5 DNA techniques

3.5.1 DNA isolation

DNA isolation from the DAC-pretreated cell pellets (see 3.3.11) was performed using the DNeasy Blood and Tissue kit according to the manufacturer's protocol. DNA was eluted in 50 μ l of DNase and RNase free water after 10 min incubation on the column. The concentration was determined using a NanoDrop 1000 spectrophotometer.

3.5.2 DNA methylation analysis

3.5.2.1 Bisulfite treatment of DNA

To determine the methylation status of isolated DNA (see 3.5.1), 400 ng DNA was subjected to bisulfite conversion, causing the deamination of cytosine residues to uracil while not affecting 5-methylcytosine residues. Bisulfite conversion was performed according to the manufacturer's instructions using the MethylampTM DNA Modification kit with small modifications.

Centrifugation times were increased from 15 seconds to 30 seconds. The centrifugation time after the second application of 90 % ethanol was increased to 1 min to dry the column. After the first centrifugation step, the flow-through was re-added to the column and the centrifugation step was repeated before discarding the flow-through. Elution of DNA was performed by adding 19 μ l DNase-/RNase-free water directly to the column followed by 10 min incubation at room temperature before elution.

3.5.2.2 LINE-1 PCR amplification

The methylation of three CpGs in the LINE-1 retrotransposon was used as a marker for overall DNA methylation status [274–276], amplifying a 146 bp product with CpGs at position 318, 321 and 328 through PCR [277] using primer sequences (see 2.5) from Kile *et al.* [275].

1.5 μ l bisulfite-modified DNA (see 3.5.2.1) was mixed with 23.5 μ l master mix in sterile PCR reaction tubes and centrifuged briefly before running the PCR reaction (Tab. 20).

Table 20: LINE-1 PCR mixture using Hot MOLPol PCR reagents (left) and applied PCR conditions (right).

LINE-1 PCR mixture		LINE-1 PCR programme		
Bisulfite-modified DNA	1.5 μ l	94 °C	12 min	1 x
DNase-/RNase-free water	15.7 μ l	94 °C	60 sec	} 50 x
10 x PCR buffer B2	2.5 μ l	54 °C	60 sec	
MgCl ₂ [25 mM]	3 μ l	65 °C	60 sec	
dNTPs [10 mM]	0.5 μ l	65 °C	6 min	1 x
Primer LINE1-fwd_01 [25 μ M]	0.8 μ l	4 °C	hold	
Primer LINE1-rev-biot_01 [25 μ M]	0.8 μ l			
Hot MOLPol DNA Polymerase	0.2 μ l			

Three samples without template DNA were setup as negative controls, replacing the missing volume with water. PCR reactions were pipetted under sterile conditions and were cooled using metal cooling blocks placed in ice. Sufficient amplification and possible contamination of PCR runs was controlled by agarose gel electrophoresis (see 3.5.2.3).

3.5.2.3 PCR product analysis by gel electrophoresis

To control successful PCR amplification, a 2% (w/v) agarose gel was prepared by boiling agarose in 1 x TBE buffer (see 2.9) in a microwave at 800 W until it was completely dissolved. After cooling down to 60 °C, 5 µl Midori Green DNA stain was added per 100 ml of solution and dissolved carefully before pouring the solution into a gel chamber and removing the air bubbles. The polymerised gel was placed into an electrophoresis chamber in 1 x TBE buffer. 5 µl PCR product was mixed with 3 µl 6 x Orange DNA loading dye and loaded into the pockets. To determine the band sizes, 5 µl 100 bp DNA ladder was mixed with 3 µl 6 x Orange DNA loading dye and loaded onto the gel. The gel was run at 132 V and 150 W for 1 h and DNA was visualised by UV light. If contaminations were detected in the negative controls, the PCR run was repeated.

3.5.2.4 LINE-1 sequencing

To analyse CpG methylation, LINE-1 PCR products (see 3.5.2.2) were subjected to pyrosequencing [278–280]. Pyrosequencing was performed using the Qiagen PyroMark Q24 platform according to the manufacturer’s instructions. The time for binding of biotinylated DNA to the streptavidin-coated beads was increased to 25 min. Assay setup was performed using the Qiagen PyroMark Q24 software obtaining the required amounts of substrate, dNTPs, and enzyme (Tab. 21). LINE-1 sequencing primer (LINE1-pyrseq-01, 10 µM) (see 2.5) was diluted in Annealing Buffer to obtain a final concentration of 0.3 µM.

Data analysis was performed using the Qiagen PyroMark Q24 software to quantify the ratio of methylated to unmethylated cytosine for each CpG position.

Table 21: Bead mixture for pyrosequencing (left) and volumes of reagents loaded onto the cartridge (right).

Bead mixture		Reagent volumes	
Sepharose streptavidin beads	1 µl	Enzyme mixture	85 µl
Binding buffer	40 µl	Substrate mixture	85 µl
Water (MilliQ)	19 µl	Nucleotide A	54 µl
LINE-1 PCR product	20 µl	Nucleotide C	57 µl
		Nucleotide G	59 µl
		Nucleotide T	59 µl

3.6 Protein techniques

3.6.1 Protein isolation

Cell pellets (see 3.3.7) were resuspended in RIPA buffer supplemented with protease inhibitor (10 µl/1 ml) and transferred to 1.5 ml reaction tubes. The samples were sonicated for 10 sec with 30 % power using the Sonopuls HD 2070 homogeniser to disrupt the cellular structure. Subsequently, the samples were incubated 30 min on ice before centrifuging them at 14,000 rpm (20,817 g) for 15 min at 4 °C. The supernatant was transferred to a new tube and used to determine the protein concentration (seen 3.6.2).

3.6.2 Determination of protein concentration by Bradford assay

Protein concentration of cellular lysates was determined using Bradford assay [281]. Protein samples in RIPA buffer (see 3.6.1) were diluted in RNase free water at least 1:6 to prohibit the interaction of RIPA buffer with the Bradford reagent. Cell lysates in 0.2 M NaOH did not require dilution in water to prohibit interaction with the reagent. NaOH lysates were diluted in NaOH (1:2 - 1:10) to avoid protein concentrations higher than the used standard.

Samples and BSA protein standards (0.75, 0.5, 0.25, 0.125, 0.0625, 0.0) were at least prepared in duplicates and 5 µl/well was added to a 96-well plate. 250 µl of Bradford solution (1:5 in H₂O) was added and the plate was incubated 5 - 10 min at room temperature. The absorption was measured at 595 nm using a plate reader and the obtained standard curve was used to calculate the protein concentrations.

3.6.3 Sodium dodecylsulfate-polyacrylamide gel electrophoresis

Proteins were separated according to their size by sodium dodecylsulfate-polyacrylamide gel electrophoresis (SDS-PAGE) [282]. 20 µg of protein lysates (see 3.6.2) were diluted in 4 x Laemmli buffer and water to a final volume of 30 µl. The diluted protein and 6 µl protein standard were loaded on a 4 - 20 % polyacrylamide gel in 1 x TGS running buffer. Separation was performed for 75 min at 35 mA.

3.6.4 Western blot

Proteins separated by SDS-PAGE (see 3.6.3) were transferred to a PVDF membrane (0.45 µm) using a semi-dry blotting system [283]. For each gel, 2 Whatman[®] filter papers were soaked in buffer I, 3 in buffer II and 5 in buffer III for approximately 15 min. The PVDF membrane was activated for 1 min in methanol, followed by 5 min in deionised water and was transferred to buffer II for 10 min. The gel was equilibrated in buffer III for 5 min. The transfer sandwich was stacked as following: anode (+), filter papers buffer I, filter papers buffer II, PVDF membrane, gel, filter papers buffer III, cathode (-). The transfer was performed for 1 h at 230 mA.

The membrane was blocked in 5 % milk for 1 h at room temperature and incubated with the primary antibody in 5 % milk over night at 4 °C. After 6 washing steps with TBS-T (5 min), the membrane was incubated with the horseradish peroxidase (HRP)-labelled secondary antibody (5 % milk) for 1 h at room temperature. Antibody dilutions are listed in table 4. The membrane was washed and proteins were visualised using enhanced chemiluminescence (ECL) and the ChemiDoc imaging system. Protein sizes were determined using the pre-stained protein standard. Afterwards, the membrane was washed twice in TBS-T (5 min) and bound antibodies were removed by incubating the membrane for 30 min in pre-warmed (37 °C) stripping solution. The membrane was washed twice in TBS-T to allow the detection of other proteins.

3.7 Paraffin processing of tissue and staining procedures

3.7.1 Paraffin embedding and cutting of tissue sections

Formalin fixed samples were hydrated for at least 2 h under rotation and water was changed regularly. The samples were placed into a tissue processor for paraffin infiltration over night (Tab. 22). On the next day, the tissues were embedded into paraffin blocks for preparation of thin tissue sections. The blocks were frozen over night at -20 °C and thin tissue sections were produced using a microtome. The sections were carefully placed into a 37 °C water bath and transferred to glass slides. The slides were dried over night at 37 °C.

In case of OTCs (see 3.3.13), the cultures were placed into water for at least 2 h, before dehydration in 30 %, 50 % and 60 % ethanol (1 h each) with constant stirring. Afterwards, over night paraffin infiltration was performed (Tab. 22). The paraffin blocks were cooled on ice and sections are dried over night at 50 °C.

3.7.2 Deparaffinisation of tissue slides

Tissue slides were deparaffinised by placing them 3 times into xylene followed by a decreasing ethanol series (100 %, 100 %, 96 %, 70 %). After 5 min in each bath, the slides were washed in deionised water and staining was performed.

3.7.3 Haematoxylin and eosin staining

The deparaffinised slides (see 3.7.2) were stained for 2 min in haematoxylin and blued in tap water for 5 min. Afterwards, they were placed for 30 sec into eosin solution and washed with deionised water four times. Washing was performed by dipping and slightly shaking the slides in deionised water, then moving the slides to a fresh bath repeating the procedure.

Mounting was performed by dipping the slides consecutively in water with glacial acetic acid, 70 % EtOH, 96 % EtOH and 100 % EtOH. After two incubation steps in xylene for 3 min, the slides were mounted with histofluid and dried at room temperature. To allow further analysis of the staining, the slides were scanned using a NanoZoomer S210 Digital slide scanner (40 x objective).

Table 22: Applied programme for tissue dehydration and paraffin infiltration.

Alcohol	Duration	Temperature
70 % EtOH	45 min	35 °C
80 % EtOH	45 min	35 °C
80 % EtOH	90 min	35 °C
90 % EtOH	90 min	35 °C
90 % EtOH	90 min	35 °C
96 % EtOH	90 min	35 °C
96 % EtOH	90 min	35 °C
Isopropyl alcohol	90 min	35 °C
Isopropyl alcohol	90 min	35 °C
Xylene	2 h 30 min	40 °C
Xylene	2 h 30 min	40 °C
Paraffin	2 h 30 min	56 °C
Paraffin	2 h 30 min	56 °C
Paraffin	2 h 30 min	56 °C

3.7.4 Immunohistochemical staining

Following the deparaffinisation (see 3.7.2), antigen retrieval was performed by placing the slides into 10 mM citrate buffer and heating them 3 times (560 W, 5 min) in a microwave. After each heating step, the level of buffer was controlled and refilled, if necessary, to prevent drying of the slides. The slides were allowed to cool down for at least 20 min before washing them 4 - 6 times with deionised water.

The endogenous peroxidase activity was blocked for 20 min in 200 ml methanol containing 4 ml 30 % hydrogen peroxide solution. Afterwards, the slides were washed in deionised water (4 - 6 x) and the tissue section was encircled with a water repelling pen. The slides were incubated in PBS-T for 2 - 5 min with slight agitation, before blocking in 10 % horse serum in PBS for 30 min in a humid chamber. The following incubation with the primary antibody was performed over night at 4 °C. The antibody was diluted in PBS with 1 % horse serum. Applied antibodies and their dilutions are listed in table 4.

The primary antibody solution was removed and the slides were rinsed with PBS-T, before washing them twice with PBS-T for 5 min. The secondary biotinylated antibody (Tab. 4) was diluted in PBS with 1 % horse serum and incubated on the slides for 30 min in a humid chamber. Simultaneously, complex A and B solutions from the Vectastain ABC kit were mixed in PBS (each 1:50) and incubated for 30 min at 4 °C. After incubation with the secondary antibody, the slides were washed with PBS-T (2 x, 5 min) and the A-B-complex solution was added for 30 min. The slides were again washed with PBS-T (2 x, 5 min) and stained using the

liquid DAB+ Substrate Chromogen System (1 drop DAB+ chromogen per 1 ml buffer solution). The reaction was stopped by placing the slides in deionised water, washing them several times. Afterwards, haematoxylin was used as a nuclear counterstaining. The slides were blued in tap water, washed twice with deionised water and mounted with Aquatex. For further analysis, the slides were scanned with the NanoZoomer S210.

3.7.5 Fluorescence staining

Glass slides containing treated tumour cells (see 3.3.6) were adjusted to room temperature, if stored at -20°C , and different sections for staining were encircled using a water repelling pen. The slides were rehydrated and blocked using 3 % BSA solution for 30 min. If the cells were previously labelled with the proliferation marker EdU, the reaction cocktail was prepared according to the manufacturer's protocol and incubated on the slides for 30 min in a light protected humid chamber. Afterwards, the slides were washed 3 times with 3 % BSA. Incubation with the primary antibody was performed over night at 4°C in a light protected humid chamber. Primary antibodies (Tab. 4) were diluted in 3 % BSA.

The slides were allowed to adjust to room temperature before removing the primary antibody. The slides were placed into 0.02 % Triton X-100 solution for 5 min. Subsequently, the slides were washed twice in PBS⁺ for 5 min and dipped shortly into tap water. Secondary antibodies (Tab. 4) were diluted in 3 % BSA solution containing 2 $\mu\text{g}/\text{ml}$ DAPI. Incubation with the secondary antibody was performed for 30 min at 37°C followed by 30 min at room temperature in a light protected humid chamber. Washing steps were performed as described above and the slides were mounted with mowiol containing 25 mg DABCO/ml.

3.8 *In vivo* experiments

3.8.1 Animals

All animal experiments were approved by the Regierungspräsidium (Karlsruhe, Germany) and performed according to government and institutional guidelines and regulations. Immunodeficient female Rag2^{-/-}Il2rg^{-/-} mice were purchased from Envigo and housed in the animal facility of the German Cancer Research Centre (DKFZ) (Heidelberg, Germany). Mice were kept under pathogen-free conditions in individually ventilated cages in a temperature-controlled environment receiving water and food *ad libitum*.

3.8.2 Xenograft model

HCT116 cells were cultured as described in 3.1.1. To improve the comparability between the xenograft experiments, HCT116 cells were expanded and cryopreserved (see 3.1.2) to ensure usage of the same cell batch for all experiments.

HCT116 cells were harvested, counted (see 3.1.1) and resuspended in PBS for *subcutaneous* (*s.c.*) injection into the right flank of the immunodeficient Rag2^{-/-}Il2rg^{-/-} mice. Tumour growth and weight were monitored three times a week. Tumour size was measured using a caliper and tumour volume was calculated ($V = W^2 * L / 2$) [284]. Mice were sacrificed if a termination criterion was reached, according to the authorities' regulations.

3.8.3 *In vivo* screening to determine the optimal treatment dosages and combination in xenograft-bearing mice

IMD substances were solubilised in DMSO (10 µg/µl). 2DG (99 %, ACROS Organics) was solubilised in *aqua ad injectabilia* (250 µg/µl). All solutions were sterilised using a 0.22 µm filter. All substances were stored in small aliquots at -20 °C to avoid repeated freezing and thawing cycles. Directly prior to usage, the treatments were diluted under sterile conditions to obtain the applied treatment concentrations keeping the amount of solvent constant for each injection (100 µl H₂O + 10 µl DMSO).

Xenograft-bearing mice (see 3.8.2) either received single treatment with a flavagline derivative (0.2 mg/kg, 0.5 mg/kg, 1.0 mg/kg), 2DG (100 mg/kg, 200 mg/kg, 400 mg/kg), or a combination of both (Fig. 8) in groups of six to determine the most effective dosage and treatment combination for further experiments.

The treatment was started 10 days after *s.c.* tumour cell injection. The mice received 3 treatments per week over a maximum of 4 weeks (Fig. 9) or until any termination criterion was reached, depending on what happened first. The treatment was administered through *intraperitoneal* (*i.p.*) injection.

Group	1			2			3			4			5			6			7			8			9			10		
Subgroup	1	2	3	4	5	6	7	8	9	10	11	12	13	14	15	16	17	18	19	20	21	22	23	24	25	26	27	28		
IMD-1	-	-	-	-	A	B	C	A	B	C	A	B	C	A	B	C	-	-	-	-	-	-	-	-	-	-	-	-		
IMD-3	-	-	-	-	-	-	-	-	-	-	-	-	-	-	-	-	A	B	C	A	B	C	A	B	C	A	B	C		
2DG	-	1	2	3	-	-	-	1	1	1	2	2	2	3	3	3	-	-	-	1	1	1	2	2	2	3	3	3		

Legend:

Flavagline concentration

A	0.2 mg/kg
B	0.5 mg/kg
C	1.0 mg/kg

2DG concentration

1	100 mg/ml
2	200 mg/ml
3	400 mg/ml

Figure 8: Treatment combinations of synthetic flavagline derivatives and 2DG to determine the optimal dosage and combination.

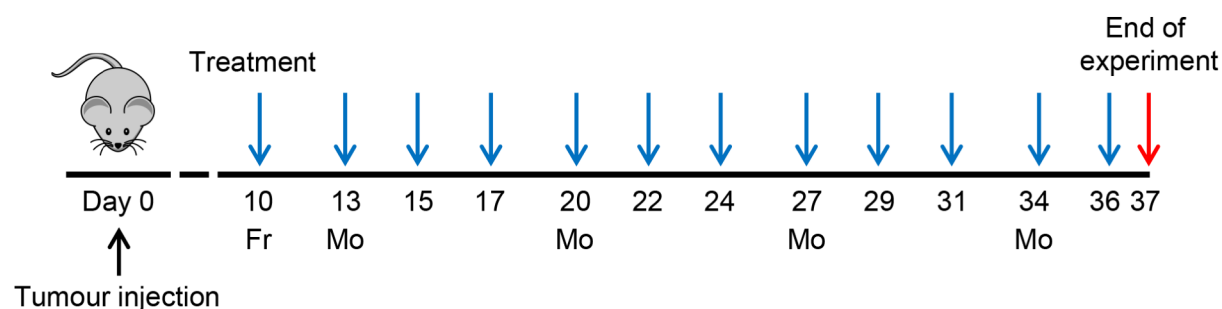


Figure 9: Schematic illustration of the applied treatment schedule to determine the optimal treatment dosage and combination. Each treatment group consisted of 6 mice and HCT116 xenografts were injected *s.c.*. *I.p.* treatment injections were started at day 10 with a maximum of 12 injections over 4 weeks. The mice remained in the experiment until any termination criterion was reached or until day 37 after tumour injection.

3.8.4 Efficacy and side effect profiling of optimal treatment dosage in xenograft-bearing mice

Upon optimisation of treatment dosage and combination (see 3.8.3), the combination with the greatest efficacy (IMD-3 1.0 mg/kg \pm 2DG 100 mg/kg) was applied to xenograft-bearing mice in a larger setting. Each treatment group consisted of 27 mice and tumours were injected as described in 3.8.2. Treatments were prepared as described in 3.8.3. The mice were split in three smaller separate experiments (4 x 9 mice) to facilitate the handling process (Fig.10) and received up to 12 *i.p.* treatment injections over 4 weeks starting at day 10. The mice remained in the experiment until any termination criterion was reached or they reached an age of 52 weeks.

To assess the influence of synthetic flavagline treatment on glucose uptake into the tumour, three mice of each treatment group were subjected to MRI and PET/CT scans, performed after 2 treatment injections (day 14), 5 injections (day 21) and 11 injections (day 35) (Fig.10). Imaging mice were distributed equally over the three smaller experiments, imaging one mouse of each treatment condition in each small experiment (Fig.10).

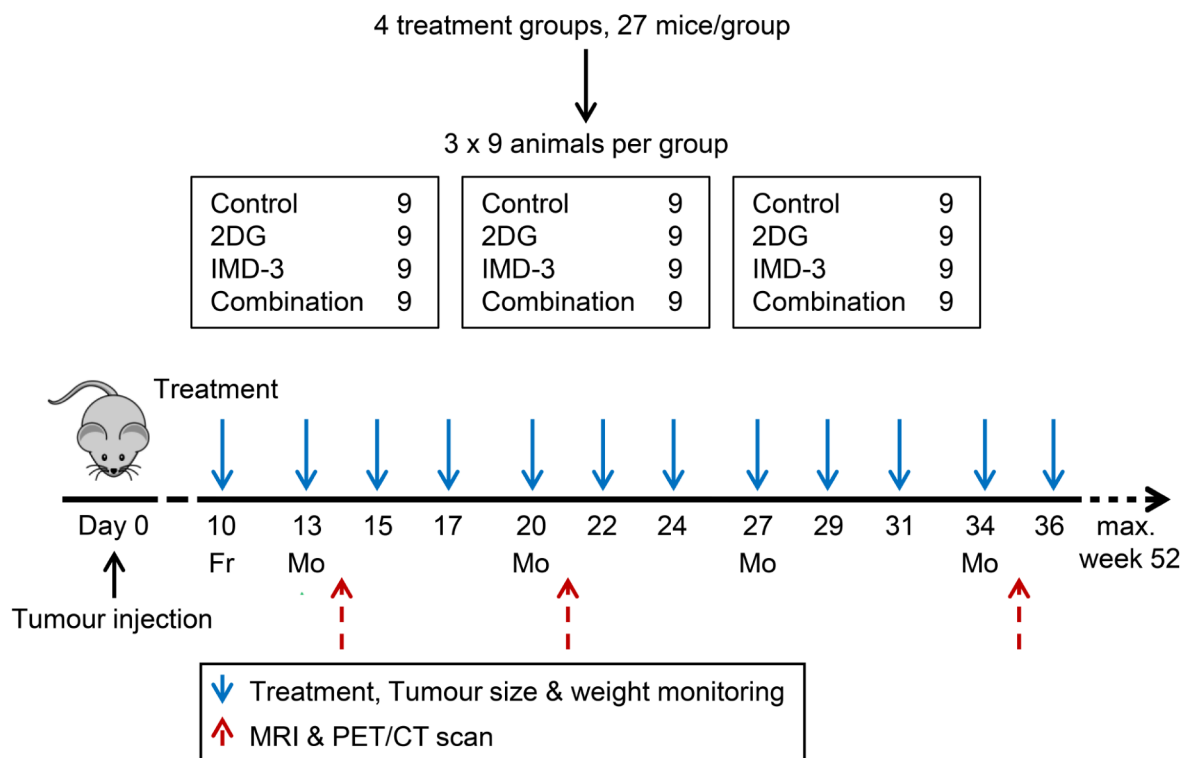


Figure 10: Schematic treatment and imaging schedule of the optimised flavagline concentration (IMD-3 1.0 mg/kg \pm 2DG 100 mg/kg). HCT116 xenografts were injected *s.c.* and *i.p.* treatment injections were started at day 10 with a maximum of 12 injections over 4 weeks. MRI and PET/CT scans were performed at day 14, 21 and 35. The mice remained in the experiment until any termination criterion was reached or they reached an age of 52 weeks.

To allow sufficient incorporation of FDG into the tumours, the imaging mice were fasted for 12 h prior to tracer injection with free access to drinking water. For imaging, mice were anaesthetised and the MRI scan was performed using a Bruker BioSpec 3 Tesla with ParaVision software 360 V1.1. For lesion detection, T2 weighted imaging was performed using a T2-TurboRARE sequence: TE = 47.5 ms, TR = 2195 ms, FOV 30 x 30 mm, slice thickness 1.0 mm, averages = 7, rare factor 10, slices 10, voxel size 0.2344 x 0.2344 x 1 mm³, image size 128 x 128. Tumour volume was determined by manual segmentation using the Bruker ParaVision software 6.0.1. Mice were kept anaesthetised and warm using a heating pad. For PET analysis, mice were injected with 6 - 8 MBq of FDG in a total volume of 100 μ l via the lateral tail vein. After 10 min to allow distribution of the tracer, imaging was performed using an InveonTM dedicated PET docked with a multimodality CT. PET scans were acquired using dynamic imaging over 30 min separated in 6 frames of 5 min (frame 1: 0 - 5 min; frame 6: 25 - 30 min). Reconstruction was performed using iterative reconstruction algorithm (OSEM2D). Anatomical CT scans were used

for fusion imaging. The scanning parameters were an x-ray voltage of 50 kV with an anode current of 500 μ A and an exposure time of 200 ms. 360 rotation steps were performed with a total rotation of 360°. The field of view was set to 90.56 mm x 53.09 mm and the binning factor was 4. For image reconstruction, a downsample factor of 2 was used. Analysis of the reconstructed images was performed using the vendor software package InveonTM Research Workspace (IRW) software 2.2. Incorporation of FDG into the tumours was evaluated by drawing a region of interest (ROI) around the tumour to determine the maximum standardised uptake value (SUV_{max}). SUV_{max} values were corrected for the background value in the muscle tissue. The MRI and PET/CT scans and analysis were performed at the Small Animal Imaging Centre of the German Cancer Research Centre (DKFZ, Heidelberg).

3.8.5 Application of IMD-3 solubilised in HSA

To assess the efficacy-enhancing effect of HSA *in vivo*, HCT116 xenograft-bearing mice (see 3.8.2) were treated with 1.0 mg/kg IMD-3 alone or in combination with 100 mg/kg 2DG solubilised in HSA solution. The treatment schedule of the previous experiment (Fig. 10) was applied. Each treatment group consisted of six mice. MRI and PET/CT imaging was not performed.

200 g/l HSA solution (Baxalta) was diluted to a concentration of 10 mg/ml. 2DG (ACROS Organics) was solubilised in 10 mg/ml HSA solution to a final concentration of 250 μ g/ μ l, sterilised using a 0.22 μ m filter and stored at 4 °C. IMD-3 was solubilised in DMSO (10 μ g/ μ l), sterilised and stored in small aliquots at -20 °C to avoid repeated freezing and thawing cycles. Directly prior to usage, the treatments were diluted under sterile conditions to obtain the final treatment concentrations keeping the amount of solvent constant for each injection (100 μ l HSA solution + 10 μ l DMSO).

3.8.6 Sample preparation

The tumour and organs (pancreas, liver, kidney, lung, heart, brain) were removed and one half was fixed in 3.7 % formalin, whereas the second half was directly frozen in liquid nitrogen and stored at -80 °C.

To prepare the digestive tract, the small intestine was cut in 2-3 pieces and the appendix was removed from the colon. Small intestine and colon were carefully rinsed with PBS to remove faeces followed by 10 % buffered formalin (see 2.9). The tissue was arranged in a spiral in a tissue cassette, a tissue foam pad was placed on top and the closed cassette was submerged in 10 % buffered formalin for fixation. The stomach was opened along the greater curvature and carefully rinsed with PBS followed by 10 % buffered formalin. The stomach was placed into a tissue cassette with the inner side facing downward and a tissue pad was used to fix the position. The cassette was submerged in 10 % buffered formalin for fixation. Samples were collected over one week before dehydration and paraffin infiltration (see 3.7.1).

3.9 IMD-3 characterisation

3.9.1 UV spectroscopy

The IMD-3 DMSO stock was diluted in water *ad injectabilia* to obtain a concentration of 100 μM . 400 μl solution were pipetted into a quartz cuvette and an absorption spectrum was measured from 200 nm to 350 nm using a spectrophotometer. During the measurement, the solution was kept at room temperature. Background measurement of the solvent without IMD-3 was performed and subtracted to obtain the IMD-3 spectrum.

3.9.2 Electrospray ionisation mass spectrometry (ESI-MS) analysis of IMD-3-treated cell culture samples and mouse tumours

To determine if IMD-3 was present in the xenograft tumours, high resolution electrospray ionisation mass spectrometry (ESI-MS) was performed. IMD-3-treated cell culture pellets were used as a positive control to establish the methodology before analysis of xenograft tumours.

Three IMD-3-treated HCT116 cell pellets (100 nM, 48 h) (see 3.3.7) were resuspended in 50 μl PBS, pooled in a new reaction tube and centrifuged at 1,200 rpm (290 g) for 10 min. The cell pellet was lysed in 250 μl acetonitrile and sonicated for 10 sec with 30 % power using the Sonopuls HD 2070 homogeniser. After 30 min incubation on ice, the lysate was centrifuged at 14,000 rpm (20,817 g) and 4 °C for 15 min. The supernatant was transferred to a new reaction tube. 10 % of 0.1 % trifluoroacetic acid (TFA) solution in acetonitrile and water (7:3) was added to achieve a TFA concentration of 0.01 % for ESI-MS measurement.

Frozen xenograft tumours were weighted and at least 50 mg of tissue were lysed in 250 μl acetonitrile and sonicated for 30 sec with 30 % power using the Sonopuls HD 2070 homogeniser. The samples were stored on ice to cool down before repeating the sonication step. The lysates were placed on ice for 30 min before centrifugation at 14,000 rpm (20,817 g) and 4 °C for 15 min. The supernatant was transferred to a new reaction tube and stored over night at 4 °C for ESI-MS measurement on the next day. 10 % of 0.1 % trifluoroacetic acid (TFA) solution in acetonitrile and water (7:3) was added to achieve a TFA concentration of 0.01 % directly before the measurement.

The high resolution ESI-MS measurements were performed by Prof. Dr. Jürgen Gross at the MS facility of the Institute of Organic Chemistry (University of Heidelberg) using a Bruker ApexQe FT-ICR instrument. Between every sample the injection tube was cleaned with acetonitrile to avoid cross-contamination of the samples.

3.10 Statistical analysis

Data are presented as the mean \pm standard deviation. If normalisation was required, error propagation was performed. Statistical calculations to compare two groups were performed using unpaired t-test of the GraphPad Prism 9.0.0 software. Comparison of multiple groups was performed using ANOVA followed by Tukey's post-hoc test using GraphPad Prism 9.0.0 software, if not otherwise stated. Significance level of 0.05 was chosen for post-hoc tests and multiplicity adjusted p-values are given for multiple comparisons (ANOVA), reporting the significance level at which the comparison would be considered significant for the family of comparisons [285]. For the survival analysis, all possible pairwise combinations of survival curves were performed using the Log-rank test implemented in GraphPad Prism 9.0.0 software. The obtained p-values were corrected for multiple testing using the Bonferroni-method, correcting the significance level of 0.05 by dividing it by number of performed comparisons [286].

P-values smaller 0.05 were considered significant and depicted with asterisks as following:

* $p \leq 0.05$; ** $p \leq 0.01$; *** $p \leq 0.001$; **** $p \leq 0.0001$; ns, non-significant.

4 Results

4.1 Anti-cancer activity of synthetic flavagline derivatives and their influence on cellular metabolism

4.1.1 Synthetic flavagline derivatives reduce cell viability in a broad spectrum of different cancer cell lines

Previous studies have shown anti-cancer efficacy of synthetic flavagline derivatives (IMD-1, IMD-3) in CRC cell lines (HCT116, HT29), revealing an enhanced growth-inhibitory effect in combination with 2DG [287]. To further assess the applicability of synthetic flavaglines as new anti-cancer therapeutics in a broad spectrum of cancer entities and to deduce first information on the susceptibility of different cancer entities to the treatment, 35 cell lines, including colorectal, breast, brain, lung, pancreas, prostate, and HPV-related cancers, were screened for the efficacy of IMD-1 or IMD-3 alone and in combination with 2DG (Tab. 23, Fig. 11, 12, 13, 14, S1). IMD substances were applied in different concentrations (25, 50, 100, 200 nM), whereas the 2DG concentration (1 mM) was based on the safety and toxicity data reported by clinical studies [31].


Application of 2DG alone did not strongly affect the viability in the majority of cell lines and only reduced the viability in one cell line (KM12) to below 50 % ($p = 7.600 \cdot 10^{-14}$) (Tab. 23). In contrast, treatment with synthetic flavaglines more effectively reduced cell viability in various cancer cell lines, with a higher efficacy of IMD-3 compared to IMD-1 observed consistently in all cell lines (Tab. 23). To determine the half maximal inhibitory concentrations (IC_{50}) of IMD substances non-linear regression was performed. IC_{50} values for IMD-1 could only be determined in 7 out of 35 tested cell lines with an average IC_{50} of approximately 176 nM (Fig. S1). This value could be decreased to ca. 137 nM in 13 cell lines by the addition of 2DG. IMD-3 showed an average IC_{50} concentration of approximately 65 nM in 22 cell lines, which was further reduced by the addition of 2DG to ca. 44 nM in 30 out of 35 tested cell lines (Fig. S1).

The efficacy of synthetic flavaglines did not increase at concentrations higher than 100 nM in the majority of cell lines (Fig. 11, 12, 13, 14, S1). Therefore, this concentration was chosen as working concentration for further experiments. Comparison of the efficacy of IMD substances alone and in combination with 2DG revealed a significant increase of treatment efficacy upon combination with 2DG in 17 out of 35 tested cell lines for IMD-1 and in 24 cell lines for IMD-3, respectively (Tab. 23). For IMD-1 an enhanced growth-inhibitory effect of the combination with 2DG could be detected in 11 cell lines, whereas the combination of IMD-3 and 2DG led to an enhanced growth-inhibitory effect in 14 cell lines. An enhanced growth-inhibitory effect was present if the combination of the synthetic flavagline with 2DG reduced the viability of the cells further than expected from the addition of the single treatment effects. The extent of the enhanced growth-inhibitory effect upon combination of IMD-3 and 2DG strongly depended on

the tested cell line. While 2DG enhanced the effect of IMD-3 by a maximum of approximately 48 % in the CRC cell line HCT15, it only increased the effect in the HPV-transformed cell line SW756 by approximately 10 %.

Table 23: Summary of relative cell viability (compared to vehicle-treated control cells) of different cancer cell entities upon 48 h treatment with 100 nM synthetic flavagline and 1 mM 2DG alone and in combination. Combination treatments marked in bold are significantly different from both single treatments (IMD or 2DG). Cell lines exhibiting an enhanced growth-inhibitory effect (definition see p. 72) of the treatment combination are marked with an asterisk. Multiplicity-adjusted p-values are listed in table ES1.

Cell line	2DG (1 mM)	IMD-1 (100 nM)	IMD-1 (100 nM) + 2DG (1 mM)	IMD-3 (100 nM)	IMD-3 (100 nM) + 2DG (1 mM)	Cancer entity
HCT116	97.7	93.4	89.7	25.2	13.5*	Colon carcinoma (MSI)
HT29	102.4	93.4	95.0	72.5	64.0	Colon adenocarcinoma (MSS)
Colo205	74.6	101.0	72.0	93.5	47.9*	Colon adenocarcinoma (MSS)
SW620	75.5	101.9	68.2*	71.4	36.0*	Colon adenocarcinoma (MSS)
DLD-1	69.8	95.6	72.5	48.7	23.4	Colon adenocarcinoma (MSI)
HCT15	76.6	108.2	68.5*	91.7	43.4*	Colon adenocarcinoma (MSI)
KM12	30.2	95.0	30.1	35.1	17.0	Colon carcinoma (MSI)
Hap1 (wt)	69.9	62.3	43.7	12.5	10.1	Chronic myeloid leukaemia
Hap1 Δ MLH1 c11	84.8	67.5	52.0*	15.2	12.8	Chronic myeloid leukaemia
Hap1 Δ MLH1 c29	78.7	68.0	53.8	14.6	12.8	Chronic myeloid leukaemia
Hap1 Δ MLH1 c30	79.5	63.5	52.3	17.7	15.7	Chronic myeloid leukaemia
Hap1 Δ MLH1 c44	73.9	62.8	50.5	14.2	12.3	Chronic myeloid leukaemia
C33A	78.5	82.5	68.1	22.3	17.4	Cervical squamous cell carcinoma (HPV negative)
CaSki	82.0	90.1	60.9*	43.4	26.3	HPV-related cervical squamous cell carcinoma (HPV 16)
HeLa	92.6	94.6	87.7	68.4	54.2*	HPV-related endocervical adenocarcinoma (HPV 18)
SiHa	100.0	99.3	94.4	77.1	50.8*	HPV-related cervical squamous cell carcinoma (HPV 16)
SW756	98.5	101.2	92.0*	85.7	76.1*	HPV-related cervical squamous cell carcinoma (HPV 18)
UM-SCC-47	56.4	96.4	61.6	52.4	33.4	Tongue squamous cell carcinoma (HPV16)
UM-SCC-104	85.5	84.5	58.4*	78.7	34.1*	Floor of mouth squamous cell carcinoma (HPV 16)
UPCI-SCC-90	67.6	75.3	37.9*	48.4	20.4	Tongue squamous cell carcinoma (HPV 16)
UPCI-SCC-152	77.3	60.6	38.8	45.1	24.1	Tongue squamous cell carcinoma (HPV 16)
HaCaT	90.4	101.0	89.4	50.0	46.0	Immortal (spontan) keratinocytes
MCF7	104.8	85.4	82.2	34.3	27.4	Invasive ductal carcinoma
T-47D	93.2	99.9	80.8*	51.8	43.0	Invasive ductal carcinoma
SW872	79.9	86.4	63.6*	42.5	25.1	Liposarcoma
HT-1080	70.5	91.8	58.8*	31.5	17.0	Fibrosarcoma
SW1353	63.4	87.3	62.6	37.5	22.9	Primary central chondrosarcoma
U251	95.2	97.9	92.1	83.1	64.4*	Astrocytoma
HL-60	86.6	99.5	92.9	79.1	83.6	Acute myeloid leukaemia
RPMI-8226	91.3	99.1	90.0	36.2	26.4*	Multiple myeloma
A549	89.9	92.5	85.7	56.4	35.9*	Non-small-cell lung carcinoma
Dan-G	79.9	102.4	76.2	79.8	52.9*	Pancreatic adenocarcinoma
MIA PaCa-2	86.5	98.7	83.5	69.9	38.5*	Pancreatic ductal adenocarcinoma
DU-145	87.0	91.4	84.8	78.6	56.0*	Prostate carcinoma
PC-3	80.8	90.2	65.1*	39.7	29.2	Prostate carcinoma

Relative viable cells (% control) 0%  100%

As cell lines reacted to different extents to the treatment with synthetic flavaglines, the influence of specific molecular phenotypes on the treatment efficacy was investigated. For instance, isocitrate dehydrogenase 1 and 2 (IDH1, IDH2) mutation are strongly associated with reprogramming of cellular metabolism, as mutant IDH leads to accumulation of the oncometabolite D-2-hydroxyglutarate in the cells [288]. At a concentration of 100 nM, IMD-1 treatment was significantly more effective in IDH-wild type (WT) SW872 cells reducing their viability to 86.4 % compared to IDH1-mutant HT-1080 cells (91.8 %, $p = 0.0162$) (Fig. 11), while no significant difference was detected between WT and IDH2-mutant SW1353 cells or both IDH-mutant cell lines. Upon combination of 100 nM IMD-1 with 2DG, WT SW872 cells were less sensitive to the treatment compared to IDH1-mutant HT-1080 cells (Fig. 11). Both IDH-mutant cell lines, HT-1080 and SW1353, were significantly more sensitive towards 100 nM IMD-3 treatment compared to WT SW872 cells ($p \leq 0.0033$) (Fig. 11). However, WT SW872 cells were significantly more susceptible towards lower concentrations of IMD-3 (25 nM) in comparison to IDH1-mutant HT-1080 cells, while no difference between WT and mutant SW1353 cells was detected. Thus, the comparison did not reveal any consistent influence of IDH mutation status on the efficacy of synthetic flavagline treatment (Fig. 11).

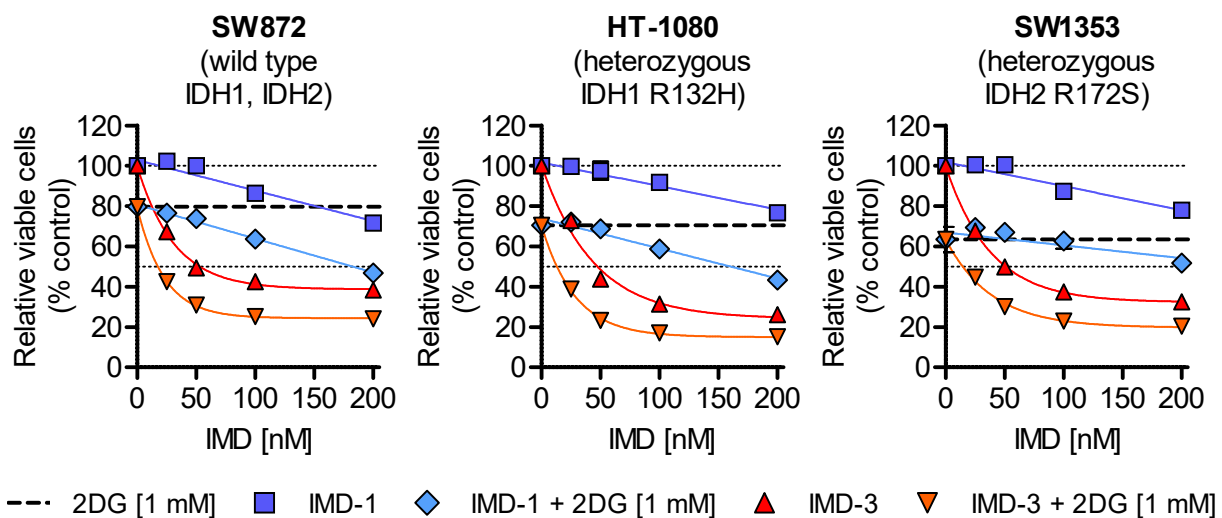


Figure 11: Sensitivity of IDH WT and IDH-mutant cell lines towards 48 h of synthetic flavagline treatment alone and in combination with 2DG (1 mM). Multiplicity-adjusted p-values are listed in table ES1 and ES2.

Another molecular phenotype frequently observed in CRC is microsatellite instability (MSI). MSI arises due to deficient function of mismatch repair (MMR) proteins (MSH2, MLH1, MSH6, PMS2) and has a major implication for patients' prognosis and response to therapy [185]. Previous experiments have shown differences in the sensitivity HCT116 (MSI) and HT29 (MSS) cells [287]. This difference could be reproduced in a new experiment, confirming the higher sensitivity of MSI HCT116 cells towards IMD-3 treatment compared to MSS HT29 cells (Fig. 12A, Tab. ES3). HCT116 cells showed a higher responsiveness towards

all IMD-3 concentrations applied alone or in combination with 2DG ($p \leq 4.060 \cdot 10^{-13}$) except for the single application of 25 nM IMD-3. No significant difference in the responsiveness of both cell lines towards IMD-1 treatment was detected. Higher efficacy of IMD-3 treatment compared to IMD-1 could be confirmed in both cell lines. While a concentration of 100 nM IMD-1 only slightly influenced the viability of HCT116 and HT29 cells (93.4 %), IMD-3 treatment significantly reduced the viability to 25.2 % ($p = 7.305 \cdot 10^{-12}$) and 72.5 % ($p = 5.901 \cdot 10^{-7}$), respectively.

Besides differences in TP53, KRAS or BRAF mutations [289], a major difference between both cell lines is their microsatellite instability phenotype. To analyse whether the observed differences were cell line-specific or generalisable for a broader spectrum of MSI and MSS cell lines, the influence of the MSI phenotype on the efficacy of the treatment was investigated by screening two MSS (Fig. 12B) and three MSI (Fig. 12C) cancer cell lines. Additionally, the influence of *MLH1* knockout in haploid leukaemia cells on the treatment efficacy was examined (Fig. 13).

No significant difference between MSS and MSI cell lines treated with 100 nM IMD-1 was detected, except for HT29 (MSS) cells exhibiting a higher sensitivity towards IMD-1 than HCT15 (MSI) cells (Fig. 12). However, upon combination of 100 nM IMD-1 with 2DG, MSS HT29 cells were significantly less sensitive towards the treatment compared to three out of four MSI cell lines (DLD-1, HCT15, KM12, $p \leq 1.730 \cdot 10^{-13}$). While the other two MSS cell lines, Colo205 and SW620, exhibited a higher susceptibility towards the combination than MSI HCT116 cells ($p \leq 9.870 \cdot 10^{-13}$), but were less responsive than MSI KM12 cells ($p = 1.200 \cdot 10^{-13}$).

Comparison of sensitivities of MSS and MSI cell lines towards 100 nM IMD-3 treatment revealed that three out of four MSI cell lines (HCT116, DLD-1, KM12) showed a significantly more pronounced reduction of cell viability compared to all three MSS cell lines ($p \leq 1.697 \cdot 10^{-7}$) (Fig. 12). Similarly, these three MSI cell lines were more sensitive towards the combination of 100 nM IMD-3 with 2DG than all three MSS cell lines ($p \leq 1.890 \cdot 10^{-13}$). The fourth MSI cell line, HCT15, was significantly less sensitive towards 100 nM IMD-3 treatment, compared to two MSS cell lines (HT29, SW620), while no difference between HCT15 and Colo205 cells was detected. However, upon combination of 100 nM IMD-3 with 2DG, MSI HCT15 cells showed a higher responsiveness than MSS cell lines HT29 and Colo205.

Investigation of the influence of *MLH1* knockout on the responsiveness of cell lines did not reveal significant differences towards treatment with 100 and 200 nM of both IMD substances (Fig. 13, Tab. ES4). However, WT cells already showed a pronounced sensitivity towards synthetic flavagline treatment, especially towards IMD-3, which might mask an influence of *MLH1* knockout in those cell lines.

Taken together, these results suggest that MSI phenotype does not influence the sensitivity of CRC cells towards treatment with IMD-1 but might slightly enhance the responsiveness towards IMD-3. The observed difference in the sensitivity of HCT116 and HT29 cells makes them suitable candidates to further study the molecular mechanisms of synthetic flavagline treatment.

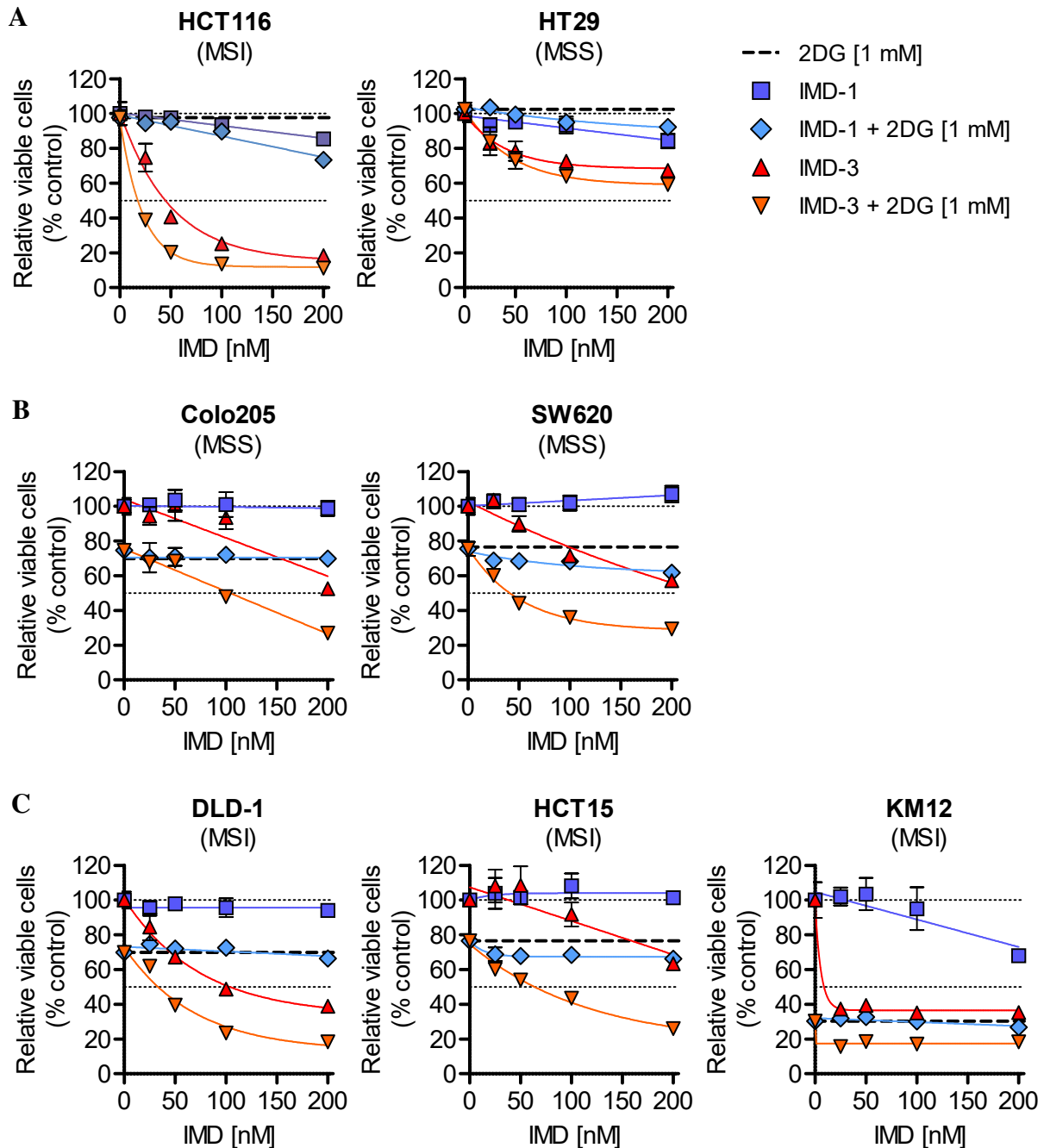


Figure 12: Sensitivity of MSS and MSI CRC cell lines towards 48 h synthetic flavagline treatment alone and in combination with 2DG (1 mM). (A) Sensitivity of CRC cell lines HCT116 (MSI) and HT29 (MSS) towards synthetic flavagline treatment. (B) Sensitivity of MSS CRC cell lines Colo205 and SW620. (C) Sensitivity of MSI CRC cell lines DLD-1, HCT15 and KM12. Experiments with Colo205, SW620, DLD-1, HCT15 and KM12 cells were performed by Angela Salnikov during her internship. Multiplicity-adjusted p-values are listed in table ES1 and ES3.

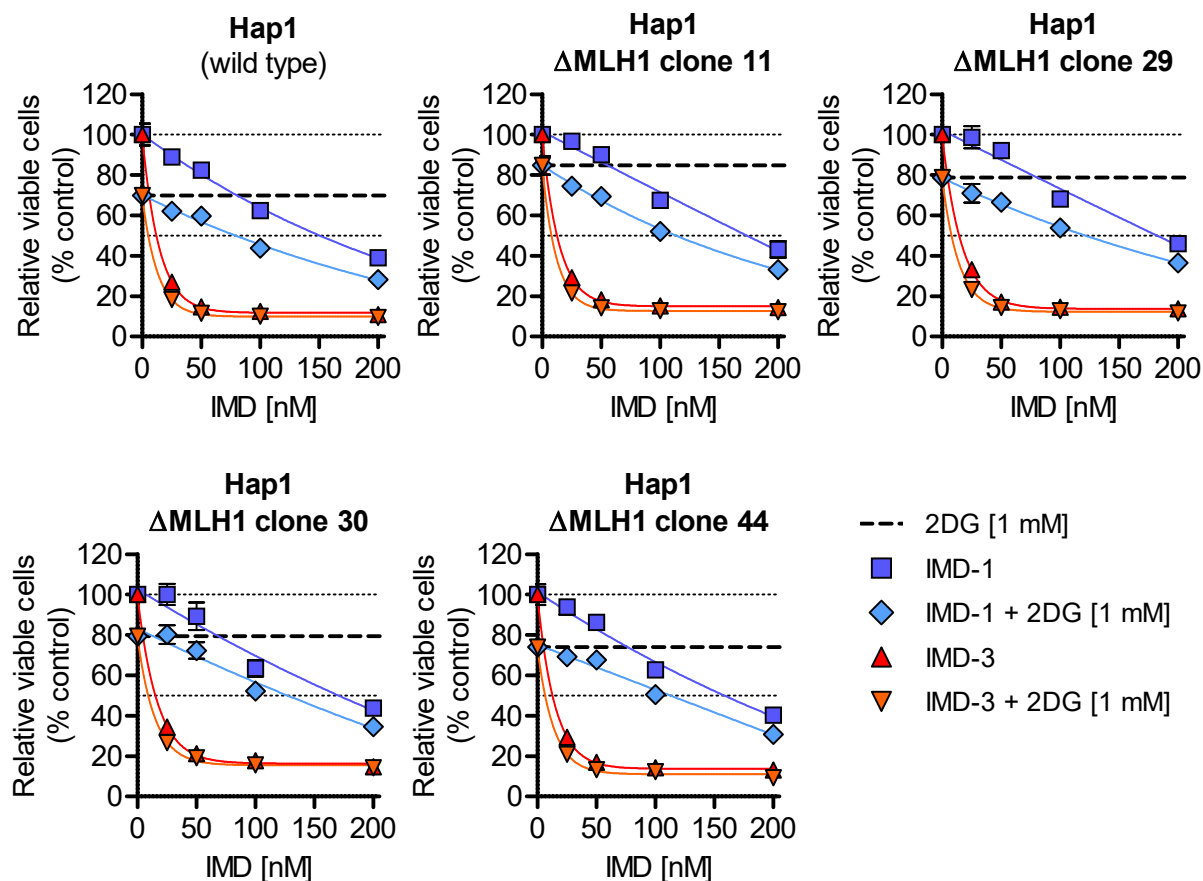


Figure 13: Sensitivity of haploid cell lines with wild type MLH1 (Hap1) or MLH1 knockout clones towards 48 h synthetic flavagline treatment alone and in combination with 2DG (1 mM). Multiplicity-adjusted p-values are listed in table ES1 and ES4.

The third molecular subtype of cancer influencing the disease course and therapy response is HPV-transformed cancers. Therefore, the efficacy of synthetic flavagline treatment in combination with 2DG was examined in four HPV-positive cervical cancer cell lines (CaSki, HeLa, SiHa, SW756), one HPV-negative cervical cancer cell line (C33A) (Fig. 14A), and four HPV-positive head and neck squamous cell carcinoma (HNSCC) cell lines (UM-SCC-47, UM-SCC-104, UPCI-SCC-90, UPCI-SCC-152) (Fig. 14B).

HPV-negative C33A cells, exhibiting a reduced cell viability of 82.5 % upon 100 nM IMD-1 treatment, were significantly more sensitive than two out of four HPV-positive cervical cancer cell lines (SiHa, SW756, $p \leq 0.0266$), but less sensitive than the HPV-positive HNSCC cell line UPCI-SCC-152 ($p = 0.0009$). HPV-negative C33A cells also showed a significantly more pronounced response towards IMD-3 treatment (100 nM) compared to all HPV-positive cell lines ($p \leq 0.0002$). But upon combination of IMD-3 (100 nM) with 2DG, HPV-negative C33A and HPV-positive HNSCC cell lines (UPCI-SCC-90, UPCI-SCC-152) exhibited a similar responsiveness towards the treatment.

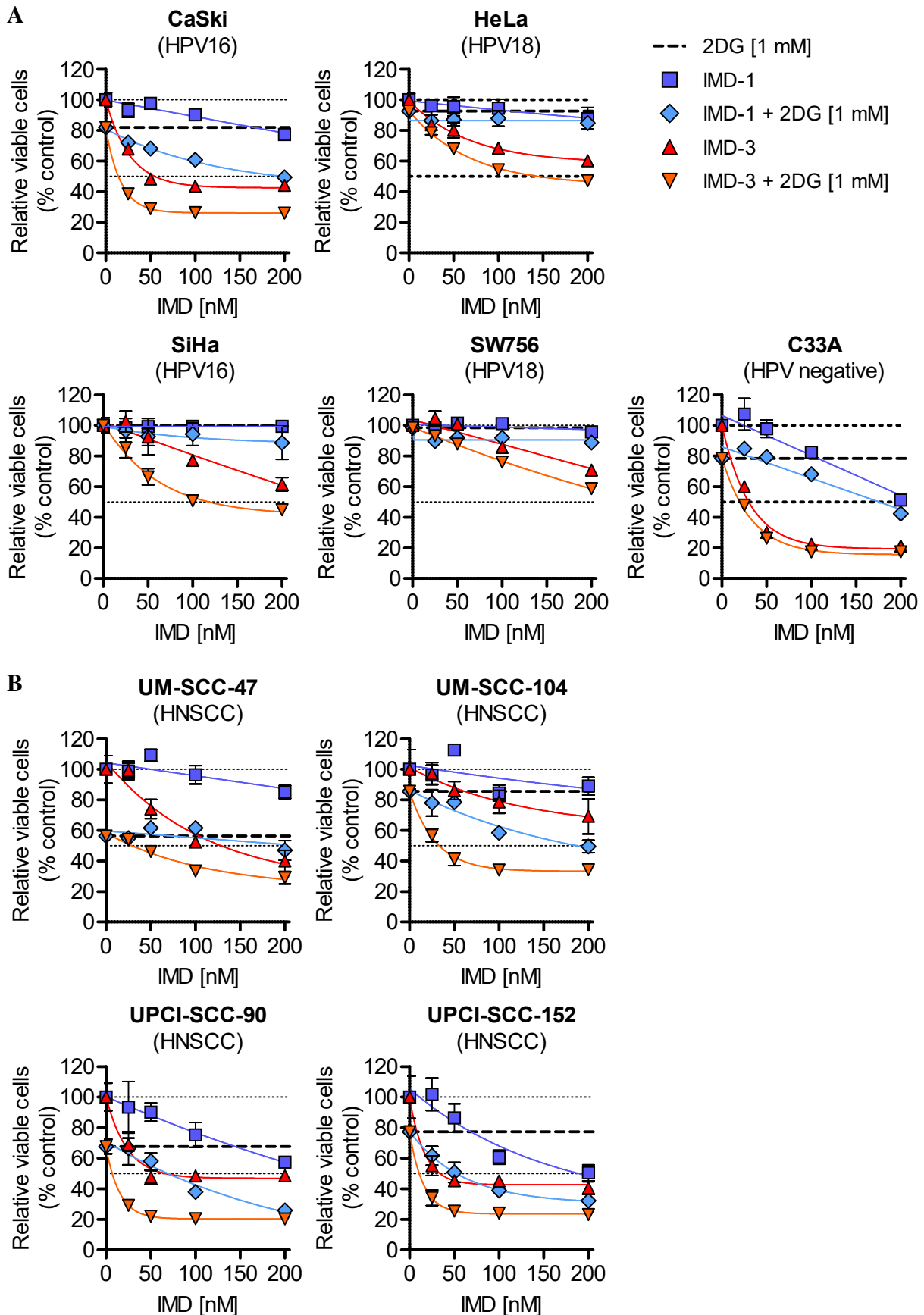


Figure 14: Sensitivity of HPV-positive and HPV-negative cancer cell lines towards 48 h synthetic flavagline treatment alone and in combination with 2DG (1 mM). (A) Sensitivity of HPV-positive and HPV-negative cervical cancer cell lines. (B) Sensitivity of HPV-positive HNSCC cell lines. Multiplicity-adjusted p-values are listed in table ES1 and ES5.

HPV-negative cervical cancer cells C33A seem to be more sensitive towards synthetic flavagline treatment, especially IMD-3, although their higher responsiveness towards IMD-3 might be influenced by their MSI-phenotype. Overall, the comparison of HPV-positive and HPV-negative cells was limited by the fact that only one HPV-negative cervical cell line was analysed and more cell lines shall be compared in order to draw definitive conclusions. For further analysis, HPV-positive cervical cell lines CaSki and SiHa were selected representing one sensitive (CaSki) and one more resistant (SiHa) cell line. HPV-positive HNSCC UPCI-SCC-90 cells were also selected for further analysis, as they were more sensitive towards IMD-1 in comparison to the other cell lines and 2DG addition led to an enhanced growth-inhibitory effect (Tab. 23).

In summary, the combination of synthetic flavaglines, especially IMD-3, with 2DG exhibited pronounced efficacy in several different cancer cell lines. In the following, CRC and HPV-positive cervical and HNSCC cell lines were used to examine the mechanisms underlying synthetic flavagline efficacy in greater detail.

4.1.2 Synthetic flavagline derivatives mainly exert anti-tumour effect through proliferation inhibition

Synthetic flavaglines have shown great potential in the reduction of cell viability in different cancer cell lines. However, to evaluate their potential clinical applicability it is essential to understand the mechanisms underlying synthetic flavagline activity.

Programmed cell death through apoptosis inductions displays one major mechanism, which can be induced through treatment with chemotherapeutics including cisplatin [290]. Several natural and synthetic flavaglines were found to induce apoptosis in cancer cells or sensitise them towards apoptosis induction [156,169,291]. Additionally, previous work with HCT116 and HT29 cells revealed partial induction of apoptosis upon synthetic flavagline treatment, especially by IMD-3 [287]. Therefore, apoptosis induction through IMD-1 and IMD-3 was investigated in HPV-transformed cell lines using fluorescence staining for cleaved caspase-3, an enzyme of the apoptotic pathway, and caspase-cleaved cytokeratin 18. Cisplatin-induced apoptosis was used as a positive control for apoptosis induction in HPV-positive cells.

Consistent with observed lower efficacy of IMD-1 (Fig. 14), its application alone and in combination with 2DG did not induce apoptosis in HPV-positive cancer cells CaSki, SiHa and UPCI-SCC-90 (Fig. 15, 16, 17). Also, 2DG treatment alone did not induce apoptosis, whereas IMD-3 treatment led to a slight increase in the number of apoptotic cells compared to the vehicle-treated control in all three cell lines. However, the effect was less pronounced compared to cisplatin treatment, which strongly induced apoptosis (Fig. 15, 16, 17).

IMD-3-induced apoptosis in HPV-positive cells and previously observed induction in CRC cell lines HCT116 and HT29 [287] cannot fully explain strong reduction of cell viability observed in these cell lines (Fig. 12A, 14), hence the question arose through which other mechanisms synthetic flavaglines reduce cell viability.

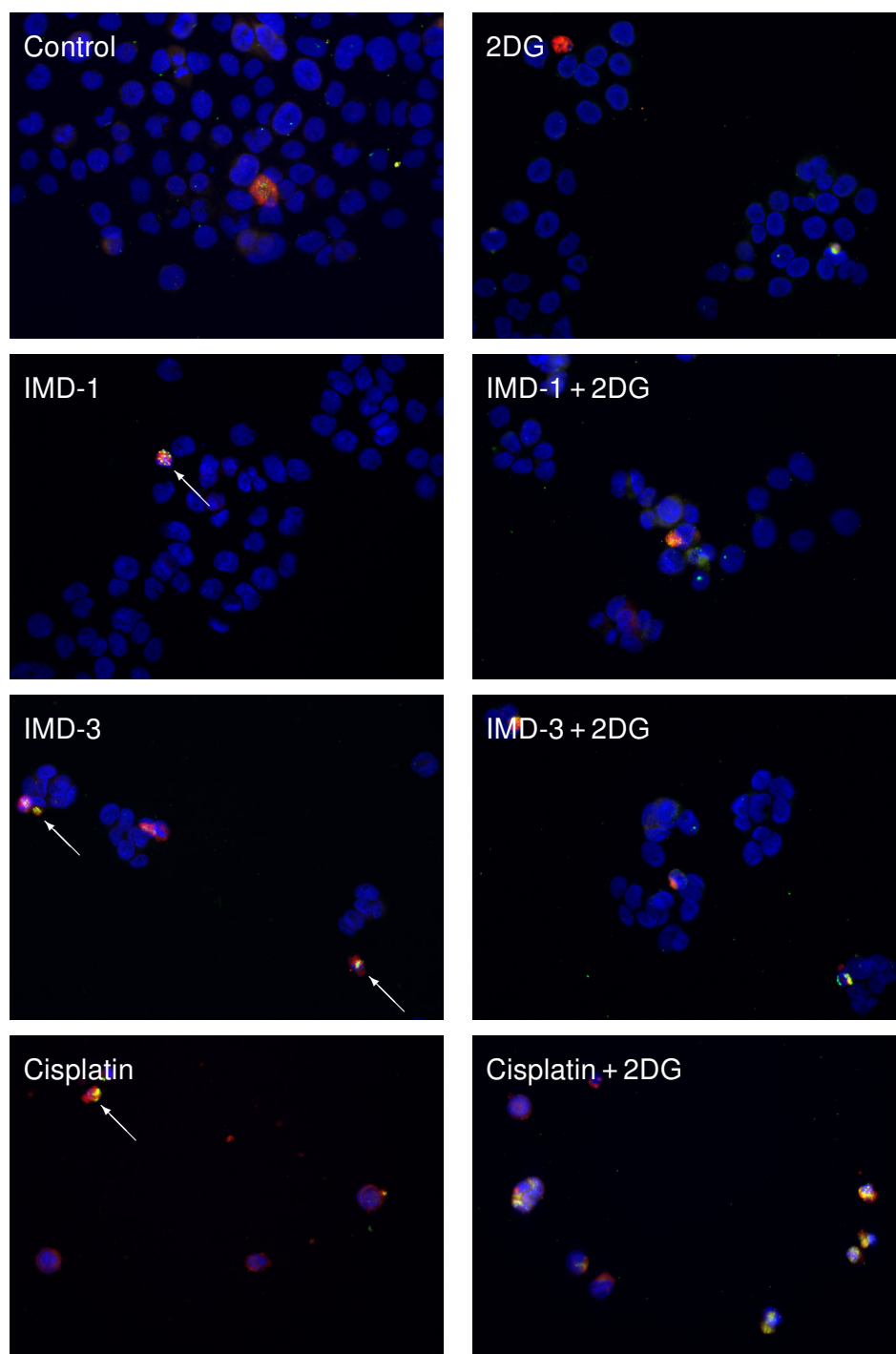


Figure 15: Apoptosis induction in CaSki cells indicated by cleaved caspase-3 (red) and caspase-cleaved cytokeratin 18 (green). Nuclei were counterstained with DAPI (blue). White arrows indicate apoptotic cells. 2DG: 1 mM; IMD-1, IMD-3: 100 nM; Cisplatin: 75 μ M; Treatment: 48 h. Images: Olympus AX79 microscope, 400 x magnification.

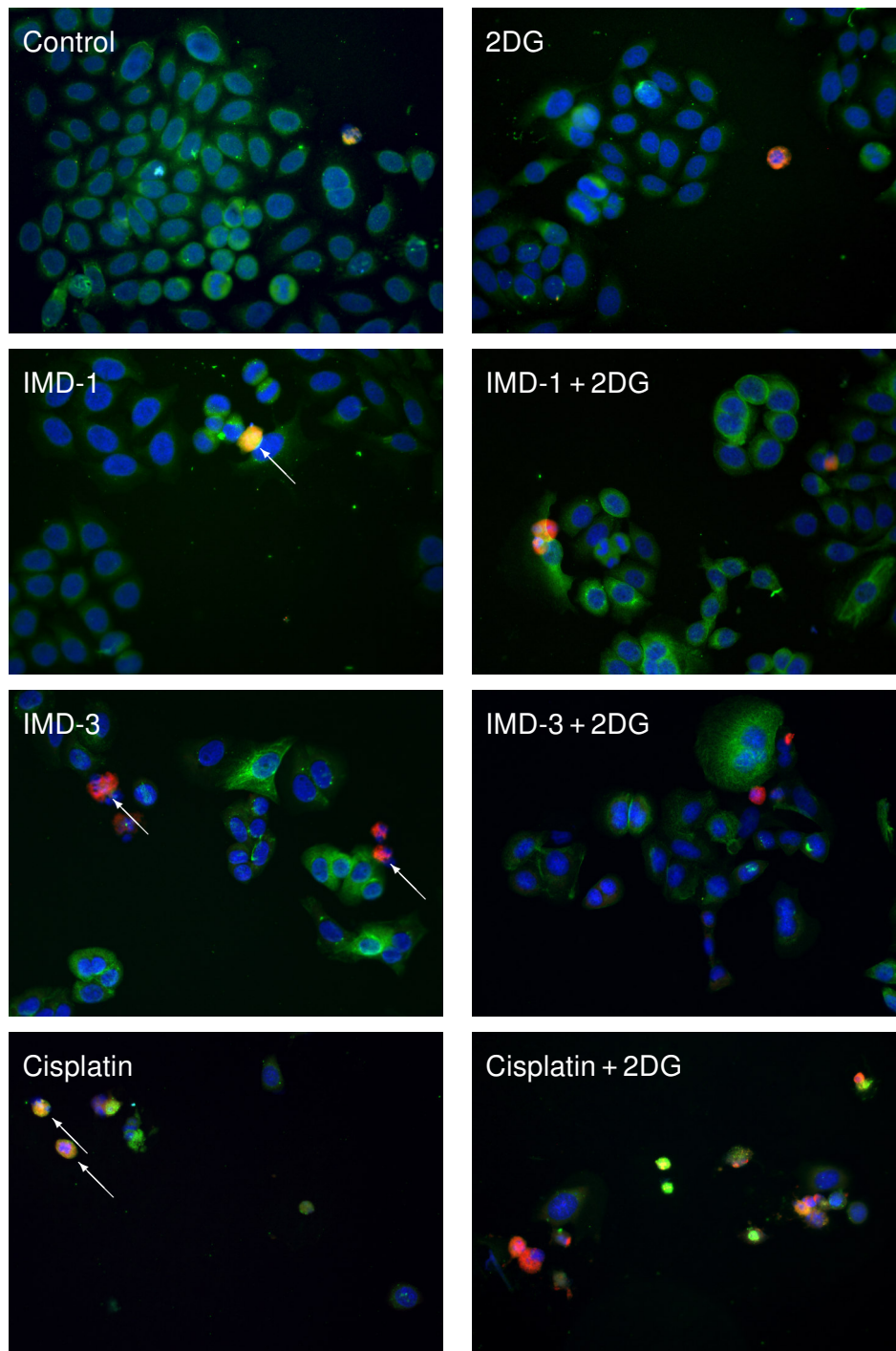


Figure 16: Apoptosis induction in SiHa cells indicated by cleaved caspase-3 (red) and caspase-cleaved cytokeratin 18 (green). Cytoplasm was counterstained for cytokeratin 7 (green) and nuclei were stained with DAPI (blue). White arrows indicate apoptotic cells. Due to the lack of cytokeratin 18 (CK18) expression in SiHa cells, it was not possible to stain for the caspase-cleaved product of CK18. 2DG: 1 mM; IMD-1, IMD-3: 100 nM; Cisplatin: 75 μ M; Treatment: 48 h. Images: Olympus AX79 microscope, 400 x magnification.

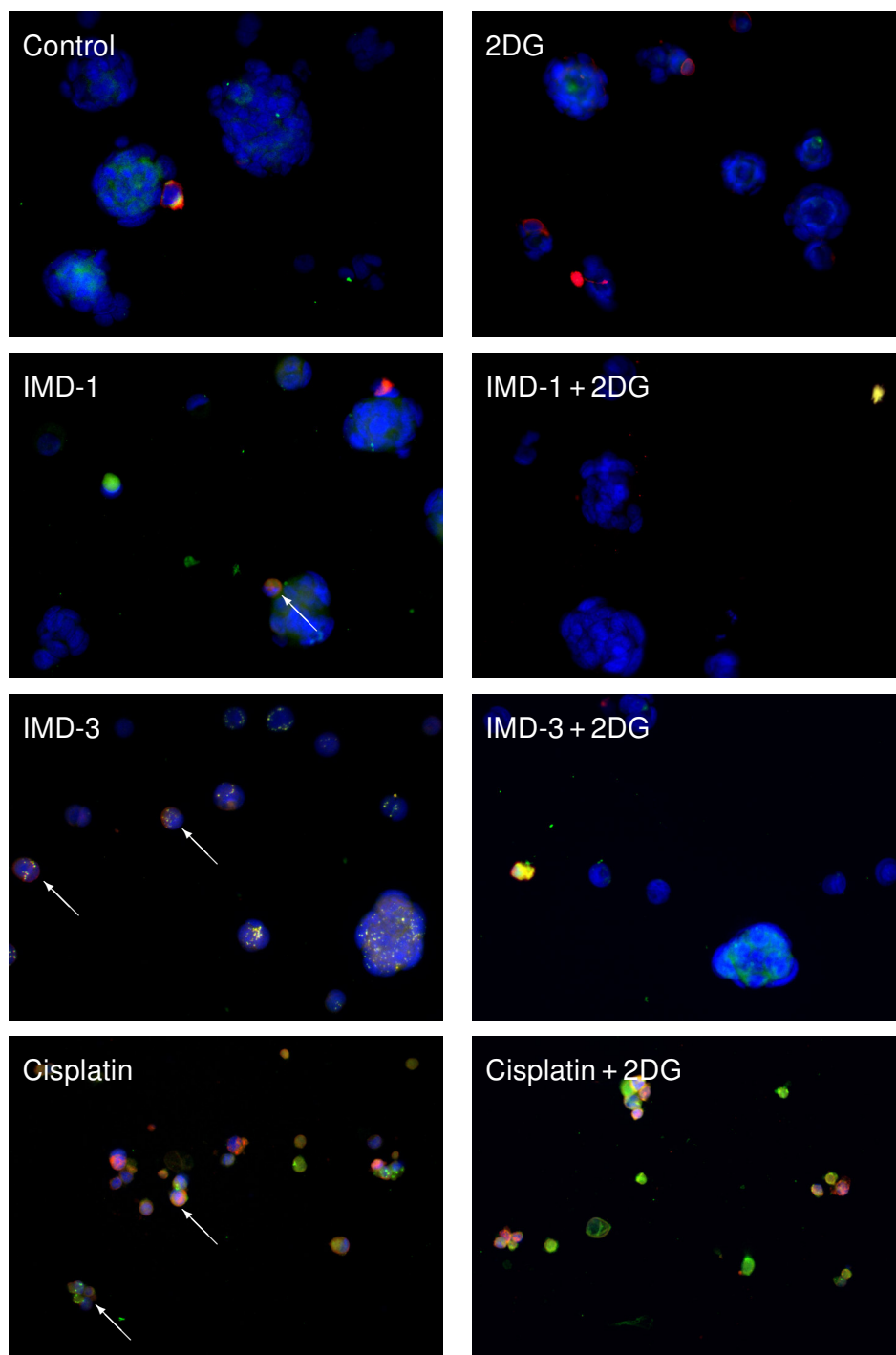


Figure 17: Apoptosis induction in UPCI-SCC-90 cells indicated by cleaved caspase-3 (red) and caspase-cleaved cytokeratin 18 (green). Nuclei were counterstained with DAPI (blue). White arrows indicate apoptotic cells. 2DG: 1 mM; IMD-1, IMD-3: 100 nM; Cisplatin: 75 μ M; Treatment: 48 h. Images: Olympus AX79 microscope, 400 x magnification.

First, general cytotoxicity of synthetic flavaglines was assessed by measuring the amount of released methyl- 3 H-thymidine from previously labelled cells upon treatment. As expected, the amount of released tracer increased over the duration of treatment in both CRC cell lines (Fig. 18A). The amount of released tracer from vehicle-treated control cells indicated the amount of spontaneous cell death occurring during the experiment. Subtraction of spontaneous cell

death from treatment conditions resulted in treatment-induced cytotoxic cell death (Fig. 18B). 2DG and IMD-1 treatment induced cytotoxic cell death in less than 5 % of treated HCT116 cells after 48 h (Fig. 18B). In comparison, IMD-3 treatment alone and in combination with 2DG induced cytotoxic cell death in approximately 15 % of treated cells. Although the extent of this effect correlates with the previously observed induction of apoptosis in HCT116 cells [287], it does not fully explain the observed reduction of cell viability upon IMD-3 treatment (Fig. 12A).

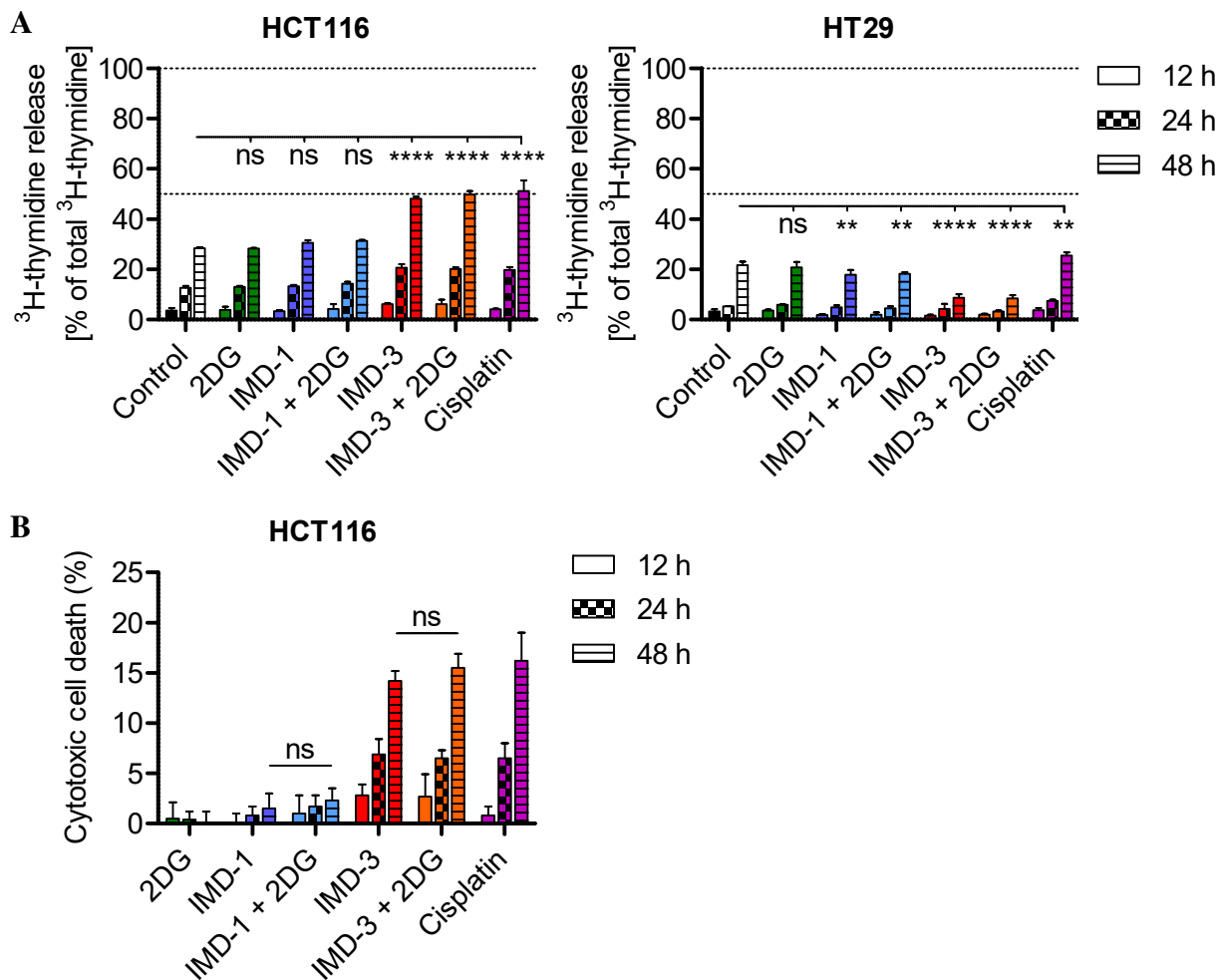


Figure 18: Cytotoxic effects of synthetic flavagline treatment on CRC cells. (A) Percent of released ³H-thymidine from labelled HCT116 and HT29 cells into the medium upon treatment for 12, 24 or 48 h. (B) Cytotoxic cell death induced by treatment in HCT116 cells based on the release of ³H-thymidine. Spontaneous cell death (release observed in control cells) was subtracted to obtain cytotoxic cell death for each substance. In HT29 cells, the release of ³H-thymidine upon IMD treatment was lower in comparison to the control, therefore it was not possible to calculate cytotoxic cell death. 2DG: 1 mM; IMD-1, IMD-3: 100 nM; Cisplatin: 75 μ M. Significance levels (here and in the following) are indicated as: * $p \leq 0.05$; ** $p \leq 0.01$; *** $p \leq 0.001$; **** $p \leq 0.0001$; ns, non-significant. Only p-values of the 48 h time point are indicated in the graphs. Multiplicity-adjusted p-values are listed in table ES6.

Additionally, the released amount of methyl-³H-thymidine in HT29 cells was significantly lower in IMD-treated cells, independent from the addition of 2DG, compared to control cells (Fig. 18A). This effect was more pronounced in IMD-3-treated cells compared to cells treated with IMD-1. This observation of reduced methyl-³H-thymidine release under treatment raised the question, whether decreased release of tracer under IMD-3 treatment occurred due to inhibition of cell proliferation.

The influence of synthetic flavagline derivatives on cell proliferation was investigated in CRC cells measuring incorporation of methyl-³H-thymidine into the DNA during treatment. Strikingly, IMD-3 treatment significantly inhibited cell proliferation in both cell lines (Fig. 19). Addition of 2DG slightly improved the inhibitory effect of IMD-3, although the effect was only significant in HCT116 cells ($p=0.0011$) consistent with the observed strong effect of the combination in this cell line (Tab. 23, Fig.12A). In contrast to IMD-3, application of 2DG or IMD-1 treatment alone only slightly decreased cell proliferation of HCT116 cells, exhibiting a significantly stronger effect in combination compared to IMD-1 alone ($p=1.971*10^{-9}$) (Fig. 19A). No significant effect of 2DG and IMD-1 on proliferation was observed in the less sensitive cell line HT29 (Fig. 19B).

Taken together, inhibition of proliferation is the most likely mechanism responsible for the strong reduction of cell viability observed upon IMD-3 treatment, aided by apoptosis induction.

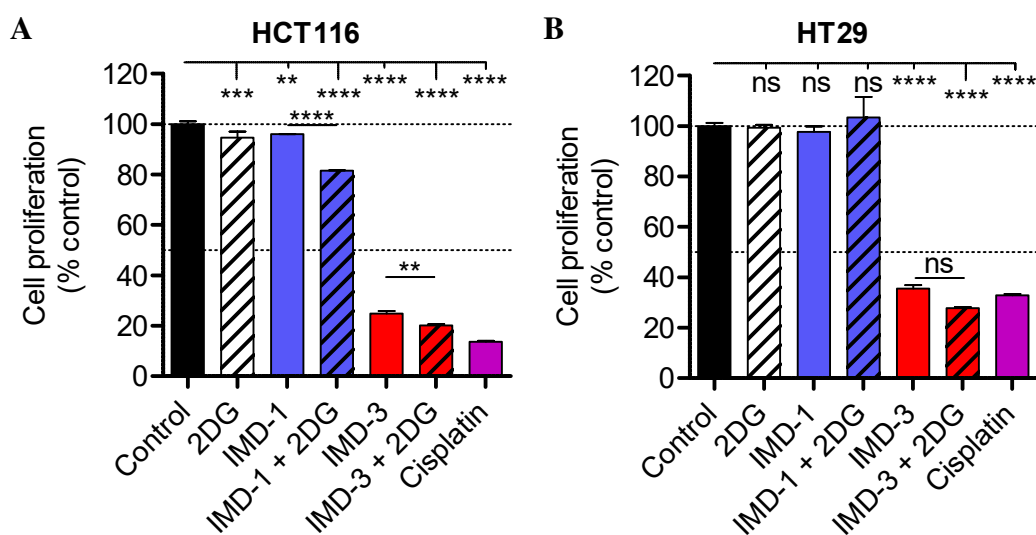
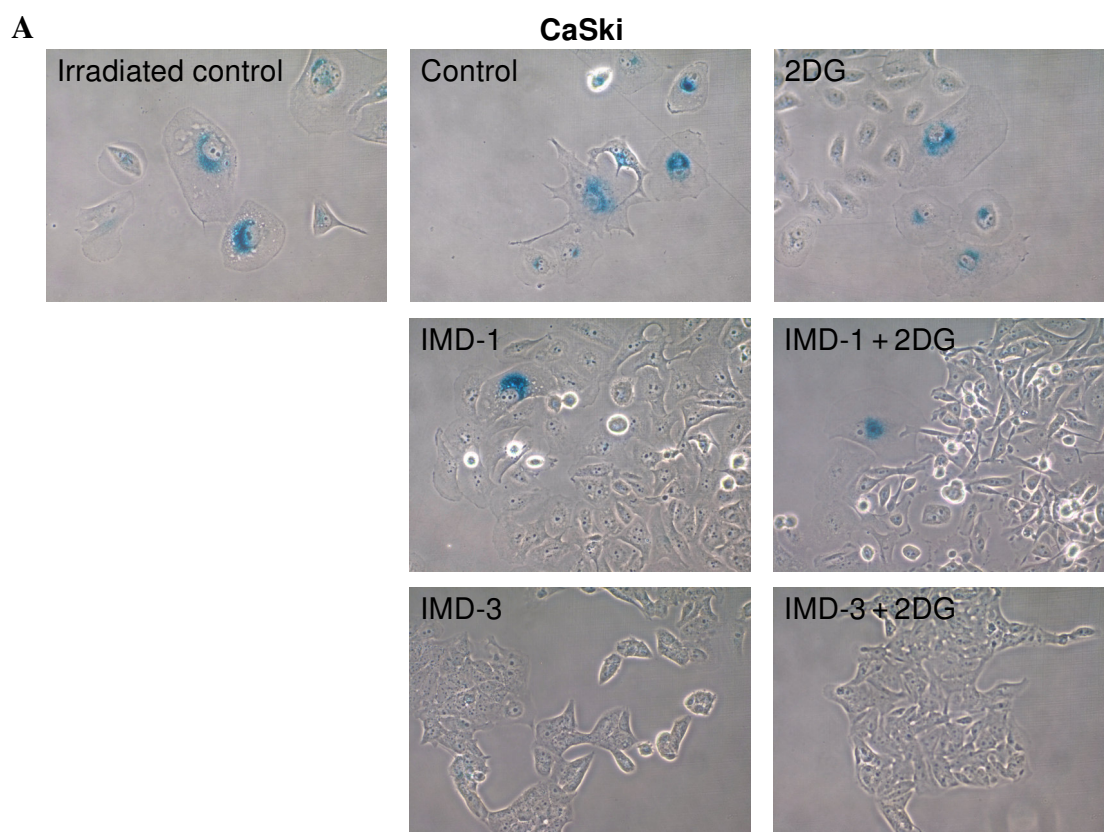


Figure 19: Proliferation inhibition of HCT116 (A) and HT29 (B) cells. Proliferation was measured by the incorporation of ³H-thymidine during treatment. 2DG: 1 mM; IMD-1, IMD-3: 100 nM; Cisplatin: 75 μ M; Treatment: 48 h. Multiplicity-adjusted p-values are listed in table ES7.

4.1.3 Synthetic flavagline derivatives inhibit cell proliferation independent of senescence induction

One prominent mechanism, which inhibits cell growth and proliferation through induction of cell cycle arrest, is cellular senescence [292]. Previous research on CRC cell lines (HCT116, HT29) had not shown senescence induction upon treatment with synthetic flavaglines [287]. To analyse whether senescence induction plays a role in HPV-transformed cancer cell lines upon treatment with synthetic flavaglines, X-gal staining of senescence-associated β -galactosidase was performed. Irradiated cells were used as a positive control for senescence induction.

One week after radiation, irradiated controls of all three HPV-transformed cell lines showed senescent morphology, including enlarged, flattened cytoplasm and higher granularity, as well as positive (blue) X-gal staining for senescence-associated β -galactosidase activity (Fig. 20). Sporadic senescent cells were detected in vehicle-treated control cells of the cervical cancer cell lines CaSki and SiHa (Fig. 20A, 20B), as well as upon 2DG and IMD-1 treatment alone and in combination, while this was not the case for HNSCC cells UPCI-SCC-90 (Fig. 20C). No senescent cells were detected in IMD-3-treated samples independent from the addition of 2DG in all three cell lines (Fig. 20). These results indicate that, although IMD-3 mainly exerts its anti-cancer effect through proliferation inhibition, the underlying mechanism is likely to be independent from senescence induction.



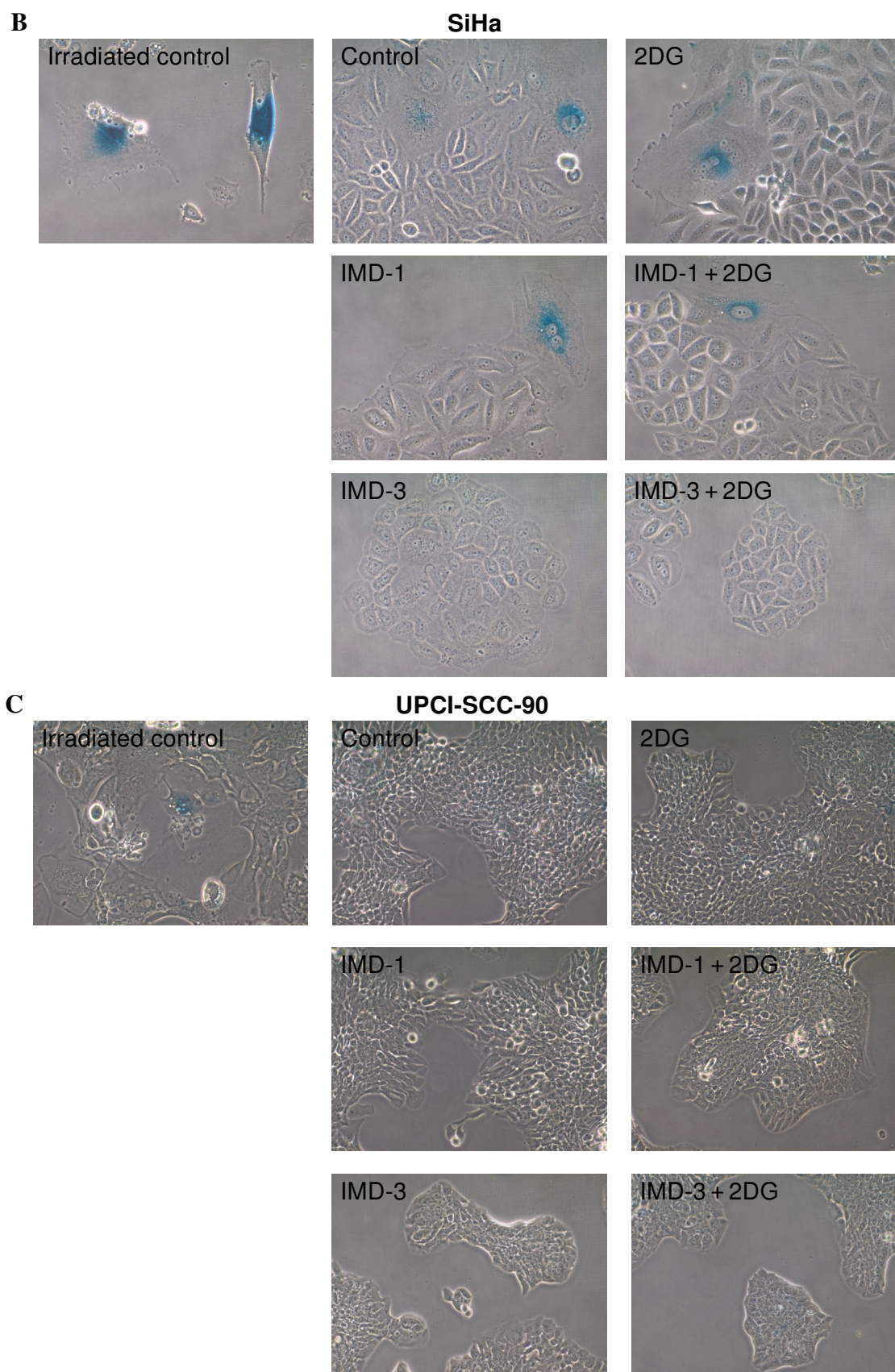


Figure 20: Senescence induction in cervical cancer cells CaSki (A) and SiHa (B), and HNSCC cells UPCI-SCC-90 (C). Senescence-associated β -galactosidase activity at pH 6.0 was detected using X-gal staining (blue). As a positive control for senescence induction irradiated cells (10 Gy) were used. 2DG: 1 mM; IMD-1, IMD-3: 100 nM; Cisplatin: 75 μ M; Treatment: 48 h. Images: Olympus CK40 microscope, 200 x magnification. Images were modified to align their brightness.

4.1.4 Downregulation of GLUT-1 expression and deregulation of glucose metabolism is a common characteristic of IMD-3 treatment

Previous studies on natural and synthetic flavaglines provided first evidence on possible modulation of cellular glucose metabolism upon treatment with these compounds [165, 174]. IMD-1 and IMD-3 examined for their influence on glucose metabolism also showed a pronounced effect on glucose metabolism reflected by downregulation of glucose uptake (Fig. S2), lactate production and inhibition of glucose transporter GLUT-1 expression in CRC cells [287]. To answer whether modulation of glucose metabolism is a common characteristic of IMD treatment shared among various cell lines or restricted to CRC cells, alterations of glucose metabolism upon treatment were analysed in HPV-transformed cell lines.

First, influence of IMD treatment on glucose uptake in CaSki cells was measured through accumulation of radioactively labelled ^3H -2DG at various medium glucose concentrations (Fig. 21A). Correlating with its lower growth-inhibitory efficacy, IMD-1 did not inhibit glucose uptake in CaSki cells, whereas IMD-3 significantly inhibited glucose uptake at all three tested medium glucose concentrations (1.0 g/l: $p = 2.450 \cdot 10^{-7}$) (Fig. 21A). Overall, IMD-3 treatment led to an average inhibition of glucose uptake by ca. 45 %, inhibiting uptake at 1.0 g/l glucose (fasting blood glucose concentration [131]) by approximately 33 % ($p = 2.450 \cdot 10^{-7}$) (Fig. 21A, Tab. S2).

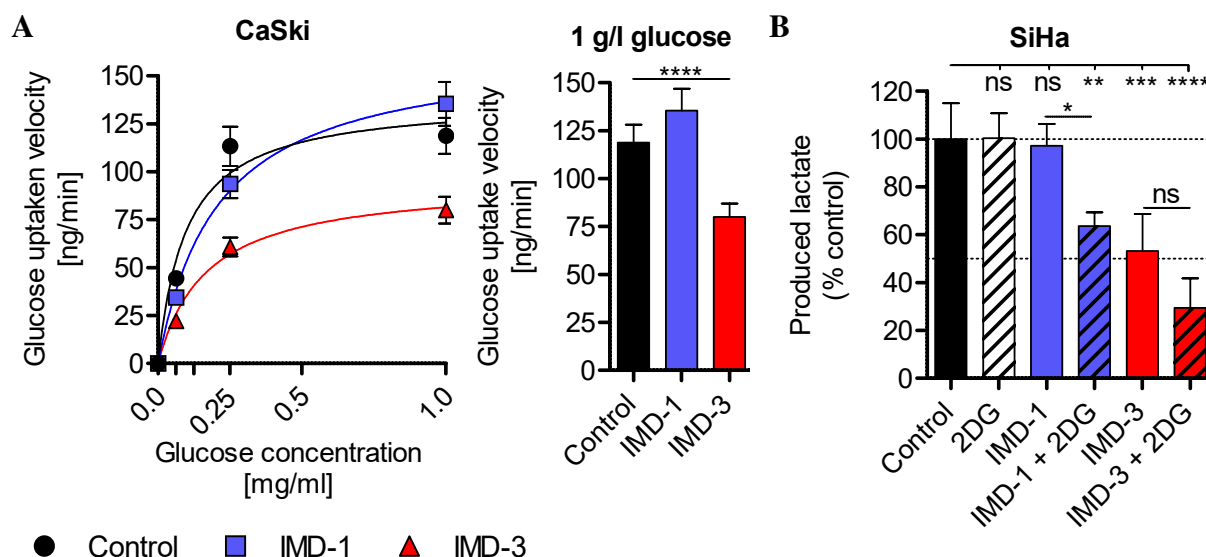


Figure 21: Influence of synthetic flavaglines on glucose metabolism of HPV-transformed cell lines. (A) Glucose uptake velocity of CaSki at various medium glucose concentrations (0.0, 0.0625, 0.25, 1.0 g/l) measured through accumulation of 2-[1- ^3H]-2DG (left). Comparison of glucose uptake velocity at 1 g/l glucose (fasting blood glucose concentration [131]) (right). Multiplicity-adjusted p-values are listed in table ES8. (B) Lactate production of SiHa cells. 2DG: 1 mM; IMD-1, IMD-3: 100 nM; Treatment: 24 h. Multiplicity-adjusted p-values are listed in table ES9.

Next, the activity of aerobic glycolysis was determined measuring the amount of secreted lactate upon treatment in SiHa cells (Fig. 21B). 2DG treatment did not influence the amount of produced lactate despite its hexokinase-based anti-glycolytic activity [104], which can be explained by the much higher abundance of glucose in the medium ($4.5 \text{ g/l} \approx 25 \text{ mM}$) compared to 2DG (1 mM). Similarly, IMD-1 alone did not inhibit aerobic glycolysis, whereas the combination of IMD-1 and 2DG significantly reduced the amount of produced lactate compared to the vehicle-treated control ($p = 0.0055$). The same was observed for the combination of IMD-3 with 2DG ($p = 2.650 \cdot 10^{-6}$). Strikingly, IMD-3 alone was also able to strongly inhibit aerobic glycolysis ($p = 0.0004$), substantiating the previous results obtained in CRC cells [287].

In CRC cells IMD-3 mediated its effect on glucose metabolism through complete elimination (HCT116) or downregulation (HT29) of the most abundant glucose transporter GLUT-1 [287], which is overexpressed in the majority of human tumours [293–295].

In all four tested HPV-transformed cell lines, reduction of GLUT-1 protein levels upon IMD-3 treatment was observed as well (Fig. 22), indicating glucose uptake inhibition through GLUT-1 downregulation as a general mechanism of flavagline-based therapy.

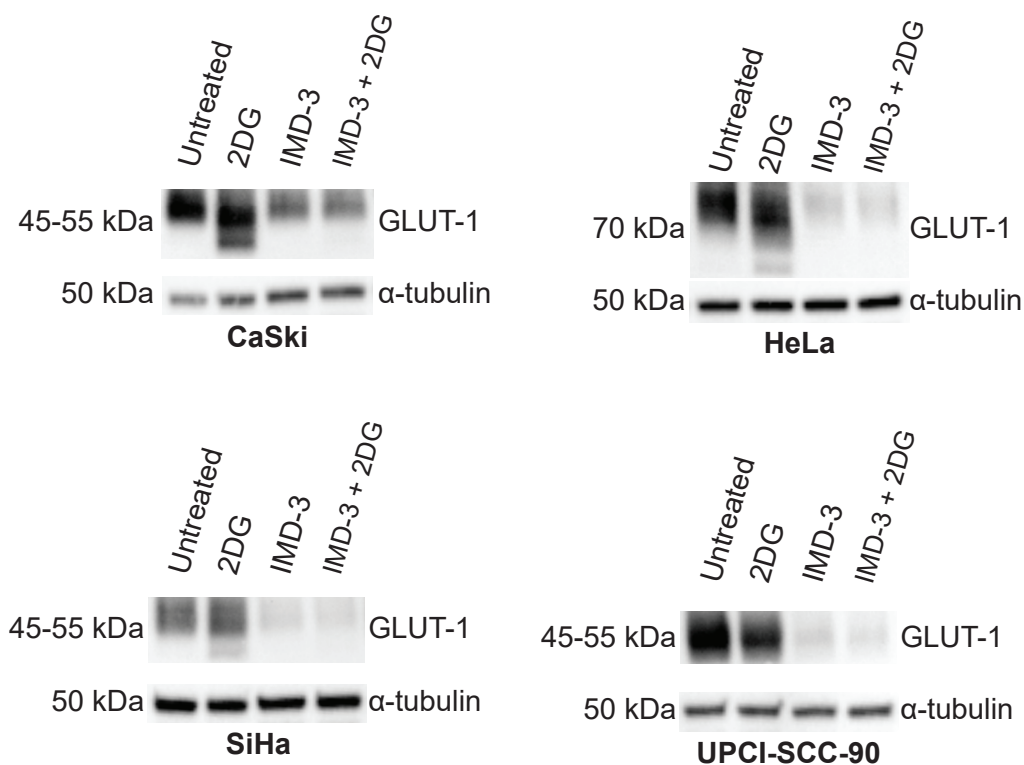


Figure 22: Glucose transporter GLUT-1 protein levels in HPV-transformed cancer cell lines. Depending on the extent of glycosylation, GLUT-1 exhibits a size between 45 - 55 kDa. Increased size of GLUT-1 in HeLa cells occurs due to altered glycosylation [296], whereas the second GLUT-1 transporter band at 37 kDa occurring in 2DG-treated cells indicates missing glycosylation [297]. α -tubulin was used as loading control. 2DG: 1 mM; IMD-3: 100 nM; Treatment: 48 h.

The inhibitory effect of IMD-3 treatment on GLUT-1 protein expression, demonstrated using Western Blot technique, could be confirmed by fluorescence staining (green) of treated cells (Fig. 23, 24, 25) revealing that pronounced downregulation of GLUT-1 occurs upon IMD-3 treatment but not upon IMD-1 treatment. Besides GLUT-1 staining, the treated cells were incubated with the proliferation marker EdU, a thymidine analogue. Performing fluorescence staining of incorporated EdU (red) confirmed pronounced inhibition of cell proliferation upon IMD-3 treatment also in HPV-transformed cells (Fig. 23, 24, 25).

Taken together, these results indicate that deregulation of glucose metabolism and downregulation of GLUT-1 expression display a common characteristic of IMD-3 treatment. Furthermore, deregulation of glucose metabolism could explain the strong inhibition of cell proliferation due to the lack of energy produced by metabolisation of glucose through glycolysis.

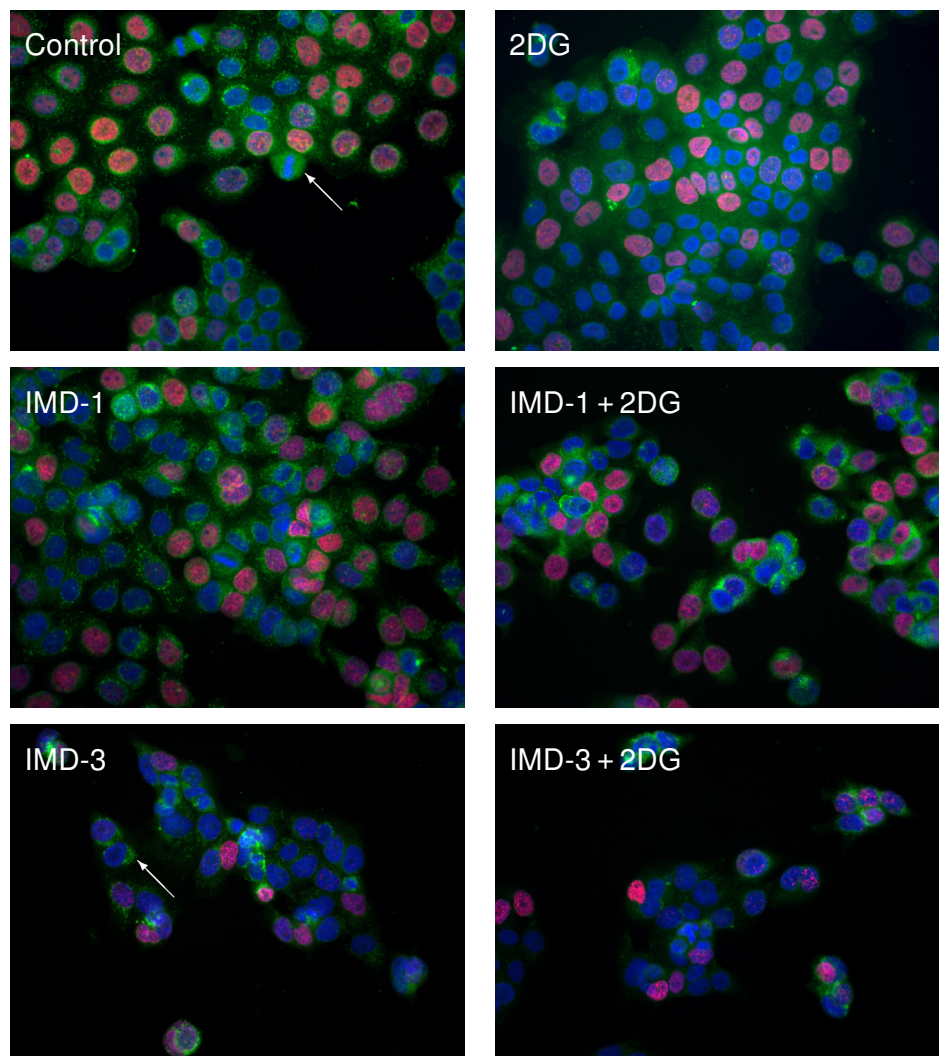


Figure 23: Fluorescence staining of glucose transporter GLUT-1 (green) and cell proliferation through EdU incorporation (red) in CaSki cells. Nuclei were counterstained with DAPI (blue). White arrows indicate the GLUT-1 staining of the tumour cell membrane. All pictures were taken with the same exposure times. IMD-3 treatment caused shrinking of cells leading to local accumulation of GLUT-1 (bright spots). 2DG: 1 mM; IMD-1, IMD-3: 100 nM; Treatment: 48 h. Images: Olympus AX79 microscope, 400 x magnification.

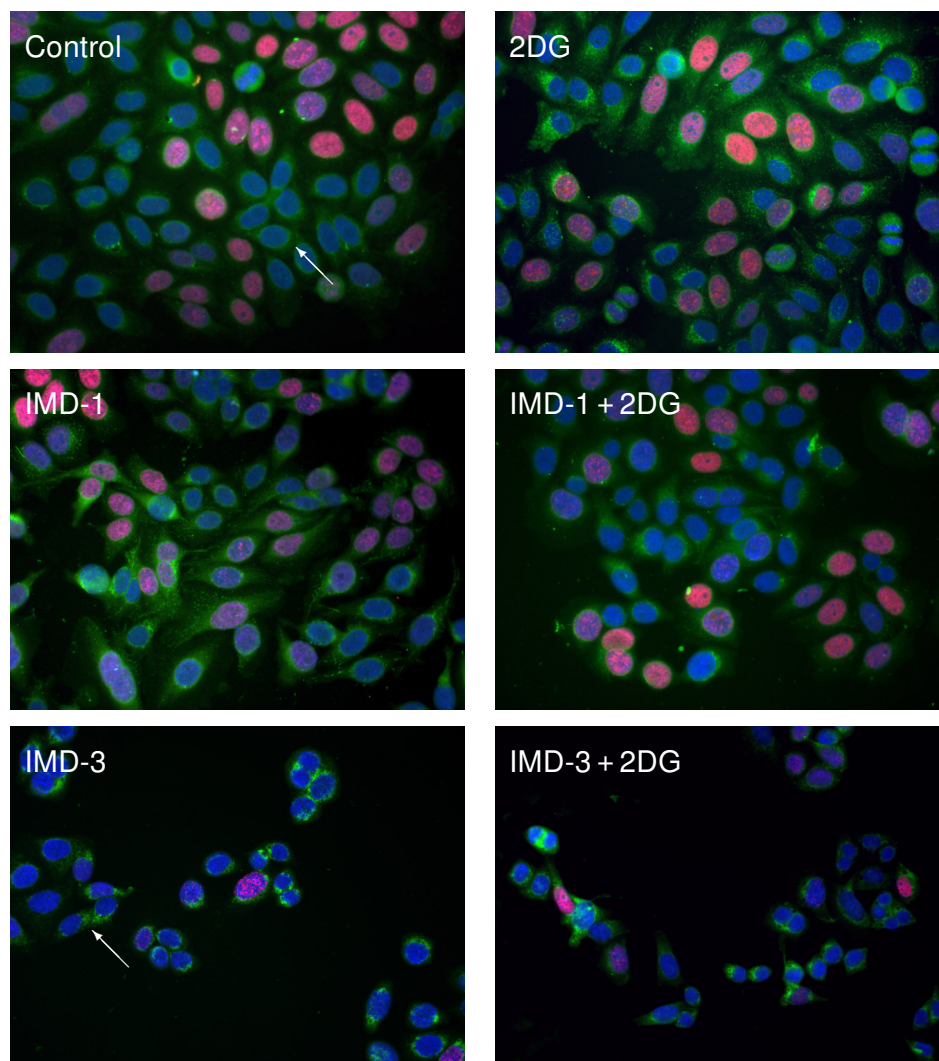


Figure 24: Fluorescence staining of glucose transporter GLUT-1 (green) and cell proliferation through EdU incorporation (red) in SiHa cells. Nuclei were counterstained with DAPI (blue). White arrows indicate the GLUT-1 staining of the tumour cell membrane. All pictures were taken with the same exposure times. IMD-3 treatment caused shrinking of cells leading to local accumulation of GLUT-1 (bright spots). 2DG: 1 mM; IMD-1, IMD-3: 100 nM; Treatment: 48 h. Images: Olympus AX79 microscope, 400 x magnification.

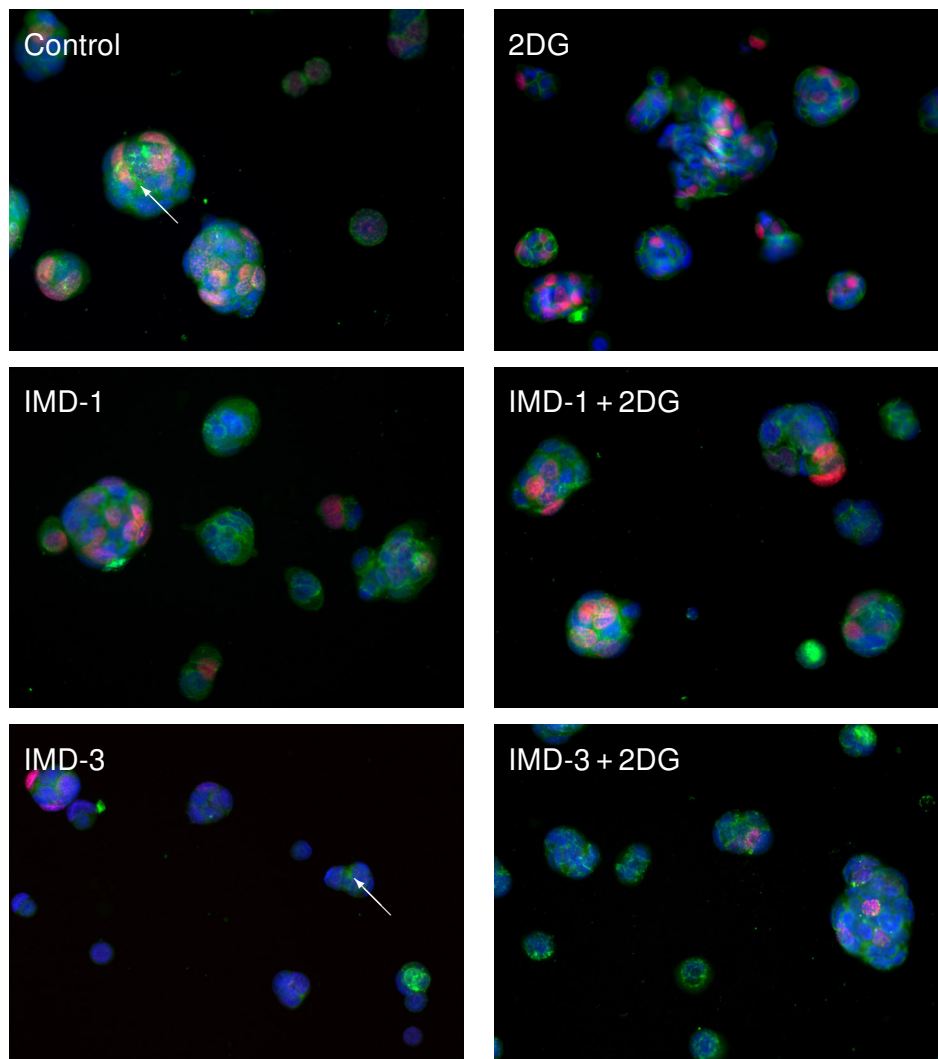


Figure 25: Fluorescence staining of glucose transporter GLUT-1 (green) and cell proliferation through EdU incorporation (red) in UPCI-SCC-90 cells. Nuclei were counterstained with DAPI (blue). White arrows indicate the GLUT-1 staining of the tumour cell membrane. All pictures were taken with the same exposure times. IMD-3 treatment caused shrinking of cells leading to local accumulation of GLUT-1 (bright spots). 2DG: 1 mM; IMD-1, IMD-3: 100 nM; Treatment: 48 h. Images: Olympus AX79 microscope, 400 x magnification.

4.1.5 Glucose utilisation is not shifted towards the pentose phosphate pathway upon IMD-3 treatment

Besides its utilisation in glycolysis, glucose is also metabolised through the pentose phosphate pathway (PPP) to generate cellular building blocks (pentoses) required for nucleotide synthesis and NADPH. To analyse whether upon inhibition of glycolysis highly proliferative cancer cells shift glucose usage to the PPP, the activity of the PPP was examined using radioactively labelled glucose and tracing the incorporation of tritium into RNA in CRC cells.

In both CRC cell lines, 2DG treatment did not influence the activity of the PPP significantly (Fig. 26), which can be explained by the low ratio of 2DG to glucose in the culture medium (1:25) as mentioned above (see 4.1.4). In contrast, IMD-3 treatment strongly inhibited pentose synthesis from glucose and their incorporation into RNA in both cell lines ($p \leq 4.150 \cdot 10^{-6}$), whereas the addition of 2DG did not further improve the inhibitory effect (Fig. 26). This finding indicates that inhibition of glycolysis through IMD-3 treatment does not cause increase metabolisation of glucose through the PPP to compensate for the loss of produced energy in glycolysis and fuel cell proliferation by building block synthesis and NADPH generation.

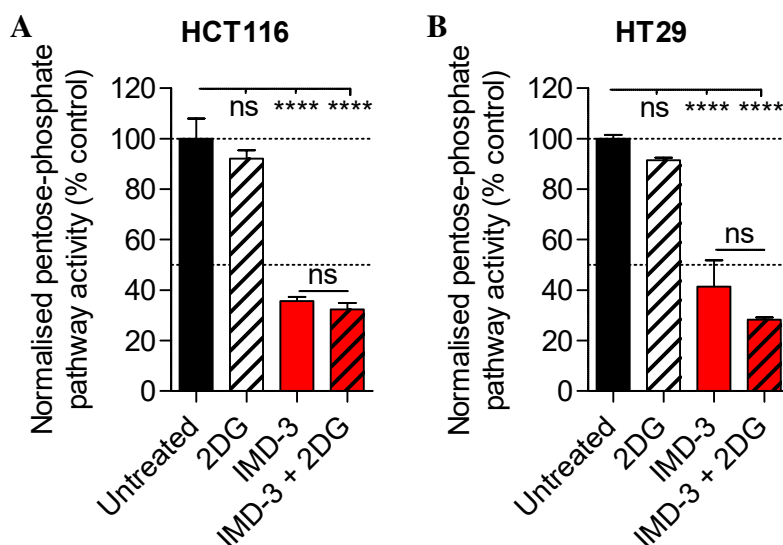


Figure 26: Pentose phosphate pathway activity of HCT116 (A) and HT29 (B) cells. During treatment cells were incubated with D-[^3H -(U)]-glucose and incorporation of tritium into RNA was measured. RNA concentration was used for normalisation. 2DG: 1 mM; IMD-3: 100 nM; Treatment: 24 h. Multiplicity-adjusted p-values are listed in table ES10.

4.1.6 Transcriptome analysis confirms proliferation inhibition, modulation of glucose metabolism and indicates ROS induction upon IMD-3 treatment

To further elucidate the mechanism underlying anti-cancer activity of IMD-3, mediating inhibition of glucose metabolism and proliferation, RNA transcriptome analysis of IMD-3-treated CRC (HCT116, HT29) and HPV-transformed cell lines (CaSki, HeLa, SiHa, UPCI-SCC-90) was performed using the Illumina bead chip platform (HumanHT-12 v4). Subsequent analysis of differentially expressed genes (DEGs) between IMD-3 and vehicle-treated control cells was performed revealing significant deregulation of several thousand genes in each tested cell line (Tab. 24). Genes were considered significantly deregulated if they exhibited a Benjamini-Hochberg (BH)-corrected p-value ≤ 0.05 and at least a 2-fold deregulation (up: $\log_2FC \geq 1$; down: $\log_2FC \leq -1$). To obtain an overview of alterations induced by IMD-3 treatment, pathway analysis considering all significantly deregulated genes was performed using the Ingenuity Pathway Analysis (IPA) software.

Table 24: Overview of significantly DEGs and pathways upon IMD-3 treatment (100 nM, 48 h) in CRC and HPV-transformed cells. Significantly DEGs were subjected to pathway analysis resulting in significantly altered pathways (IPA: p-value ≤ 0.05). DEGs are listed in table ES11.

IMD-3 vs. Control	Total deregulated genes	Upregulated genes	Downregulated genes	IPA Pathways
HCT116	2720	1245	1475	65
HT29	4415	1941	2474	178
CaSki	2801	1368	1433	113
HeLa	3030	1234	1796	147
SiHa	2753	1231	1522	83
UPCI-SCC-90	3573	1497	2076	89

Using the information on DEGs and the IPA pathway database, for each cell line a list of deregulated pathways was generated (Tab. 24, Fig. S3, S4). The deregulated pathways were subjected to comparison analysis among the tested cell lines, revealing 303 pathways commonly deregulated upon IMD-3 treatment, of which 181 pathways were significantly deregulated in at least two cell lines (IPA: p-value ≤ 0.05) (Fig. 27, Tab. ES11). Several of the most significantly deregulated pathways among cell lines were associated with cell cycle arrest and replication, including ‘cell cycle: G2/M DNA damage checkpoint regulation’, ‘cell cycle: G1/S checkpoint regulation’ and ‘cell cycle control of chromosomal replication’ (Fig. 27A). Whereas DNA replication initiation was inhibited, cell cycle checkpoint pathways were upregulated, both presumably contributing to the anti-proliferative effect of IMD-3. Furthermore, downregulation of glutathione (GSH) pathways and upregulation of NRF2-mediated oxidative stress response indicated IMD-3-mediated depletion of GSH and increase of ROS, which enhance oxidative stress and induce DNA damage [298].

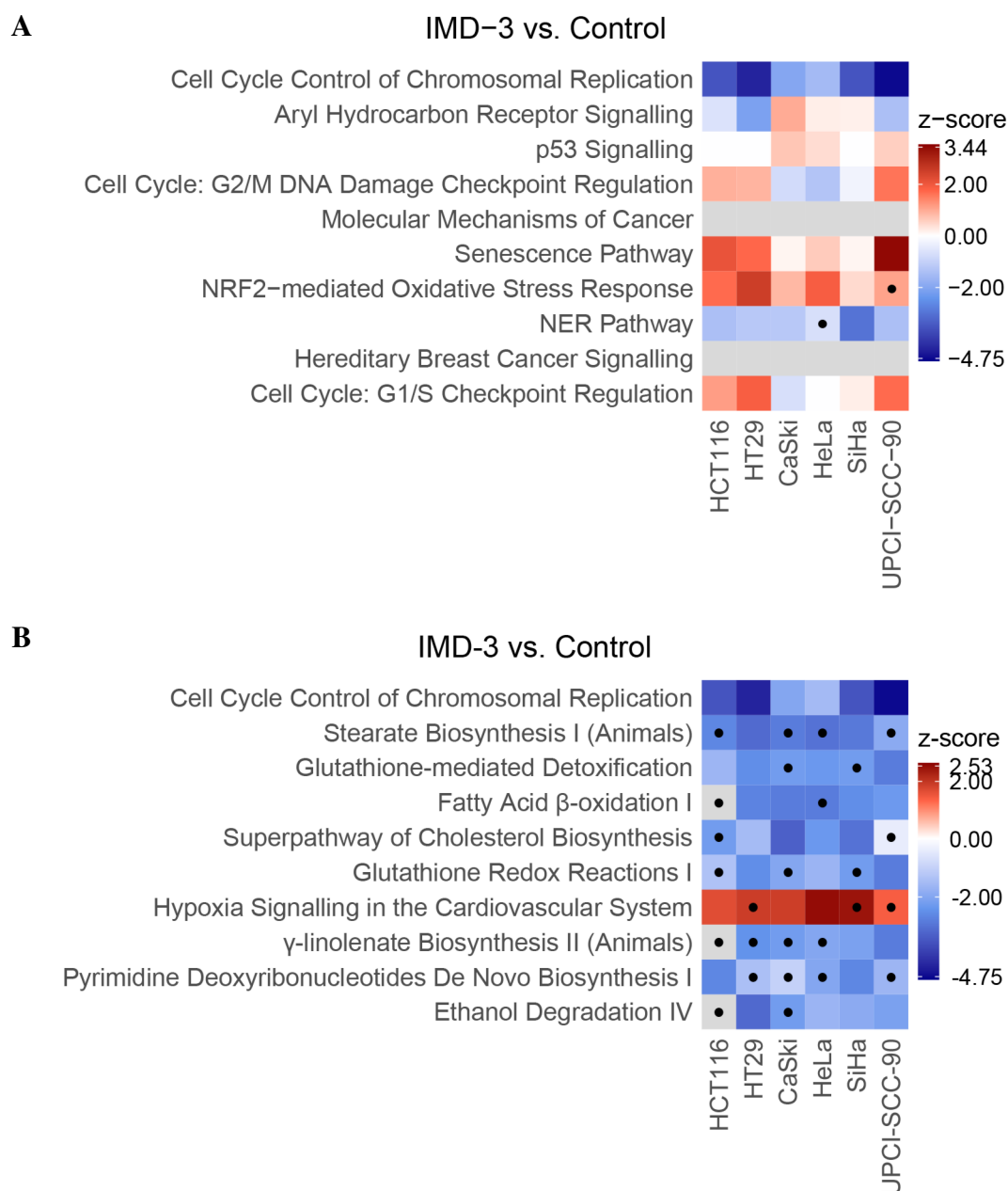


Figure 27: Top 10 deregulated pathways commonly deregulated in CRC and HPV-positive cancer cells upon IMD-3 treatment (100 nM, 48 h). Significantly DEGs in IMD-3-treated cells (compared to control cells) were used to identify altered pathways for each cell line. Displayed z-scores predict activation ($z\text{-score} \geq 2$; red) or inhibition ($z\text{-score} \leq -2$; blue) of the pathways based on transcriptome data. If no direction could be predicted, the z-score is 0 (white). If no z-score could be calculated, pathways are labelled in grey. Non-significant pathways ($p\text{-values} > 0.05$) are marked with a dot. (A) Comparison of altered pathways sorted by their p-value. z-scores and p-values are listed in table S3. (B) Comparison of altered pathways sorted by their z-score. z-scores and p-values are listed in table S4. Identification of DEGs was performed jointly with Simon Kalteis.

Adaptation of cellular metabolism to high metabolic demands of cancer cells is regulated by the heat shock transcription factor (HSF1) linking translation and metabolism [174]. Although *HSF1* expression itself was not affected in any of the tested cell lines, IMD-3-induced downregulation of heat shock protein 70 (HSP70) family members *HSPA8* (4-fold, $p = 2.750 \times 10^{-7}$) in HCT116 and *HSPA1A* (3.6-fold, $p = 5.455 \times 10^{-14}$) in CaSki cells (Fig. 28, Tab. S5).

Furthermore, a strong increase up to 10-fold (HT29: $p = 4.380 \times 10^{-10}$) in expression levels of *TXNIP*, an important negative regulator of glucose metabolism [299], upon treatment was observed in all tested cell lines except HCT116 (Fig. 28, Tab. S5). Observed downregulation of GLUT-1 on protein level (Fig. 22) was reflected on transcript level only in CaSki cells exhibiting a 2.3-fold downregulation ($p = 4.071 \times 10^{-11}$), indicating a possible post-transcriptional effect of IMD-3 on GLUT-1 expression. This possibility was substantiated by downregulation of serine/threonine kinase AKT, responsible for membrane stabilisation of GLUT-1 [96], in four out of six cell lines (Tab. S5). Additionally, AKT signalling is required for fatty acid synthesis [96] explaining downregulation of associated pathways (stearate, γ -linolenate, cholesterol biosynthesis, and fatty acid β -oxidation) (Fig. 27). Also, several subunits of PI3K (*PIK3CB*, *PIK3R2*, *PIK3R1*) were downregulated upon IMD-3 treatment (Fig. 28, Tab. S5), indicating treatment-induced inhibition of PI3K/AKT/mTOR pathway. IMD-3 treatment also inhibited *de novo* synthesis of deoxyribonucleotides (Fig. 27), which could be due to inhibited glucose metabolism. This finding supports the observed downregulation of the PPP described above (see 4.1.5).

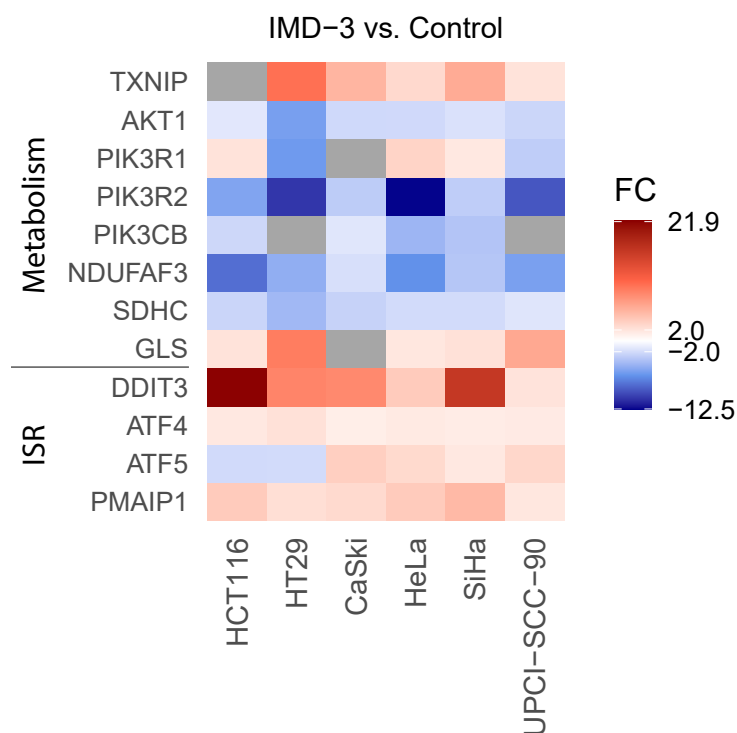


Figure 28: Heat map of fold changes (FC) for selected DEGs for relevance in metabolism and ISR in CRC and HPV-positive cell lines. Upregulation (red) and downregulation (blue) of significantly DEGs. Genes, which are not significantly deregulated (BH-corrected p -values > 0.05), are depicted in grey. FC and p -values are shown in table S5.

Besides treatment-induced downregulation of glucose metabolism, IMD-3 also mediated inhibition of oxidative phosphorylation by downregulation of ETC genes, including *NDUFAF3* (max. 8-fold, $p = 1.710 \times 10^{-8}$, HCT116) required for the assembly of complex I and complex II subunit *SDHC* (max. 4-fold, $p = 1.930 \times 10^{-7}$, HT29) (Fig. 28, Tab. S5). However, the majority of cell lines showed a treatment-induced increase of glutaminase (*GLS*) expression (Fig. 28, Tab. S5). One of the most upregulated genes in all cell lines, showing a significant increase between 2-fold in UPCI-SCC-90 cells ($p = 8.295 \times 10^{-8}$) and 22-fold in HCT116 cells ($p = 1.600 \times 10^{-9}$), was the DNA damage inducible transcript 3 (*DDIT3*) (Fig. 28, Tab. S5). Other genes of the integrated stress response (ISR) [300, 301] showed increased expression in the majority of cell lines, including *ATF4*, *ATF5* and especially *PMAIP1/NOXA* (Tab. S5). IPA analysis also showed significant activation ($z\text{-score} \geq 2$) of the unfolded protein response (UPR) in both CRC cell lines (Tab. S3). Also, three out of four HPV-positive cell lines (CaSki, HeLa, SiHa) showed a significant regulation of UPR with HeLa and SiHa cells exhibiting a positive $z\text{-score}$ of 1.5 and 1.9, indicating that UPR might be also enhanced in these cell lines upon IMD-3 treatment (Tab. S3). Overall, transcriptome analysis confirmed previously observed proliferation inhibition upon IMD-3 treatment indicating cell cycle arrest might be mediated through increased oxidative stress and activation of the ISR. Furthermore, IMD-3 downregulation of glucose metabolism could be confirmed on transcriptome level.

4.1.7 Anti-cancer activity of IMD-3 could be confirmed in 3D cell culture models

2D cultures are of great value for studying mechanisms of actions of drug compounds on cancer cells, however they carry certain limitations with regard to representation of cell-cell interactions and tissue microenvironment under physiological conditions [302]. These aspects are of particular importance for drug evaluation studies aiming at assessment of tissue penetrance by compounds and measurement of the treatment effect on tissues surrounding tumour cells. Therefore, the efficacy of the more potent synthetic flavagline IMD-3 was evaluated in different 3D cell culture models of HPV-transformed cells, including spheroid culture and an organotypic co-culture model of SiHa cells and normal keratinocytes.

3D spheroids of CaSki and SiHa cells were treated with rising concentrations of IMD-3 to first assess the efficacy of the treatment in a simplified 3D context. As expected, higher concentrations of IMD-3 were required in CaSki spheroids to achieve anti-cancer effects (Fig. 29A) similar to those previously observed in 2D culture after 2 days of treatment (Fig. 14A). However, increasing the treatment duration from 2 to 4 days reduced the required treatment dose, achieving a similar reduction of cell viability to 72 % already at the lowest concentration of IMD-3 (100 nM) after 4 days as after 2 days with 2 μM IMD-3 (Fig. 29A). Similar effects were observed in SiHa spheroids treated with IMD-3 for 4 days (Fig. 29B). Importantly, prolonging treatment duration to 11 days led to further decrease of the required IMD-3 dose, with 100 nM IMD-3 achieving a similar effect on the spheroid viability (19.4 %, $p = 1.885 \times 10^{-12}$) as 2 μM IMD-3

upon 4 days of treatment (15.0 %, $p = 1.138 \cdot 10^{-12}$). These results indicate a concentration- and time-dependent growth-inhibitory effect of IMD-3 in a 3D tumour model.

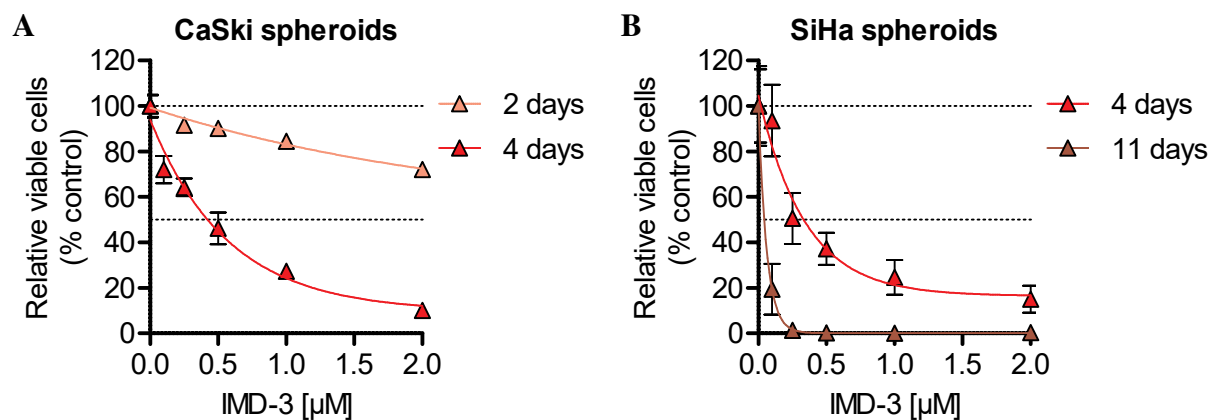


Figure 29: Sensitivity of HPV-related cervical cancer cell 3D spheroids towards IMD-3 treatment over different time intervals. (A) Relative viability of CaSki spheroids after IMD-3 treatment for 2 and 4 days. (B) Relative viability of SiHa spheroids after IMD-3 treatment for 4 and 11 days. Multiplicity-adjusted p-values are listed in table ES12.

To assess the efficacy of IMD-3 treatment in a more sophisticated 3D-setting and at the same time analyse the treatment influence on normal cells, an organotypic co-culture of SiHa cells and normal keratinocytes, modelling tumour cell clusters in the skin, was used.

To visualise the tumour cell clusters within the dermal equivalents, HE-stained 3D co-culture sections were imaged (Fig. 30). As expected, the comparison of control cultures fixed before the start of the treatment (day 0) with control cultures after 7 days of vehicle treatment revealed proliferation of tumour cell clusters during the culture period. The 2DG-treated 3D co-cultures did not reveal a decrease in tumour cluster size, whereas tumour clusters under IMD-3 treatment decreased in size with increasing IMD-3 concentrations. Furthermore, the disrupted cellular structure and granularisation of the nuclei, indicating cell death in tumour clusters, increased with rising IMD-3 concentrations alone and in combination with 2DG. However, no significant difference with regard to the tumour cluster size of IMD-3-treated samples compared to the samples treated with the drug combination was visible in the HE-stained co-cultures (Fig. 30).

Due to the strong downregulation of glucose transporter GLUT-1 observed in 2D culture, co-culture models were examined for alterations of GLUT-1 protein levels upon treatment. In fact, a decrease of GLUT-1 was observed in 3D co-culture models after 7 days of IMD-3 treatment (Fig. 31). The effect seemed to be particularly pronounced in tumour cells, whereas GLUT-1 was retained in keratinocytes. To monitor cell proliferation, the 3D cultures were labelled with EdU prior to fixation. Compared to tumour cells in vehicle-treated cultures, tumour cells in cultures treated with IMD-3 alone or in combination with 2DG showed decreased proliferation (Fig. 31).

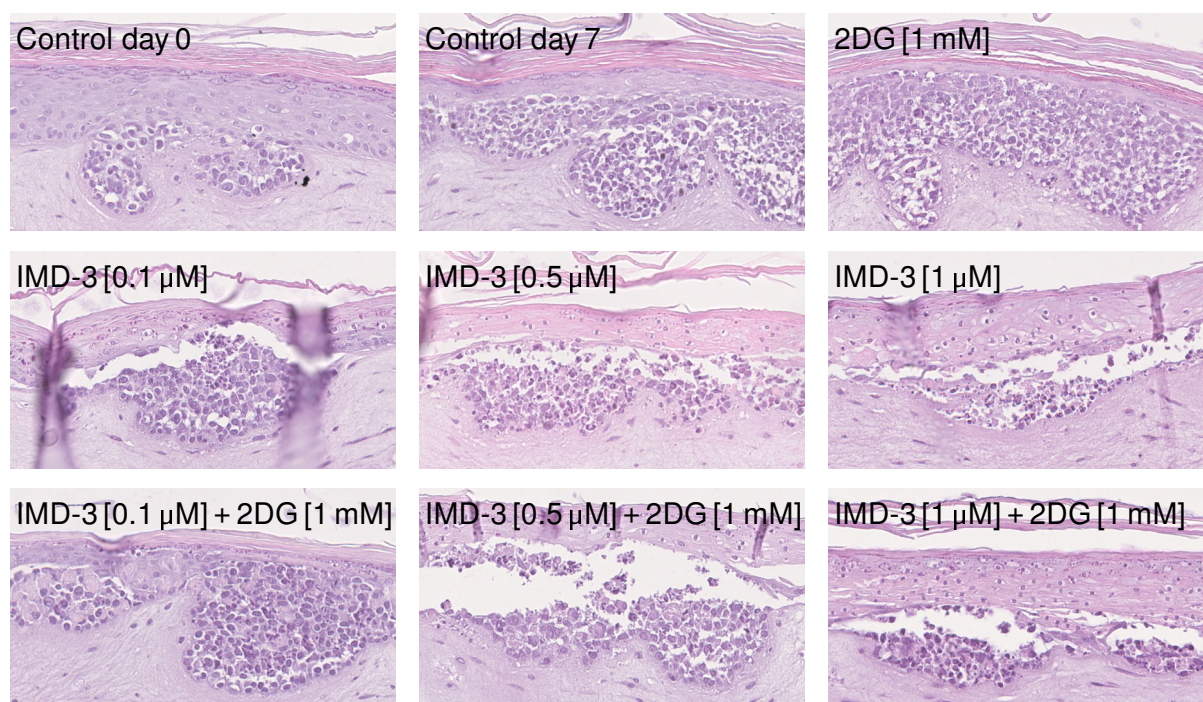


Figure 30: HE staining of 3D co-culture models of SiHa cells and normal keratinocytes after 7 days of treatment. Nuclei are stained in purple, the cytoplasm is stained in light red. Images: NanoZoomer S210 Digital slide scanner, 40 x objective.

Apoptosis induction in the 3D co-culture models was monitored using cleaved caspase-3 staining (Fig. 31B), showing rising numbers of apoptotic tumour cells with increasing IMD-3 concentrations. Although, at the highest IMD-3 concentration (1 μM), a proportion of keratinocytes also showed signs of apoptosis induction.

Interestingly, some co-cultures treated with IMD-3 demonstrated separation of the keratinocyte layer from the fibroblasts modelling the connective tissue. To assess, whether the effect was caused by the reaction of the keratinocytes to IMD-3 treatment, organotypic cultures containing only keratinocytes were generated and treated with IMD-3. After 7 days, dissociation of the keratinocyte layer from the connective tissue was observed (Fig. 32), indicating that IMD-3 treatment influenced the expression of cellular adhesion molecules in keratinocytes of the basal layer. Although decreased thickness of the basal and spinous layer upon IMD-3 treatment in keratinocyte-only cultures was detected, this effect was much less pronounced in co-cultures containing tumour cells, suggesting possible accumulation of IMD-3 preferably in the tumour cells in the co-culture models (Fig. 30).

In summary, the 3D culture experiments provided a first hint towards a possible therapeutic window of IMD substances when applied to normal and cancer cells and encouraged the validation of the observed effects in an *in vivo* setting.

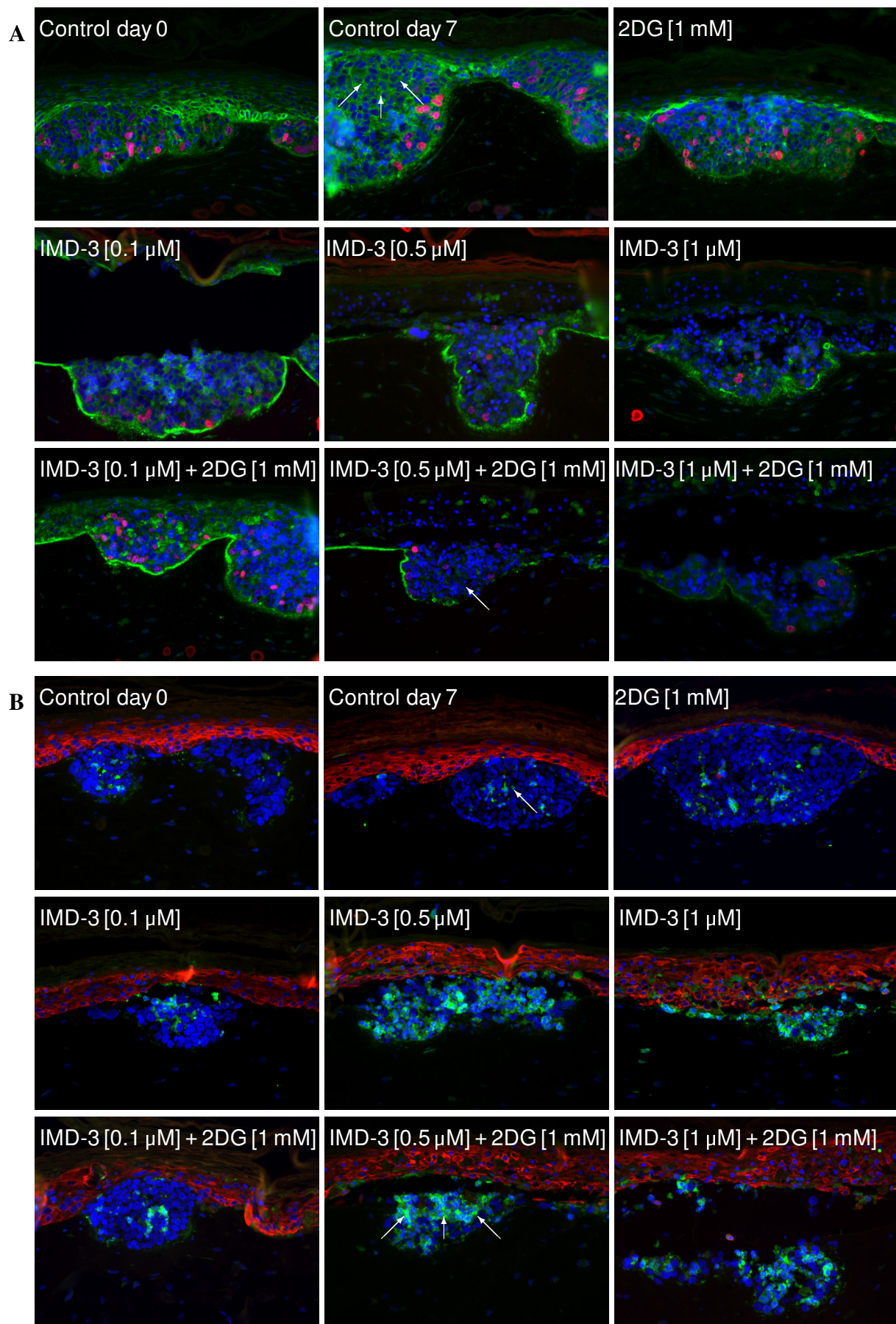


Figure 31: Fluorescence staining of 3D co-culture models of SiHa cells and normal keratinocytes after 7 days of treatment. (A) Reduced proliferation (red) and glucose transporter GLUT-1 expression (green, arrows). (B) Apoptosis induction indicated by cleaved caspase-3 (green, arrows) staining. Keratinocytes are stained for cytokeratin 14 (red). Nuclei are stained with DAPI (blue). Images: Olympus AX70 microscope, 400 x magnification.

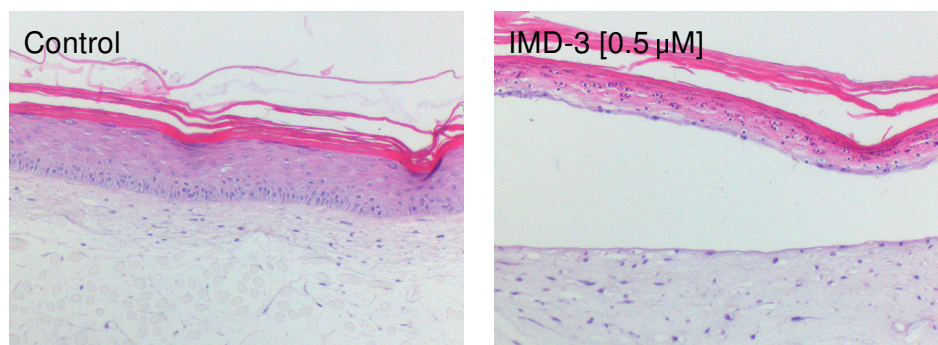


Figure 32: HE staining of 3D co-culture models only containing keratinocytes (without tumour cells) after 7 days of IMD-3 treatment (500 nM). Treatment led to a dissociation of the keratinocyte layer from the fibroblasts modelling the connective tissue. Nuclei are stained in purple, the cytoplasm is stained in light red. Images: Olympus BX43 microscope, 100 x magnification.

4.2 Identification of resistance mechanisms against synthetic flavagline treatment

4.2.1 Gene-trap mutagenesis led to the generation of a long-term IMD-3-resistant cell line

To further elucidate the molecular mechanisms underlying anti-cancer activity of synthetic flavagline derivatives and assess possible mechanisms of treatment resistance, a gene-trap (GT) mutagenesis approach was used to generate IMD-3-resistant haploid cells.

GT mutagenesis of nearly haploid cells was performed by random insertion of a GT cassette consisting of a splice acceptor, reporter gene, and a termination sequence into the genome causing gene disruption at the integration site (Fig. 33A) [261]. Mutagenised cells were treated over several weeks with IMD-3 to select for IMD-3-resistant cells, which gave rise to an IMD-3-resistant cell line HGC176 from its wild type (WT) equivalent HGC178. While treatment with 31 nM IMD-3 was sufficient to reduce the cell viability of WT HGC178 cells to approximately 50 %, a concentration of 500 nM IMD-3 was required to achieve a similar effect in resistant HGC176 cells (Fig. 33B). At 125 nM IMD-3, WT cells exhibited a reduction of cell viability to 21 %, while the resistant HGC176 cells were significantly less sensitive and only showed a cell viability reduction to 73. % ($p = 7.491 \cdot 10^{-12}$).

To investigate, whether the induced resistance has a transient or permanent character, both cell lines were cultured over a period of over 5 weeks (ca. 15 passages) and the treatment sensitivity of cells from low and high passages were compared. Importantly, the sensitivity of the resistant HGC176 cell line remained consistent in growing cell passages (Fig. 33B), pointing at a stable character of the induced resistance.

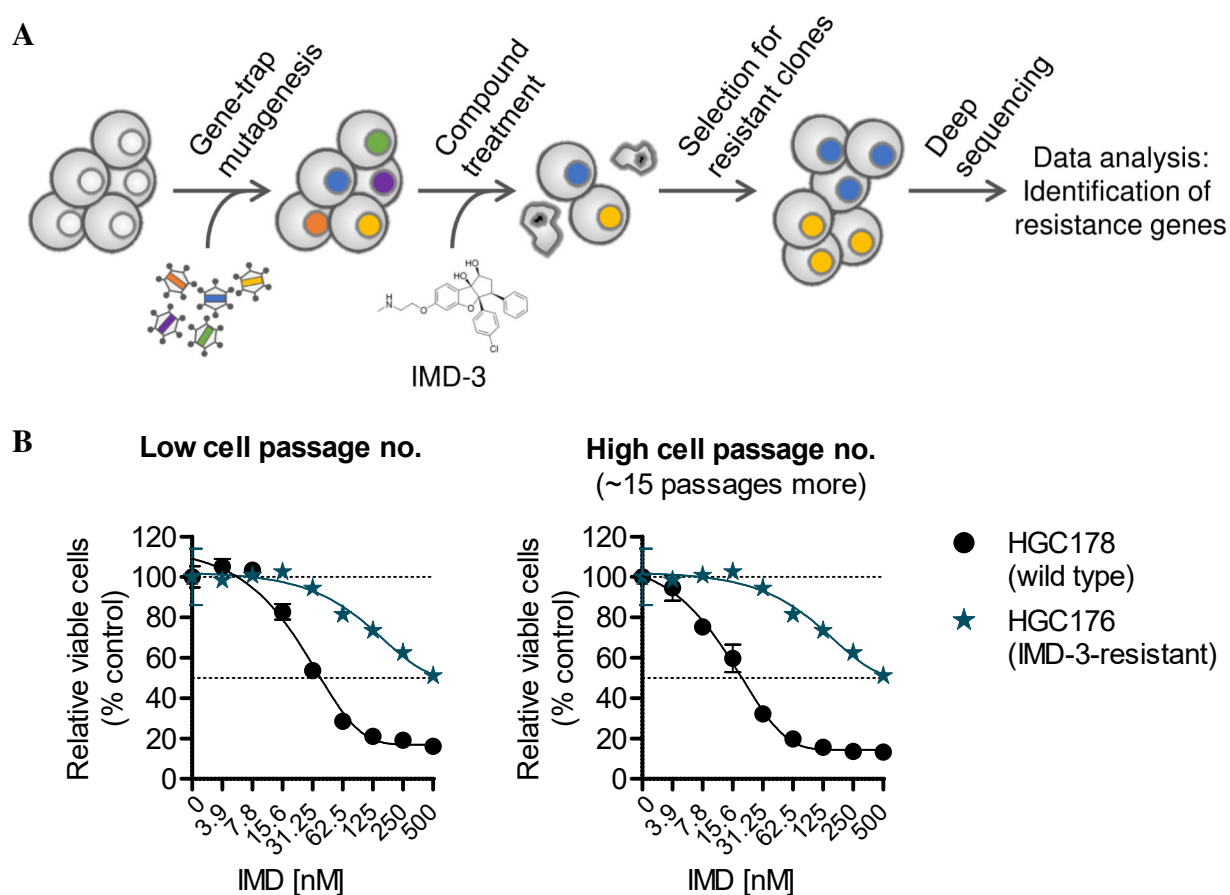


Figure 33: Generation of a long-term IMD-3-resistant cell line. (A) Schematic description of IMD-3-resistant cell line generation. IMD-3-resistant cells were generated by Haplogen GmbH (Vienna, Austria) using gene-trap mutagenesis of near-haploid cells. (B) Relative cell viability of IMD-3 sensitive HGC178 and resistant HGC176 cells at a low and high passage number (ca. 15 passages more). Multiplicity-adjusted p-values are listed in table ES13.

4.2.2 Anti-proliferative effect of IMD-3 is overcome in resistant cells

Experiments in 2D and 3D cultures described above pointed out the crucial importance of proliferation inhibition as one of the major mechanisms of cell viability reduction by synthetic flavaglines. Therefore, the influence of acquired IMD-3 resistance on cell proliferation was assessed using two independent methods: real-time impedance measurement and incorporation of methyl-³H-thymidine.

Real-time proliferation monitoring revealed a striking difference in the response to IMD-3 treatment between WT and resistant cells. Whereas IMD-3 significantly inhibited cell growth of WT HGC178 cells already after 48 h of treatment, no effect on the proliferation of IMD-3-resistant HGC176 cells was detected (Fig. 34A). Although treatment interruption after 48 h caused re-growth of WT cells, IMD-3 re-application efficiently inhibited cell growth again (Fig. 34B). On the contrary, treatment interruption and re-application did not influence the response of IMD-3-resistant cells. Interestingly, addition of 2DG did not measurably improve treatment efficacy in

WT HGC178 cells, but slightly enhanced IMD-3 activity in resistant HGC176 cells. 2DG treatment alone did not influence proliferation of WT or resistant cells in both treatment schemes. However, both cell lines showed high sensitivity towards cisplatin treatment, which could be attributed to their haploid genotype making them more susceptible to DNA damaging agents.

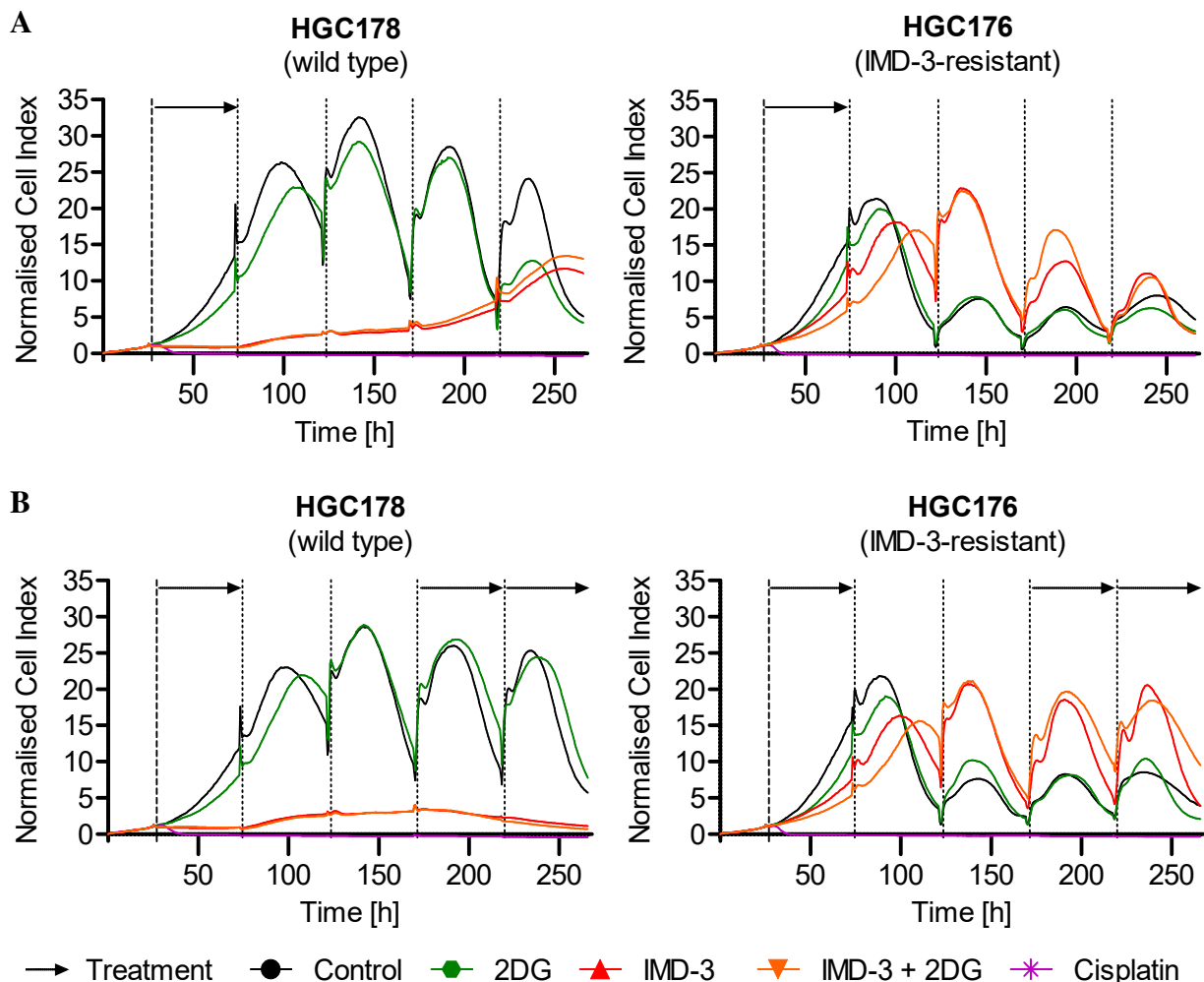


Figure 34: Real-time cell proliferation monitoring of WT HGC178 and IMD-3-resistant HGC176 cells using impedance measurement. Peaks of the cell index result from medium changes every 48 h and decline of the maximal cell index is caused by overconfluence and subsequent detachment of cells. (A) Cell proliferation of WT and IMD-3-resistant cells receiving treatment for 48 h. After 48 h treatment was replaced with drug-free medium. (B) Influence of treatment interruption of 96 h on proliferation of WT and IMD-3-resistant cells. Mean values of the cell index ($n=3$) are displayed to enhance readability of the graph. 2DG: 1 mM, IMD-3: 100 nM, Cisplatin: 75 μ M.

The observed growth inhibition caused by synthetic flavagline treatment can either be caused through proliferation inhibition or cell death, which cannot be distinguished using impedance measurement. Thus, influence of synthetic flavaglines on cell proliferation and their cytotoxicity were assessed using methyl- 3 H-thymidine incorporation.

Confirming the observations from impedance measurement, cell proliferation was significantly inhibited by over 50 % in WT HGC178 upon IMD-3 treatment ($p = 3.766 \cdot 10^{12}$), whereas no

effect was detected in resistant HGC176 cells (Fig. 35). Interestingly, in both cell lines the anti-proliferative effect of IMD-3 could be increased significantly by combination with 2DG (HGC178: $p=0.0176$; HGC176: $p=0.0002$). Both cell lines were highly susceptible to cisplatin treatment, while IMD-1 and 2DG treatment did not influence proliferation.

Next, cytotoxicity was assessed in WT and resistant cells. However, due to the high turnover rate of cells, the majority of ^3H -thymidine was released, also from vehicle-treated cells, and cytotoxicity could not be calculated from the obtained release values (Fig. S5).

In summary, IMD-3 treatment strongly inhibited proliferation in WT HGC178 cells as observed previously in CRC cells (see 4.1.2), whereas the anti-proliferative effect of IMD-3 was strongly impaired in IMD-3-resistant HGC176 cells.

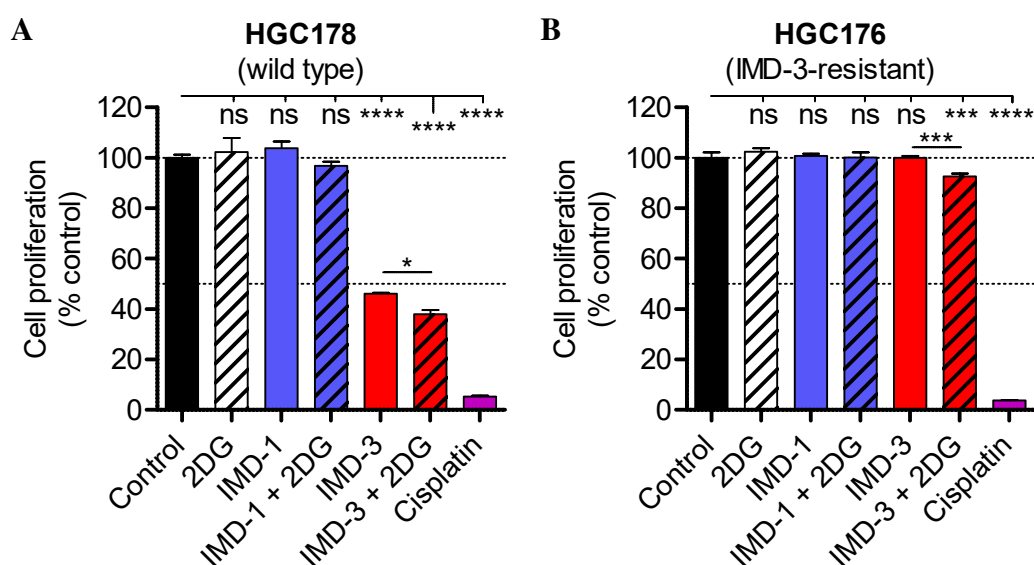


Figure 35: Proliferation inhibition of WT HGC178 (A) and IMD-3-resistant HGC176 cells (B). Proliferation was measured by the incorporation of ^3H -thymidine during treatment. 2DG: 1 mM; IMD-1, IMD-3: 100 nM; Cisplatin: 75 μM ; Treatment: 48 h. Multiplicity-adjusted p-values are listed in table ES7.

4.2.3 IMD-3-induced modulation of glucose metabolism is absent in resistant cells, while GLUT-1 expression is preserved

IMD-3 had shown a drastic effect on glucose uptake and GLUT-1 expression in several human cancer cell lines; therefore, both were analysed in WT HGC178 and resistant HGC176 cells upon IMD-3 treatment.

Measurement of glucose uptake revealed that both cell lines (vehicle-treated controls) exhibit a similar glucose uptake kinetic without any significant difference in glucose uptake velocity at 1 g/l medium glucose concentration (Fig. 36). This indicated that acquired IMD-3 resistance did not influence glucose incorporation directly. While IMD-1 treatment did not influence glucose uptake in both cell lines, IMD-3 treatment strongly inhibited glucose uptake in WT HGC178 cells, leading to an average inhibition of 57 % over all analysed medium glucose concentra-

tions. In IMD-3-resistant HGC176 cells, the effect declined to 19 % (Fig. 36A, Tab. S6). Thus, IMD-3-resistant cells were significantly less sensitive towards IMD-3-induced inhibition of glucose uptake compared to WT HGC178 cells (1 g/l glucose: $p = 0.0007$) (Fig. 36B).

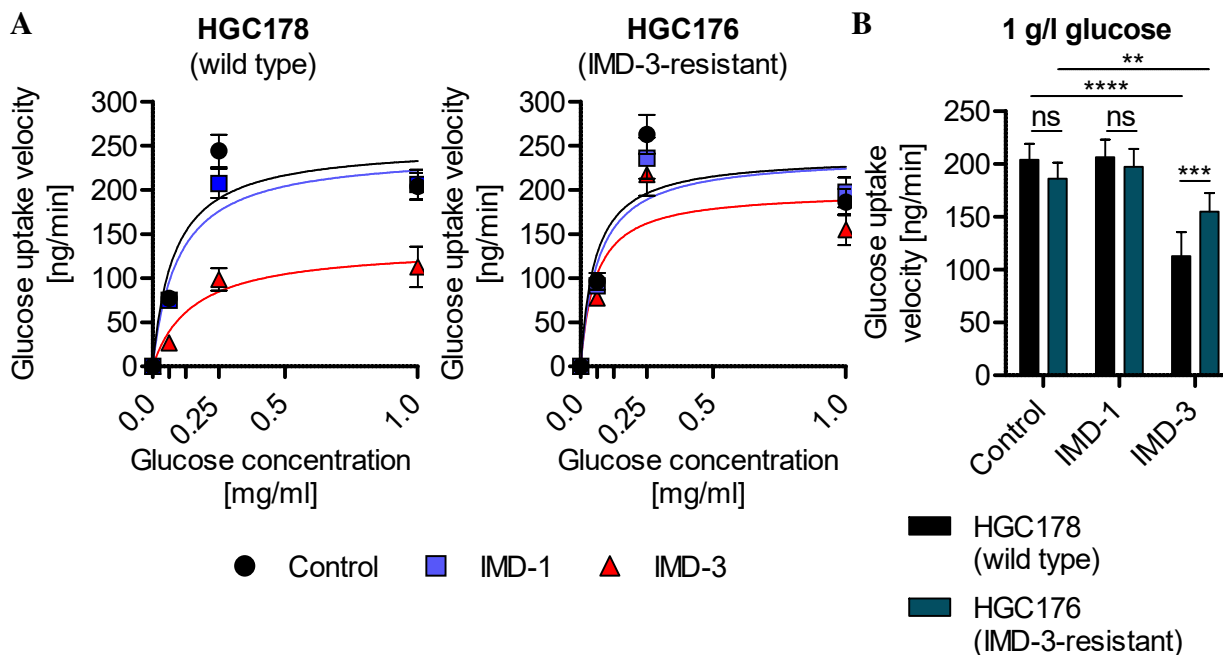


Figure 36: Glucose uptake velocity of WT HGC178 and IMD-3-resistant HGC176 cancer cells. (A) Glucose uptake velocity dependent on the medium glucose concentration (1.0, 0.25, 0.0625, 0.0 g/l). (B) Comparison of glucose uptake velocity at 1 g/l glucose (fasting blood glucose concentration [131]). IMD-1, IMD-3: 100 nM; Treatment: 24 h. Multiplicity-adjusted p-values are listed in table ES8.

To assess whether the less pronounced effect of IMD-3 on glucose uptake is supported by the GLUT-1 expression pattern, GLUT-1 expression was examined in both cell lines upon treatment with IMD-3. As observed previously in CRC [287] and HPV-transformed cell lines, IMD-3 treatment inhibited GLUT-1 expression in WT HGC178 cells, while 2DG did not affect GLUT-1 expression (Fig. 37A). Strikingly, GLUT-1 expression was retained in resistant HGC176 cells upon IMD-3 treatment, explaining its substantially less pronounced effect on glucose uptake (Fig. 37B).

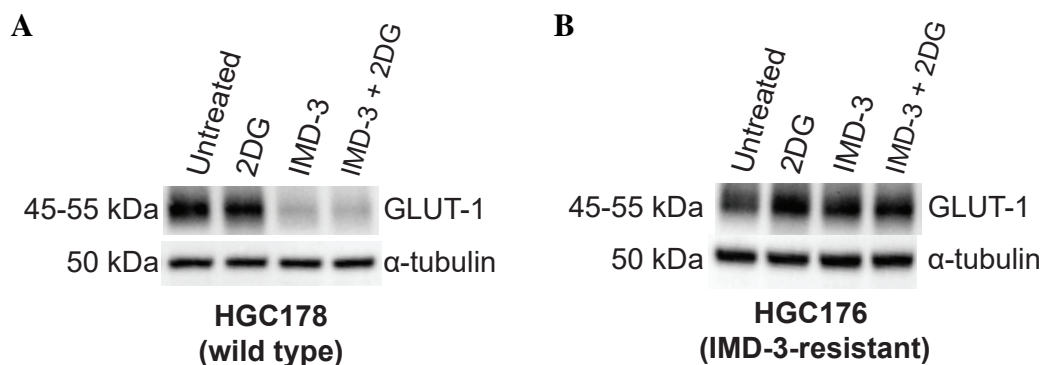


Figure 37: Glucose transporter GLUT-1 protein levels in WT HGC178 (A) and resistant HGC176 cells (B). Depending on glycosylation extent, GLUT-1 size varies between 45 - 55 kDa. α -tubulin was used as loading control. 2DG: 1 mM; IMD-3: 100 nM; Treatment: 48 h.

4.2.4 Pentose phosphate pathway activity remains unchanged in IMD-3-resistant cells

Previous experiments with CRC cells have shown that glucose utilisation is not shifted towards the PPP upon IMD-3 treatment, however it is unclear how acquired IMD-3 resistance influences glucose utilisation.

Similar to observations in CRC cells (see 4.1.5), IMD-3 treatment significantly inhibited PPP activity by approx. 80 % in WT HGC178 cells ($p = 3.000 \cdot 10^{-14}$) (Fig. 38A). Interestingly, also the less active substance IMD-1 decreased PPP activity by approx. 40 % ($p = 4.260 \cdot 10^{-12}$), while 2DG treatment exhibited an even stronger inhibitory effect on PPP activity (ca. 50 %, $p = 9.100 \cdot 10^{-13}$). Addition of 2DG enhanced the inhibitory effect of both synthetic flavaglines in WT cells significantly ($p \leq 0.0007$). In contrast to WT cells, IMD-3-resistant HGC176 cells did not show PPP inhibition upon IMD-1 treatment and IMD-3 inhibited PPP activity only by approximately 16 % ($p = 0.0070$) (Fig. 38A). Strikingly, 2DG treatment exhibited the most pronounced effect (ca. 30 % inhibition), when comparing application of single substances. The combination of 2DG with IMD-1 ($p = 7.660 \cdot 10^{-6}$) or IMD-3 ($p = 3.750 \cdot 10^{-6}$) significantly enhanced their inhibitory effect on PPP activity in resistant cells.

Comparing the total amount of incorporated tritium into RNA, after normalisation, revealed that IMD-3-resistant HGC176 cells incorporated almost twice as much tritium as WT HGC178 cells ($p = 5.501 \cdot 10^{-7}$) (Fig. 38B). Thus, acquired IMD-3 resistance led to an increase in PPP activity, possibly resulting in a metabolic shift from glycolysis to PPP. This could indicate that HGC176 cells acquired resistance through adaptation of glucose metabolism.

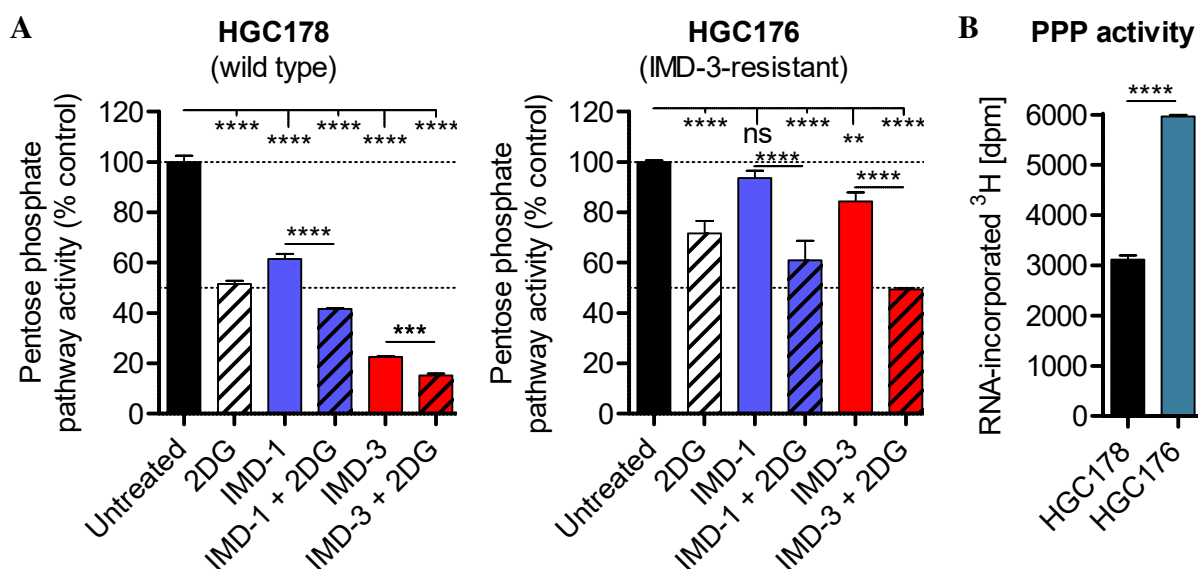


Figure 38: PPP activity in WT HGC178 and IMD-3-resistant HGC176 cancer cells. (A) Pentose phosphate pathway activity of WT and resistant cells in comparison to vehicle-treated control cells. (B) RNA-incorporated tritium from D-[³H-(U)]-glucose in vehicle-treated WT HGC178 and IMD-3-resistant HGC176 cells normalised to RNA concentration. 2DG: 1 mM; IMD-1, IMD-3: 100 nM; Treatment: 48 h. Multiplicity-adjusted p-values are listed in table ES10.

4.2.5 Genetic and epigenetic analysis does not reveal reasons for the acquired resistance

To investigate which molecular alterations caused IMD-3 resistance and identify genes disrupted upon GT mutagenesis responsible for resistance acquisition, the IMD-3-resistant cell line HGC176 was subjected to next generation sequencing (NGS). In total 138 genes with a disruptive insertion were identified by NGS. However, the screening did not reveal any genes, which were significantly overrepresented, exhibiting multiple disruptive insertions, which would indicate their importance for the mechanism of action and thus resistance acquisition (Fig. 39). This indicates that long-term IMD-3 resistance in HGC176 cells might be caused by a genetics-independent mechanism.

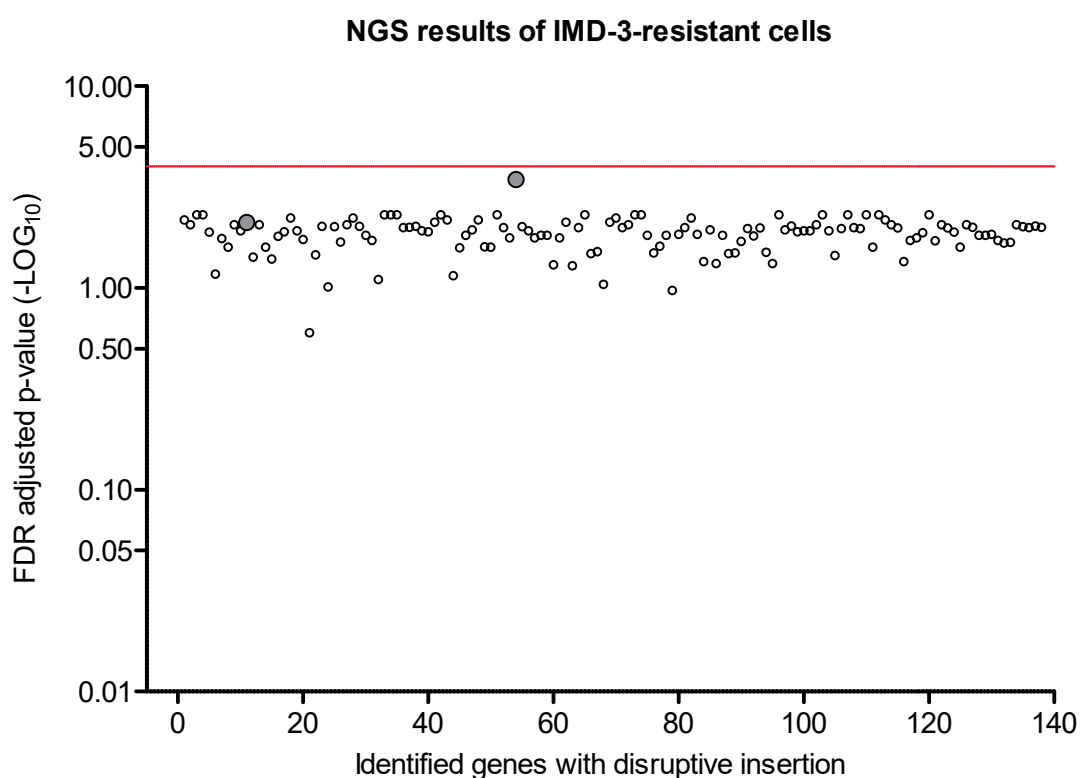


Figure 39: NGS screening of IMD-3-resistant HGC176 cells. NGS screening identified 138 genes with a disruptive insertion upon GT mutagenesis. Only one disruptive insertion was identified for 136 genes, while two genes exhibited two disruptive insertions (grey). No genes were significantly overrepresented (above red line: FDR adjusted p-value = 0.0001), exhibiting multiple disruptive insertion, which would indicate their importance for resistance development. Screening was performed by Haplogen GmbH (Vienna, Austria). An example of a positive screening result provided by Haplogen GmbH is shown in Fig. S6.

The possibility of epigenetic modifications, e.g. DNA methylation, causing IMD-3 resistance in HGC176 cells was investigated by pretreatment of WT and resistant cells with 5-aza-2'-deoxycytidine (DAC), a demethylating agent, before application of IMD-3.

Pretreatment of WT HGC178 cells with 0.1 μ M or 0.5 μ M DAC for one week did not influence their sensitivity towards IMD-3 treatment, whereas the sensitivity of resistant HGC176 cells

towards IMD-3 seemed to increase with increasing DAC concentrations though not achieving the sensitivity level of WT cell (Fig. 40A). However, when comparing the viability of 0.1 and 0.5 μM DAC-treated cells, a significant effect of DAC-pretreatment on the viability of WT and resistant cells was revealed (Fig. 40B). DAC-pretreatment with 0.1 and 0.5 μM reduced the viability of WT cells to 52.6 % ($p = 8.940 \cdot 10^{-13}$) and 17.3 % ($p = 6.500 \cdot 10^{-14}$), respectively. IMD-3 resistant HGC176 cells were even more sensitive towards DAC-pretreatment showing a viability reduction to 31.6 % ($p = 6.500 \cdot 10^{-14}$) upon application of 0.1 μM DAC, while almost no viable cells remained after application of 0.5 μM DAC (1.7 %, $p = 6.500 \cdot 10^{-14}$).

Therefore, the observed increased sensitivity of resistant HGC176 cells towards IMD-3 after DAC-pretreatment might be caused by the strong cytotoxicity induced by DAC. To reduce the cytotoxic influence of DAC while still achieving a demethylating effect, a lower concentration of DAC (0.01 μM) was applied as pretreatment over two weeks. As expected, the lower DAC concentration had no cytotoxic effect on the viability of WT and IMD-3-resistant cells (Fig. 40B), but also did not restore the sensitivity of resistant HGC176 cells towards IMD-3 (Fig. 40C).

To evaluate the extent of DNA demethylation upon DAC-pretreatment, the methylation status of three CpG sites in the LINE-1 DNA sequence, a long interspersed element (LINE) retrotransposon comprising approximately 17 % of the genome [303], was analysed using pyrosequencing. High concentrations of DAC (0.1, 0.5 μM) successfully demethylated LINE-1 CpG sites in both cell lines after one week pretreatment (Fig. 41A). DAC-pretreatment with 0.1 and 0.5 μM significantly reduced LINE-1 CpG methylation from 51.3 % to 15 % ($p = 3.553 \cdot 10^{-5}$) and 14.3 % ($p = 3.193 \cdot 10^{-5}$) in WT cells. A similar demethylating effect of DAC was observed in IMD-3-resistant HGC176 cells decreasing LINE-1 CpG methylation from 57 % to 17.3 % ($p = 0.0001$) and 12.7 % ($p = 5.560 \cdot 10^{-5}$). Although pretreatment with high concentrations of DAC successfully demethylated the DNA, sensitivity of resistant HGC176 cells towards IMD-3 was not restored (Fig. 40A) and observed decrease of cell viability can be attributed to the direct cytotoxicity of DAC-pretreatment (Fig. 40B).

Pretreatment with the lowest DAC concentration (0.01 μM) also did not change the sensitivity of WT cells towards IMD-3 (Fig. 40C), although they did show demethylation (Fig. 41B). In resistant HGC176 cells 0.01 μM DAC exhibited a slightly demethylating effect (Fig. 41B), not reaching significance in this experiment, which however did not restore the sensitivity of the cell line (Fig. 40C). Comparison of LINE-1 CpG methylation of DMSO-treated WT and IMD-3-resistant cells did not reveal any difference in methylation between the cell lines (Fig. 41C).

In summary, DAC-induced demethylation did not restore sensitivity of resistant cells towards IMD-3 treatment indicating that long-term resistance of this cell line is not caused by altered DNA methylation.

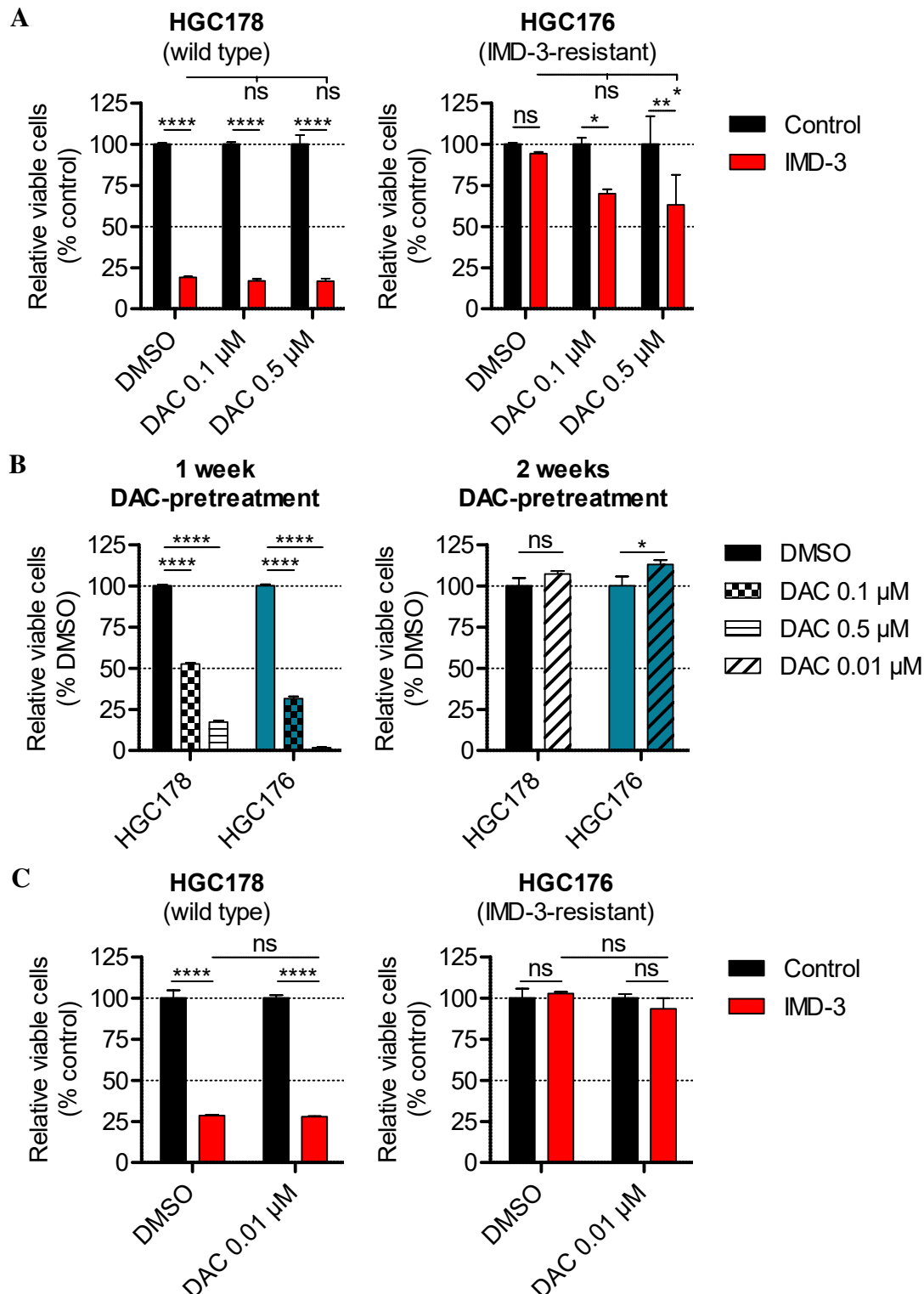


Figure 40: Influence of DAC-pretreatment on IMD-3 sensitivity and viability of WT HGC178 and resistant HGC176 cells. (A) Relative cell viability after IMD-3 treatment (100 nM, 48 h) upon 1 week DAC-pretreatment (0.1, 0.5 μ M). (B) Relative viability of HGC178 and HGC176 cells after DAC-treatment over 1 week (0.1, 0.5 μ M) or over 2 weeks (0.01 μ M). (C) Relative cell viability after IMD-3 treatment (100 nM, 48 h) upon 2 weeks DAC-pretreatment (0.01 μ M). For all experiments, viability of control/DMSO-treated cells was set to 100 % to determine the relative viability of treated cells. Multiplicity-adjusted p-values are listed in table ES14.

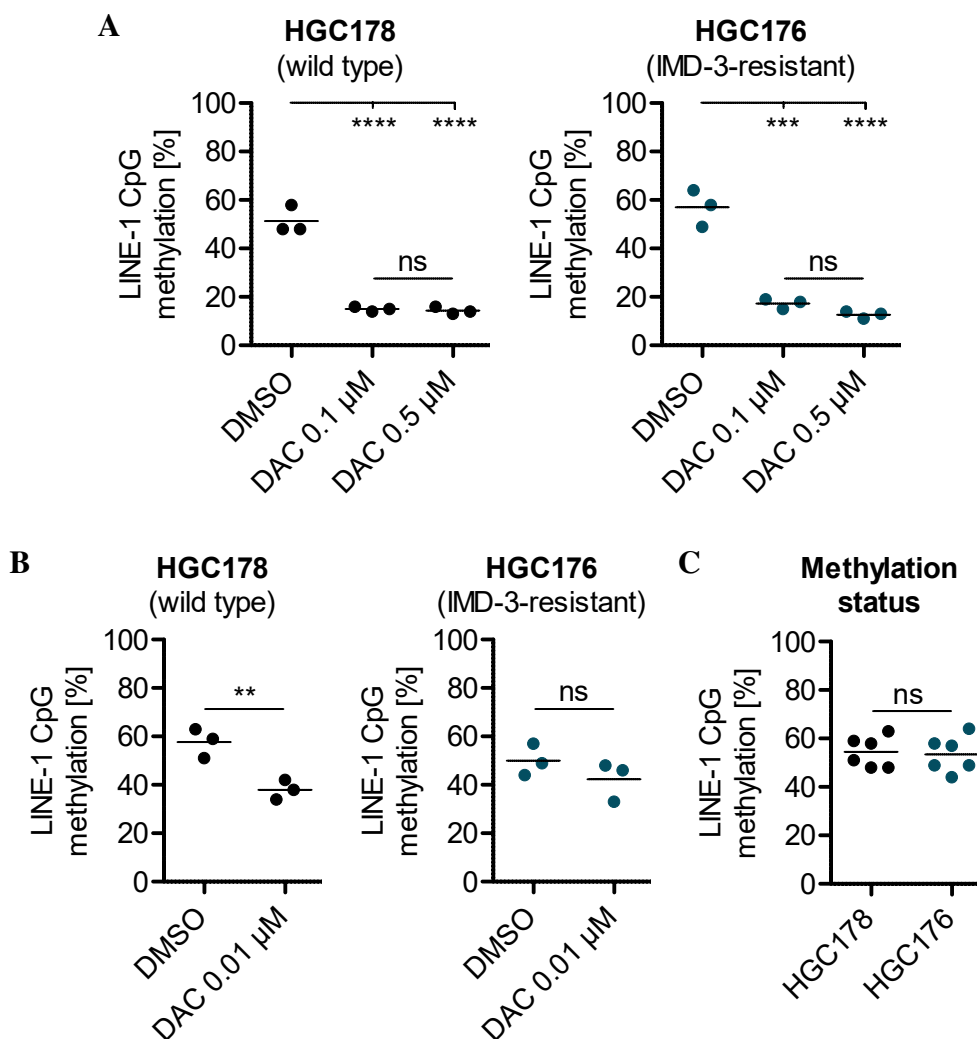


Figure 41: Methylation status of three LINE-1 CpG sites of DAC-pretreated WT and IMD-3-resistant cancer cells. (A) LINE-1 CpG methylation after one week of DAC-pretreatment (0.1, 0.5 μ M). (B) LINE-1 CpG methylation after two weeks of DAC-pretreatment (0.01 μ M). (C) Comparison of LINE-1 CpG methylation between DMSO-treated (1 and 2 weeks) WT HGC178 and IMD-3-resistant HGC176 cells. Mean values are indicated. Multiplicity-adjusted p-values are listed in table ES14.

4.2.6 Transcriptome analysis reveals decreased glycolytic activity in IMD-3-resistant cells

To further elucidate the differences between IMD-3-resistant and WT cells, RNA transcriptome profiling was performed using the Illumina bead chip platform (HumanHT-12 v4). Transcriptome analysis resulted in a list of over 22,500 genes, of which 379 genes were considered significantly deregulated (BH-corrected p -value ≤ 0.05 , $\log_2FC \geq 1 / \leq -1$) in resistant HGC176 cells compared to WT HGC178 cells (Tab. ES15). Overall, 160 genes were upregulated in resistant cells, while 219 genes were downregulated.

Pathway analysis of DEGs between IMD-3-resistant and WT cells revealed significant deregulation of 43 pathways (IPA p -value $\leq 0.05 / -\log_{10}(p\text{-value}) \geq 1.301$) including downregulation of eIF2 signalling and metabolic pathways such as glycolysis and cholesterol biosynthesis (Fig. 42,

Tab. ES15). Resistant cells also exhibited a decreased expression level of the HSP70 family member *HSPA8* (7.7-fold, $p=1.789 \times 10^{-9}$), displaying the second most downregulated gene, and slightly reduced *TXNIP* expression (1.7-fold, $p=0.0002$) compared to WT cells (Tab. S7). Thus, several pathways, which seem to be relevant in IMD-3 function, are downregulated in resistant HGC176 cells.

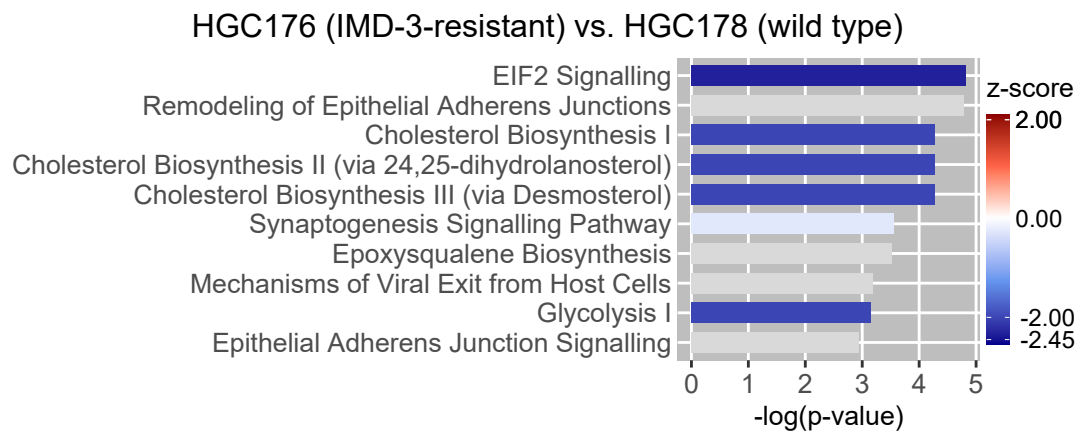


Figure 42: Top 10 deregulated pathways in IMD-3-resistant HGC176 cells compared to WT HGC178 cells. Significantly DEGs were used to identify altered pathways in IMD-3-resistant cells. Displayed z-scores predict activation ($z\text{-score} \geq 2$; red) or inhibition ($z\text{-score} \leq -2$; blue) of the pathways. If no direction could be predicted, the z-score is 0 (white). If the z-score could not be calculated, pathways are displayed in grey. Cholesterol biosynthesis pathways I, II and III describe cholesterol synthesis through different intermediates and the same genes were matched to the three pathways, thus they have the same z-score and p-value. Identification of DEGs was performed jointly with Simon Kalteis.

Decreased activity of glycolysis could be confirmed through decreased sensitivity of resistant HGC176 cells towards glycolysis inhibition by 2DG, especially at higher 2DG concentrations (Fig. 43). Resistant HGC176 cells showed a decreased viability of 80.4 % upon treatment with 4 mM 2DG, while WT HGC178 cells were significantly more sensitive showing a reduction to 62.9 % ($p=0.0010$). In combination with increased activity of the PPP (see 4.2.4), compensating decreased NADH production through glycolysis, IMD-3-resistant cells exhibit several metabolic changes, which could contribute to acquired IMD-3 resistance.

Due to the possible metabolic adaptations in resistant HGC176 cells, differences between IMD-3-induced transcriptional changes in WT and resistant cells were investigated. Overall, 2450 genes and 98 pathways were significantly deregulated upon IMD-3 treatment in WT cells, while only 60 genes and 22 pathways were affected in IMD-3-resistant cells (Tab. 25). Comparing DEGs between analysed IMD-3-sensitive cell lines (WT HGC178; colon: HCT116, HT29; HPV-positive: CaSki, HeLa, SiHa, UPCI-SCC-90) revealed that 137 genes were shared and deregulated in the same direction in these cell lines, while only three of these genes were also affected in resistant HGC176 cell line upon IMD-3 treatment (Fig. S8).

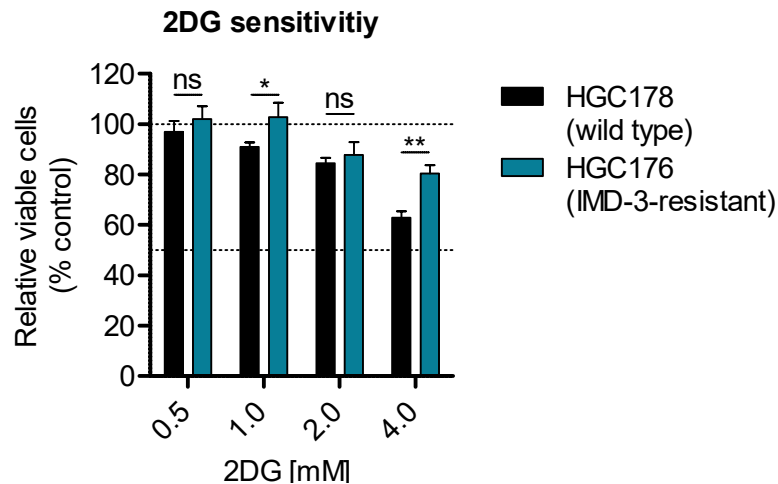


Figure 43: Sensitivity of WT HGC178 and IMD-3-resistant HGC176 towards 48 h 2DG treatment. Resistant cells show decreased sensitivity towards 2DG due to downregulation of glycolysis. Controls for each cell line were set to 100 %. Multiplicity-adjusted p-values are listed in table ES16.

Table 25: Summary of significantly deregulated genes and pathways upon IMD-3 treatment (100 nM, 48 h) in WT and resistant cells. Significantly DEGs (BH-corrected p-value ≤ 0.05 , up: $\log_2FC \geq 1$; down: $\log_2FC \leq -1$) were subjected to pathway analysis resulting in significantly altered pathways (IPA: p-value ≤ 0.05).

IMD-3 vs. Control	Total deregulated	Upregulated	Downregulated	IPA
	genes	genes	genes	Pathways
HGC178 (WT)	2450	1126	1324	98
HGC176 (IMD-3-resistant)	60	19	41	22

Comparison analysis of altered pathways upon IMD-3 treatment revealed pronounced alterations in WT cells, whereas the same pathways were not altered significantly in IMD-3-resistant cells (Fig. 44, S7). WT cells exhibited similar alterations as observed in CRC and HPV-transformed cell lines (see 4.1.6), including upregulation of NRF2-mediated oxidative stress response, while downregulating GSH-mediated detoxification and fatty acid synthesis (γ -linolenate biosynthesis). WT HGC178 cells also showed inhibition of chromosomal replication and *de novo* synthesis of purine nucleotides (Fig. 44). Additionally, WT cells showed upregulation of the UPR (Fig. 44B) as well as induction of DDIT3 expression (2.4-fold, $p=6.902 \cdot 10^{-7}$), which was also observed in all other IMD-3-sensitive cell lines (see 4.1.6). No upregulation of DDIT3 in IMD-3-treated resistant cell lines was observed. In contrast to the other sensitive cell lines, IMD-3-treatment did not enhance PMAIP1/NOXA expression over 2-fold in the WT cell line (Tab. S7). Furthermore, upregulation of the senescence pathway was detected in WT cells indicating that IMD-3 activates similar responses in all treatment sensitive cell lines, leading to increased oxidative stress, activation of UPR, inhibition of proliferation and a senescence-like phenotype [304, 305].

Although transcriptional changes in the PI3K/AKT/mTOR pathway were not as pronounced as in CRC and HPV-transformed cells (Tab. S7), experimental data confirm IMD-3-induced deregulation of glucose metabolism. *TXNIP* levels were not increased in WT cells upon IMD-3 treatment but slightly decreased (1.7-fold) in resistant cells. WT cells showed IMD-3-induced downregulation of complex I assembly factor *NDUFAF3* (20-fold, $p = 1.027 \times 10^{-17}$), displaying the second most downregulated gene, and complex II subunit *SDHC* (2-fold, $p = 4.073 \times 10^{-17}$), whereas transcription levels were not altered in IMD-3-treated resistant HGC176 cells (Tab. S7). Overall, only few alterations were detected in resistant HGC176 cells upon IMD-3 application (Fig. 44) underlining their insensitivity towards the treatment.

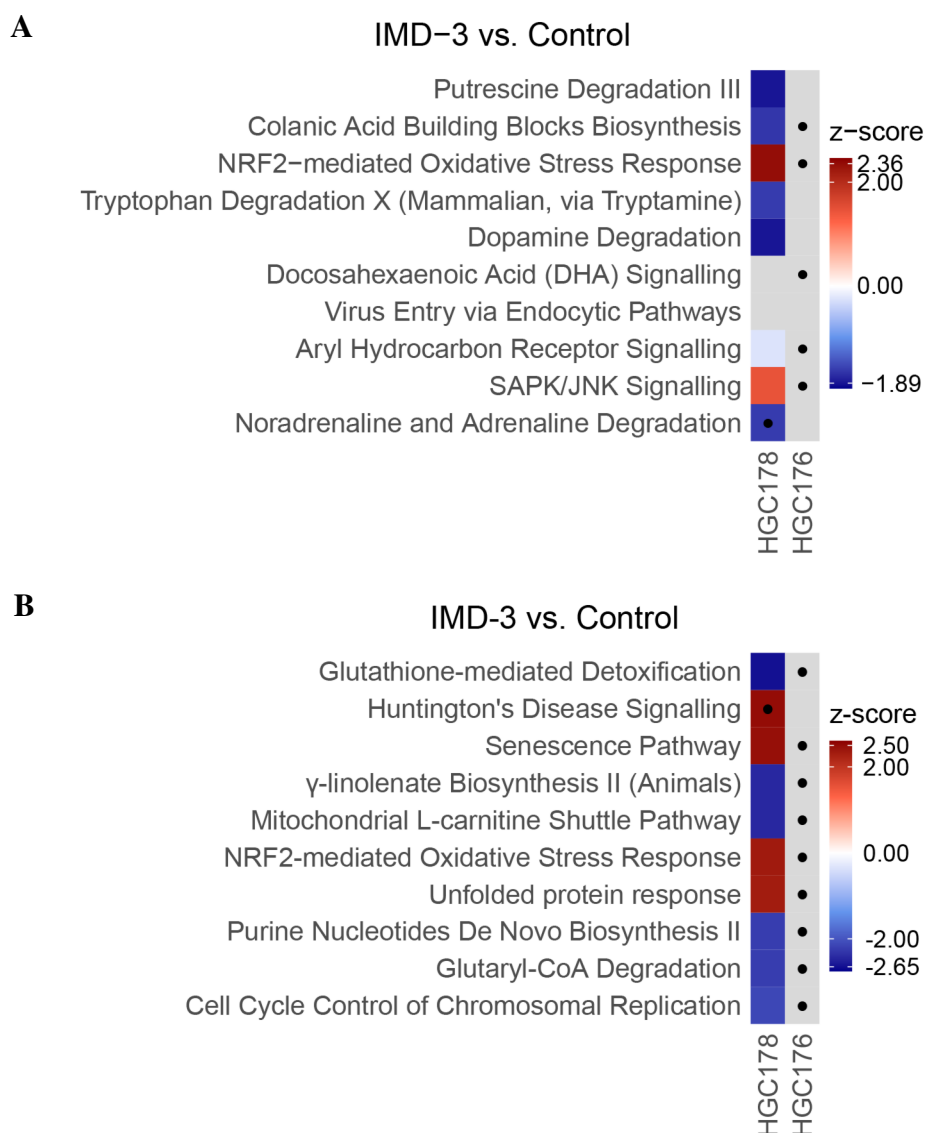


Figure 44: Top 10 deregulated pathways in WT HGC178 and IMD-3-resistant HGC176 cells upon IMD-3 treatment (100 nM, 48 h). Significantly DEGs upon IMD-3 treatment were used to identify altered pathways in each cell line. Displayed z-scores predict activation ($z\text{-score} \geq 2$; red) or inhibition ($z\text{-score} \leq -2$; blue) of the pathways based on transcriptome data. If no direction could be predicted, the z-score is 0 (white). If the z-score could not be calculated, pathways are displayed in grey. Non-significant pathways ($p\text{-values} > 0.05$) are marked with a dot. (A) Comparison of altered pathways sorted by their p-value. (B) Comparison of altered pathways sorted by their z-score. Identification of DEGs was performed jointly with Simon Kalteis. z-scores and p-values are listed in table S8.

4.3 Evaluation of synthetic flavagline treatment *in vivo*

4.3.1 Evaluation of anti-tumour efficacy *in vivo* and analysis of treatment-related side effects

4.3.1.1 Dose finding experiment and first side effect profiling of synthetic flavaglines in a xenograft model

To evaluate the suitability of synthetic flavaglines in combination with 2DG as potential anti-cancer treatment, first *in vivo* experiments were performed in xenograft-bearing Rag2^{-/-}Il2rg^{-/-} mice to select optimal drug dosages and to identify potential toxic side effects in small treatment groups (6 mice/group). As a tumour model HCT116 cells were used, which previously had shown high sensitivity towards synthetic flavagline treatment *in vitro*. Xenograft-bearing mice were treated with different concentrations of synthetic flavaglines (0.2, 0.5, 1.0 mg/kg) alone or in combination with different concentrations of 2DG (100, 200, 400 mg/kg) three times a week, receiving up to 12 *i.p.* injections over four weeks. The treatment was started 10 days after tumour injection and mice were monitored to a maximum of 37 days, with the 12th treatment injection on day 36. Due to the large number of treatment groups (n=18) and total number of animals (n=108), experiments were split and conducted in smaller portions of treatment groups. To minimise variation and ensure reproducibility between experiments, HCT116 cells from the same cryopreserved batch were injected for xenograft formation in all experiments.

Correlating with the low efficacy of 2DG treatment *in vitro*, the highest concentration of 2DG (400 mg/kg) did not inhibit tumour growth significantly compared to vehicle-treated control mice and had no significant effect on the survival of the mice (Fig. 45A, Tab. 26). Similarly, the highest concentration of IMD-1 (1.0 mg/kg) did not lead to a significant reduction in tumour growth or prolongation of survival irrespectively of the combination with 2DG (Fig. 45B, Tab. 26). The applied concentration of 2DG also did not influence the treatment response.

Due to the higher efficacy of IMD-3 in previous *in vitro* experiments compared to IMD-1 and, thus, the higher possibility of treatment-related side effects, xenograft-bearing mice were first treated with the lowest concentration of IMD-3 (0.2 mg/kg) alone and in combination with rising 2DG concentrations. Treated mice showed a slightly decreased tumour growth rate as well as slightly prolonged survival, although both effects were not significant (Fig. 46A, Tab. 26). As no acute toxic side effects at the lowest treatment concentration were observed, IMD-3 was applied in higher concentrations (0.5, 1.0 mg/kg).

Although the same batch of HCT116 cells was used for xenograft formation, tumours were growing significantly slower in one experiment already before starting treatment application. Therefore, the results obtained from these treatment groups (IMD-3: 0.5 mg/kg, 0.5 mg/kg + 2DG 200 mg/kg, 1.0 mg/kg + 2DG 200 mg/kg, 1.0 mg/kg + 2DG 400 mg/kg) were not considered in the selection of optimal dosage. Mice treated with 0.5 mg/kg IMD-3 in combination with 100 or 400 mg/kg 2DG did not show prolonged survival or tumour growth compared to

vehicle-treated mice (Fig. 46B, Tab. 26). Application of 1.0 mg/kg IMD-3 alone or in combination with 100 mg/kg 2DG seemed to slightly reduce tumour growth compared to the vehicle-treated mice (Fig. 46C), although the effect was not significant. In contrast to all other tested combinations, combining 1.0 mg/kg IMD-3 with 100 mg/kg 2DG extended the median survival of mice receiving only 1.0 mg/kg IMD-3 from 24.5 to 33.5 days (Tab. 26). The small number of mice in each group and the heterogeneous tumour growth impaired the statistical power, which was also not the aim of this explorative first step of *in vivo* evaluation. In both treatment groups (IMD-3 1.0 mg/kg \pm 2DG 100 mg/kg) two mice had not reached the maximal tumour size at day 37 (Fig. 46C) but needed to be sacrificed due the experimental design to assess side effects directly after the last treatment injection at day 36.

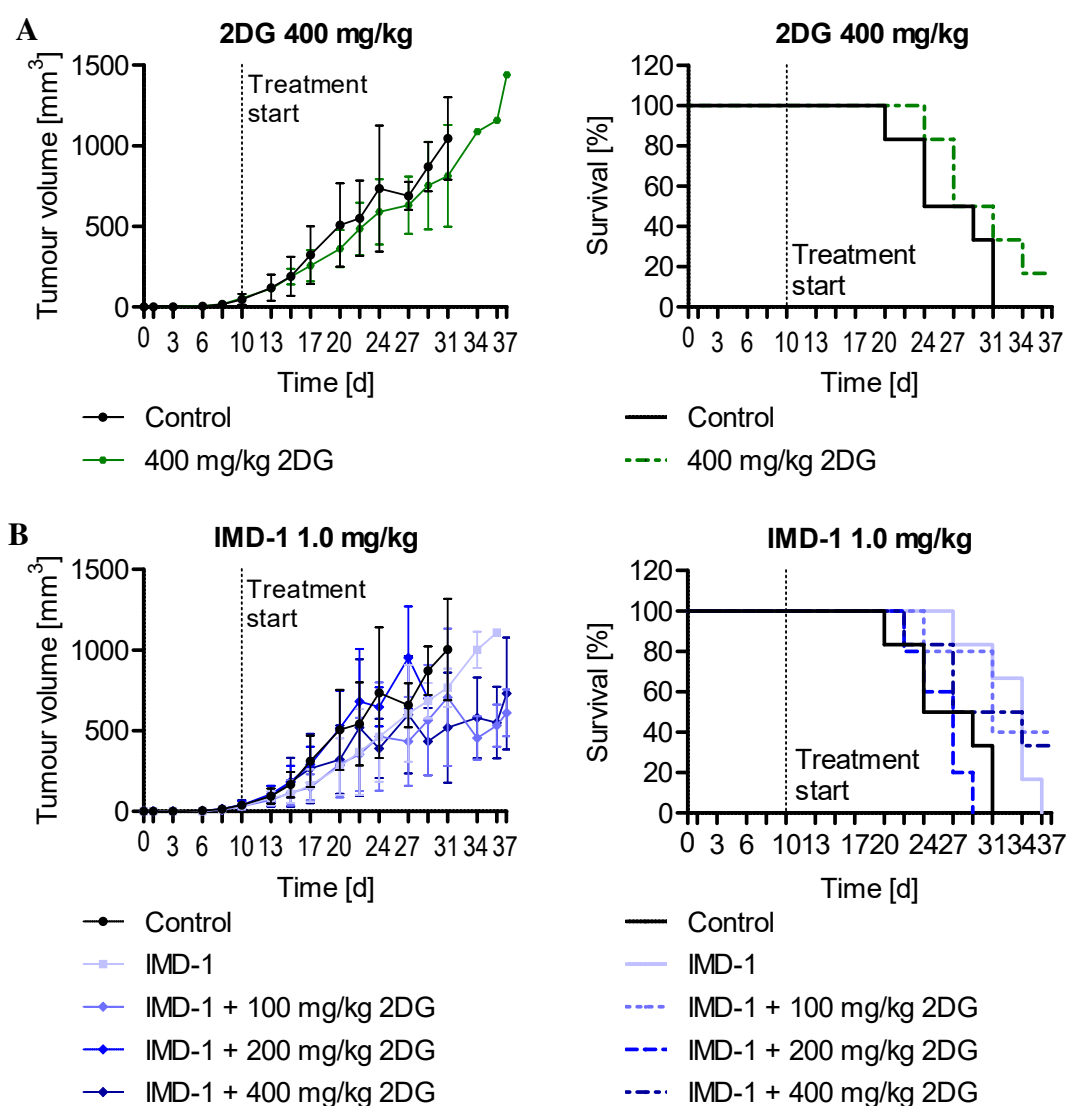


Figure 45: Tumour growth and survival of 2DG- (A) and IMD-1-treated (B) xenograft-bearing mice. After treatment start (day 10), mice were monitored up to max. day 37 (max. 12 injections, 6 mice/group). (A) Mice were treated with 400 mg/kg 2DG. (B) Mice were treated with the highest concentration of IMD-1 (1.0 mg/kg) alone and in combination with 2DG (100, 200, 400 mg/kg). One mouse in the IMD-1 + 200 mg/kg 2DG group was excluded due to lack of tumour growth and one mouse in the IMD-1 + 100 mg/kg 2DG group spontaneously deceased. Tumour growth is shown as mean \pm SD. Individual tumour growth curves are shown in Fig. S9.

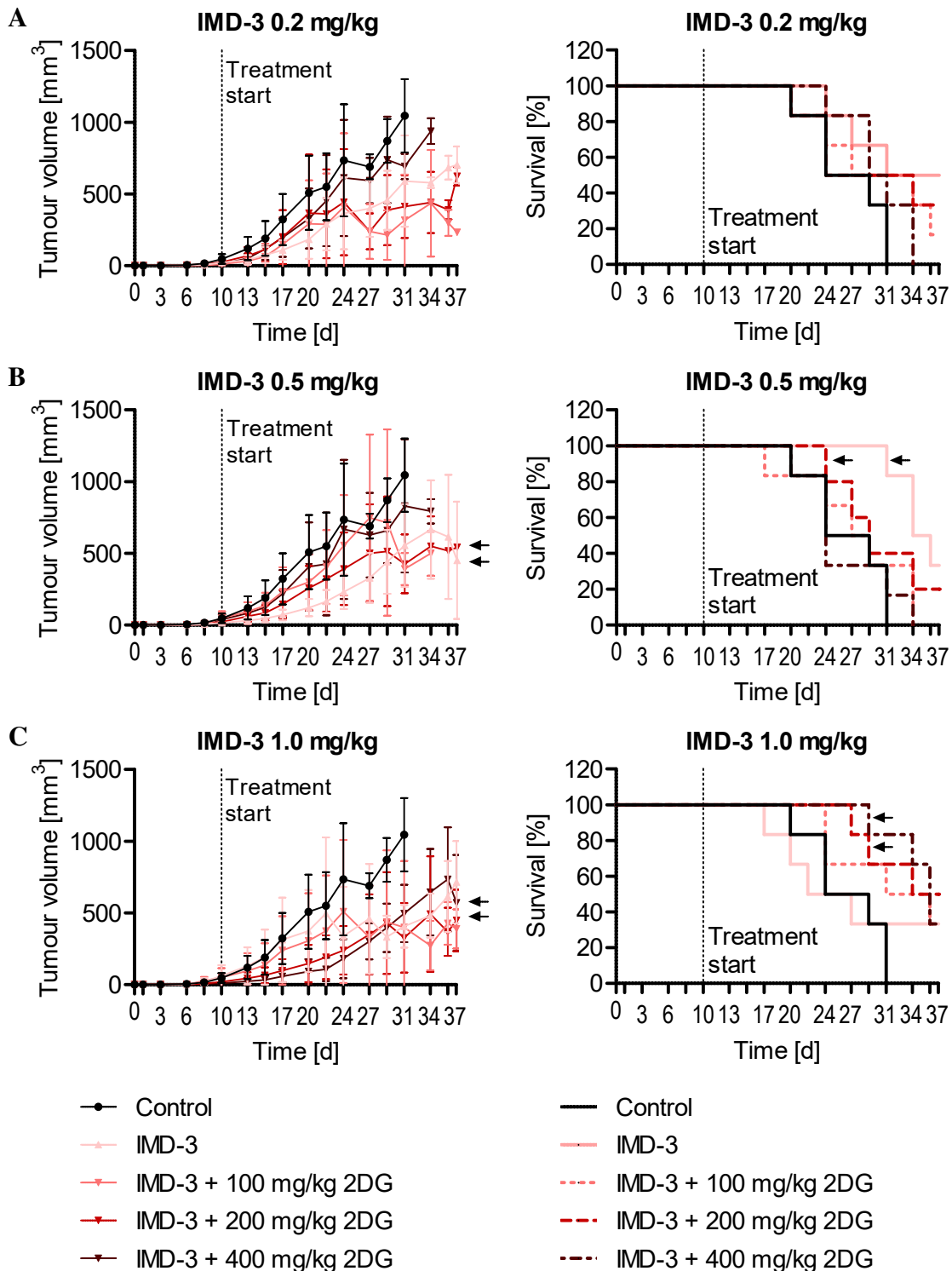


Figure 46: Tumour growth and survival of xenograft-bearing mice treated with increasing IMD-3 concentrations (0.2 mg/kg (A), 0.5 mg/kg (B), 1.0 mg/kg (C)) alone and in combination with 2DG (100, 200, 400 mg/kg). After treatment start (day 10), mice were monitored up to max. day 37 (max. 12 injections, 6 mice/group). Arrows: Tumour growth rate in control mice was significantly slower in these experiments (IMD-3: 0.5 mg/kg, 0.5 mg/kg + 200 mg/kg 2DG, 1.0 mg/kg + 200 mg/kg 2DG, 1.0 mg/kg + 400 mg/kg 2DG), compared to the others. One mouse in the IMD-3 0.5 mg/kg + 2DG 200 mg/kg group spontaneously deceased and was excluded. Tumour growth is shown as mean \pm SD. Individual tumour growth curves are shown in Fig. S10.

Table 26: Mean and median survival of xenograft-bearing mice for optimal treatment dosage and combination determination. Treatment was started at day 10 and mice were monitored to a maximum of 37 days (max. 12 treatment injections). The tumour growth rate in treatment groups highlighted in red was significantly slower already before treatment application, thus it is not possible to draw a conclusion regarding treatment efficacy. P-values for survival curves are shown in table ES17.

Treatment group	Mean survival [days]	Median survival [days]	Mice / Group
Control	26.5	26.5	6
2DG 400 mg/kg	30.0	29.0	6
IMD-1 1.0 mg/kg			
IMD-1 1.0 mg/kg	32.7	34.0	6
IMD-1 + 2DG 100 mg/kg	32.0	31.0	5
IMD-1 + 2DG 200 mg/kg	25.8	27.0	5
IMD-1 + 2DG 400 mg/kg	30.7	30.5	6
IMD-3 0.2 mg/kg			
IMD-3 0.2 mg/kg	32.2	34.0	6
IMD-3 + 2DG 100 mg/kg	29.7	30.5	6
IMD-3 + 2DG 200 mg/kg	29.3	29.0	6
IMD-3 + 2DG 400 mg/kg	30.2	30.0	6
IMD-3 0.5 mg/kg			
IMD-3 0.5 mg/kg	34.8	35.0	6
IMD-3 + 2DG 100 mg/kg	27.5	28.0	6
IMD-3 + 2DG 200 mg/kg	30.2	29.0	5
IMD-3 + 2DG 400 mg/kg	26.2	24.0	6
IMD-3 1.0 mg/kg			
IMD-3 1.0 mg/kg	26.7	24.5	6
IMD-3 + 2DG 100 mg/kg	31.5	33.5	6
IMD-3 + 2DG 200 mg/kg	33.5	35.5	6
IMD-3 + 2DG 400 mg/kg	34.8	36.0	6

Xenograft-bearing mice did not show any macroscopically visible toxic side effects upon treatment with the highest concentration of IMD-3 (1.0 mg/kg) during the experiment, thus the histological appearance of organs (brain, heart, lung, liver, kidney, pancreas, stomach, small intestine, colon) was assessed. Evaluation of organs by HE staining did not reveal any major treatment-related pathology (Fig. 47, 48).

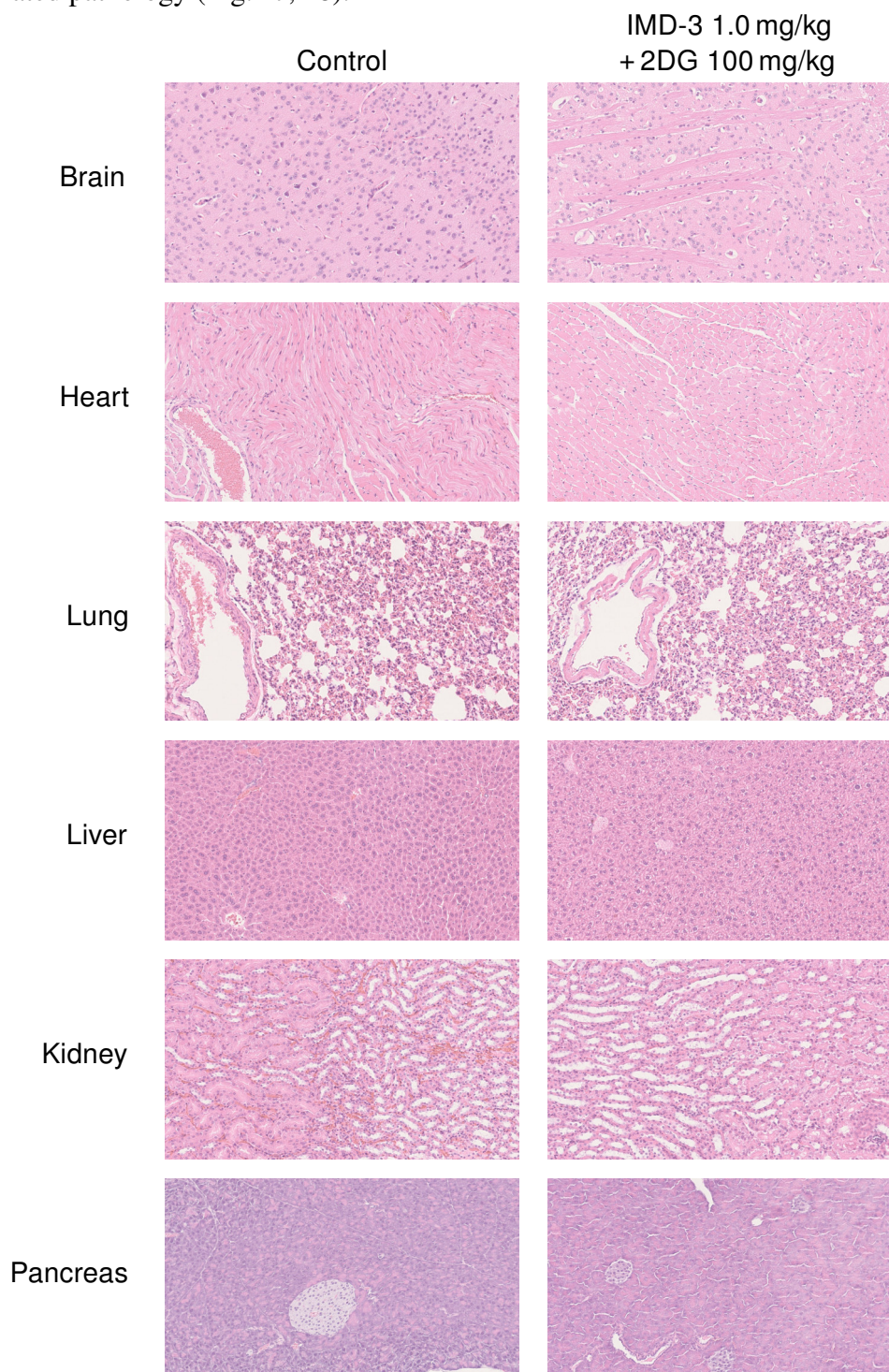


Figure 47: Overview of the histological appearance of organs in HE staining from xenograft mice treated with vehicle (left) or the combination of IMD-3 (1.0 mg/kg) and 2DG (100 mg/kg). Representative images from control and treatment groups are shown. Initial histological evaluation revealed no major treatment related adverse effects. Images: NanoZoomer S210 Digital slide scanner, 40 x objective.

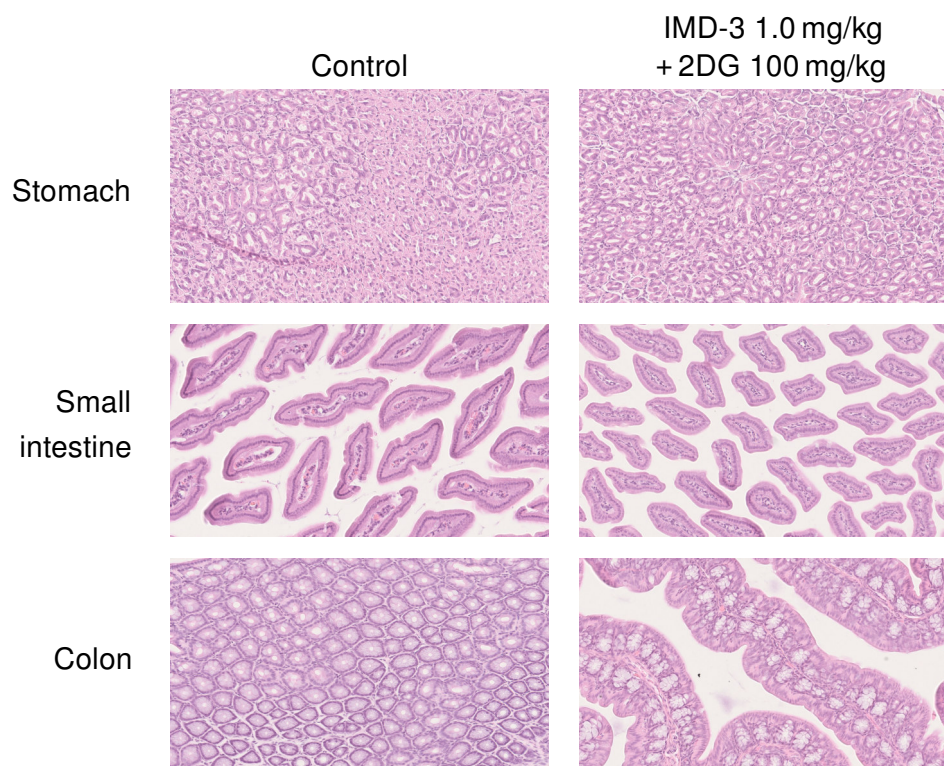


Figure 48: Overview of the histological appearance of digestive tract from xenograft mice treated with vehicle (left) or the combination of IMD-3 (1.0 mg/kg) and 2DG (100 mg/kg). Representative images from control and treatment groups are shown. Initial histological evaluation revealed no major treatment related adverse effects. Images: NanoZoomer S210 Digital slide scanner, 40 x objective.

Due to the observed IMD-3-induced proliferation inhibition and GLUT-1 downregulation *in vitro*, xenograft tumours were stained for proliferation (Ki-67) and GLUT-1 expression to evaluate if IMD-3 treatment induced similar molecular changes *in vivo* (Fig. 49A). Upon staining, the proportion of Ki-67 or GLUT-1 positive cells in the tumour was quantified using the Quantitative Pathology and Bioimage Analysis (QuPath) software (Fig. 49B).

Tumours of mice treated with 0.5 or 1.0 mg/kg IMD-3 alone and in combination with 2DG did not show proliferation inhibition upon treatment (Fig. 50A). Vehicle-treated tumours exhibited an average GLUT-1 expression of 90.8 %, which decreased slightly upon treatment with IMD-3 (Fig. 50B), showing the most pronounced effect upon 1.0 mg/kg IMD-3 and 100 mg/kg 2DG (75.1 %), although the decrease was not significant.

Taken together, these results show that the highest concentration of IMD-3 does not exhibit acute toxicity upon *in vivo* application and does not cause adverse effects in the examined organs. Due to the slight improvement of the median survival of mice treated with 1.0 mg/kg IMD-3 in combination with 100 mg/kg 2DG compared to mice only receiving IMD-3 and the detected tendency of decreased GLUT-1 expression in this treatment group, these concentrations were selected for further investigation.

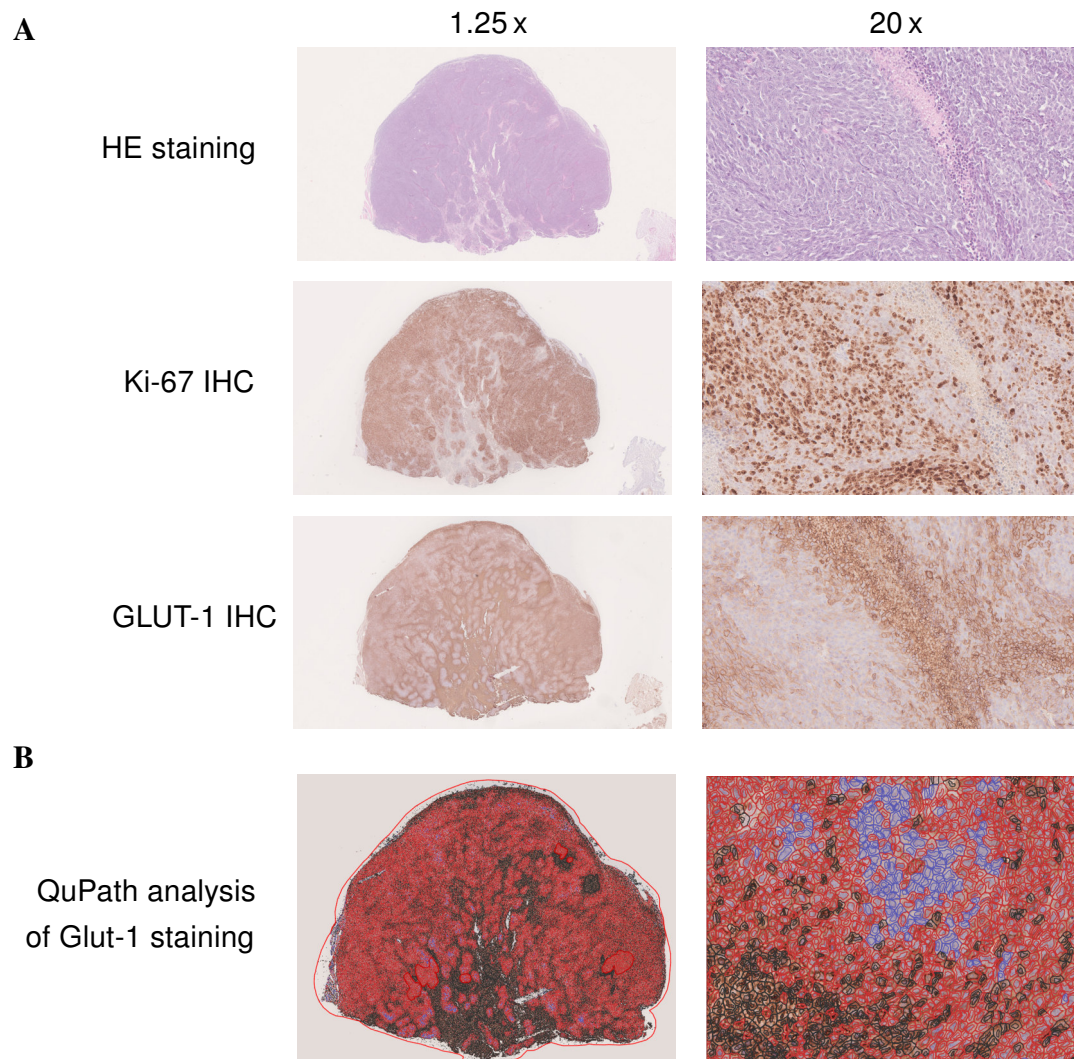


Figure 49: Exemplary images of HE, GLUT-1, and Ki-67 staining (A) and QuPath image classifier to quantify GLUT-1- or Ki-67-positive cells (B) in xenograft tumours of vehicle-treated mice. (A) Staining of tumour tissue revealed nuclear localisation of Ki-67 proliferation marker and membrane staining of GLUT-1. (B) Application of QuPath software for annotation of the tumour tissue after IHC staining and differentiation between positive and negative cells. Tumours were separated into necrotic tissue (brown), tumour tissue with positive (red) and negative (blue) staining signal. Stainings and QuPath analysis were performed by Javier Ignacio Arriaza Gonzalez as part of his medical doctor thesis. Images: NanoZoomer S210 Digital slide scanner, 40 x objective.

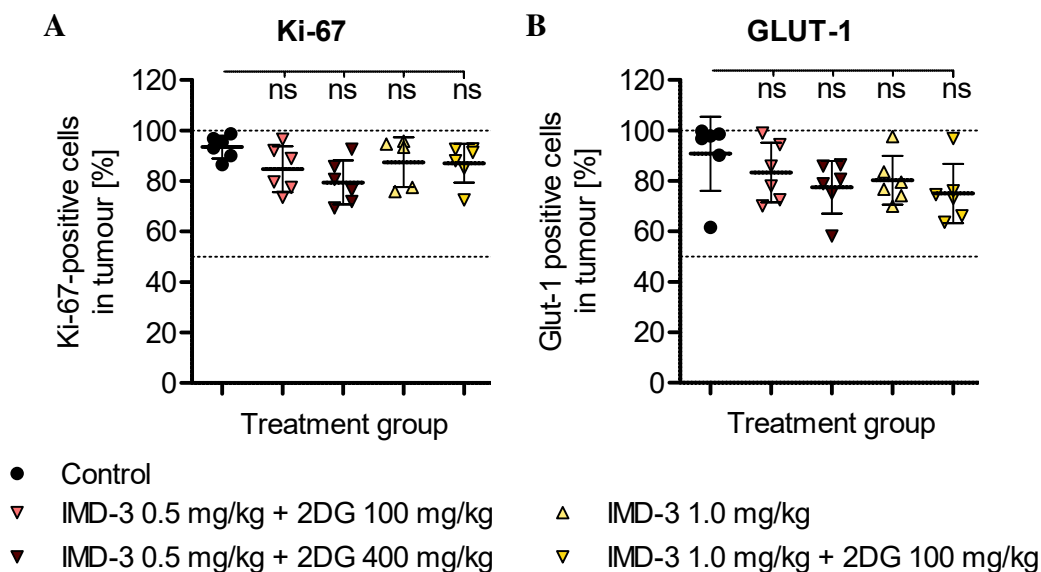


Figure 50: Expression of the proliferation marker Ki-67 and glucose transporter GLUT-1 in HCT116 xenograft tumours. (A) Percentage of Ki-67 positive cells in the tumours. (B) Percentage of GLUT-1 positive cells in the tumours. Analysis of tumour staining was performed using the QuPath software. Stainings and QuPath analysis were performed by Javier Ignacio Arriaza Gonzalez as part of his medical doctor thesis. Each treatment group consisted of 6 mice. Mean \pm SD values are indicated. Multiplicity-adjusted p-values are listed in table ES18.

4.3.1.2 The selected treatment doses show no detectable anti-tumour or side effects

The previously selected dose of 1.0 mg/kg IMD-3 in combination with 100 mg/kg 2DG was further investigated in a second experiment focusing on the assessment of anti-tumour efficacy and possible side effects in larger treatment groups (27 mice/group), also allowing to study the influence of synthetic flavaglines on glucose metabolism *in vivo* using PET imaging. Again, the experiment was split into smaller animal groups and performed in a manner stepwise increasing the number of animals in treatment groups. The same treatment schedule as described in the previous experiment was applied (see 4.3.1.1), but the mice were observed beyond the last treatment injection until a termination criterion was reached. PET scans, measuring the uptake of FDG into the tumours over a period of 30 minutes, were performed at day 14, 21 and 35 after tumour injection.

The experiment was terminated before reaching the initially planned number of animals per treatment group (16 mice/group instead of 27), as no difference in the tumour growth or survival could be detected upon treatment with 1.0 mg/kg IMD-3 alone or in combination with 100 mg/kg 2DG (Fig. 51). Also, the previously observed slight difference in survival between mice receiving IMD-3 alone and the treatment combination could not be confirmed (Tab. 27).

In line with the absent anti-tumour effect of the treatment described above, PET scans after two (day 14) and five treatment injections (day 21) did not show a difference in the maximum incorporation of FDG into the tumours (Fig. 52A, 52B). It was not possible to assess the difference in FDG uptake after 11 treatment injections (day 35) as all mice planned to undergo imaging, except for one 2DG-treated mouse, reached a termination criterion before day 35 (Fig. 52B). The performed MRI scan prior to PET imaging also showed no difference in the tumour size upon treatment (Fig. 52C), confirming the results obtained by manual tumour size measurement (Fig. 51A).

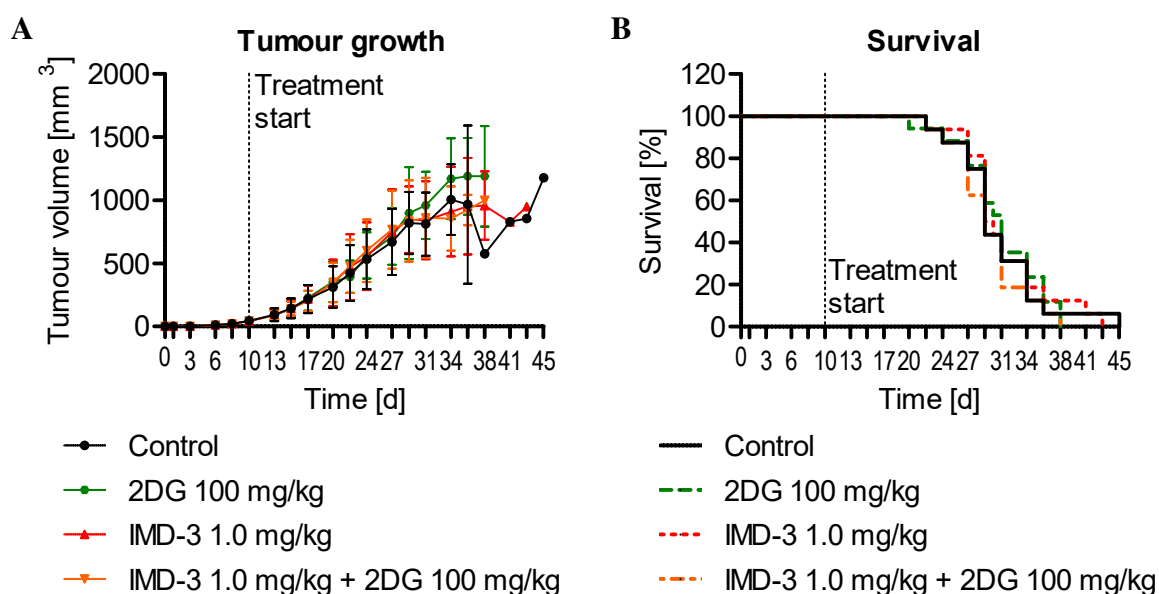


Figure 51: Tumour growth (A) and survival (B) of xenograft-bearing mice treated with 1.0 mg/kg MID-3 alone and in combination with 2DG 100 mg/kg. Mice received up to 12 *i.p.* injections starting at day 10 after tumour injection and were monitored until a termination criterion was reached. The groups receiving vehicle, IMD-3, or the combination of IMD-3 and 2DG consisted of 16 mice. One mouse of the combination group had to be excluded as it deceased unrelated to the treatment. The 2DG-treated group consisted of 17 mice. Tumour growth is shown as mean \pm SD. Individual tumour growth curves are shown in Fig. S11.

Table 27: Mean and median survival of xenograft-bearing mice upon treatment. Mice received up to 12 *i.p.* injections starting at day 10 after tumour injection and were monitored until a termination criterion was reached. P-values for survival curves are shown in table ES17.

Treatment group	Mean survival [days]	Median survival [days]	Mice/ Group
Control	30.63	29.0	16
2DG 100 mg/kg	30.82	31.0	17
IMD-3 1.0 mg/kg	31.31	29.5	16
IMD-3 1.0 mg/kg + 2DG 100 mg/kg	29.56	29	16

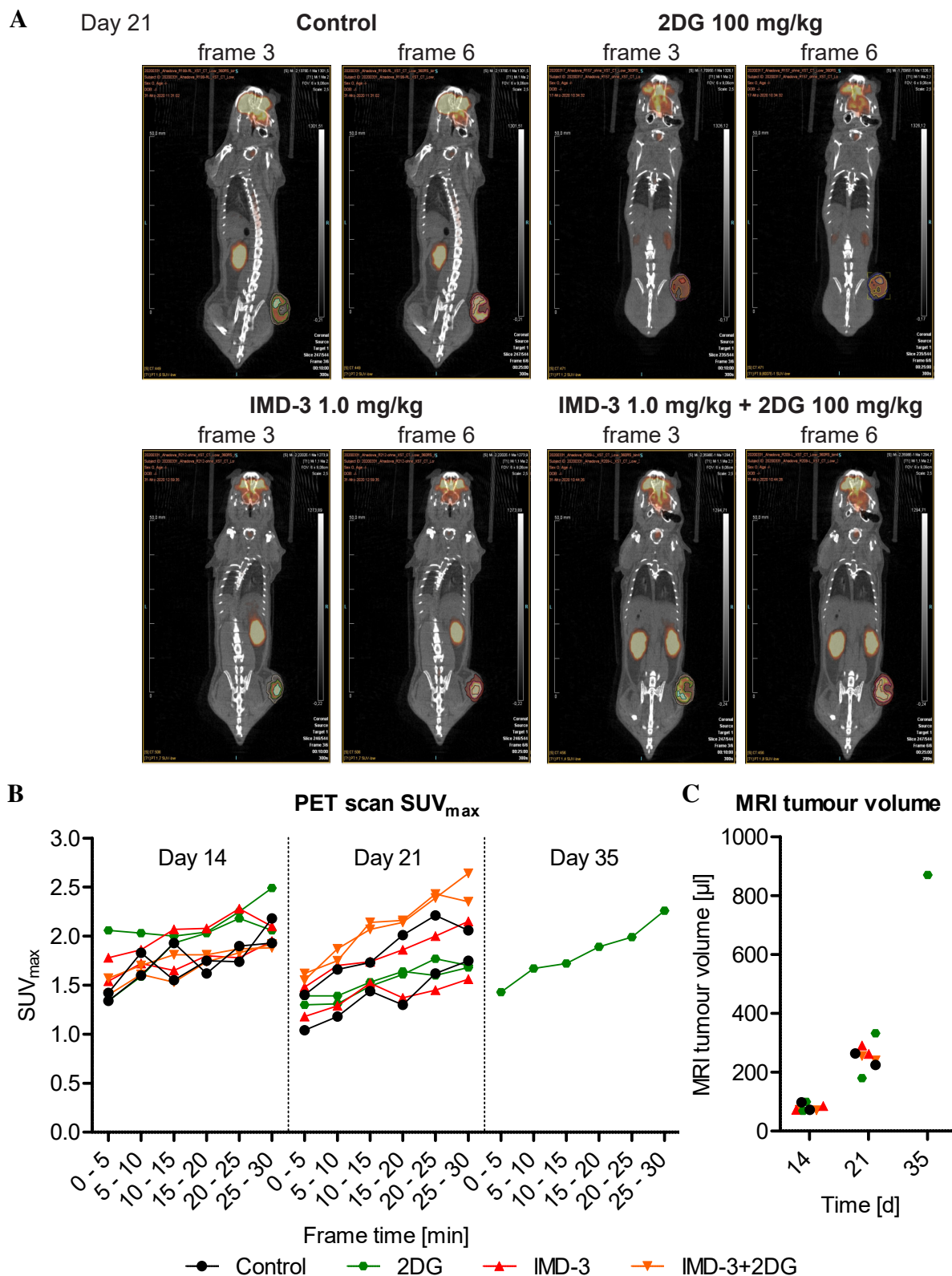


Figure 52: PET/CT and MRI analysis of xenograft mice treated with 1.0 mg/kg IMD-3 alone or in combination with 100 mg/kg 2DG. (A) PET scans of xenograft mice at day 21 (5 treatment injections). FDG accumulation was observed over 30 min. PET scans of frame 3 (10-15 min) and 6 (25-30 min) are shown. (B) Maximum FDG uptake (SUV_{max}) in the tumour over 30 min. SUV_{max} background correction could not be performed for one IMD-3-treated mouse at day 14 (lower red curve) as the CT scan failed and muscle tissue could not be identified. No difference between SUV_{max} values was detected. (C) MRI tumour volume. No difference between the treatment groups was detected. Multiplicity-adjusted p-values are listed in table ES20.

4.3.2 Analysis of possible reasons for discordance between *in vitro* and *in vivo* drug efficacy

The experiments described below aimed to analyse the influence of cell line sensitivity, drug solubility and drug delivery issues on the *in vivo* drug efficacy.

One possibility for decreased *in vivo* efficacy of synthetic flavaglines could have been the loss of sensitivity of HCT116 cells towards the synthetic flavaglines due to long time storage in liquid nitrogen between the first, explorative and the second, large *in vivo* experiment.

The sensitivity of the HCT116 cell batch used for all *in vivo* experiments had been assessed before starting xenograft experiments (Fig. 53A), confirming high sensitivity of HCT116 cells towards IMD-3 treatment. Repetition of the experiment with HCT116 cells stored in liquid nitrogen for approximately 8 months showed no significant change of their sensitivity towards different IMD-3 concentrations (50, 100 and 200 nM) alone and in combination with 2DG (Fig. 53B), thus excluding altered sensitivity of the used cell line batch as a reason for the observed results.

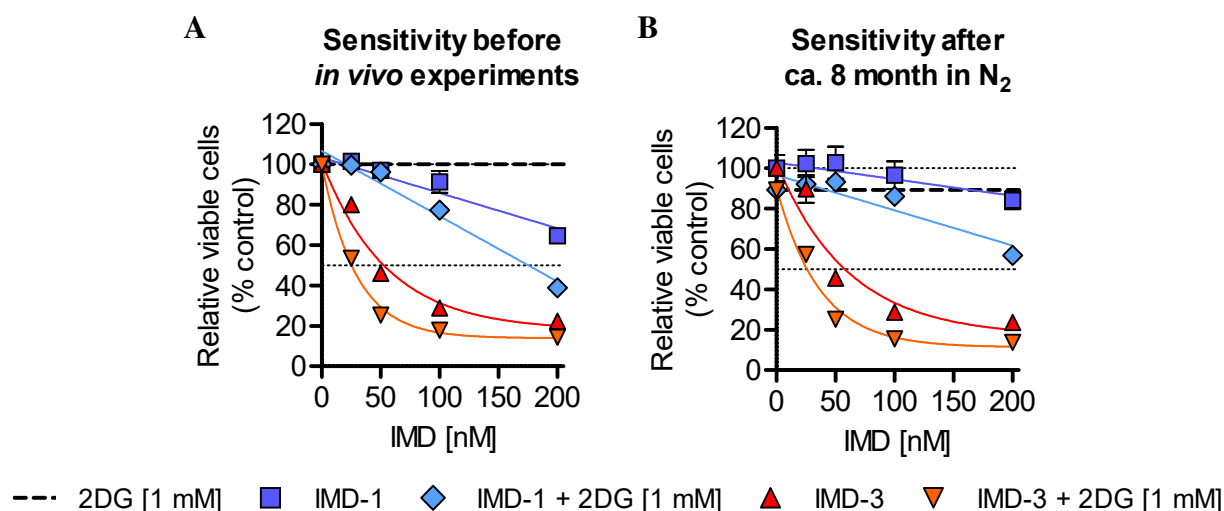


Figure 53: Influence of long-term liquid nitrogen storage on synthetic flavagline efficacy in HCT116 cells. For all experiments, cells were seeded in supplemented cell culture medium (4.5 g/l glucose, 10 % FBS, 1 % P/S). 10 x treatment stocks were diluted into the wells. (A) Sensitivity of HCT116 cells before cryopreservation for later xenograft injection performed before the start of the *in vivo* experiments. (B) Sensitivity of HCT116 cells (same batch as (A)) used for xenograft injection performed after storage for ca. 8 months in liquid nitrogen. Treatment: 48 h. Multiplicity-adjusted p-values are listed in table ES21.

Another possible reason behind the discordance between *in vitro* and *in vivo* efficacy of IMD-3 could be differences in the treatment application. Therefore, the application schemes applied for *in vivo* and *in vitro* experiments were carefully compared. This analysis revealed a difference in the treatment preparation: Whereas the treatment dilution for *in vitro* experiments was performed in supplemented cell culture medium containing 4.5 g/l glucose, 10 % FBS, and 1 % P/S (supplemented medium), treatment preparation for *in vivo* application was performed in water and DMSO in a ratio of 10:1, as previously agreed upon with the supplier of IMD substances (Fig. 54).

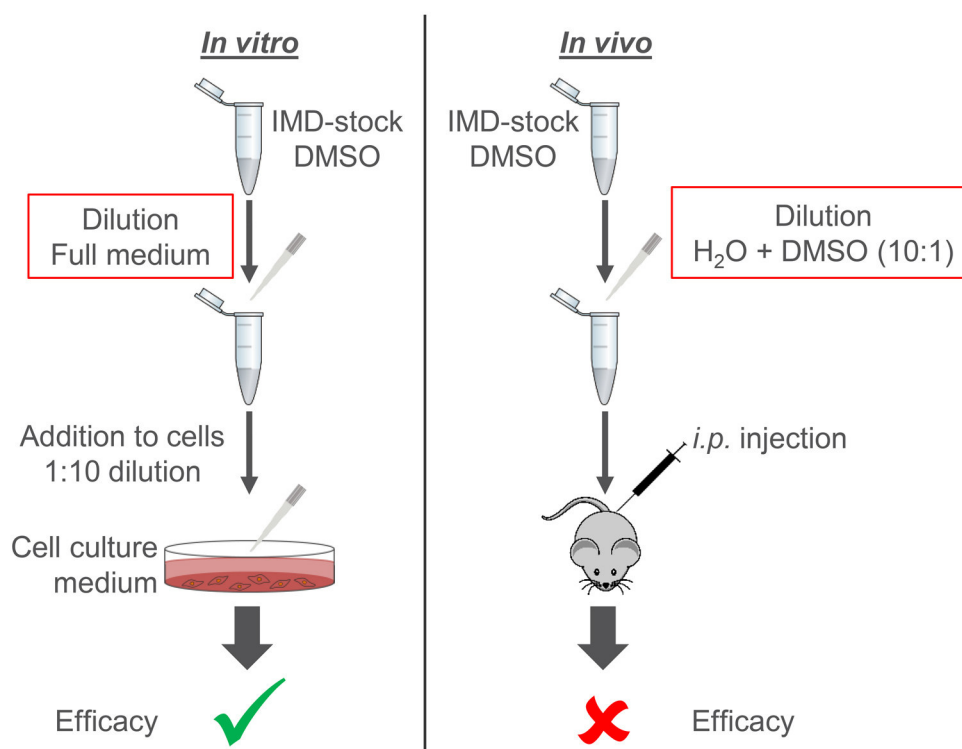


Figure 54: Schematic description of the difference in treatment preparation for *in vitro* and *in vivo* experiments. While IMD-3 application *in vitro* showed great efficacy, application *in vivo* did not show any significant effect.

Due to the great difference between the supplemented medium preparation applied *in vitro* and the water-DMSO mixture *in vivo*, the influence of the treatment preparation was first investigated by preparing IMD dilutions in cell culture medium lacking glucose, FBS and P/S (deprived medium) narrowing down the differences to three components. Strikingly, a significant decrease in treatment efficacy for all applied IMD-3 concentrations was observed in HCT116 cells (Fig. 55B) compared to the preparation in supplemented cell culture medium (Fig. 55A). The decreased efficacy was particularly pronounced at lower IMD-3 concentrations (25, 50, 100 nM, $p \leq 9.610 \cdot 10^{-8}$).

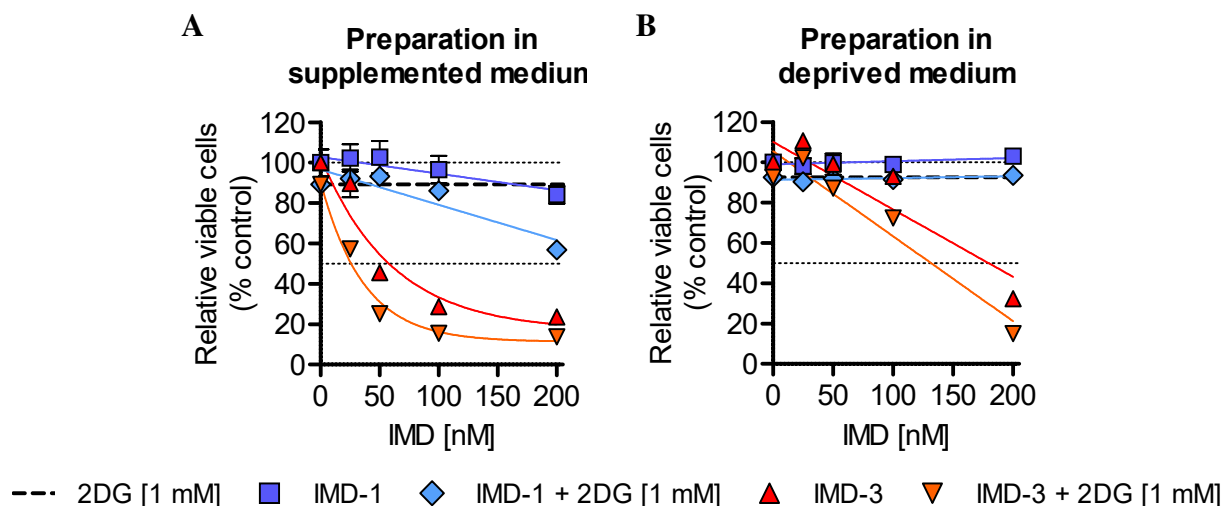


Figure 55: Influence of medium composition during treatment preparation on synthetic flavagline efficacy in HCT116 cells. For all experiments, cells were seeded in supplemented cell culture medium (4.5 g/l glucose, 10 % FBS, 1 % P/S). 10 x treatment stocks were diluted into the wells. (A) Sensitivity of HCT116 cells towards treatment prepared in supplemented cell culture medium (4.5 g/l glucose, 10 % FBS, 1 % P/S). Same graph as Fig. 53B. (B) Decreased sensitivity of HCT116 cells (the same cells as used in (B)) towards treatment prepared in deprived cell culture medium (no glucose, FBS, P/S). Treatment: 48 h. Multiplicity-adjusted p-values are listed in table ES21.

To determine whether the decreased efficacy was caused by the lack of glucose, FBS or P/S, deprived cell culture medium was supplemented separately with the different components and used for treatment preparation. Strikingly, at a concentration of 100 nM IMD-3 all treatment preparations containing 10 % FBS significantly reduced the cell viability to ca. 25 % ($p \leq 1.090 \cdot 10^{-13}$), while preparations without FBS did not influence cell viability (Fig. 56A). At a concentration of 500 nM, the IMD-3 preparation lacking FBS reduced the viability of HCT116 cells to 73.6 % compared to vehicle-treated controls ($p = 2.017 \cdot 10^{-6}$), while the preparation in supplemented medium (10 % FBS) reduced the cell viability to 14.2 % ($p = 1.680 \cdot 10^{-11}$). Although, influence of lacking FBS had a less pronounced effect at 500 nM than at 100 nM IMD-3, the preparation containing FBS was nevertheless significantly more effective than the preparation without FBS ($p = 1.078 \cdot 10^{-8}$). Similar results were obtained when using water for drug solution preparation, as performed for *in vivo* experiments (Fig. 56B). Upon addition of 10 % FBS, cell viability was reduced from 100.1 % to 32.6 % ($p = 1.900 \cdot 10^{-14}$) in cells treated with 100 nM IMD-3.

Presence of FBS influenced the drug efficacy in a manner dependent on the dose of FBS and of IMD-3 (Fig. 57A). Efficacy of 100 nM IMD-3 increased with increasing FBS concentrations, whereas efficacy of 500 nM IMD-3 was not substantially influenced at FBS concentrations in the solution above 10 %.

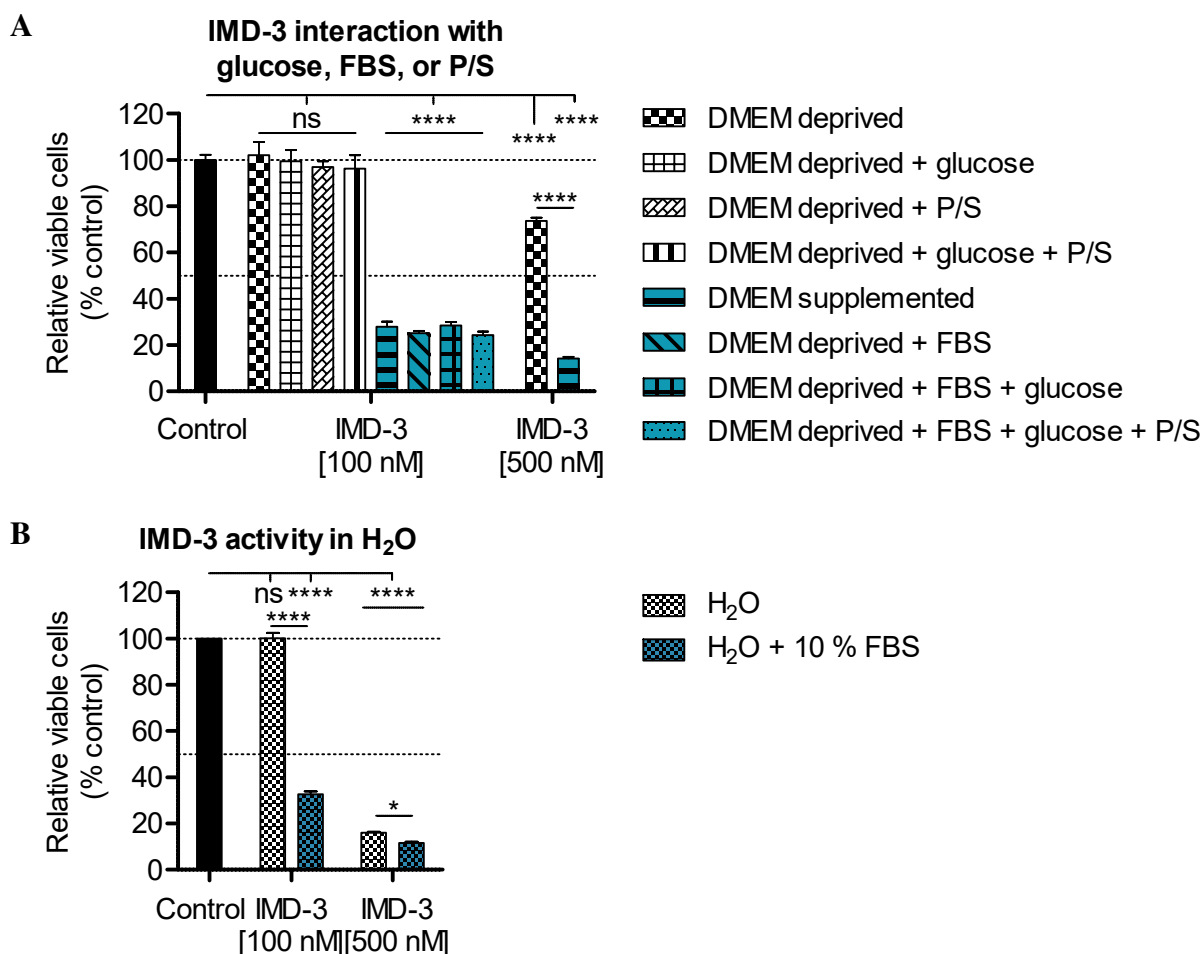


Figure 56: Presence of FBS during IMD-3 treatment preparation is essential for the efficacy in HCT116 cells. For all experiments, cells were seeded in supplemented cell culture medium (4.5 g/l glucose, 10 % FBS, 1 % P/S). The treatment preparations containing the indicated supplements were added by diluting 10 x treatment stocks into the wells. (A) Presence of FBS in the treatment preparation increases the efficacy of IMD-3. (B) FBS addition to H₂O *ad injectabilia* enhances the efficacy of IMD-3. Treatment: 48 h. Multiplicity-adjusted p-values are listed in table ES22.

The most abundant component of FBS is albumin, which has been previously reported to interact with different drugs [306]. Therefore, its influence on IMD-3 efficacy was examined using the concentration range of albumin in FBS as provided by the supplier. The influence of different concentrations of bovine serum albumin (BSA) and human serum albumin (HSA) on IMD-3 efficacy were examined, with 3 mg/ml corresponded to the maximum albumin concentration in the medium, 5 mg/ml to the maximum total protein concentration and 10 mg/ml to the total protein in medium containing 20 % FBS.

Increasing the BSA and HSA concentration from 3 mg/ml to 10 mg/ml significantly improved the efficacy of IMD-3, further reducing the cell viability to 13.6 % ($p=0.0023$) for BSA and 11.0 % ($p=2.110 \cdot 10^{-6}$) for HSA (Fig. 57B). No significant difference between BSA or HSA preparations containing the same concentrations was observed. Increasing the HSA concentration above 10 mg/ml did not further enhance IMD-3 efficacy (Fig. 57C).

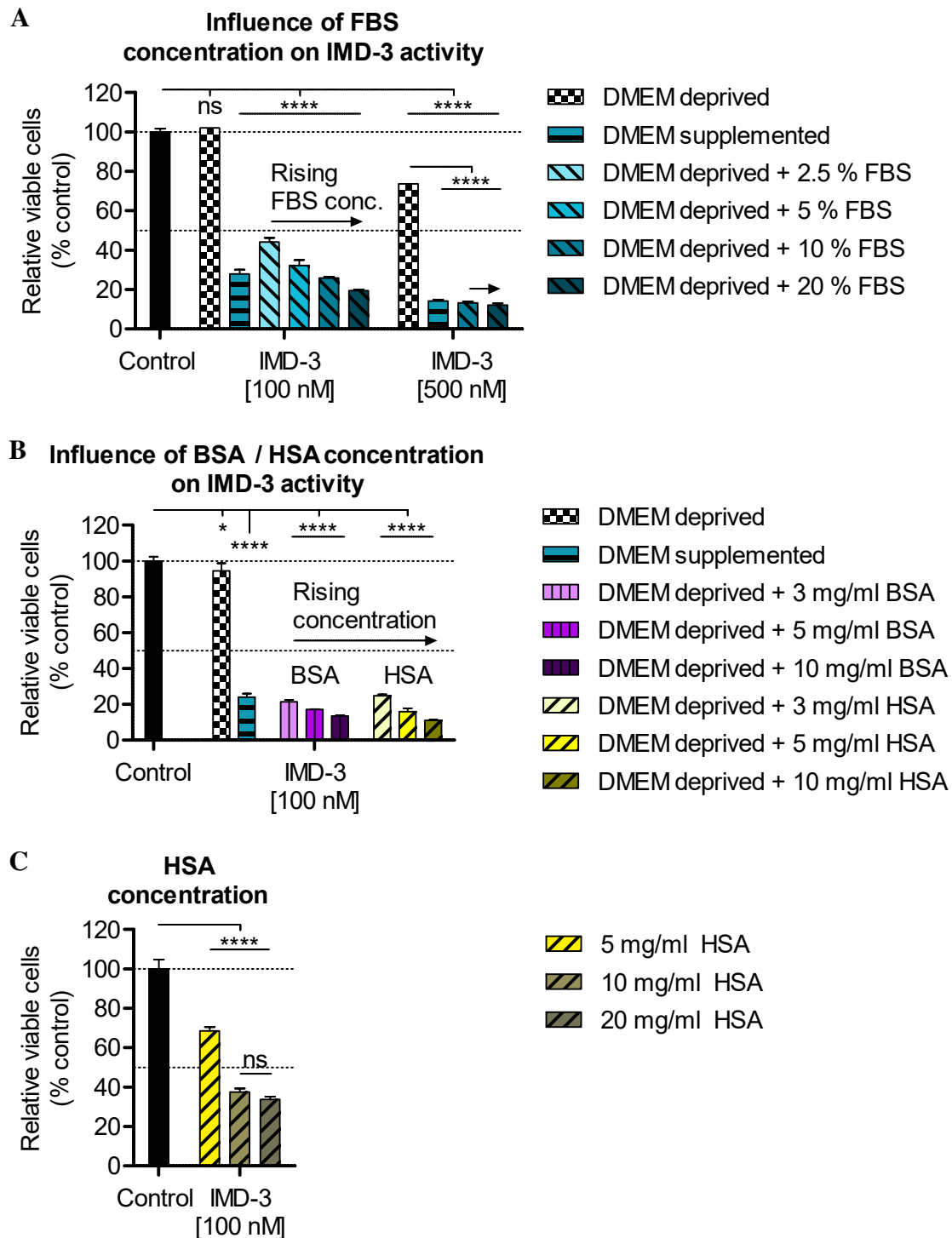


Figure 57: Increasing FBS and albumin concentration enhance the efficacy of IMD-3 treatment in HCT116 cells. For all experiments, cells were seeded in supplemented cell culture medium (4.5 g/l glucose, 10 % FBS, 1 % P/S). The treatment preparations containing the indicated supplements were added by diluting 10 x treatment stocks into the wells. (A) The efficacy of IMD-3 rises with increasing FBS concentrations (2.5, 5, 10, 20 %). (B) BSA and HSA enhance the efficacy of IMD-3 similar to FBS. 3 mg/ml represents the maximum amount of albumin present in medium containing 10 % FBS, whereas 5 mg/ml represent the maximum amount of total protein. (C) HSA concentrations higher than 10 mg/ml in the treatment preparation did not increase the efficacy of IMD-3. The same HSA solution, which was later applied in *in vivo* experiments was used. Treatment: 48 h. Multiplicity-adjusted p-values are listed in table ES23.

Improved efficacy of IMD-3 in the presence of FBS or albumin might be caused by the stabilisation of IMD-3 or due to increased solubility of IMD-3 in aqueous solution. The stability of IMD-3 in aqueous solution was assessed by measuring its absorption at approximately 280 nm, caused by its aromatic ring structure. No change in the absorption spectrum of IMD-3 was detected after 120 min (Fig. 58A, S12). The time frame was chosen to represent twice the time required for treatment preparation and injection in xenograft experiments.

The influence of FBS on IMD-3 solubility was analysed by comparing efficacy of IMD-3 in FBS-containing solution with its efficacy in DMSO-containing solution. All three IMD-3 preparations containing either FBS, DMSO or both were significantly more effective ($p \leq 0.0129$) compared to the preparation without FBS and negligible DMSO concentration (< 0.0004 % per well) (Fig. 58B).

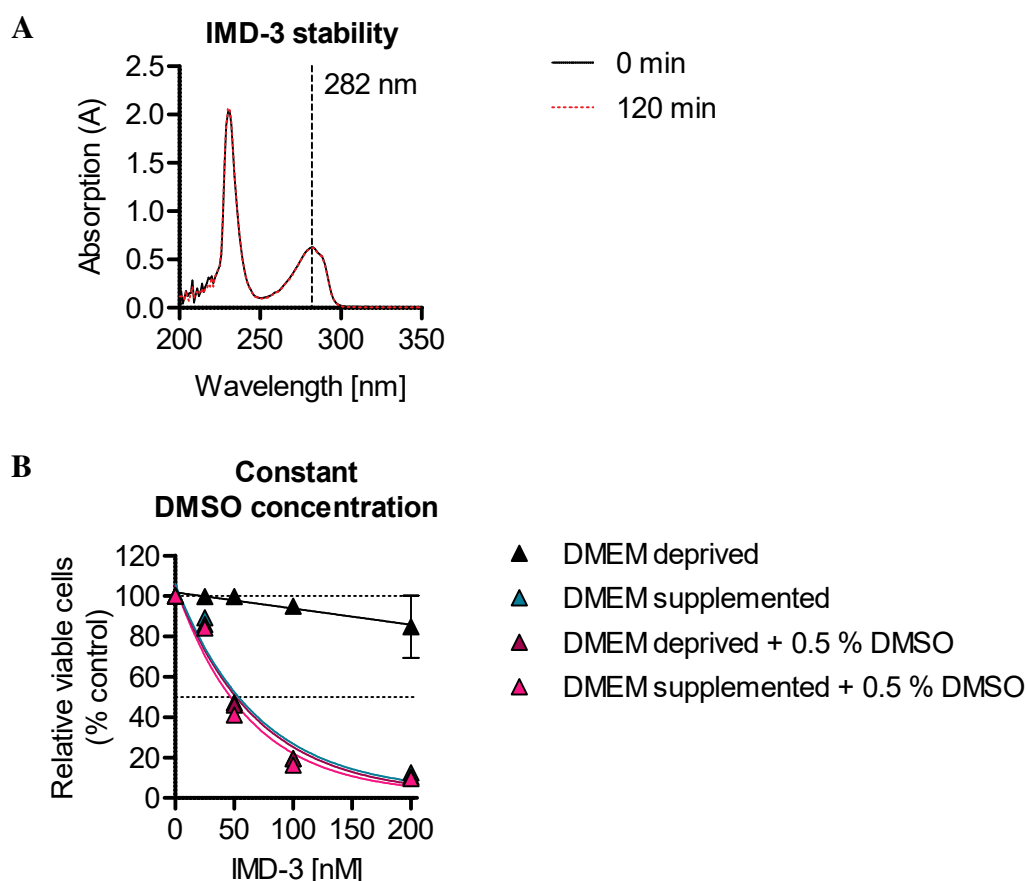


Figure 58: Stability of IMD-3 in aqueous solution and influence of DMSO concentration on the efficacy in HCT116 cells. (A) Stability of IMD-3 (100 μ M) solubilised in aqueous solution was determined by measuring its absorption directly after preparation (0 min) and after 120 min at room temperature. The band at 282 nm can be attributed to IMD-3 due to its aromatic absorption, whereas the band at 230 nm can be attributed to DMSO present in the solution. (B) Responsiveness of HCT116 cells to IMD-3 (48 h) if the DMSO concentration (0.5 % per well) is kept constant compared to an IMD-3 preparation in medium containing 10 % FBS (DMEM supplemented) or lacking FBS (DMEM deprived). Multiplicity-adjusted p-values are listed in table ES24.

4.3.2.1 *In vivo* application of IMD-3 solubilised in HSA shows no anti-tumour effect

To investigate the influence of HSA addition on the efficacy of IMD-3 *in vivo*, the concentration of HSA in the treatment solution (10 mg/ml) was determined taking into account the protein concentration in the peritoneal fluid of mice (20 - 25 mg/ml [307, 308]) and the HSA concentration after which no further improvement of IMD-3 efficacy could be detected (Fig. 57C).

Xenograft-bearing mice received treatment with 1.0 mg/kg IMD-3 or 100 mg/kg 2DG alone and in combination (6 mice/group) applying the same treatment schedule as in the previous experiments to ensure comparability. However, in contrast to the *in vitro* results, preparation of IMD-3 in HSA-containing solution did not improve the efficacy of IMD-3 *in vivo* and no reduction in tumour growth or extended survival was observed (Fig. 59, Tab. 28). Also, in contrast to reduced GLUT-1 expression observed upon IMD-3 treatment *in vitro* (see 4.1.4), IMD-3 did not influence the expression of GLUT-1 in the tumours significantly (Fig. 60).

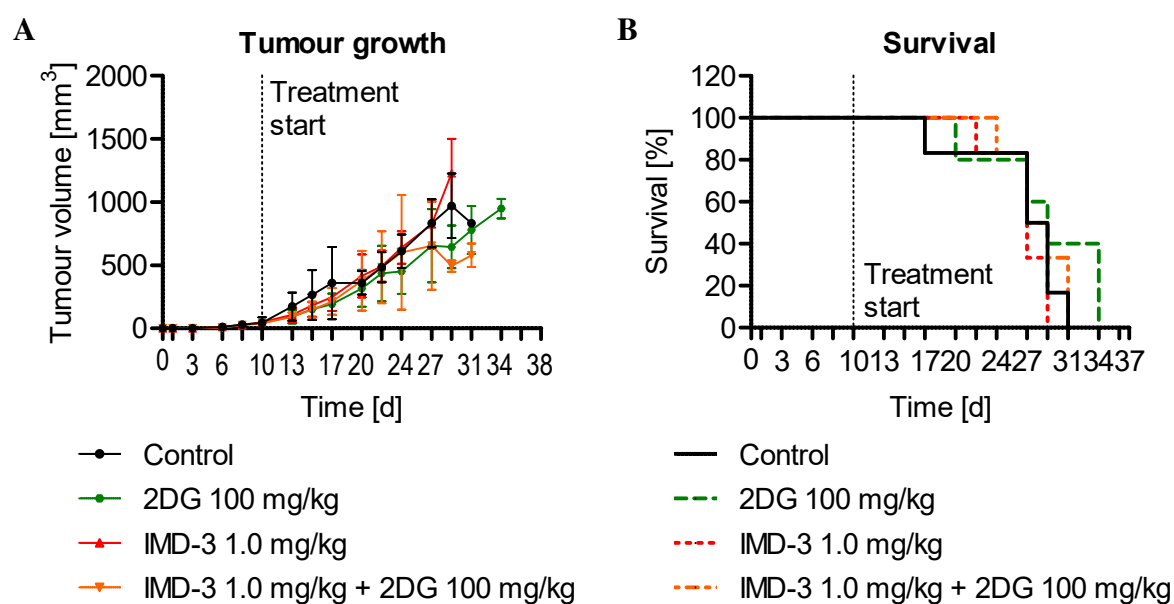


Figure 59: Tumour growth (A) and survival (B) of xenograft-bearing mice treated with IMD-3 1.0 mg/kg alone and in combination with 2DG 100 mg/kg solubilised in 10 mg/ml HSA solution. Mice received up to 12 *i.p.* injections (6 mice/group) starting at day 10 after tumour injection and were monitored until a termination criterion was reached. One mouse perished one day before tumour injection; thus, it was not possible to replace it on such a short notice and only 5 mice were incorporated in the 2DG treatment group. Individual tumour growth curves are shown in Fig. S13.

Table 28: Mean and median survival of mice treated with 1.0 mg/kg IMD-3 alone and in combination with 100 mg/kg 2DG solubilised in 10 mg/ml HSA solution. Mice received up to 12 *i.p.* injections (6 mice/group) starting at day 10 after tumour injection and were monitored until a termination criterion was reached. P-values for survival curves are shown in table ES25.

Treatment group	Mean survival [days]	Median survival [days]	Mice/ Group
Control	26.7	28.0	6
2DG 100 mg/kg	29.2	29.0	5
IMD-3 1.0 mg/kg	26.5	27.0	6
IMD-3 1.0 mg/kg + 2DG 100 mg/kg	28.2	28.0	6

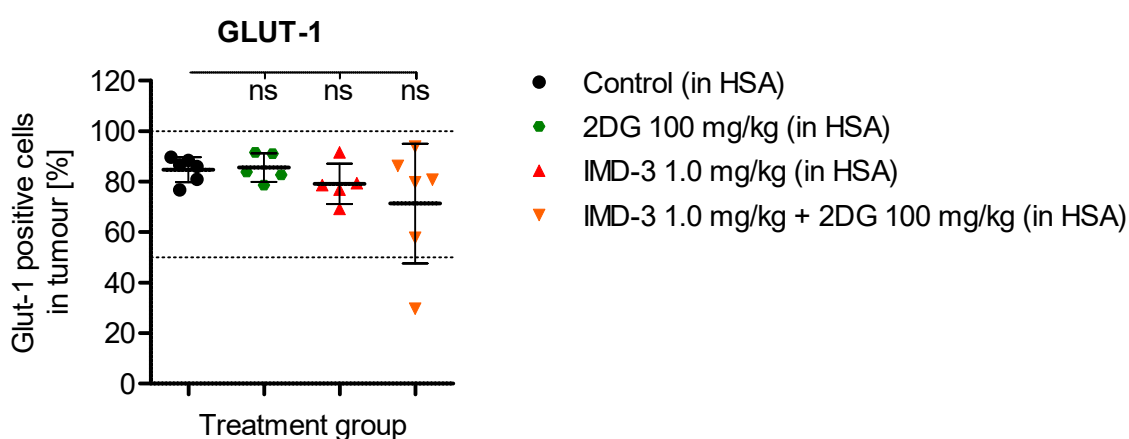


Figure 60: Expression of glucose transporter GLUT-1 in HCT116 xenograft tumours after treatment with 1.0 mg/kg IMD-3 and 100 mg/kg 2DG solubilised in HSA solution. Each treatment group consisted of 6 mice except the 2DG-treated group which comprised 5 mice. The staining of one tumour from the 1.0 mg/kg IMD-3-treated group could not be analysed. Mean \pm SD values are indicated. Analysis of tumour staining was performed using the QuPath software. Stainings and QuPath analysis were performed by Javier Ignacio Arriaza Gonzalez as part of his medical doctor thesis. Multiplicity-adjusted p-values are listed in table ES18.

4.3.2.2 Mass spectrometry analysis reveals presence of IMD-3 in xenograft tumours

To evaluate if IMD-3 reached the xenograft tumour cells upon *i.p.* application, IMD-3 was detected in tumour lysates using high-resolution electrospray ionisation mass spectrometry (HR-ESI-MS).

To assess the suitability of the method to detect IMD-3, IMD-3 was analysed as a single substance and in cell lysates obtained from *in vitro* culture. To facilitate the formation of $[M + H]^+$ species to detect IMD-3 ($C_{26}H_{26}ClNO_4$), small amounts of TFA were added. Using ESI-MS, a mass-to-charge (m/z) ratio of 452.1625 was obtained, which could be attributed to IMD-3 in a pure 10^{-7} M (= 100 nM) solution (calculated m/z value: 452.1623) (Fig. 61A). Furthermore, IMD-3 + H^+ could be detected at a m/z value of 452.1624 in cell lysate of HCT116 cells previously treated with 100 nM IMD-3 for 48 h (Fig. 61B).

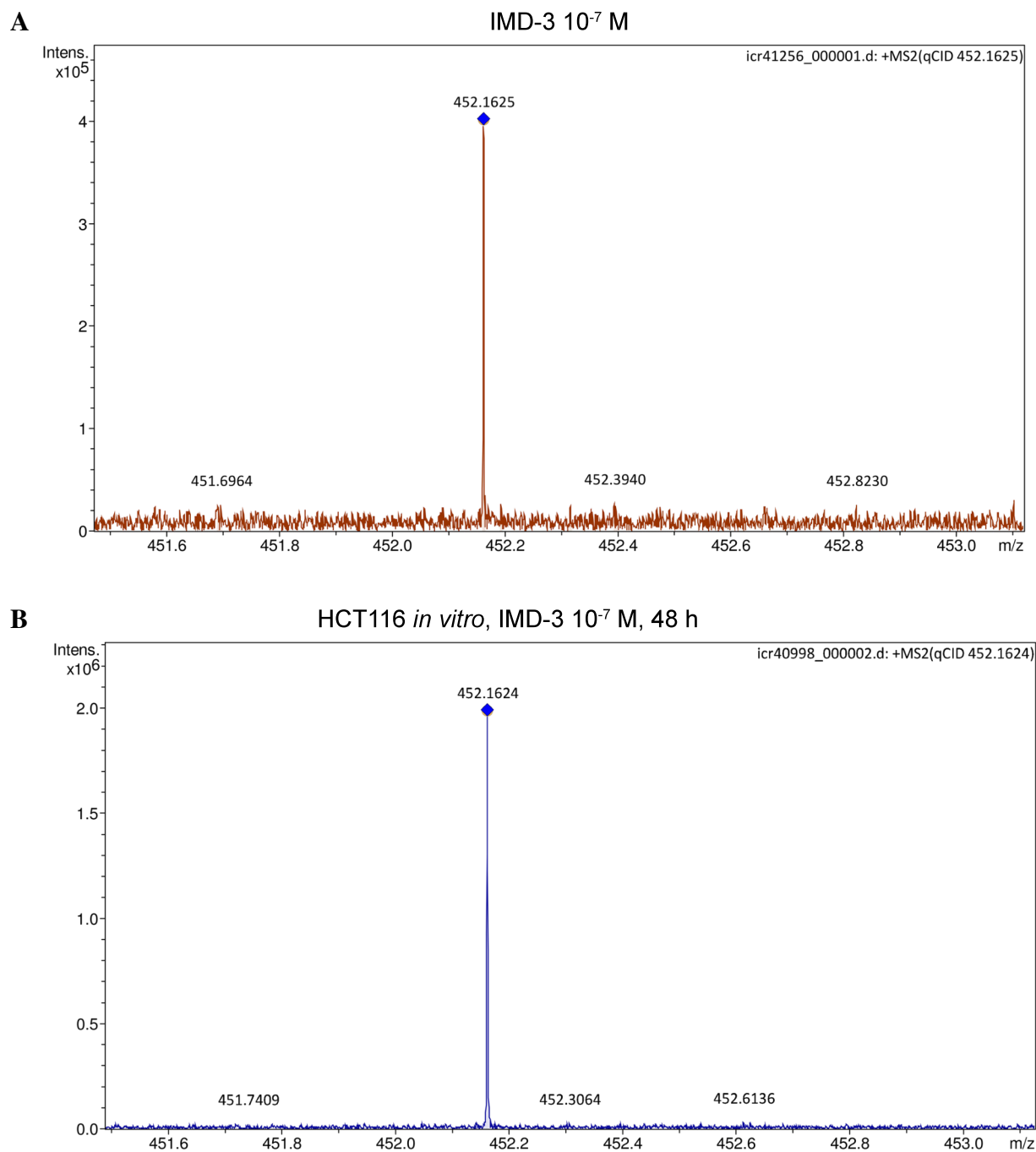


Figure 61: Detection of IMD-3 upon ESI-MS measurement of the single substance (A) and lysate of IMD-3-treated HCT116 cells (B). IMD-3 + H⁺ exhibits a theoretical m/z value of 452.1623. (A) IMD-3 (10^{-7} M) in acetonitrile with 0.01 % TFA was detected with a m/z value of 452.1625. (B) HCT116 cells treated for 48 h with 100 nM IMD-3 (10^{-7} M) were lysed in acetonitrile with 0.01 % TFA and IMD-3 was detected with a m/z value of 452.1624 (marked peak).

Next, tumour lysates from mice receiving treatment with vehicle or with 1.0 mg/kg IMD-3 either solubilised in water (n=3) (see 4.3.1.2) or in 10 mg/ml HSA (n=3) (see 4.3.2.1) were analysed with ESI-MS. IMD-3 was not detected in both vehicle-treated control mice (Tab. 29, Fig. 62A, S14A). In contrast, five out of six tumour lysates from IMD-3-treated mice (4-12 injections) showed presence of IMD-3 + H⁺ with m/z values from 452.1624 to 452.1626 with a maximum deviation of 0.0003 from the theoretical m/z value (Tab. 29, Fig. 62B, S14, S15). IMD-3 was not detected in one xenograft tumour of an IMD-3-treated mouse, which had remained 7 days in the experiment after the last (12th) IMD-3 application (Tab. 29, Fig. S14D). In contrast all other IMD-3-treated mice had been sacrificed maximum three days after the last IMD-3 injection (Tab. 29).

The used methodology did not allow quantitative analysis of IMD-3 in tumour tissue, but qualitative analysis revealed presence of IMD-3 in the tumour lysates of treated mice.

Table 29: ESI-MS measurement results to detect IMD-3 in tumours from xenograft-bearing mice treated with IMD-3 1.0 mg/kg with and without addition of HSA. IMD-3 + H⁺ exhibits a theoretical m/z value of 452.1623. Mice received treatment solubilised in water (top) or in HSA solution (bottom). IMD-3 + H⁺ was not detected in vehicle-treated mice, but in all IMD-3-treated mice expect for one mouse which had remained another 7 days in the experiment after the last treatment injection. All ESI-MS measurements are shown in Fig. S14, S15.

Treatment group	HSA addition	Total injections	Days since last injection	IMD-3 + H ⁺ measured m/z
Control	-	(8)	2	not found
IMD-3 1.0 mg/kg	-	5	2	452.1625
IMD-3 1.0 mg/kg	-	11	2	452.1625
IMD-3 1.0 mg/kg	-	12	7	not found
Control	+	(7)	2	not found
IMD-3 1.0 mg/kg	+	4	3	452.1626
IMD-3 1.0 mg/kg + 2DG 100 mg/kg	+	6	2	452.1626
IMD-3 1.0 mg/kg	+	8	2	452.1624

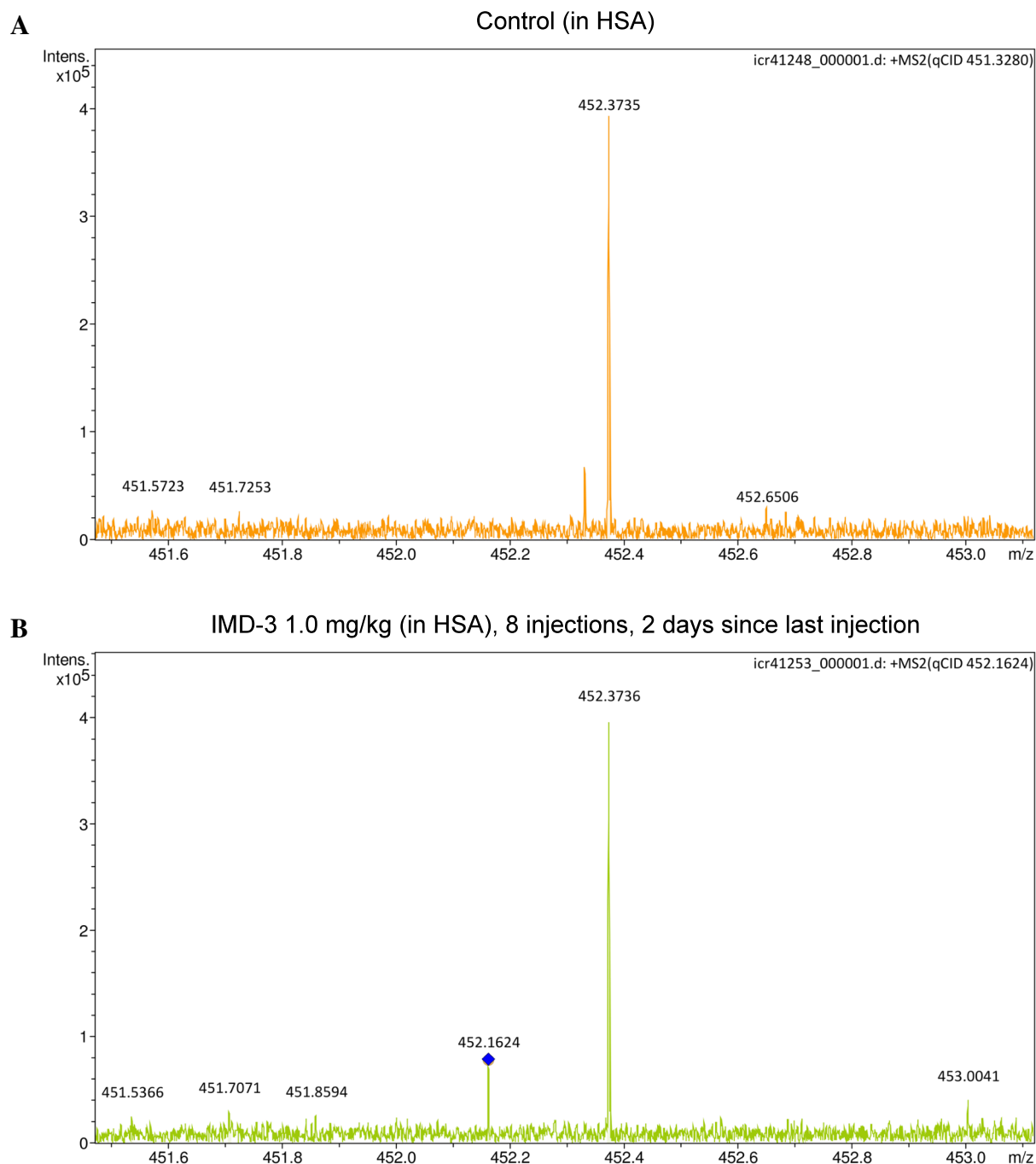


Figure 62: Exemplary images of ESI-MS measurements of lysed xenograft tumours to detect IMD-3. IMD-3 ($C_{26}H_{26}ClNO_4$) + H^+ exhibits a theoretical m/z value of 452.1623. Tumour lysates in acetonitrile with 0.01 % TFA were subjected to ESI-MS measurement. (A) Tumour from vehicle-treated mouse received 7 *i.p.* injections with HSA solution. IMD-3 was not detected. (B) Tumour from IMD-3-treated mouse receiving 8 *i.p.* injections with 1.0 mg/kg IMD-3 solubilised in HSA solution. IMD-3 was detected with a m/z value of 452.1624 (marked peak), the other m/z values could not be matched. ESI-MS measurements of all other analysed xenograft tumours are shown in Fig. S14, S15.

5 Discussion

Severe side effects and treatment resistance are major obstacles in cancer therapy, highlighting the emerging need for novel therapeutic approaches specifically targeting cancer cells and circumventing therapy resistance. Although each tumour is unique in its developmental process [3], abnormal growth and survival require common traits shared across cancers. These common cancer hallmarks display promising targets for novel therapeutic approaches.

Reprogramming of cancer cell metabolism is a common cancer hallmark [8] and includes reprogramming of glucose metabolism, leading to increased glucose uptake in cancer cells, due to the ‘Warburg effect’ [79–81]. Although several preclinical studies have shown the anti-tumour activity of the glucose anti-metabolite 2DG through inhibition of glycolysis [104,111–115] and its sensitising effect on chemo- and radiotherapy [118–125], 2DG has shown limited efficacy in clinical application [31,32]. Flavaglines, secondary plant metabolites, were shown to have pronounced anti-cancer activity throughout different cancer entities [139,145,291] particularly in combination with 2DG [287,309]. However, the preclinical and clinical evaluation of the flavagline-2DG combination was hampered by the complicated extraction process of natural flavaglines, yielding low amounts of active compound [138,139]. Successful chemical synthesis of flavagline derivatives could recently solve the substance availability issue and provided the unique opportunity to perform first steps towards clinical translation of flavaglines as anti-cancer therapeutics.

The present thesis aimed to investigate the mechanisms underlying the anti-cancer activity of two novel synthetic flavagline derivatives and examine their influence on cellular glucose metabolism. Based on previous experiments showing promising effects of the combination of natural flavaglines with 2DG [309] and the correlation between HIF-1 signalling and altered glucose metabolism [92,99–102], the influence of 2DG on the efficacy of both synthetic flavagline derivatives was investigated. Furthermore, potential resistance mechanisms towards treatment with synthetic flavaglines were investigated by assessing the differences between a newly generated flavagline-resistant haploid cell line and the WT flavagline-sensitive cell line. First *in vivo* evaluation of synthetic flavaglines in combination with 2DG was performed in a xenograft model to find optimal treatment dosages, assess the treatment efficacy and influence on glucose uptake of xenograft tumour cells and analyse potential side effects (Fig. 63).

5.1 *In vitro* characterisation of synthetic flavaglines

First, the treatment efficacy of both synthetic flavagline derivatives, IMD-1 and IMD-3, was assessed in a broad spectrum of 35 cancer cell lines from different tissues, including colorectal, breast, brain, lung, pancreas, prostate and HPV-related cancers. Overall, a dose dependent growth-inhibitory effect of synthetic flavaglines was detected, which increased from 25 to 100 nM IMD-1 and IMD-3 concentrations in most cell lines. As a consequence, 100 nM was chosen as the working concentration for *in vitro* experiments in 2D cell culture.

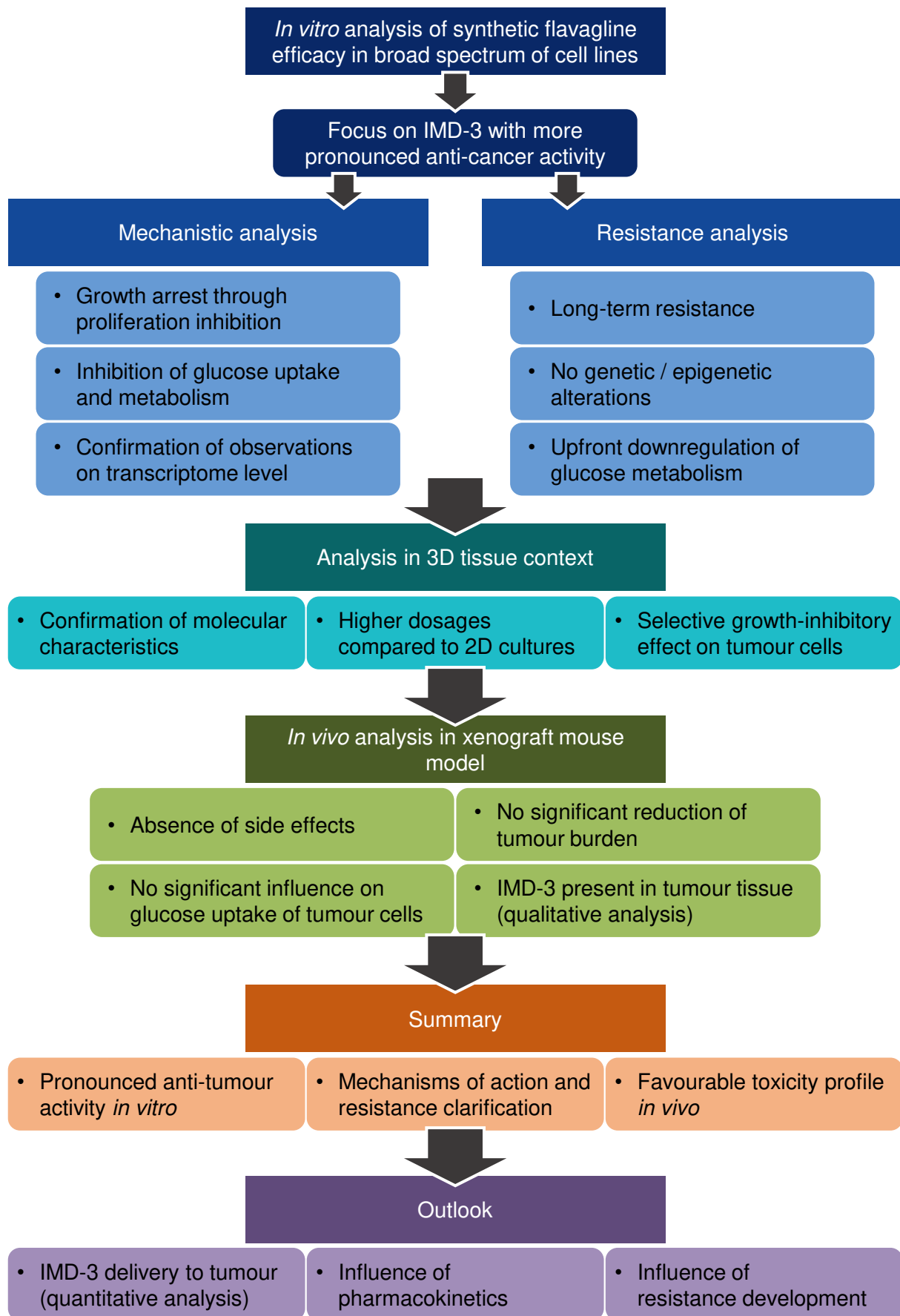


Figure 63: Path to clinical translation of synthetic flavaglines.

In all tested cell lines, IMD-3 exhibited a higher anti-tumour efficacy compared to IMD-1, leading to an average reduction of cell viability by approximately 50 %, while IMD-1 only caused a reduction of ca. 10 %. Although the exact reasons for the pronounced difference in the anti-proliferative efficacy of the two studied flavagline derivatives, consistently observed in all tested cell lines, were not analysed in further detail, the observed difference could be rooted in the chemical structures of the compounds: in contrast to IMD-3, IMD-1 exhibits a pyrrolidine ring, which points at the possible essentiality of the methylamino group of IMD-3 for the anti-proliferative effect.

Previous work of the Department pointed at a strong potential of a combinational treatment approach with flavaglines and 2DG to achieve more pronounced anti-tumour effects, while sparing normal tissue [309]. Therefore, the effect of the combination of synthetic flavaglines with 2DG was analysed. Indeed, synthetic flavaglines as well showed a more pronounced anti-tumour effect when combined with 2DG. 2DG enhanced the average growth-inhibitory effect of both synthetic flavaglines by approximately 20 %, although the impact of 2DG strongly depended on the tested cell line. Overall, the extent of growth inhibition upon synthetic flavagline treatment alone and in combination with 2DG varied between the examined cell lines and no specific cancer entity showed an outstanding sensitivity of all related cell lines tested towards synthetic flavagline treatment.

5.1.1 Molecular phenotype and sensitivity towards synthetic flavagline treatment

As no specific tumour entity could be identified with particular high sensitivity towards synthetic flavagline treatment, further analysis focused on the dissection between molecular phenotypes examining the influence of MSI, HPV status and IDH mutation status.

First, the influence of MSS and MSI on the treatment efficacy of synthetic flavaglines in CRC cell lines was examined. In contrast to Santagata *et al.* reporting higher sensitivity of MSS cell lines towards the synthetic flavagline RHT, MSI CRC cell lines were found to have a slightly enhanced sensitivity towards treatment with IMD-3 compared to MSS cell lines. One MSI cell line HCT15 did not respond to IMD-3 treatment and showed less sensitivity compared to the three tested MSS cell lines. However, upon combination of IMD-3 with 2DG, sensitivity of HCT15 cells increased significantly, resulting in it being more sensitive towards IMD-3 and 2DG treatment than two out of three MSS cell lines. Moreover, among the MSI cell lines, the *MLH1*-deficient cell lines HCT116 [310] and KM12 [311] were significantly more sensitive towards IMD-3 compared to the *MSH2/MSH6*-deficient cell lines DLD-1 and HCT15 [310, 312]. Thus, it seems that MSI cell lines have enhanced sensitivity towards IMD-3 treatment.

Previously differential sensitivity of MSI and MSS tumours towards various chemotherapeutic substances has been demonstrated [185, 202–204], pointing at the possible role of the MMR functionality for the responsiveness towards therapy. Therefore, the influence of MMR system functionality on the sensitivity towards IMD substances was analysed using *MLH1* knock-

out in a haploid cell line. However, due to the extremely high sensitivity of the WT cell line (approx. 90 %), no further effect improvement could be detected upon *MLH1* knockout. Thus, no clear causal relationship between treatment sensitivity and MMR system function could be determined.

The overall higher sensitivity of MSI CRC cell lines towards IMD-3 compared to MSS cell lines might be related to IMD-3-mediated inhibition of GSH pathways and presumed increase of ROS, observed upon pathway analysis of the transcriptome data. Cell lines carrying the MSI phenotype might be more sensitive towards ROS-induced DNA damage [313] due to their deficient MMR system. Furthermore, the MSI phenotype was found to correlate with increased FDG uptake in PET/CT imaging in gastric cancer patients [314], which might render MSI cell lines more susceptible towards IMD-3-mediated inhibition of glucose metabolism. MSI cell lines were also shown to exhibit a higher sensitivity towards inhibition of the PI3K/AKT/mTOR pathway [315], a major regulator of aerobic glycolysis [77], indicating their higher dependence on aerobic glycolysis compared to MSS cancer cell lines.

Other molecular phenotypes, such as IDH mutation or HPV status, did not influence the efficacy of synthetic flavaglines and treatment responses varied between cell lines. Thus, synthetic flavaglines seem to be applicable in a variety of cancer entities and higher sensitivity of MSI cancers towards IMD-3 could be exploited in novel treatment approaches. For instance, varying response of MSI cancer patients towards ICB due to treatment resistances [316] could be addressed exploiting the high sensitivity of MSI cancer cell lines towards synthetic flavaglines.

5.1.2 Inhibition of proliferation and glucose metabolism by synthetic flavagline derivatives

Cancer therapy aims to hamper disease progression and induce cancer remission through inhibition of cancer cell proliferation and cell death induction, which can be achieved through several mechanisms, including necrosis, apoptosis, cell cycle arrest and senescence. Overall cytotoxicity assessment of synthetic flavagline treatment showed that IMD-3 only caused cytotoxic cell death in 15 % of MSI CRC cells. This finding was supported by the observation that apoptosis induction plays only a minor role in IMD-3 activity, inducing apoptosis only in a small fraction of cancer cells in 2D and 3D culture models. IMD-1 and 2DG treatment did not induce apoptosis, correlating with their observed lower treatment efficacy and cytotoxicity. Several other flavagline derivatives were also found to mediate their anti-tumour effect through other mechanisms with apoptosis induction accounting only for a minor part of their efficacy [153].

As apoptosis induction and cytotoxicity of synthetic flavaglines alone did not explain their pronounced anti-cancer activity, proliferation of cancer cells was monitored. Significant proliferation inhibition was detected in CRC and HPV-transformed cancer cells upon IMD-3 treatment, while IMD-1 and 2DG did not exhibit an anti-proliferative effect. Inhibition of cell proliferation was not caused by senescence induction, but through IMD-3-mediated upregulation of

cell cycle checkpoints, G₁/S and G₂/M, as well as decreased chromosomal replication, which were detected through pathway analysis of transcriptome expression data. Similar molecular characteristics were shown to be involved in the anti-cancer activity of the natural flavagline RocA, which enhanced ROS [159], caused cell cycle arrest through DNA damage stress [160] and induced or sensitised cells towards apoptosis [156, 159, 317], pointing at the overlap in mechanisms of action of natural and synthetic flavaglines.

Next, the molecular mechanisms causing synthetic flavagline mediated proliferation inhibition and cell cycle arrest were investigated. Two previous studies have indicated the influence of two flavagline derivatives on glucose metabolism [165, 174] and both investigated synthetic flavaglines were previously found to inhibit HIF-1 signalling [175], an important regulator of altered glucose metabolism [92,99–102]. Due to the enhanced growth-inhibitory effect obtained by combination with 2DG and preliminary results obtained in CRC cell lines on the influence of synthetic flavaglines on glucose metabolism [287], it was investigated whether modulation of glucose metabolism displays a common characteristic of IMD substances.

It could be demonstrated that IMD-3 treatment caused downregulation of GLUT-1 protein levels, which is most abundant in cancer cells [92], in all investigated HPV-transformed cell lines, supporting previous findings in CRC cell lines [287]. Consequently, IMD-3 treatment was also found to hamper glucose uptake and lactate production. Thus, modulation of glucose metabolism can be considered a common characteristic of synthetic flavagline treatment, especially IMD-3. *In vitro* and *in vivo* experiments on lung cancer cells have linked GLUT-1 inhibition with deregulation of glycolysis, cell cycle arrest and inhibition of cell proliferation [318]. Thus, observed proliferation inhibition and cell cycle arrest might be the direct consequences of GLUT-1 downregulation through synthetic flavagline treatment.

Importantly, CRC cells did not compensate for glycolysis inhibition upon synthetic flavagline treatment by redirecting glucose metabolism towards the PPP but showed inhibited PPP activity upon IMD-3 treatment. Decreased PPP activity could be correlated with inhibited *de novo* synthesis of deoxyribonucleotides and increased oxidative stress detected on transcriptome level, as the PPP is responsible for pentose generation, which are required for nucleic acid synthesis, and maintenance of cellular redox capacity [78].

To determine which molecular changes are induced upon synthetic flavagline treatment and are commonly affected in different cancer cell lines, transcriptome analysis of IMD-3-treated CRC and HPV-transformed cells was performed. In each cell line several thousand genes were differentially expressed upon IMD-3 treatment. To obtain a better understanding of the cellular processes deregulated by synthetic flavagline treatment, pathway analysis was performed based on the significantly DEGs in IMD-3-treated cells. In addition to the above-mentioned upregulation of cellular checkpoints and inhibition of deoxyribonucleotide synthesis and chromosomal replication, pathway analysis revealed IMD-3-induced inhibition of GSH redox pathways

and activation of the oxidative stress response indicating increased cellular oxidative stress. Increased oxidative stress and NRF2-activation were found to induce cell cycle arrest predominantly in G2 phase, resulting in a senescence-like phenotype [304, 305]. This phenomenon could explain observed upregulation of senescence pathway detected upon pathway analysis of transcriptome data in all sensitive cell lines, although senescence was not detected by β -galactosidase staining. This also indicates that IMD-3 treatment may not reactivate expression of E2 protein, the master regulator of viral expression [214, 223], in HPV-transformed cell lines, which have been shown to undergo senescence upon re-activation of E2 [319]. GSH downregulation and increased oxidative stress are usually associated with enhanced cellular ROS [254] causing DNA damage [313]. This can be correlated to the observed inhibition of replication and induction of cell cycle arrest, which are caused by DNA damage [33]. The same pathways were also affected in the treatment-sensitive haploid WT HGC178 cell line, discussed later. This indicates that IMD-3 treatment affects similar pathways in all analysed treatment sensitive cell lines.

Previous observations by Santagata *et al.* have linked inhibition of HSF1-dependent transcription by the synthetic flavagline RHT with downregulation of glucose metabolism through TXNIP upregulation [174]. Enhanced transcription levels of TXNIP were found in five out of seven treatment-sensitive cell lines, comprising CRC and HPV-transformed cells as well as the haploid WT cell line HGC178, supporting the observation of decreased glucose uptake upon IMD-3 treatment *in vitro*. Similar to RHT [174], IMD-3 treatment did not influence HSF1 expression in all analysed cell lines. However, expression levels of the heat shock family members *HSPA8* and *HSPA1A*, HSF1 target genes, which were downregulated by RHT [174], were only decreased in HCT116 and CaSki cells, respectively. Thus, IMD-3 seems not to interact with HSF1 transcription and observed upregulation of *TXNIP* might be independent from HSF1 transcription inhibition, as discussed later.

IMD-3-induced downregulation of GLUT-1 was absent on transcriptome level, indicating post-transcriptional regulation of GLUT-1 expression upon IMD-3 treatment. Indeed, live monitoring of GLUT-1 in cancer cells showed GLUT-1 internalisation and lysosomal degradation upon glucose deprivation [320], displaying one possible mechanism for IMD-3-induced decrease of GLUT-1 on protein level. This is supported by IMD-3-induced downregulation of AKT kinase, which stabilises GLUT-1 in the plasma membrane [96, 321], and TXNIP upregulation, which was found to bind GLUT-1 and mediate its internalisation [322]. Additionally, downregulation of PI3K subunits as well as genes belonging to complex I and II of the ETC suggest disruption of glucose metabolism upon IMD-3 treatment. However, further investigations are required as increased *TXNIP* expression levels were not detected in HCT116 and IMD-3-sensitive WT HGC178 cells, which might indicate post-transcriptional or -translational modifications leading to increased TXNIP protein levels [323].

Interestingly, both tested CRC cell lines and two HPV-transformed cell lines were found to ex-

hibit increased glutaminase expression upon IMD-3 treatment, indicating increased glutaminolysis as a possible mechanism to overcome inhibition of glucose metabolism. Cisplatin-resistant tumours were previously found to switch from glucose to glutamine metabolism [324], although increased glutamine metabolism slowed cell growth [325]. Furthermore, another synthetic flavagline derivative has been shown to increase dependence of pancreatic cancer cells on glutaminolysis and combination with glutaminase inhibitors enhanced the observed anti-tumour activity [165]. Thus, IMD-3 treatment might cause a similar metabolic shift towards glutaminolysis and the sensitivity of cancer cells towards synthetic flavaglines might be enhanced upon combination with glutaminolysis inhibitors. Increased glutamine metabolism should also be considered as a possible resistance mechanism against synthetic flavagline treatment.

5.1.3 Molecular characteristics of synthetic flavagline derivatives in 3D culture models

Due to the limitations of 2D cultures with regard to cell-cell interactions and tumour microenvironment [302], the efficacy of IMD-3 was analysed in two 3D culture models. Assessment of drug efficacy in 3D models is essential as they are thought to improve *in vivo* transferability [326]. Due to their shape introducing a gradient of nutrient supply in different cell layers, spheroid structures are able to model *in vivo* tumour growth [326] and thus are suitable to assess the efficacy of synthetic flavagline treatment in a 3D context. Interestingly, the analysis of treatment efficacy in spheroids demonstrated that higher treatment dosages or extension of the treatment duration are required to obtain similar sensitivity towards IMD-3 treatment in spheroid culture compared to 2D culture. This knowledge was used in the following 3D culture and *in vivo* experiments.

To assess the toxicity of synthetic flavagline treatment on normal cells and evaluate the influence of tumour microenvironment and 3D characteristics, such as lower oxygen or nutrient supply in the tumour core [326], on treatment sensitivity, a 3D co-culture model was used. Embedded tumour cell clusters in dermal equivalents of keratinocytes were used to resemble the growth of tumours in normal skin structure. Similarly to spheroid cultures, IMD-3 efficiently inhibited cancer cell growth and proliferation of HPV-transformed tumour cell clusters at increased concentrations and a prolonged treatment period compared to 2D culture. Observed proliferation inhibition, apoptosis induction and GLUT-1 downregulation upon IMD-3 treatment was restricted to HPV-transformed tumour cells and almost absent in keratinocytes. High specificity of natural flavaglines for tumour cells and low toxicity in normal tissue was detected previously in several studies [145, 148, 149]. Experiments in the 3D co-culture model indicate similar selectivity of synthetic flavaglines for tumour cells. Furthermore, tumour cells possibly accumulate more IMD-3 compared to normal cells, as shown by low toxicity on normal cells in co-culture models and more pronounced effect on normal cells in 3D cultures without tumour cells. The low metabolic rate of keratinocytes [327] might render them less susceptible towards synthetic flavagline treatment compared to tumour cells, which usually exhibit enhanced glucose metabolism to enable fast growth and proliferation [82].

Detected separation of the basal keratinocyte layer from the underlying fibroblast scaffold in 3D cultures without tumour cells upon IMD-3 treatment indicates altered expression of adhesion molecules in the basal layer of the dermal equivalent. These alterations might cause possible side effects of IMD-3 treatment in clinical application. Further experiments will be required to determine which molecules were affected by IMD-3 treatment using immunofluorescence staining of cellular adhesion molecules expressed in keratinocytes.

Both used 3D culture models demonstrated the applicability of synthetic flavagline treatment in more complex tumour structures and encouraged their examination *in vivo*. However, all examined 3D model systems were based on readily available models with HPV-transformed cells and the establishment of 3D models using the CRC cell line HCT116 would have to be performed in future for more direct comparison. However, in first experiments towards establishing an HCT116-based 3D co-culture model, pronounced invasive and irregular growth of HCT116 cells in co-culture with keratinocytes was observed. This displays a known obstacle of 3D culture models, as not all cell lines are suitable for each model [326]. However, molecular characteristics of IMD-3 treatment observed in 2D culture, including proliferation inhibition, apoptosis induction and GLUT-1 downregulation, could be confirmed in 3D cultures models of HPV-transformed cells.

5.2 Assessment of resistance towards synthetic flavaglines

Initial and acquired treatment resistances display a major obstacle in cancer therapy [241]. Thus, the examination of possible resistance mechanisms parallel to drug development is essential to understand the molecular mechanisms of action and optimise treatment strategies. The successful generation of a long-term IMD-3-resistant cell line upon GT mutagenesis of a haploid cell line allowed the assessment of molecular mechanisms involved in synthetic flavagline activity and resistance comparing the IMD-3-resistant cell line HGC176 with the treatment-sensitive WT cell line HGC178. To characterise the IMD-3-resistant cell line, the molecular characteristics of synthetic flavagline treatment detected in CRC and HPV-transformed cells were investigated.

Previously observed strong proliferation inhibition by synthetic flavagline treatment was examined using ^3H -thymidine to monitor the short-term treatment effect after 48 h, while impedance measurement was used to perform live-monitoring of cell proliferation over 11 days in treatment-sensitive WT and resistant cells. Significant proliferation inhibition in WT cells upon IMD-3 treatment was already detected in the short-term experiment, while IMD-1 treatment had no effect. Proliferation of IMD-3-resistant cells was not altered upon synthetic flavagline treatment. In both cell lines, the combination of 2DG slightly improved the inhibitory effect of IMD-3 on proliferation, while 2DG itself did not show any anti-tumour effect. Both cell lines were highly

susceptible towards cisplatin treatment, which could be attributed to their haploid genotype, rendering them highly susceptible towards DNA damage.

Long-term proliferation monitoring using impedance measurement confirmed weak effect of IMD-3 on proliferation in the resistant cell line, while proliferation of WT cells was significantly inhibited. IMD-3 treatment reduced proliferation of WT almost to the level of cisplatin treatment. However, cessation of IMD-3 treatment after 48 h caused regrowth of WT cells over 10 days, which could be prohibited by re-application of IMD-3 after four days treatment interruption. No newly induced treatment resistance could be observed upon treatment interruption in WT cells. The different treatment schedules with continuous or interrupted treatment did not alter the sensitivity of IMD-3-resistant cells. Thus, IMD-3-resistant cells must have acquired alterations persisting over time, which circumvent IMD-3-mediated proliferation inhibition.

5.2.1 Altered glucose metabolism in IMD-3-resistant cells

As described above, synthetic flavagline treatment inhibited glucose metabolism in treatment-sensitive CRC and HPV-transformed cancer cells, therefore it was important to analyse whether glucose metabolism is influenced in IMD-3-resistant cells. IMD-3 treatment significantly inhibited glucose uptake in WT cells upon downregulation of GLUT-1 on protein level. In contrast, GLUT-1 protein expression was retained upon IMD-3 treatment in the resistant cell line. As a consequence, the resistant cell line was significantly less sensitive towards IMD-3-induced downregulation of glucose uptake compared to the sensitive WT cell line. As proliferation inhibition, cell cycle arrest and deregulated glycolysis can be attributed to GLUT-1 downregulation [318] and were detected in all examined treatment-sensitive cell lines, retention of GLUT-1 expression in the IMD-3-resistant cell line seems to be essential to circumvent molecular alterations induced by synthetic flavaglines.

Furthermore, PPP activity in the WT cell line was significantly inhibited upon synthetic flavagline treatment, while its activity was not hampered in the resistant cell line. In both cell lines, 2DG treatment significantly decreased PPP activity, which was not observed in both CRC cell lines. The pronounced effect of 2DG might be attributed to the higher glucose uptake velocity in WT and IMD-3-resistant cells of approximately 200 ng glucose per minute compared CRC cell lines, which only exhibited a velocity of approximately 80 ng glucose per minute at a medium glucose concentration of 1 g/l. Thus, WT and IMD-3-resistant cells incorporated more glucose as well as 2DG compared to CRC cell lines, which might explain the observed inhibitory effect of 2DG on the PPP activity.

Importantly, comparison of the PPP activity between untreated WT and resistant cells revealed an almost doubled PPP activity in the IMD-3-resistant cells line. Enhanced PPP activity was previously found to be associated with increased cellular redox capacity and drug resistance [253, 254]. Thus, increased PPP activity of IMD-3-resistant cells might counteract IMD-3-mediated inhibition of GSH pathways and enhancement of NRF2-mediated oxidative stress response observed in treatment-sensitive cell lines on transcriptome level.

Pathway analysis of transcriptional changes in the untreated IMD-3-resistant cell line compared to the sensitive WT cell line revealed significant inhibition of glycolysis, which was confirmed by the decreased sensitivity of resistant cells towards 2DG treatment. Furthermore, the second most downregulated gene identified by transcriptome analysis (7.7-fold) in IMD-3-resistant cells was the chaperone HSPA8, a binder of TXNIP protein [328]. *HSPA8* levels were previously found to decrease upon treatment with the synthetic flavagline RHT, accompanied by increasing *TXNIP* levels and inhibition of glucose metabolism [174]. However, IMD-3 treatment only decreased *HSPA8* transcript levels in sensitive HCT116 cells, indicating that IMD-3 efficacy is independent of *HSPA8* inhibition. Yet, *HSPA8* interaction with *TXNIP* might be important for IMD-3 resistance. Due to its chaperone characteristics, *HSPA8* binding of *TXNIP* [328] might be required for proper folding and *TXNIP* activity, although this interaction has not been sufficiently studied. One can speculate that decreased *HSPA8* levels, accompanied by slightly reduced *TXNIP* expression (1.7-fold), in untreated IMD-3-resistant cells might prevent *TXNIP* increase upon IMD-3 treatment, which was observed in the majority of treatment-sensitive cancer cell lines. Although IMD-3 treatment increased *HSPA8* expression levels in resistant cells by approximately 3-fold, this increase might not have been sufficient to counteract the up-front 7.7-fold downregulation in resistant cells and restore *HSPA8* levels to normal expression. Furthermore, the observed slightly decreased levels of *TXNIP* (1.7-fold) in IMD-3-treated resistant cells could explain the retained GLUT-1 protein expression, as *TXNIP* inhibits glucose uptake through binding and internalisation of GLUT-1 [322]. However, treatment sensitive HCT116 cells, exhibiting decreased *HSPA8* (4.2-fold) and unaltered *TXNIP* expression levels upon IMD-3 treatment, still showed pronounced downregulation of GLUT-1 protein expression [287]. Thus, *HSPA8* downregulation in resistant cells cannot be the major factor mediating acquired IMD-3 resistance but might contribute to decreased *TXNIP* levels.

Taken together, these findings indicate that alterations in glucose metabolism of resistant cells are essential for acquired IMD-3 resistance.

5.2.2 Genetic and epigenetic analysis of IMD-3-resistance

GT mutagenesis used to generate the resistant cell line is based on random integration of a defined gene cassette into the genome of haploid cells disrupting the gene at the integration site. Subsequent selection pressure using IMD-3 gave rise to a long-term resistant cell population, consisting of cells with different integration sites. NGS was applied to identify the integration sites and the affected disrupted genes. Genes essential for resistance acquisition should be overrepresented in the NGS results. However, no gene was significantly overrepresented after NGS of the IMD-3-resistant cell line HGC176, indicating that IMD-3 resistance is not caused by the disruption of specific genes and might be caused by genetics-independent mechanisms. However, long-term resistance can still be attributed to alterations caused by GT mutagenesis, as spontaneously acquired IMD-3 resistance arising in WT haploid cells after long-term IMD-3 treatment disappeared after removal of IMD-3, while GT cells remained resistant.

Besides genetic mutations, also epigenetic DNA or histone modifications can cause treatment resistance in cancer cells [248]. Pretreatment of resistant cells with the DNA demethylating agent DAC, a cytidine analogue, successfully demethylated the DNA but did not restore the sensitivity of IMD-3-resistant cells towards IMD-3 treatment. DAC itself exhibited a pronounced cytotoxicity on WT and IMD-3-resistant cells, presumably due to their haploid genotype rendering them highly sensitive towards incorporation of DAC into DNA and RNA. Lowering the applied DAC concentration and prolonging the pretreatment period demethylated the DNA in WT and resistant cells but did not influence their sensitivity towards IMD-3 treatment. In resistant HGC176 cells, the demethylating effect of DAC did not reach significance, which could be attributed to experimental variations. This is supported by transcriptome data showing no difference in expression levels of DNA-methyltransferases between resistant and sensitive cells, which could have influenced the demethylating effect of DAC. Furthermore, methylation levels of untreated WT and resistant cells were similar, indicating that altered DNA methylation is not responsible for acquired IMD-3 resistance.

It is important to note that DNA demethylation was assessed using the methylation status of three CpG sites in the LINE-1 DNA sequence, an abundant retrotransposon [303], under the assumption that DAC pretreatment causes unspecific genome-wide demethylation. However, to determine if the methylation of specific single genes is altered in the resistant cell line, a genome-wide approach to assess DNA methylation would be required. Additionally, the influence of other epigenetic alterations, such as histone modifications, on IMD-3 resistance should be evaluated.

5.2.3 Transcriptional alterations in IMD-3-resistant cells

Besides the genetic and epigenetic approach, transcriptome analysis was performed to detect alterations in the resistant cell line compared to the WT cell line. Pathway analysis of significantly DEGs in IMD-3-resistant cells revealed downregulation of ‘eIF2 signalling’ as the most significantly deregulated pathway in resistant cells. Inhibition of ‘eIF2 signalling’ seems to activate the pro-survival function of the integrated stress response (ISR), and in absence of its cell death response, could be essential for IMD-3 treatment resistance.

eIF2 is required for translation initiation [147] and its downregulation can be induced upon stress stimuli causing eIF2 α phosphorylation [329], leading to the activation of the pro-survival ISR [300]. In NSCLC cells eIF2 α phosphorylation prohibited cisplatin-induced apoptosis [330], thus inhibition of eIF2 signalling might contribute to IMD-3 resistance. The ISR can also mediate cell death, if cellular homeostasis cannot be restored, through activation of the pro-apoptotic factor DDIT3/CHOP [300]. *DDIT3* transcript levels were found to be enhanced, between 2-fold and 22-fold, in all sensitive cell lines upon IMD-3 treatment along with other genes mediating cell death upon ISR induction [301], including *ATF5*, *PMAIP1/NOXA* and *TXNIP*. Expression of those genes was not increased in IMD-3-treated resistant cells, indicating that they circumvent cell death function of the ISR. The importance of the ISR in IMD-3

function is underlined by the upregulation of the endoplasmatic ‘unfolded protein response’ (UPR) pathway upon IMD-3 treatment in sensitive cell lines, which can cause eIF2 α phosphorylation [331] and induce TXNIP expression [323]. Thus, UPR and ISR activation upon IMD-3 treatment in sensitive cell lines could explain observed increase of *TXNIP* expression levels, independent from *HSF1*, *HSPA8* and *HSAPA1A* modulation, which was previously described by Santagata *et al.* [174]. Further evaluation, especially on protein level, is required to understand the implication of the ISR and eIF2 signalling in IMD-3-resistant and sensitive cancer cells. Pathway analysis also revealed downregulation of cholesterol biosynthesis in untreated IMD-3-resistant cells. In sensitive cell lines, IMD-3 treatment induced downregulation of the cholesterol pathway, thus its upfront downregulation in resistant cells might decrease treatment sensitivity. However, it remains unclear, how decreased cholesterol synthesis influences IMD-3 treatment resistance as, on the one hand, decreased cholesterol in the plasma membrane was found to be associated with downregulation of apoptosis [332], but, on the other hand, enhanced mitochondrial cholesterol was shown to mediate treatment resistance in liver cancer cells [333]. Overall, pathway analysis of transcriptome data revealed that IMD-3 treatment deregulated similar pathways in all sensitive cell lines, inducing the UPR and oxidative stress, while inhibiting GSH detoxification, chromosomal replication and cholesterol biosynthesis. Those pathways were not significantly altered in IMD-3-resistant cell lines upon IMD-3 application. Furthermore, transcriptome analysis of untreated resistant cells compared to sensitive WT cells revealed that majority of the pathways affected by IMD-3 treatment were altered in the untreated resistant cell line upfront. This underlines the possible transcriptional adaptation of resistant cells to circumvent molecular effects induced by IMD-3 contributing to treatment resistance.

In summary, acquired IMD-3 resistance exhibited a permanent character and molecular alterations induced by IMD-3 treatment in sensitive cancer cell lines, such as proliferation inhibition and glucose metabolism deregulation, were almost not detectable in the IMD-3-resistant cell line. Due to the absence of specific genetic alterations in the IMD-3-resistant cell line, IMD-3 resistance is presumably mediated by genetics-independent mechanisms. Although unknown, these alterations caused long-term transcriptional changes in IMD-3-resistant cells mediating adaptation of glucose metabolism and the ISR, which potentially contribute to treatment resistance and maintenance of GLUT-1 protein expression. These findings highlight the importance of altered glucose metabolism, especially maintained GLUT-1 expression and increased PPP activity, for cancer cell resistance towards synthetic flavagline treatment.

5.3 *In vivo* evaluation of synthetic flavagline activity

5.3.1 Dose finding, side effect profiling and anti-tumour activity of synthetic flavaglines in initial xenograft experiments

This project also aimed to investigate the treatment efficacy of synthetic flavaglines alone and in combination with 2DG in first *in vivo* experiments.

First, small groups of six mice were used to select the optimal dosage and treatment combination for further evaluation. Similar to their lower anti-tumour activity observed in previous *in vitro* experiments, the highest dosage of 2DG (400 mg/kg) alone or IMD-1 (1.0 mg/kg), alone and in combination with 2DG, did not influence tumour growth *in vivo*. Upon application of the more potent synthetic flavagline IMD-3 no acute toxicity was detected. The highest concentration of IMD-3 (1.0 mg/kg) slightly inhibited tumour growth compared to vehicle-treated control mice. Combination of 1.0 mg/kg IMD-3 with 100 mg/kg 2DG prolonged the median survival of this treatment group by 9 days compared to the application of IMD-3 alone. Histological analysis of the organs from mice receiving this treatment combination did not reveal any morphological changes and GLUT-1 expression in the tumours was decreased by 15 % compared to tumours from vehicle-treated mice. None of these effects were statistically significant, which might be attributed to the small number of animals per group and the fixed termination day of the experiment. Mice, which had not reached a termination criterion before, had to be sacrificed at day 37, as the experiment was planned to define the optimised dosage and acute side effects and not monitor long-term effects of the treatment. Those mice were incorporated into the survival calculation with a survival of 37 days, due to the lack of ‘actual’ survival. Another drawback was the exclusion of four treatment groups receiving IMD-3, as the xenograft tumours grew significantly slower already before treatment application despite being established from the same batch of HCT116 cells, hampering the comparability of the obtained tumour growth curves in these treatment groups with other treatment groups. All other experiments showed similar growth patterns before treatment application.

The initial experiment was conducted to assess the applicability and acute toxicity of synthetic flavagline treatment as well as determine a suitable treatment combination for further evaluation in an expanded setting. Thus, prolonged survival, decreased tumour growth and downregulation of GLUT-1 obtained upon application of 1.0 mg/kg IMD-3 with 100 mg/kg 2DG encouraged the further examination of the combination.

It was planned to further assess the treatment combination (1.0 mg/kg IMD-3 ± 100 mg/kg 2DG) in an expanded setting with treatment groups comprised of 27 mice, focusing on validation of treatment efficacy and toxicity, and examine the influence of synthetic flavaglines on glucose metabolism *in vivo* using PET/CT imaging of FDG. The experiment was terminated after evaluating 16 instead of 27 mice per treatment group, as the previously observed effect on tumour growth and survival could not be detected. Additionally, PET/CT analysis showed no

difference in glucose uptake of tumours among any treatment groups, confirming the hampered efficacy of synthetic flavagline treatment.

The differences observed in tumour growth and survival in the first experiment might have been caused by the variability of xenograft tumour growth and could not be attributed, as presumed, to a treatment-mediated effect. Thus, increasing the number of analysed mice negated the presumed effect of synthetic flavagline treatment. As previously performed *in vitro* experiments had shown great anti-tumour activity of synthetic flavaglines, different possibilities explaining the hampered *in vivo* efficacy were evaluated.

5.3.2 Influence of albumin on IMD-3 efficacy

Due to the high number of planned experiments for the *in vivo* evaluation of synthetic flavagline derivatives, HCT116 cells were expanded in cell culture and cryopreservation was performed to always use the same batch of HCT116 cells for xenograft formation. Assessment of sensitivity of HCT116 before and after long-term storage towards synthetic flavagline treatment did not reveal significant differences. It can be concluded that cells used for xenograft injection were sensitive towards synthetic flavagline treatment before xenograft formation. As next, the possibility of the treatment preparation influencing the treatment efficacy was investigated.

Treatment preparation for *in vivo* application was performed in a mixture of water and DMSO in a ratio of 10:1 to avoid toxicity of DMSO [334]. In contrast, *in vitro* preparation was performed in cell culture medium and the DMSO concentration was kept as low as possible to avoid influences of DMSO on cancer cell growth.

To narrow down the differences between cell culture medium and water on defined substances, cell culture medium lacking glucose, FBS and P/S (deprived medium) was used for treatment preparation compared to cell culture medium containing 4.5 g/l glucose, 10 % FBS and 1 % P/S (supplemented medium). The preparation of synthetic flavagline derivatives in deprived medium significantly decreased their efficacy in HCT116 cells. Although the same cells showed high sensitivity towards synthetic flavaglines when prepared in supplemented medium. It could be shown in several experiments that the addition of FBS to the aqueous preparation solvent was essential to retain IMD-3 efficacy in HCT116 cells *in vitro* (Fig. 64). Lack of FBS almost completely abolished the efficacy of 100 nM IMD-3 in HCT116 cells, while the effect was less pronounced at a concentration of 500 nM.

Previous experiments had shown that the efficacy of IMD-3 did not strongly increase at concentrations higher than 100 nM. Due to the observed influence of FBS the question arose whether this was due to the limited amount of FBS (10 %) present in the medium. However, it could be shown that increasing the FBS concentration from 10 to 20 % did not enhance the efficacy of IMD-3 in HCT116 cells and the working concentration of 100 nM had been suitable to examine the effects of synthetic flavaglines *in vitro*.

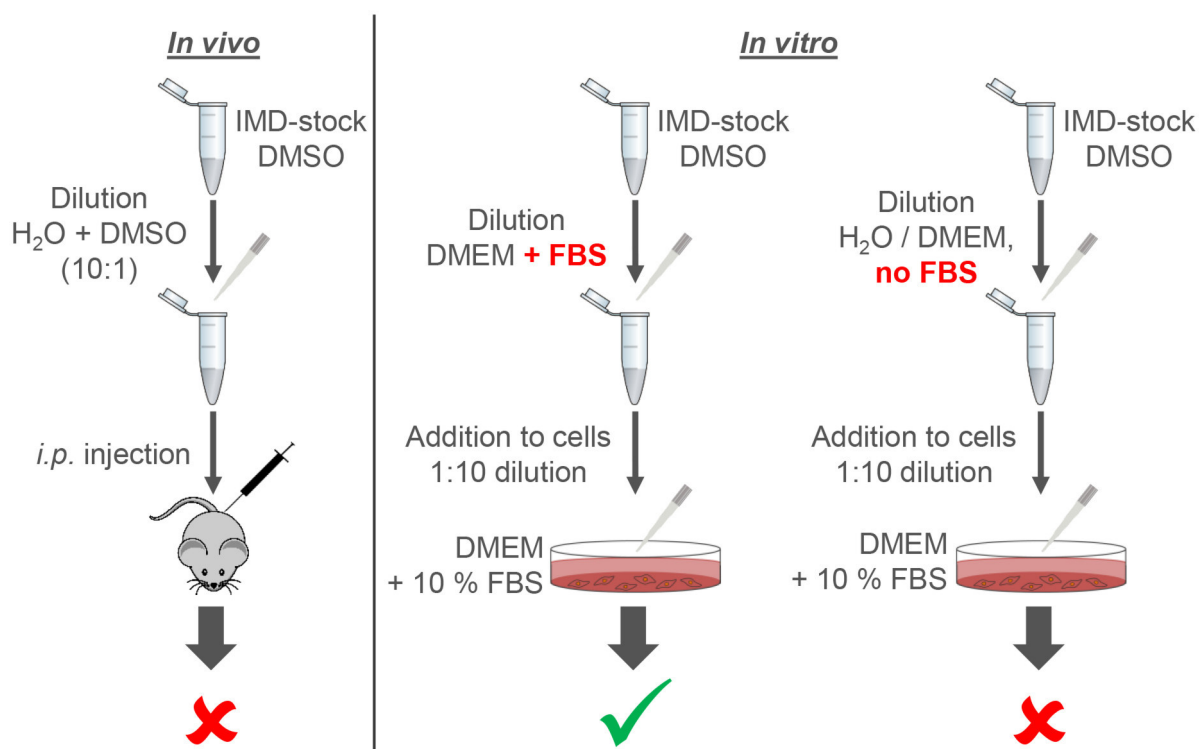


Figure 64: Schematic comparison of IMD-3 preparation and application *in vivo* and *in vitro* and its improved efficacy upon FBS addition shown *in vitro*.

Albumin is the most abundant component of FBS and has been reported to interact with different drugs thereby enhancing their efficacy [306]. Thus, it was examined if albumin was the component present in FBS responsible for enhanced efficacy of synthetic flavaglines. It could be shown that addition of albumin (BSA or HSA) to the aqueous solvent had the same promoting effect on IMD-3 efficacy as FBS. Furthermore, IMD-3 efficacy increased with rising albumin concentrations up to 10 mg/ml. Higher albumin concentrations did not further increase the anti-tumour activity of IMD-3 *in vitro*. It was concluded that albumin was responsible for increased efficacy of IMD-3 presumably through binding of IMD-3, similar to previously described drug-albumin interactions [306].

One possible explanation of enhanced IMD-3 efficacy in presence of albumin could be its stabilisation in aqueous solution. However, no change in the absorption spectrum of IMD-3 was observed, indicating stability of IMD-3 in aqueous solution over time. Thus, albumin must enhance IMD-3 efficacy through another mechanism than its stabilisation in aqueous solution. Another possibility how albumin influences the efficacy of synthetic flavaglines could be through enhancing its solubility. Synthetic flavaglines show great solubility in DMSO but its concentration was kept below 0.0004 % in all *in vitro* experiments, due to reported effects of DMSO on the transcriptome at concentrations of 0.1 % [335] and cellular toxicity at concentrations higher than 1 % [334]. Increasing the DMSO concentration to a maximum end concentration of 0.5 % (in the absence of FBS during the preparation), showed a similar increase in IMD-3 treatment efficacy compared to FBS addition. Thus, it was concluded that the interaction of albumin with IMD-3 might enhance its solubility and, thus, its efficacy.

Low solubility of drugs is a major problem during their development and hampers their absorption [336]. Previous *in vivo* application of IMD-3 in a water-DMSO mixture (10:1) did not show anti-tumour efficacy. Due to the toxicity of DMSO, a good solvent of IMD-3, it was not possible to increase its concentration. It was presumed that addition of albumin to the synthetic flavagline preparation might enhance its availability and efficacy *in vivo*. Furthermore, the interaction between IMD-3 and albumin might have had several other beneficial effects. The albumin-drug interaction was previously reported to prolong the half-life of several drugs [337, 338], facilitate their transport across the vascular endothelium and, most importantly, enhance their accumulation in the tumour, due to the increased albumin consumption of tumour cells [339–341]. Albumin-bound paclitaxel, an FDA approved drug, is applied as a treatment for breast cancer and has shown improved treatment responses and lower toxicity in metastatic breast cancer patients [342]. Also, the combination of doxorubicin with albumin is currently investigated in a clinical phase II trial [343]. Thus, exploiting the interaction of synthetic flavaglines with albumin displayed a promising possibility to increase its availability and efficacy *in vivo*.

Thus, the influence of albumin on synthetic flavagline efficacy was assessed in a small xenograft experiment, evaluating its effect on 1.0 mg/kg IMD-3 alone and in combination with 100 mg/kg 2DG. Despite all the reported beneficial effects of albumin on drug efficacy and the encouraging *in vitro* observations, no enhanced efficacy of the highest IMD-3 concentration (1.0 mg/kg) solubilised in HSA was observed in the xenograft model. Also, the addition of 100 mg/kg 2DG did not improve treatment efficacy. Similar to previous observations, GLUT-1 expression was found to be slightly decreased by approximately 15 % in IMD-3-treated tumours compared to vehicle-treated tumours but not reaching statistical significance or exhibiting an effect on tumour cell growth.

5.3.3 Mass spectrometry analysis of xenograft tumours and analysis of hampered *in vivo* treatment efficacy

Although studies of mouse serum albumin (MSA) revealed equal distribution of MSA throughout the mouse upon *i.p.* injection [344], mass spectrometry analysis was used to evaluate if the synthetic flavagline derivative had reached the tumour upon *i.p.* injection or if the lack of efficacy was caused by its hampered distribution.

Mass spectrometry is universally used to analyse small molecules as well as proteins [345]. Electrospray ionisation (ESI) does not cause ionisation through addition or removal of electrons but uses present ionic species, which commonly arise through the addition of a hydrogen cation (H^+) leading to the detection of the molecule as a ‘quasi-molecular ion’ with $[M + H]^+$. Thus, ESI technique allows detection of the intact IMD-3 molecule, which exhibits a theoretical m/z value of 452.1623, as ESI does not cause fragmentation of the molecules [346].

To assess whether ESI-MS was suitable for the detection of IMD-3 in tumour lysates and to optimise the measurement parameters, IMD-3 was analysed as a single substance. Additionally, lysate of IMD-3-treated HCT116 cells from *in vitro* experiments was used to examine the feasibility to reliably detect IMD-3 among other native cellular molecules. Upon optimisation using 0.01 % TFA to facilitate the ionisation process, it was possible to identify IMD-3 at concentrations as low as 100 nM, also in the cell lysate. IMD-3 was detected with a deviation of 0.0002 and 0.0001 from the theoretical m/z ratio for the single substance and the cell lysate, respectively. Thus, ESI-MS was found to be a suitable method to detect IMD-3 in xenograft tumours, as IMD-3 could be identified with high accuracy in the cellular lysate.

Subsequently, tumour lysates from four mice receiving IMD-3 solubilised in water-DMSO and four mice receiving IMD-3 solubilised in HSA-DMSO were analysed. Each group contained one vehicle-treated control mouse, for which IMD-3 was not detected in the tumour lysate. Tumours from IMD-3-treated mice were chosen to represent a broad range of the number of treatment injections received (4 - 12). It was possible to identify IMD-3 in five out of six tumour lysates of IMD-3-treated mice with no influence of the applied solvent mixture on the detection. IMD-3 + H⁺ was identified with a maximum deviation of 0.0003 from the theoretical m/z ratio of 452.1623. Thus, IMD-3 was present in these tumours, indicating successful distribution upon *i.p.* injection.

IMD-3 was not detected in one mouse, which had 12 injections with 1.0 mg/kg IMD-3 but had received the last injection 7 days prior to experiment termination. This indicates that IMD-3 is cleared from the tumours between three to seven days after the injection. Thus, the applied treatment intervals of two to three day should have been suitable to establish a constant level of IMD-3, even lead to an accumulation over time, as the mice received the next treatment injection before the substance was completely cleared from the tumour.

It is important to note that ESI-MS is a merely qualitative method, thus no conclusion about the amount of IMD-3 present in the tumours can be drawn. Furthermore, the method to lyse the tumours was not optimised to maximise IMD-3 yield from the tumour cells and extraction was rather performed by simple lysis and sonication of tumour tissue in acetonitrile. Thus, it is also not possible to perform a semi-quantitative comparison correlating the obtained peak height of IMD-3 from xenograft tumours with the peak height of IMD-3 as a single substance with a defined concentration. Thus, although the presence of IMD-3 could be clearly demonstrated in all tumours treated with IMD-3 less than 3 days prior to experiment termination, the amount of IMD-3 in the tumour tissue cannot be deduced from this experiment.

It is possible to speculate that the amount of IMD-3 substance reaching the tumour was too small to induce a growth-inhibitory effect. This is supported by the small effect of the synthetic flavagline on GLUT-1 protein expression *in vivo* compared to the observed pronounced effect in 2D and 3D models *in vitro*. The simplest approach to increase the available amount of synthetic

flavagline derivative in the tumour would be to increase the applied dosage. However, preliminary toxicity studies, performed by the manufacturer of the synthetic flavagline derivatives, showed that 1.0 mg/kg displays the highest applicable dosage without acute toxicity. Alternatively, the injection intervals could be shortened to daily injections. This would presumably require lowering the applied dosage, due to observed accumulation of the drug and possible toxicity. One study, investigating the anti-tumour activity of the synthetic flavagline CR-1-31-B, showed prolonged survival upon daily application of 0.2 mg/kg and improved efficacy through combination with glutaminase inhibitors [165]. Transcriptome analysis of IMD-3-treated cell had shown increased glutaminase activity in four out of seven treatment sensitive cell lines, the increase ranging between 2- and 9.4-fold. Thus, the possibility of synthetic flavagline combination with glutaminase inhibitors should be further investigated.

It is important to note that a different tumour and mouse model was used in the study analysing CR-1-31-B activity [165]. It was shown for the natural flavagline silvestrol that the tolerable dosage strongly depends on the used mouse strain, showing a 5-fold difference between BALB/c nude mice and NOD/SCID mice [347]. Thus, efficacy of synthetic flavaglines might also depend on the used mouse model.

Furthermore, usage of an immunodeficient mouse model did not allow the evaluation of the influence of the immune system on synthetic flavagline treatment. Although no influence of the immune system would have been expected, it cannot be excluded in any of the settings and thus should be addressed in the future.

To enhance the amount of synthetic flavagline reaching the tumour, alternative injection methods could be applied. Here, *i.p.* administration was chosen as it is a suitable method for pharmacological studies to evaluate drug efficacy if not focusing on formulation influences [307]. Substances absorbed after *i.p.* administration partially pass through the liver resulting in a first pass effect [307]. However, studies performed by the manufacturer of the investigated synthetic flavagline derivatives did not show any significant influence of the first pass effect. Thus, this should not have influenced the efficacy of synthetic flavaglines in the xenograft experiments. Furthermore, *i.p.* injection might be more considerate for mice compared to repetitive *i.v.* injection over four weeks [307].

Alternative application routes include *i.v.* and oral administration. However, several studies have shown no great difference between *i.p.* and *i.v.* administration, leading to similar AUC and maximum plasma concentrations [348–352]. Thus, *i.p.* injection can be considered close to *i.v.* injection [307] and significant improvement of synthetic flavagline activity upon *i.v.* injection is very unlikely.

An alternative approach could be oral application, as it also displays a convenient, cost-effective and non-invasive method for later clinical application [353]. However, possible influence of the pH or microbiota in the gastro-intestinal tract should be taken into consideration [353]. Also, several studies have shown adverse effects of oral administration compared to *i.p.* and *i.v.* on drug availability [348–352].

The decreased *in vivo* efficacy could also arise from adaptation of cancer cell metabolism after xenograft formation. Metabolism is strongly influenced by the tumour environment [30], which significantly differs between *in vitro* and *in vivo* conditions. Lung tumour cells in mice were found to fuel the TCA cycle through glucose, while they used glutamine *in vitro* [354]. Additionally, metabolic heterogeneity was detected in lung tumours with highly perfused regions depending less on glucose utilisation [355] and several previous studies have associated altered metabolism with drug resistance [89,253,356,357]. Furthermore, interactions between the tumour cells and components of the tumour stroma, such as fibroblasts or structural proteins, can also influence drug sensitivity of tumour cells [358]. To reduce the impact of such influences, synthetic flavaglines had been evaluated in different 3D culture models to mimic altered tumour environment and assess their efficacy in complex settings. Although such models improve transferability and could highlight possible obstacles, they are limited in their ability to exactly mimic the *in vivo* situation [326]. Thus, microenvironment-related changes in cellular metabolism of HCT116 cells after xenograft formation compared to previous cell culture could have hampered their sensitivity towards synthetic flavagline derivatives *in vivo*.

Taken together, there are several factors which could diminish synthetic flavagline efficacy *in vivo* compared to their pronounced anti-cancer activity *in vitro*. Detailed investigation of those factors is required to understand the complex influences on synthetic flavagline efficacy and to develop novel strategies enabling the application of synthetic flavaglines as cancer therapeutics.

5.4 Outlook

In vitro evaluation of synthetic flavagline derivatives in sensitive and resistant cancer cell lines has elucidated several important molecular aspects of their mechanism of action, potential mechanisms contributing to treatment resistance and underlined their great potential for cancer therapy. However, the presented results demonstrated hampered ability of synthetic flavaglines to reduce tumour burden in the used xenograft model. Therefore, to successfully translate synthetic flavagline derivatives into clinical application, further research should be focused on the improvement of synthetic flavagline efficacy *in vivo* and a structured investigation of possible factors influencing their *in vivo* activity should be performed.

Adaptation of tumour metabolism *in vivo* could be one possible reason for decreased synthetic flavagline efficacy. Thus, the sensitivity of HCT116 xenograft tumours should be investigated *ex vivo*. A suitable experimental setting needs to be established, taking into consideration the high metabolic flexibility of tumours [359] to avoid distortion of the results.

Another possibility, to assess whether the amount of synthetic flavagline reaching the tumour was too low to induce a pronounced growth-inhibitory effect, would be to inject the drug mix-

ture directly at the tumour site. Although this model would neglect systemic distribution and other influences on the drug before reaching the tumour, it would allow to assess the ability of synthetic flavaglines to hamper tumour growth *in vivo* and encourage the development of novel treatment strategies if efficacy could be shown. Local implantation of drug carriers at the tumour site have been shown to prolong survival and reduce tumour recurrence in several studies [360]. Thus, using drug carries, such as gels or polymeric films, could improve synthetic flavagline efficacy *in vivo*. Alternatively, usage of drug nanocarriers, such as liposomes or polymeric nanoparticles, was found to enhance drug efficacy through selective drug accumulation in tumour tissue, improvement of pharmacodynamics and -kinetics, and reduction of toxic side effects [361]. Furthermore, some carrier systems allow site-specific release of the drug using magnetic or electric fields [361]. Therefore, alternative formulations of synthetic flavaglines using nanocarriers might have the potential to enhance their *in vivo* efficacy.

Investigations focusing on improvement of synthetic flavagline efficacy *in vivo* could be supported with *in vitro* experiments further examining treatment resistance. Examination of the resistant cell line has revealed retained GLUT-1 expression upon IMD-3 treatment as an important mechanism for synthetic flavagline resistance. As GLUT-1 internalisation was found to occur through clathrin-coated pits [322], the influence of clathrin-dependent endocytosis on synthetic flavagline sensitivity should be examined. However, it needs to be taken in consideration that endocytosis is important for several different cell functions and it should be ensured that the observed effect is caused by retained GLUT-1 expression. However, several different inhibitors of clathrin-dependent endocytosis are available, acting through different mechanisms [362], enhancing the chances to find a suitable inhibitor. Furthermore, the influence of the ISR on IMD-3 treatment efficacy should be evaluated to better understand the molecular adaptations mediating synthetic flavagline resistance.

The presented results demonstrate the pronounced anti-tumour activity of two novel synthetic flavagline derivatives targeting glucose metabolism in cancer cell *in vitro* and elucidate the possibility of metabolic adaptations leading to treatment resistance. Although synthetic flavagline efficacy could be demonstrated in 2D and 3D cell culture models, their decreased efficacy *in vivo* highlights the challenges of extrapolating *in vitro* drug efficacy to more complex real-world scenarios. However, the demonstrated tumour-selective effect of synthetic flavaglines and 2DG *in vitro* and absence of acute toxicity *in vivo* underline the great potential of these substances for cancer treatment and represent major steps towards clinical translation of synthetic flavagline derivatives, encouraging their further investigation.

References

- [1] World Health Organization. Global action plan for the prevention and control of non-communicable diseases 2013-2020, 2013.
- [2] Bray, F., Ferlay, J., Soerjomataram, I., Siegel, R. L., Torre, L. A., and Jemal, A. Global cancer statistics 2018: GLOBOCAN estimates of incidence and mortality worldwide for 36 cancers in 185 countries. *CA-Cancer J Clin*, 68(6):394–424, 2018.
- [3] American Cancer Society. Global cancer facts and figures 4th edition. *National Home Office: American Cancer Society Inc.*, 1:1–73, 2018.
- [4] Plummer, M., de Martel, C., Vignat, J., Ferlay, J., Bray, F., and Franceschi, S. Global burden of cancers attributable to infections in 2012: a synthetic analysis. *Lancet Glob Health*, 4(9):e609–e616, 2016.
- [5] Stewart, B. and Wild, C. World Cancer Report 2014. *World Health Organization*, 630, 2014.
- [6] Feitelson, M. A., Arzumanyan, A., Kulathinal, R. J., Blain, S. W., Holcombe, R. F., Mahajna, J., Marino, M., Martinez-Chantar, M. L., Nawroth, R., Sanchez-Garcia, I., Sharma, D., Saxena, N. K., Singh, N., Vlachostergios, P. J., Guo, S., Konoki, K., Fujii, H., Georgakilas, A. G., Bilsland, A., Amedei, A., Niccolai, E., Amin, A., Ashraf, S. S., Boosani, C. S., Guha, G., Ciriolo, M. R., Aquilano, K., Chen, S., Mohammed, S. I., Azmi, A. S., Bhakta, D., Halicka, D., Keith, W. N., and Newsheer, S. Sustained proliferation in cancer: Mechanisms and novel therapeutic targets. *Semin Cancer Biol*, 35:S25–S54, 2015.
- [7] Hanahan, D. and Weinberg, R. A. The hallmarks of cancer. *Cell*, 100(1):57–70, 2000.
- [8] Hanahan, D. and Weinberg, R. A. Hallmarks of cancer: the next generation. *Cell*, 144(5):646–674, 2011.
- [9] Wee, P. and Wang, Z. Epidermal growth factor receptor cell proliferation signaling pathways. *Cancers*, 9(5):52, 2017.
- [10] Counter, C. M., Avilion, A. A., LeFeuvre, C. E., Stewart, N. G., Greider, C. W., Harley, C. B., and Bacchetti, S. Telomere shortening associated with chromosome instability is arrested in immortal cells which express telomerase activity. *EMBO J*, 11(5):1921–1929, 1992.
- [11] Kim, N. W., Piatyszek, M. A., Prowse, K. R., Harley, C. B., West, M. D., Ho, P. L. C., Coviello, G. M., Wright, W. E., Weinrich, S. L., and Shay, J. W. Specific association of human telomerase activity with immortal cells and cancer. *Science*, 266:2011–2015, 1994.
- [12] Chin, L., Artandi, S. E., Shen, Q., Tam, A., Lee, S.-L., Gottlieb, G. J., Greider, C. W., and DePinho, R. A. p53 deficiency rescues the adverse effects of telomere loss and cooperates with telomere dysfunction to accelerate carcinogenesis. *Cell*, 97(4):527–538, 1999.

- [13] Symonds, H., Krall, L., Remington, L., Saenz-Robles, M., Lowe, S., Jacks, T., and Van Dyke, T. p53-dependent apoptosis suppresses tumor growth and progression in vivo. *Cell*, 78(4):703–711, 1994.
- [14] Adams, J. and Cory, S. The Bcl-2 apoptotic switch in cancer development and therapy. *Oncogene*, 26(9):1324–1337, 2007.
- [15] Holmgren, L., O’Reilly, M. S., and Folkman, J. Dormancy of micrometastases: balanced proliferation and apoptosis in the presence of angiogenesis suppression. *Nat Med*, 1(2):149–153, 1995.
- [16] Parangi, S., O’Reilly, M., Christofori, G., Holmgren, L., Grosfeld, J., Folkman, J., and Hanahan, D. Antiangiogenic therapy of transgenic mice impairs de novo tumor growth. *Proc Natl Acad Sci USA*, 93(5):2002–2007, 1996.
- [17] Bergers, G. and Benjamin, L. E. Tumorigenesis and the angiogenic switch. *Nat Rev Cancer*, 3(6):401–410, 2003.
- [18] Carmeliet, P. VEGF as a key mediator of angiogenesis in cancer. *Oncology*, 69(Suppl. 3):4–10, 2005.
- [19] Dunn, G. P., Bruce, A. T., Ikeda, H., Old, L. J., and Schreiber, R. D. Cancer immunoediting: from immunosurveillance to tumor escape. *Nat Immunol*, 3(11):991–998, 2002.
- [20] Patel, S. P. and Kurzrock, R. PD-L1 expression as a predictive biomarker in cancer immunotherapy. *Mol Cancer Ther*, 14(4):847–856, 2015.
- [21] Mantovani, A., Allavena, P., Sica, A., and Balkwill, F. Cancer-related inflammation. *Nature*, 454(7203):436–444, 2008.
- [22] Fadaka, A., Ajiboye, B., Ojo, O., Adewale, O., Olayide, I., and Emuowhochere, R. Biology of glucose metabolization in cancer cells. *Journal of Oncological Sciences*, 3(2):45–51, 2017.
- [23] Ansell, S. M., Lesokhin, A. M., Borrello, I., Halwani, A., Scott, E. C., Gutierrez, M., Schuster, S. J., Millenson, M. M., Cattry, D., Freeman, G. J., Rodig, S. J., Chapuy, B., Ligon, A. H., Zhu, L., Grosso, J. F., Kim, S. Y., Timmerman, J. M., Shipp, M. A., and Armand, P. PD-1 blockade with nivolumab in relapsed or refractory Hodgkin’s lymphoma. *New Engl J Med*, 372(4):311–319, 2015.
- [24] Le, D. T., Uram, J. N., Wang, H., Bartlett, B. R., Kemberling, H., Eyring, A. D., Skora, A. D., Lubner, B. S., Azad, N. S., Laheru, D., Biedrzycki, B., Donehower, R. C., Zaheer, A., Fisher, G. A., Crocenzi, T. S., Lee, J. J., Duffy, S. M., Goldberg, R. M., de la Chapelle, A., Koshiji, M., Bhaijee, F., Hübner, T., Hruban, R. H., Wood, L. D., Cuka, N., Pardoll, D. M., Papadopoulos, N., Kinzler, K. W., Zhou, S., Cornish, T. C., Taube, J. M., Anders, R. A., Eshleman, J. R., Vogelstein, B., and Diaz Jr., L. A. PD-1 blockade in tumors with mismatch-repair deficiency. *New Engl J Med*, 372(26):2509–2520, 2015.
- [25] Le, D. T., Durham, J. N., Smith, K. N., Wang, H., Bartlett, B. R., Aulakh, L. K., Lu, S., Kemberling, H., Wilt, C., Lubner, B. S., Wong, F., Azad, N. S., Rucki, A. A., Laheru, D., Donehower, R., Zaheer, A., Fisher, G. A., Crocenzi, T. S., Lee, J. J., Greten, T. F., Duffy,

- A. G., Ciombor, K. K., Exring, A. D., Lam, B. H., Joe, A., Kang, S. P., Holdhoff, M., Danilova, L., Cope, L., Meyer, C., Zhou, S., Goldberg, R. M., Armstrong, D. K., Bever, K. M., Fader, A. N., Taube, J., Housseau, F., Spetzler, D., Xiao, N., Pardoll, D. M., Papadopoulos, N., Kinzler, K. W., Eshleman, J. R., Vogelstein, B., Andres, R. A., and Diaz Jr, L. A. Mismatch repair deficiency predicts response of solid tumors to PD-1 blockade. *Science*, 357(6349):409–413, 2017.
- [26] Yang, J. C., Haworth, L., Sherry, R. M., Hwu, P., Schwartzentruber, D. J., Topalian, S. L., Steinberg, S. M., Chen, H. X., and Rosenberg, S. A. A randomized trial of bevacizumab, an anti-vascular endothelial growth factor antibody, for metastatic renal cancer. *N Engl J Med*, 349(5):427–434, 2003.
- [27] Kabbinavar, F., Hurwitz, H. I., Fehrenbacher, L., Meropol, N. J., Novotny, W. F., Lieberman, G., Griffing, S., and Bergsland, E. Phase II, randomized trial comparing bevacizumab plus fluorouracil (FU)/leucovorin (LV) with FU/LV alone in patients with metastatic colorectal cancer. *J Clin Oncol*, 21(1):60–65, 2003.
- [28] Johnson, D. H., Fehrenbacher, L., Novotny, W. F., Herbst, R. S., Nemunaitis, J. J., Jablons, D. M., Langer, C. J., DeVore III, R. F., Gaudreault, J., Damico, L. A., Holmgren, E., and Kabbinavar, F. Randomized phase II trial comparing bevacizumab plus carboplatin and paclitaxel with carboplatin and paclitaxel alone in previously untreated locally advanced or metastatic non-small-cell lung cancer. *J Clin Oncol*, 22(11):2184–2191, 2004.
- [29] Luengo, A., Gui, D. Y., and Vander Heiden, M. G. Targeting metabolism for cancer therapy. *Cell Chem Biol*, 24(9):1161–1180, 2017.
- [30] Vander Heiden, M. G. and DeBerardinis, R. J. Understanding the intersections between metabolism and cancer biology. *Cell*, 168(4):657–669, 2017.
- [31] Stein, M., Lin, H., Jeyamohan, C., Dvorzehinski, D., Gounder, M., Bray, K., Eddy, S., Goodin, S., White, E., and DiPaola, R. S. Targeting tumor metabolism with 2-deoxyglucose in patients with castrate-resistant prostate cancer and advanced malignancies. *Prostate*, 70(13):1388–1394, 2010.
- [32] Raez, L. E., Papadopoulos, K., Ricart, A. D., Chiorean, E. G., DiPaola, R. S., Stein, M. N., Lima, C. M. R., Schlesselman, J. J., Tolba, K., Langmuir, V. K., Kroll, S., Jung, D. T., Kurtoglu, M., Rosenblatt, J., and Lampidis, T. J. A phase I dose-escalation trial of 2-deoxy-D-glucose alone or combined with docetaxel in patients with advanced solid tumors. *Cancer Chemother Pharmacol*, 71(2):523–530, 2013.
- [33] Alberts, B., Johnson, A., Lewis, J., Raff, M., Roberts, K., and Walter, P. *Molecular Biology of the Cell*. Garland Science New York, 5 edition, 2008.
- [34] Galluzzi, L., Vitale, I., Aaronson, S. A., Abrams, J. M., Adam, D., Agostinis, P., Alnemri, E. S., Altucci, L., Amelio, I., Andrews, D. W., et al. Molecular mechanisms of cell death: recommendations of the Nomenclature Committee on Cell Death 2018. *Cell Death Differ*, 25(3):486–541, 2018.

- [35] Hernandez-Segura, A., Nehme, J., and Demaria, M. Hallmarks of cellular senescence. *Trends Cell Biol*, 28(6):436–453, 2018.
- [36] Campisi, J. Aging, cellular senescence, and cancer. *Annu Rev Physiol*, 75:685–705, 2013.
- [37] Kurz, D. J., Decary, S., Hong, Y., and Erusalimsky, J. D. Senescence-associated (beta)-galactosidase reflects an increase in lysosomal mass during replicative ageing of human endothelial cells. *J Cell Sci*, 113(20):3613–3622, 2000.
- [38] Dimri, G. P., Lee, X., Basile, G., Acosta, M., Scott, G., Roskelley, C., Medrano, E. E., Linskens, M., Rubelj, I., and Pereira-Smith, O. A biomarker that identifies senescent human cells in culture and in aging skin in vivo. *PNAS*, 92(20):9363–9367, 1995.
- [39] Hayflick, L. and Moorhead, P. S. The serial cultivation of human diploid cell strains. *Exp Cell Res*, 25(3):585–621, 1961.
- [40] Coppé, J.-P., Desprez, P.-Y., Krtolica, A., and Campisi, J. The senescence-associated secretory phenotype: the dark side of tumor suppression. *Annu Rev Pathol*, 5:99–118, 2010.
- [41] Lee, A. C., Fenster, B. E., Ito, H., Takeda, K., Bae, N. S., Hirai, T., Yu, Z.-X., Ferrans, V. J., Howard, B. H., and Finkel, T. Ras proteins induce senescence by altering the intracellular levels of reactive oxygen species. *J Biol Chem*, 274(12):7936–7940, 1999.
- [42] Serrano, M., Lin, A. W., McCurrach, M. E., Beach, D., and Lowe, S. W. Oncogenic ras provokes premature cell senescence associated with accumulation of p53 and p16 INK4a. *Cell*, 88(5):593–602, 1997.
- [43] Myrianthopoulos, V., Evangelou, K., Vasileiou, P. V., Cooks, T., Vassilakopoulos, T. P., Pangalis, G. A., Kouloukoussa, M., Kittas, C., Georgakilas, A. G., and Gorgoulis, V. G. Senescence and senotherapeutics: a new field in cancer therapy. *Pharmacol Ther*, 193:31–49, 2019.
- [44] Kuilman, T., Michaloglou, C., Mooi, W. J., and Peeper, D. S. The essence of senescence. *Genes Dev*, 24(22):2463–2479, 2010.
- [45] Saleh, T., Bloukh, S., Carpenter, V. J., Alwohoush, E., Bakeer, J., Darwish, S., Azab, B., and Gewirtz, D. A. Therapy-Induced Senescence: An "Old" Friend Becomes the Enemy. *Cancers (Basel)*, 12(4):822, 2020.
- [46] Demaria, M., O’Leary, M. N., Chang, J., Shao, L., Liu, S., Alimirah, F., Koenig, K., Le, C., Mitin, N., Deal, A. M., Alston, S., Academia, E. C., Kilmarx, S., Valdovinos, A., Wang, B., de Bruin, A., Kennedy, B. K., Melov, S., Zhou, D., Sharpless, N. E., Muss, H., and Campisi, J. Cellular senescence promotes adverse effects of chemotherapy and cancer relapse. *Cancer Discov*, 7(2):165–176, 2017.
- [47] Elmore, S. Apoptosis: a review of programmed cell death. *Toxicol Pathol*, 35(4):495–516, 2007.
- [48] Shi, Y. Mechanisms of caspase activation and inhibition during apoptosis. *Mol Cell*, 9(3):459–470, 2002.

- [49] Strasser, A., O'Connor, L., and Dixit, V. M. Apoptosis signaling. *Annu Rev Biochem*, 69(1):217–245, 2000.
- [50] Chen, M. and Wang, J. Initiator caspases in apoptosis signaling pathways. *Apoptosis*, 7(4):313–319, 2002.
- [51] Jin, Z. and El-Deiry, W. S. Overview of cell death signaling pathways. *Cancer Biol Ther*, 4(2):147–171, 2005.
- [52] Jänicke, R. U., Sprengart, M. L., Wati, M. R., and Porter, A. G. Caspase-3 is required for DNA fragmentation and morphological changes associated with apoptosis. *J Biol Chem*, 273(16):9357–9360, 1998.
- [53] Bratton, S. B. and Salvesen, G. S. Regulation of the Apaf-1–caspase-9 apoptosome. *J Cell Sci*, 123(19):3209–3214, 2010.
- [54] Wajant, H., Pfizenmaier, K., and Scheurich, P. Tumor necrosis factor signaling. *Cell Death Differ*, 10(1):45–65, 2003.
- [55] Thorburn, A. Death receptor-induced cell killing. *Cell Signal*, 16(2):139–144, 2004.
- [56] Ashkenazi, A. and Dixit, V. M. Death receptors: signaling and modulation. *Science*, 281(5381):1305–1308, 1998.
- [57] Fulda, S. and Debatin, K.-M. Extrinsic versus intrinsic apoptosis pathways in anticancer chemotherapy. *Oncogene*, 25(34):4798–4811, 2006.
- [58] Chen, G. and Goeddel, D. V. TNF-R1 signaling: a beautiful pathway. *Science*, 296(5573):1634–1635, 2002.
- [59] Ashkenazi, A. and Dixit, V. M. Apoptosis control by death and decoy receptors. *Curr Opin Cell Biol*, 11(2):255–260, 1999.
- [60] Kalkavan, H. and Green, D. R. MOMP, cell suicide as a BCL-2 family business. *Cell Death Differ*, 25(1):46–55, 2018.
- [61] Letai, A. Cell death and cancer therapy: don't forget to kill the cancer cell! *Clin Cancer Res*, 21(22), November 2015.
- [62] Legler, K., Hauser, C., Egberts, J.-H., Willms, A., Heneweer, C., Boretius, S., Röcken, C., Glüer, C.-C., Becker, T., Kluge, M., Hill, O., Gieffers, C., Fricke, H., Kalthoff, H., Lemke, J., and Trauzold, A. The novel TRAIL-receptor agonist APG350 exerts superior therapeutic activity in pancreatic cancer cells. *Cell Death Dis*, 9(5):1–15, 2018.
- [63] Zerp, S. F., Bibi, Z., Verbrugge, I., Voest, E. E., and Verheij, M. Enhancing radiation response by a second-generation TRAIL receptor agonist using a new in vitro organoid model system. *Clin Transl Radiat Oncol*, 24:1–9, 2020.
- [64] Cristofanon, S. and Fulda, S. ABT-737 promotes tBid mitochondrial accumulation to enhance TRAIL-induced apoptosis in glioblastoma cells. *Cell Death Dis*, 3(11):e432–e432, 2012.
- [65] Kroemer, G., Dallaporta, B., and Resche-Rigon, M. The mitochondrial death/life regulator in apoptosis and necrosis. *Annu Rev Physiol*, 60(1):619–642, 1998.

- [66] Degterev, A., Huang, Z., Boyce, M., Li, Y., Jagtap, P., Mizushima, N., Cuny, G. D., Mitchison, T. J., Moskowitz, M. A., and Yuan, J. Chemical inhibitor of nonapoptotic cell death with therapeutic potential for ischemic brain injury. *Nat Chem Biol*, 1(2):112–119, 2005.
- [67] Degterev, A., Hitomi, J., Germscheid, M., Ch'en, I. L., Korkina, O., Teng, X., Abbott, D., Cuny, G. D., Yuan, C., Wagner, G., Hedrick, S. M., Gerber, S. A., Lugovskoy, A., and Yuan, J. Identification of RIP1 kinase as a specific cellular target of necrostatins. *Nat Chem Biol*, 4(5):313–321, 2008.
- [68] Degterev, A., Zhou, W., Maki, J. L., and Yuan, J. Assays for necroptosis and activity of RIP kinases. In *Methods Enzymol*, volume 545, pages 1–33. Elsevier, 2014.
- [69] Kroemer, G., Galluzzi, L., Vandenabeele, P., Abrams, J., Alnemri, E. S., Baehrecke, E. H., Blagosklonny, M. V., El-Deiry, W. S., Golstein, P., Green, D. R., Hengartner, M., Knight, R. A., Kumar, S., Lipton, S. A., Malorni, W., Nuñez, G., Peter, M. E., Tschopp, J., Yuan, J., Piacentini, M., Zhivotovsky, B., Melino, G., and Nomenclature Committee on Cell Death 2009. Classification of cell death: recommendations of the Nomenclature Committee on Cell Death 2009. *Cell Death Differ*, 16(1):3–11, 2009.
- [70] Tait, S. W., Ichim, G., and Green, D. R. Die another way—non-apoptotic mechanisms of cell death. *J Cell Sci*, 127(10):2135–2144, 2014.
- [71] Pasparakis, M. and Vandenabeele, P. Necroptosis and its role in inflammation. *Nature*, 517(7534):311–320, 2015.
- [72] Kroemer, G. and Levine, B. Autophagic cell death: the story of a misnomer. *Nat Rev Mol Cell Bio*, 9(12):1004–1010, 2008.
- [73] Liu, Y. and Levine, B. Autosis and autophagic cell death: the dark side of autophagy. *Cell Death Differ*, 22(3):367–376, 2015.
- [74] Mizushima, N. Autophagy: process and function. *Genes Dev*, 21(22):2861–2873, 2007.
- [75] Mizushima, N. Autophagy in protein and organelle turnover. *Cold Spring Harb Symp Quant Biol*, 76:397–402, 2011.
- [76] Galluzzi, L., Vitale, I., Abrams, J., Alnemri, E., Baehrecke, E., Blagosklonny, M., Dawson, T. M., Dawson, V., El-Deiry, W., Fulda, S., Gottlieb, E., Green, D. R., Hengartner, M. O., Kepp, O., Knight, R. A., Kumar, S., Lipton, S. A., Lu, X., Madeo, F., Malorni, W., Mehlen, P., Nuñez, G., Peter, M. E., Piacentini, M., Rubinsztein, D. C., Shi, Y., Simon, H.-U., Vandenabeele, P., White, E., Yuan, J., Zhivotovsky, B., Melino, G., and Kroemer, G. Molecular definitions of cell death subroutines: recommendations of the Nomenclature Committee on Cell Death 2012. *Cell Death Differ*, 19(1):107–120, 2012.
- [77] Vander Heiden, M. G., Cantley, L. C., and Thompson, C. B. Understanding the Warburg effect: the metabolic requirements of cell proliferation. *Science*, 324(5930):1029–1033, 2009.

- [78] Kruger, N. J. and von Schaewen, A. The oxidative pentose phosphate pathway: structure and organisation. *Curr Opin Plant Biol*, 6(3):236–246, 2003.
- [79] Warburg, O. Über den stoffwechsel der Carcinomzelle. *Naturwissenschaften*, 12(50):1131–1137, 1924.
- [80] Warburg, O., Wind, F., and Negelein, E. The metabolism of tumors in the body. *J Gen Physiol*, 8(6):519, 1927.
- [81] Warburg, O. On the origin of cancer cells. *Science*, 123(3191):309–314, 1956.
- [82] Gatenby, R. A. and Gillies, R. J. Why do cancers have high aerobic glycolysis? *Nat Rev Cancer*, 4(11):891–899, 2004.
- [83] Liberti, M. V. and Locasale, J. W. The Warburg effect: how does it benefit cancer cells? *Trends Biochem Sci*, 41(3):211–218, 2016.
- [84] Barron, C. C., Bilan, P. J., Tsakiridis, T., and Tsiani, E. Facilitative glucose transporters: implications for cancer detection, prognosis and treatment. *Metabolism*, 65(2):124–139, 2016.
- [85] Macheda, M. L., Rogers, S., and Best, J. D. Molecular and cellular regulation of glucose transporter (GLUT) proteins in cancer. *J Cell Physiol*, 202(3):654–662, 2005.
- [86] Martinez-Zaguilan, R., Seftor, E. A., Seftor, R. E., Chu, Y.-W., Gillies, R. J., and Hendrix, M. J. Acidic pH enhances the invasive behavior of human melanoma cells. *Clin Exp Metastasis*, 14(2):176–186, 1996.
- [87] Sonveaux, P., Végran, F., Schroeder, T., Wergin, M. C., Verrax, J., Rabbani, Z. N., De Saedeleer, C. J., Kennedy, K. M., Diepart, C., Jordan, B. F., Kelley, M. J., Gallez, B., Wahl, M. L., Feron, O., and Dewhirst, M. W. Targeting lactate-fueled respiration selectively kills hypoxic tumor cells in mice. *J Clin Invest*, 118(12):3930–3942, 2008.
- [88] Crabtree, H. G. Observations on the carbohydrate metabolism of tumours. *Biochem J*, 23(3):536–545, 1929.
- [89] Desbats, M. A., Giacomini, I., Prayer-Galetti, T., and Montopoli, M. Metabolic plasticity in chemotherapy resistance. *Front Oncol*, 10:281, 2020.
- [90] Weinberg, S. E. and Chandel, N. S. Targeting mitochondria metabolism for cancer therapy. *Nat Chem Biol*, 11(1):9, 2015.
- [91] DeBerardinis, R. J., Mancuso, A., Daikhin, E., Nissim, I., Yudkoff, M., Wehrli, S., and Thompson, C. B. Beyond aerobic glycolysis: transformed cells can engage in glutamine metabolism that exceeds the requirement for protein and nucleotide synthesis. *Proc Natl Acad Sci USA*, 104(49):19345–19350, 2007.
- [92] Hoxhaj, G. and Manning, B. D. The PI3K–AKT network at the interface of oncogenic signalling and cancer metabolism. *Nat Rev Cancer*, 20(2):74–88, 2020.
- [93] Jin, L., Alesi, G., and Kang, S. Glutaminolysis as a target for cancer therapy. *Oncogene*, 35(28):3619–3625, 2016.
- [94] Al Moustafa, A.-E., Achkhar, A., and Yasmeen, A. EGF-receptor signaling and epithelial-mesenchymal transition in human carcinomas. *Front Biosci*, 4:671–684, 2011.

- [95] DeBerardinis, R. J. and Chandel, N. S. Fundamentals of cancer metabolism. *Sci Adv*, 2(5):e1600200, 2016.
- [96] Galluzzi, L., Kepp, O., Vander Heiden, M. G., and Kroemer, G. Metabolic targets for cancer therapy. *Nat Rev Drug Discov*, 12(11):829–846, 2013.
- [97] Koundouros, N. and Poulogiannis, G. Reprogramming of fatty acid metabolism in cancer. *Brit J Cancer*, 122(1):4–22, 2020.
- [98] Yang, Y., Sun, M., Wang, L., and Jiao, B. HIFs, angiogenesis, and cancer. *J Cell Biochem*, 114(5):967–974, 2013.
- [99] Bensinger, S. J. and Christofk, H. R. New aspects of the Warburg effect in cancer cell biology. *Semin Cell Dev Biol*, 23:352–361, 2012.
- [100] Weidemann, A. and Johnson, R. Biology of HIF-1 α . *Cell Death Differ*, 15(4):621–627, 2008.
- [101] Chen, C.-L., Chu, J.-S., Su, W.-C., Huang, S.-C., and Lee, W.-Y. Hypoxia and metabolic phenotypes during breast carcinogenesis: expression of HIF-1 α , GLUT1, and CAIX. *Virchows Arch*, 457(1):53–61, 2010.
- [102] Semenza, G. L. HIF-1: upstream and downstream of cancer metabolism. *Curr Opin Genet Dev*, 20(1):51–56, 2010.
- [103] Jones, R. G. and Thompson, C. B. Tumor suppressors and cell metabolism: a recipe for cancer growth. *Genes Dev*, 23(5):537–548, 2009.
- [104] Kuntz, S., Mazerbourg, S., Boisbrun, M., Cerella, C., Diederich, M., Grillier-Vuissoz, I., and Flament, S. Energy restriction mimetic agents to target cancer cells: Comparison between 2-deoxyglucose and thiazolidinediones. *Biochem Pharmacol*, 92(1):102–111, 2014.
- [105] Christofk, H. R., Vander Heiden, M. G., Harris, M. H., Ramanathan, A., Gerszten, R. E., Wei, R., Fleming, M. D., Schreiber, S. L., and Cantley, L. C. The M2 splice isoform of pyruvate kinase is important for cancer metabolism and tumour growth. *Nature*, 452(7184):230–234, 2008.
- [106] Li, L., Li, L., Li, W., Chen, T., Zou, B., Zhao, L., Wang, H., Wang, X., Xu, L., Liu, X., Wand, D., Li, B., Mak, T. W., Du, W., Yang, X., and Jiang, P. TAp73-induced phosphofructokinase-1 transcription promotes the Warburg effect and enhances cell proliferation. *Nat Commun*, 9(1):1–13, 2018.
- [107] Czernin, J. and Phelps, M. E. Positron emission tomography scanning: current and future applications. *Annu Rev Med*, 53(1):89–112, 2002.
- [108] Gambhir, S. S. Molecular imaging of cancer with positron emission tomography. *Nat Rev Cancer*, 2(9):683–693, 2002.
- [109] Shan, X. H., Hu, H., Xiong, F., Gu, N., Geng, X. D., Zhu, W., Lin, J., and Wang, Y. F. Targeting Glut1-overexpressing MDA-MB-231 cells with 2-deoxy-d-glucose modified SPIOs. *Eur J Radiol*, 81(1):95–99, 2012.

- [110] Zhu, A., Lee, D., and Shim, H. Metabolic positron emission tomography imaging in cancer detection and therapy response. *Semin Oncol*, 38(1):55–69, 2011.
- [111] Hong, S. Y. and Hagen, T. 2-Deoxyglucose induces the expression of thioredoxin interacting protein (TXNIP) by increasing O-GlcNAcylation—Implications for targeting the Warburg effect in cancer cells. *Biochem Biophys Res Commun*, 465(4):838–844, 2015.
- [112] Wick, A. N., Drury, D. R., Nakada, H. I., and Wolfe, J. B. Localization of the primary metabolic block produced by 2-deoxyglucose. *J Biol Chem*, 224(2):963–969, 1957.
- [113] Kang, H. T. and Hwang, E. S. 2-Deoxyglucose: an anticancer and antiviral therapeutic, but not any more a low glucose mimetic. *Life Sci*, 78(12):1392–1399, 2006.
- [114] Pelicano, H., Martin, D., Xu, R., and Huang, P. Glycolysis inhibition for anticancer treatment. *Oncogene*, 25(34):4633–4646, 2006.
- [115] Ahadova, A., Gebert, J., von Knebel Doeberitz, M., Kopitz, J., and Kloor, M. Dose-dependent effect of 2-deoxy-D-glucose on glycoprotein mannosylation in cancer cells. *IUBMB Life*, 67(3):218–226, 2015.
- [116] Aykin-Burns, N., Ahmad, I. M., Zhu, Y., Oberley, L. W., and Spitz, D. R. Increased levels of superoxide and H₂O₂ mediate the differential susceptibility of cancer cells versus normal cells to glucose deprivation. *Biochem J*, 418(1):29–37, 2009.
- [117] Maher, J. C., Krishan, A., and Lampidis, T. J. Greater cell cycle inhibition and cytotoxicity induced by 2-deoxy-D-glucose in tumor cells treated under hypoxic vs aerobic conditions. *Cancer Chemother Pharmacol*, 53(2):116–122, 2004.
- [118] Zhang, Y., Huang, F., Wang, J., Luo, H., and Wang, Z. 2-DG-Regulated RIP and c-FLIP Effect on Liver Cancer Cell Apoptosis Induced by TRAIL. *Med Sci Monitor*, 21:3442, 2015.
- [119] Yamada, M., Tomida, A., Yun, J., Cai, B., Yoshikawa, H., Taketani, Y., and Tsuruo, T. Cellular sensitization to cisplatin and carboplatin with decreased removal of platinum-DNA adduct by glucose-regulated stress. *Cancer Chemother Pharmacol*, 44(1):59–64, 1999.
- [120] Chuang, J.-H., Chou, M.-H., Tai, M.-H., Lin, T.-K., Liou, C.-W., Chen, T., Hsu, W.-M., and Wang, P.-W. 2-Deoxyglucose treatment complements the cisplatin-or BH3-only mimetic-induced suppression of neuroblastoma cell growth. *Int J Biochem Cell B*, 45(5):944–951, 2013.
- [121] Cay, O., Radnell, M., Jeppsson, B., Ahren, B., and Bengmark, S. Inhibitory effect of 2-deoxy-D-glucose on liver tumor growth in rats. *Cancer Res*, 52(20):5794–5796, 1992.
- [122] Coleman, M. C., Asbury, C. R., Daniels, D., Du, J., Aykin-Burns, N., Smith, B. J., Li, L., Spitz, D. R., and Cullen, J. J. 2-deoxy-D-glucose causes cytotoxicity, oxidative stress, and radiosensitization in pancreatic cancer. *Free Radical Bio Med*, 44(3):322–331, 2008.
- [123] Maschek, G., Savaraj, N., Priebe, W., Braunschweiger, P., Hamilton, K., Tidmarsh, G. F., De Young, L. R., and Lampidis, T. J. 2-deoxy-D-glucose increases the efficacy of adri-

- amycin and paclitaxel in human osteosarcoma and non-small cell lung cancers in vivo. *Cancer Res*, 64(1):31–34, 2004.
- [124] Cao, J., Cui, S., Li, S., Du, C., Tian, J., Wan, S., Qian, Z., Gu, Y., Chen, W. R., and Wang, G. Targeted cancer therapy with a 2-deoxyglucose–based adriamycin complex. *Cancer Res*, 73(4):1362–1373, 2013.
- [125] Kaplan, O., Navon, G., Lyon, R. C., Faustino, P. J., Straka, E. J., and Cohen, J. S. Effects of 2-deoxyglucose on drug-sensitive and drug-resistant human breast cancer cells: toxicity and magnetic resonance spectroscopy studies of metabolism. *Cancer Res*, 50(3):544–551, 1990.
- [126] Sahra, I. B., Laurent, K., Giuliano, S., Larbret, F., Ponzio, G., Gounon, P., Le Marchand-Brustel, Y., Giorgetti-Peraldi, S., Cormont, M., Bertolotto, C., Deckert, M., Auberger, P., Tanti, J.-F., and Bost, F. Targeting cancer cell metabolism: the combination of metformin and 2-deoxyglucose induces p53-dependent apoptosis in prostate cancer cells. *Cancer Res*, 70(6):2465–2475, 2010.
- [127] Singh, D., Banerji, A. K., Dwarakanath, B. S., Tripathi, R. P., Gupta, J. P., Mathew, T. L., Ravindranath, T., and Jain, V. Optimizing cancer radiotherapy with 2-deoxy-D-glucose. *Strahlenther Onkol*, 181(8):507–514, 2005.
- [128] Venkataramana, N. K., Venkatesh, P., Dwarakanath, B., and Vani, S. Protective effect on normal brain tissue during a combinational therapy of 2-deoxy-d-glucose and hypofractionated irradiation in malignant gliomas. *Asian J Neurosurg*, 8(1):9, 2013.
- [129] Landau, B. R., Laszlo, J., Stengle, J., and Burk, D. Certain metabolic and pharmacologic effects in cancer patients given infusions of 2-deoxy-D-glucose. *J Nat Cancer I*, 21(3):485–494, 1958.
- [130] Mohanti, B. K., Rath, G. K., Anantha, N., Kannan, V., Das, B. S., Chandramouli, B. A., Banerjee, A. K., Das, S., Jena, A., Ravichandran, R., Sahi, U. P., Kumar, R., Kapoor, N., Kalia, V. K., Dwarakanath, B. S., and Jain, V. Improving cancer radiotherapy with 2-deoxy-D-glucose: phase I/II clinical trials on human cerebral gliomas. *Int J Radiat Oncol Biol Phys*, 35(1):103–111, 1996.
- [131] WHO. Mean fasting blood glucose. <https://www.who.int/data/gho/indicator-metadata-registry/imr-details/2380>, 2020.10.25, 2020.
- [132] Vander Heiden, M. G. Targeting cancer metabolism: a therapeutic window opens. *Nat Rev Drug Discov*, 10(9):671–684, 2011.
- [133] Ledoux, S., Yang, R., Friedlander, G., and Laouari, D. Glucose depletion enhances P-glycoprotein expression in hepatoma cells: role of endoplasmic reticulum stress response. *Cancer Res*, 63(21):7284–7290, 2003.
- [134] Fabricant, D. S. and Farnsworth, N. R. The value of plants used in traditional medicine for drug discovery. *Environ Health Perspect*, 109(suppl 1):69–75, 2001.

- [135] Zhao, Q., Abou-Hamdan, H., and Désaubry, L. Recent advances in the synthesis of flavaglines, a family of potent bioactive natural compounds originating from traditional chinese medicine. *Eur J Org Chem*, 2016(36):5908–5916, 2016.
- [136] Bacher, M., Hofer, O., Brader, G., Vajrodaya, S., and Greger, H. Thapsakins: possible biogenetic intermediates towards insecticidal cyclopenta [b] benzofurans from *Aglaia edulis*. *Phytochemistry*, 52(2):253–263, 1999.
- [137] Ebada, S. S., Lajkiewicz, N., Porco, J. A., Li-Weber, M., and Proksch, P. Chemistry and biology of rocaglamides (= flavaglines) and related derivatives from *aglaia* species (meliaceae). In *Prog Chem Org Nat Prod*, volume 94, pages 1–58. Springer, 2011.
- [138] Pan, L., Woodard, J. L., Lucas, D. M., Fuchs, J. R., and Kinghorn, A. D. Rocaglamide, silvestrol and structurally related bioactive compounds from *Aglaia* species. *Nat Prod Rep*, 31(7):924–939, 2014.
- [139] Kim, S., Salim, A. A., Swanson, S. M., and Douglas Kinghorn, A. Potential of cyclopenta[b]benzofurans from *Aglaia* species in cancer chemotherapy. *Anticancer Agents Med Chem*, 6(4):319–345, 2006.
- [140] Harneti, D. and Supratman, U. Phytochemistry and biological activities of *Aglaia* species. *Phytochemistry*, 181:112540, 2020.
- [141] King, M. L., Chiang, C.-C., Ling, H.-C., Fujita, E., Ochiai, M., and McPhail, A. T. X-Ray crystal structure of rocaglamide, a novel antileulemic 1 H-cyclopenta-[b]-benzofuran from *Aglaia elliptifolia*. *J Chem Soc Chem Comm*, 446(20):1150–1151, 1982.
- [142] Pan, L., Acuña, U. M., Li, J., Jena, N., Ninh, T. N., Pannell, C. M., Chai, H., Fuchs, J. R., Carcache de Blanco, E. J., Soejarto, D. D., and Kinghorn, A. D. Bioactive flavaglines and other constituents isolated from *Aglaia perviridis*. *J Nat Prod*, 76(3):394–404, 2013.
- [143] An, F.-L., Wang, X.-B., Wang, H., Li, Z.-R., Yang, M.-H., Luo, J., and Kong, L.-Y. Cytotoxic rocaglate derivatives from leaves of *Aglaia perviridis*. *Sci Rep-UK*, 6:20045, 2016.
- [144] Lee, S. K., Cui, B., Mehta, R. R., Kinghorn, A. D., and Pezzuto, J. M. Cytostatic mechanism and antitumor potential of novel 1H-cyclopenta-[b]-benzofuran lignans isolated from *Aglaiaelliptica*. *Chem Biol Interact*, 115(3):215–228, 1998.
- [145] Li-Weber, M. Molecular mechanisms and anti-cancer aspects of the medicinal phytochemicals rocaglamides (= flavaglines). *Int J Cancer*, 137(8):1791–1799, 2015.
- [146] Ali, M. U., Ur Rahman, M. S., Jia, Z., and Jiang, C. Eukaryotic translation initiation factors and cancer. *Tumor Biol*, 39(6):1010428317709805, 2017.
- [147] Jackson, R. J., Hellen, C. U., and Pestova, T. V. The mechanism of eukaryotic translation initiation and principles of its regulation. *Nat Rev Mol Cell Bio*, 11(2):113–127, 2010.
- [148] Bleumink, M., Köhler, R., Giaisi, M., Proksch, P., Krammer, P. H., and Li-Weber, M. Rocaglamide breaks TRAIL resistance in HTLV-1-associated adult T-cell leukemia/lymphoma by translational suppression of c-FLIP expression. *Cell Death Differ*, 18(2):362–370, 2011.

- [149] Cencic, R., Carrier, M., Galicia-Vázquez, G., Bordeleau, M.-E., Sukarieh, R., Bourdeau, A., Brem, B., Teodoro, J. G., Greger, H., Tremblay, M. L., Porco Jr, J. A., and Pelletier, J. Antitumor activity and mechanism of action of the cyclopenta-[b]-benzofuran, silvestrol. *PLoS One*, 4(4):e5223, 2009.
- [150] Chambers, J. M., Lindqvist, L. M., Webb, A., Huang, D. C., Savage, G. P., and Rizzacasa, M. A. Synthesis of biotinylated episilvestrol: highly selective targeting of the translation factors eIF4A/II. *Org Lett*, 15(6):1406–1409, 2013.
- [151] Chu, J., Cencic, R., Wang, W., Porco, J. A., and Pelletier, J. Translation inhibition by rocaglates is independent of eIF4E phosphorylation status. *Mol Cancer Ther*, 15(1):136–141, 2016.
- [152] Iwasaki, S., Floor, S. N., and Ingolia, N. T. Rocaglates convert DEAD-box protein eIF4A into a sequence-selective translational repressor. *Nature*, 534(7608):558–561, 2016.
- [153] Hausott, B., Greger, H., and Marian, B. Flavaglines: a group of efficient growth inhibitors block cell cycle progression and induce apoptosis in colorectal cancer cells. *Int J Cancer*, 109(6):933–940, 2004.
- [154] Kim, S., Hwang, B. Y., Su, B.-N., Chai, H., Mi, Q., Kinghorn, A. D., Wild, R., and Swanson, S. M. Silvestrol, a potential anticancer rocaglate derivative from *Aglaia foveolata*, induces apoptosis in LNCaP cells through the mitochondrial/apoptosome pathway without activation of executioner caspase-3 or-7. *Anticancer Res*, 27(4B):2175–2183, 2007.
- [155] Baumann, B., Bohnenstengel, F., Siegmund, D., Wajant, H., Weber, C., Herr, I., Debatin, K.-M., Proksch, P., and Wirth, T. Rocaglamide derivatives are potent inhibitors of NF- κ B activation in T-cells. *J Biol Chem*, 277(47):44791–44800, 2002.
- [156] Nalli, A. D., Brown, L. E., Thomas, C. L., Sayers, T. J., Porco, J. A., and Henrich, C. J. Sensitization of renal carcinoma cells to TRAIL-induced apoptosis by rocaglamide and analogs. *Sci Rep-UK*, 8(1):1–11, 2018.
- [157] Lucas, D. M., Edwards, R. B., Lozanski, G., West, D. A., Shin, J. D., Vargo, M. A., Davis, M. E., Rozewski, D. M., Johnson, A. J., Su, B.-N., Goettl, V. M., Heerema, N. A., Lin, T. S., Lehman, A., Zhang, X., Jarjoura, D., Newman, D. J., Byrd, J. C., Kinghorn, A. D., and Grever, M. R. The novel plant-derived agent silvestrol has B-cell selective activity in chronic lymphocytic leukemia and acute lymphoblastic leukemia in vitro and in vivo. *Blood*, 113(19):4656–4666, 2009.
- [158] Bordeleau, M.-E., Robert, F., Gerard, B., Lindqvist, L., Chen, S. M., Wendel, H.-G., Brem, B., Greger, H., Lowe, S. W., Porco Jr, J. A., and Pelletier, J. Therapeutic suppression of translation initiation modulates chemosensitivity in a mouse lymphoma model. *J Clin Invest*, 118(7):2651–2660, 2008.
- [159] Zhao, C., He, R., Shen, M., Zhu, F., Wang, M., Liu, Y., Chen, H., Li, X., and Qin, R. PINK1/Parkin-Mediated mitophagy regulation by reactive oxygen species alleviates

- rocaglamide a-induced apoptosis in pancreatic cancer cells. *Front Pharmacol*, 10:968, 2019.
- [160] Neumann, J., Boerries, M., Köhler, R., Giaisi, M., Krammer, P. H., Busch, H., and Li-Weber, M. The natural anticancer compound rocaglamide selectively inhibits the G1-S-phase transition in cancer cells through the ATM/ATR-mediated Chk1/2 cell cycle checkpoints. *Int J Cancer*, 134(8):1991–2002, 2014.
- [161] Davey, A. E., Schaeffer, M. J., and Taylor, R. J. Synthesis of the novel anti-leukaemic tetrahydrocyclopenta [b] benzofuran, rocaglamide and related synthetic studies. *J Chem Soc, Perkin Trans 1*, 20:2657–2666, 1992.
- [162] Basmadjian, C., Thuaud, F., Ribeiro, N., and Désaubry, L. Flavaglines: potent anticancer drugs that target prohibitins and the helicase eIF4A. *Future Med Chem*, 5(18):2185–2197, 2013.
- [163] Ribeiro, N., Thuaud, F., Nebigil, C., and Désaubry, L. Recent advances in the biology and chemistry of the flavaglines. *Bioorg Med Chem*, 20(6):1857–1864, 2012.
- [164] Sadlish, H., Galicia-Vazquez, G., Paris, C. G., Aust, T., Bhullar, B., Chang, L., Helliwell, S. B., Hoepfner, D., Knapp, B., Riedl, R., Roggo, S., Schuierer, S., Studer, C., Porco Jr., J. A., Pelletier, J., and Movva, N. R. Evidence for a functionally relevant rocaglamide binding site on the eIF4A-RNA complex. *ACS Chem Biol*, 8(7):1519–1527, 2013.
- [165] Chan, K., Robert, F., Oertlin, C., Kapeller-Libermann, D., Avizonis, D., Gutierrez, J., Handly-Santana, A., Doubrovin, M., Park, J., Schoepfer, C., Da Silva, B., Yao, M., Gorton, F., Shi, J., Thomas, C. J., Brown, L. E., Porco Jr, J. A., Pollak, M., Larsson, O., Pelletier, J., and Chio, I. I. C. eIF4A supports an oncogenic translation program in pancreatic ductal adenocarcinoma. *Nat Commun*, 10(1):1–16, 2019.
- [166] Manier, S., Huynh, D., Shen, Y. J., Zhou, J., Yusufzai, T., Salem, K. Z., Ebright, R. Y., Shi, J., Park, J., Glavey, S. V., Devine, W. G., Liu, C.-J., Leleu, X., Quesnel, B., Roche-Lestienne, C., Snyder, J. K., Brown, L. E., Gray, N., Bradner, J., Whitesell, L., Porco Jr., J. A., and Ghobrial, I. M. Inhibiting the oncogenic translation program is an effective therapeutic strategy in multiple myeloma. *Sci Transl Med*, 9(389):eaal2668, 2017.
- [167] Zhang, X., Bi, C., Lu, T., Zhang, W., Yue, T., Wang, C., Tian, T., Zhang, X., Huang, Y., Lunning, M., Hao, X., Brown, L. E., Devine, W. G., Vose, J., Porco Jr., J. A., and Fu, K. Targeting translation initiation by synthetic rocaglates for treating MYC-driven lymphomas. *Leukemia*, 34(1):138–150, 2020.
- [168] Harmouch, E., Seitlinger, J., Chaddad, H., Ubeaud-Sequier, G., Barths, J., Saidu, S., Désaubry, L., Grandemange, S., Massfelder, T., Fuhrmann, G., Fioretti, F., Dentenwill, M., Benkirane-Jessel, N., and Idoux-Gillet, Y. Flavagline synthetic derivative induces senescence in glioblastoma cancer cells without being toxic to healthy astrocytes. *Sci Rep-UK*, 10(1):1–16, 2020.
- [169] Thuaud, F., Bernard, Y., Türkeri, G., Dirr, R., Aubert, G., Cresteil, T., Baguet, A., Tomasetto, C., Svitkin, Y., Sonenberg, N., Nebigil, C. G., and Désaubry, L. Synthetic

- analogue of rocaglaol displays a potent and selective cytotoxicity in cancer cells: involvement of apoptosis inducing factor and caspase-12. *J Med Chem*, 52(16):5176–5187, 2009.
- [170] Bernard, Y., Ribeiro, N., Thuaud, F., Türkeri, G., Dirr, R., Boulberdaa, M., Nebigil, C. G., and Désaubry, L. Flavaglines alleviate doxorubicin cardiotoxicity: implication of Hsp27. *PLoS One*, 6(10):e25302, 2011.
- [171] Ribeiro, N., Thuaud, F., Bernard, Y., Gaiddon, C., Cresteil, T., Hild, A., Hirsch, E. C., Michel, P. P., Nebigil, C. G., and Désaubry, L. Flavaglines as potent anticancer and cytoprotective agents. *J Med Chem*, 55(22):10064–10073, 2012.
- [172] Sikorski, R. *A Phase 1-2 Dose-Escalation and Cohort-Expansion Study of Intravenous Zotatfin (eFT226) in Subjects With Selected Advanced Solid Tumor Malignancies, NCT04092673*, <https://clinicaltrials.gov/ct2/show/NCT04092673>, 2019.
- [173] Gordon, D. E., Jang, G. M., Bouhaddou, M., Xu, J., Obernier, K., White, K. M., O’Meara, M. J., Rezelj, V. V., Guo, J. Z., Swaney, D. L., et al. A SARS-CoV-2 protein interaction map reveals targets for drug repurposing. *Nature*, 583(7816):459–468, 2020.
- [174] Santagata, S., Mendillo, M. L., Tang, Y.-c., Subramanian, A., Perley, C. C., Roche, S. P., Wong, B., Narayan, R., Kwon, H., Koeva, M., Amon, A., Golub, T. R., Porco Jr, J. A., Whitesell, L., and Lindquist, S. Tight coordination of protein translation and HSF1 activation supports the anabolic malignant state. *Science*, 341(6143):1238303–1–10, 2013.
- [175] Wabnitz, P., Henkel, T., and Lienhard Schitz, M. Inhibitors of HIF-1 protein accumulation (US20120040956A1), February 2012.
- [176] Kuipers, E. J., Grady, W. M., Lieberman, D., Seufferlein, T., Sung, J. J., Boelens, P. G., H. van de Velde, C. J., and Watanabe, T. Colorectal cancer. *Nat Rev Dis Primers*, 1, 2015.
- [177] Haggard, F. A. and Boushey, R. P. Colorectal cancer epidemiology: incidence, mortality, survival, and risk factors. *Clin Colon Rectal Surg*, 22(4):191, 2009.
- [178] O’Connell, J. B., Maggard, M. A., and Ko, C. Y. Colon cancer survival rates with the new American Joint Committee on Cancer sixth edition staging. *J Natl Cancer Inst*, 96(19):1420–1425, 2004.
- [179] Markowitz, S. D. and Bertagnolli, M. M. Molecular basis of colorectal cancer. *New Engl J Med*, 361(25):2449–2460, 2009.
- [180] Winawer, S. J., Zauber, A. G., Ho, M. N., O’Brien, M. J., Gottlieb, L. S., Sternberg, S. S., Waye, J. D., Schapiro, M., Bond, J. H., Panish, J. F., Ackroyd, F., Shike, M., Kurtz, R. C., Hornsby-Lewis, L., Gerdes, H., Stewart, E. T., and the National Polyp Study Workgroup. Prevention of colorectal cancer by colonoscopic polypectomy. *New Engl J Med*, 329(27):1977–1981, 1993.
- [181] Brenner, H., Kloor, M., and Pox, C. Colorectal cancer. *Lancet*, 383(9927):1490–1502, 2014.

- [182] German Guideline Program in Oncology. Evidence-based Guideline for Colorectal Cancer. *AWMF online*, 2.1:1–322: AWMF–Registration Number: 021/007OL, January 2019.
- [183] Siegel, R. L., Jemal, A., and Ward, E. M. Increase in incidence of colorectal cancer among young men and women in the United States. *Cancer Epidemiol Biomarkers Prev*, 18(6):1695–1698, 2009.
- [184] Vuik, F. E., Nieuwenburg, S. A., Bardou, M., Lansdorp-Vogelaar, I., Dinis-Ribeiro, M., Bento, M. J., Zadnik, V., Pellisé, M., Esteban, L., Kaminski, M. F., Suchanek, S., Ngo, O., Májek, O., Leja, M., Kuipers, E., and Spaander, M. C. Increasing incidence of colorectal cancer in young adults in Europe over the last 25 years. *Gut*, 68(10):1820–1826, 2019.
- [185] Kloor, M., Staffa, L., Ahadova, A., and von Knebel Doeberitz, M. Clinical significance of microsatellite instability in colorectal cancer. *Langenbecks Arch Surg*, 399(1):23–31, 2014.
- [186] Kinzler, K. W. and Vogelstein, B. Lessons from hereditary colorectal cancer. *Cell*, 87(2):159–170, 1996.
- [187] Lynch, H. T. and De la Chapelle, A. Hereditary colorectal cancer. *New Engl J Med*, 348(10):919–932, 2003.
- [188] Stoffel, E. M. and Kastrinos, F. Familial colorectal cancer, beyond Lynch syndrome. *Clin Gastroenterol Hepatol*, 12(7):1059–1068, 2014.
- [189] De Jong, A. E., Morreau, H., Van Puijenbroek, M., Eilers, P. H., Wijnen, J., Nagengast, F. M., Griffioen, G., Cats, A., Menko, F. H., Kleibeuker, J. H., and Vasen, H. F. A. The role of mismatch repair gene defects in the development of adenomas in patients with HNPCC. *Gastroenterology*, 126(1):42–48, 2004.
- [190] Ahadova, A., Gallon, R., Gebert, J., Ballhausen, A., Endris, V., Kirchner, M., Stenzinger, A., Burn, J., von Knebel Doeberitz, M., Bläker, H., and Kloor, M. Three molecular pathways model colorectal carcinogenesis in Lynch syndrome. *Int J Cancer*, 143(1):139–150, 2018.
- [191] Møller, P., Seppälä, T., Bernstein, I., Holinski-Feder, E., Sala, P., Evans, D. G., Lindblom, A., Macrae, F., Blanco, I., Sijmons, R., Jeffries, J., Vasen, H., Burn, J., Nakken, S., Hovig, E., Rødland, E. A., Tharmaratnam, K., de Vos tot Nederveen Cappel, W. H., Hill, J., Wijnen, J., Green, K., Lalloo, F., Sunde, L., Mints, M., Bertario, L., Pineda, M., Navarro, M., Morak, M., Renkonen-Sinisalo, L., Frayling, I. M., Plazzer, J.-P., Pylvänäinen, K., Sampson, J. R., Capella, G., Mecklin, J.-P., and Möslein, Gabriela, T. M. G. h.-g. Cancer incidence and survival in Lynch syndrome patients receiving colonoscopic and gynaecological surveillance: first report from the prospective Lynch syndrome database. *Gut*, 66(3):464–472, 2017.
- [192] Dominguez-Valentin, M., Seppälä, T. T., Sampson, J. R., Macrae, F., Winship, I., Evans, D. G., Scott, R. J., Burn, J., Möslein, G., Bernstein, I., Pylvänäinen, K., Renkonen-Sinisalo, L., Lepistö, A., Lindblom, A., Plazzer, J.-P., Tjandra, D., Thomas, H., Green,

- K., Lalloo, F., Crosbie, E. J., Hill, J., Capella, G., Pineda, M., Navarro, M., Brunet Vidal, J., Rønlund, K., Thyregaard Nielsen, R., Yilamz, M., Laurberg Elvang, L., Katz, L., Nielsen, M., ten Broeke, S. W., Nakken, S., Hovig, E., Sunde, L., Kloor, M., von Knebel Doeberitz, M., Ahadova, A., Lindor, N., Steinke-Lange, V., Holinski-Feder, E., Meckling, J.-P., and Møller, P. Survival by colon cancer stage and screening interval in Lynch syndrome: a prospective Lynch syndrome database report. *Hered Cancer Clin Pract*, 17(1):1–6, 2019.
- [193] Boland, C. R. and Goel, A. Microsatellite instability in colorectal cancer. *Gastroenterology*, 138(6):2073–2087, 2010.
- [194] Knudson, A. G. Mutation and cancer: statistical study of retinoblastoma. *Proc Natl Acad Sci USA*, 68(4):820–823, 1971.
- [195] Woerner, S. M., Kloor, M., Mueller, A., Rueschoff, J., Friedrichs, N., Buettner, R., Buzello, M., Kienle, P., Knaebel, H.-P., Kunstmann, E., Pagenstecher, C., Schackert, H. K., Möslein, G., Vogelsang, H., von Knebel Doeberitz, M., and Gebert, J. F. Microsatellite instability of selective target genes in HNPCC-associated colon adenomas. *Oncogene*, 24(15):2525–2535, 2005.
- [196] Woerner, S. M., Yuan, Y. P., Benner, A., Korff, S., von Knebel Doeberitz, M., and Bork, P. SelTar base, a database of human mononucleotide-microsatellite mutations and their potential impact to tumorigenesis and immunology. *Nucleic Acids Res*, 38(suppl_1):D682–D689, 2010.
- [197] Kloor, M. and von Knebel Doeberitz, M. The Immune Biology of Microsatellite-Unstable Cancer. *Trends Cancer*, 2(3):121–133, March 2016.
- [198] Dolcetti, R., Viel, A., Doglioni, C., Russo, A., Guidoboni, M., Capozzi, E., Vecchiato, N., Macrì, E., Fornasarig, M., and Boiocchi, M. High prevalence of activated intraepithelial cytotoxic T lymphocytes and increased neoplastic cell apoptosis in colorectal carcinomas with microsatellite instability. *Am J Pathol*, 154(6):1805–1813, 1999.
- [199] Buckowitz, A., Knaebel, H., Benner, A., Bläker, H., Gebert, J., Kienle, P., von Knebel Doeberitz, M., and Kloor, M. Microsatellite instability in colorectal cancer is associated with local lymphocyte infiltration and low frequency of distant metastases. *Brit J Cancer*, 92(9):1746, 2005.
- [200] Janikovits, J., Müller, M., Krzykalla, J., Körner, S., Echterdiek, F., Lahrmann, B., Grabe, N., Schneider, M., Benner, A., Doeberitz, M. v. K., and Kloor, M. High numbers of PDCD1 (PD-1)-positive T cells and B2M mutations in microsatellite-unstable colorectal cancer. *Oncoimmunology*, 7(2):e1390640, 2018.
- [201] Ballhausen, A., Przybilla, M. J., Jendrusch, M., Haupt, S., Pfaffendorf, E., Seidler, F., Witt, J., Hernandez Sanchez, A., Urban, K., Draxlbauer, M., Krausert, S., Ahadova, A., Kalteis, M. S., Pfuderer, P. L., Heid, D., Stichel, D., Gebert, J., Bonsack, M., Schott, S., Bläker, H., Seppälä, T., Mecklin, J.-P., Broeke, S. T., Nielsen, M., Heuveline, V., Krzykalla, J., Benner, A., Riemer, A. B., von Knebel Doeberitz, M., and Kloor, M.

- The shared frameshift mutation landscape of microsatellite-unstable cancers suggests immunoediting during tumor evolution. *Nat Commun*, 11(1):1–13, 2020.
- [202] Ribic, C. M., Sargent, D. J., Moore, M. J., Thibodeau, S. N., French, A. J., Goldberg, R. M., Hamilton, S. R., Laurent-Puig, P., Gryfe, R., Shepherd, L. E., Tu, D., Redston, M., and Gallinger, S. Tumor microsatellite-instability status as a predictor of benefit from fluorouracil-based adjuvant chemotherapy for colon cancer. *N Engl J Med*, 349(3):247–257, 2003.
- [203] Benson III, A. B., Schrag, D., Somerfield, M. R., Cohen, A. M., Figueredo, A. T., Flynn, P. J., Krzyzanowska, M. K., Maroun, J., McAllister, P., Van Cutsem, E., Brouwers, M., Charette, M., and Haller, D. G. American Society of Clinical Oncology recommendations on adjuvant chemotherapy for stage II colon cancer. *J Clin Oncol*, 22(16):3408–3419, 2004.
- [204] Fallik, D., Borrini, F., Boige, V., Viguier, J., Jacob, S., Miquel, C., Sabourin, J.-C., Ducreux, M., and Praz, F. Microsatellite instability is a predictive factor of the tumor response to irinotecan in patients with advanced colorectal cancer. *Cancer Res*, 63(18):5738–5744, 2003.
- [205] Meyerhardt, J. A. and Mayer, R. J. Systemic therapy for colorectal cancer. *New Engl J Med*, 352(5):476–487, 2005.
- [206] Jonker, D. J., O’Callaghan, C. J., Karapetis, C. S., Zalcborg, J. R., Tu, D., Au, H.-J., Berry, S. R., Krahn, M., Price, T., Simes, R. J., Tebbutt, N. C., van Hazel, G., Wierzbicki, R., Langer, C., and Moore, M. J. Cetuximab for the treatment of colorectal cancer. *New Engl J Med*, 357(20):2040–2048, 2007.
- [207] Lech, G., Słotwiński, R., Słodkowski, M., and Krasnodębski, I. W. Colorectal cancer tumour markers and biomarkers: Recent therapeutic advances. *World J Gastroenterol*, 22(5):1745, 2016.
- [208] Boyiadzis, M. M., Kirkwood, J. M., Marshall, J. L., Pritchard, C. C., Azad, N. S., and Gulley, J. L. Significance and implications of FDA approval of pembrolizumab for biomarker-defined disease. *J Immunother Cancer*, 6(1):1–7, 2018.
- [209] Hammond, W. A., Swaika, A., and Mody, K. Pharmacologic resistance in colorectal cancer: a review. *Ther Adv Med Oncol*, 8(1):57–84, 2016.
- [210] Cha, P.-H., Hwang, J.-H., Kwak, D.-K., Koh, E., Kim, K.-S., and Choi, K.-Y. APC loss induces Warburg effect via increased PKM2 transcription in colorectal cancer. *Brit J Cancer*, published online:1–11, 2020.
- [211] Wang, J., Wang, H., Liu, A., Fang, C., Hao, J., and Wang, Z. Lactate dehydrogenase A negatively regulated by miRNAs promotes aerobic glycolysis and is increased in colorectal cancer. *Oncotarget*, 6(23):19456, 2015.
- [212] Satoh, K., Yachida, S., Sugimoto, M., Oshima, M., Nakagawa, T., Akamoto, S., Tabata, S., Saitoh, K., Kato, K., Sato, S., Igarashi, K., Aizawa, Y., Kajino-Sakamoto, R., Kojima, Y., Fujishita, T., Enomoto, A., Hirayama, A., Ishikawa, T., Taketo, M. M., Kushida, Y.,

- Haba, R., Okano, K., Tomita, M., Suzuki, Y., Fukuda, S., Aoki, M., and Soga, T. Global metabolic reprogramming of colorectal cancer occurs at adenoma stage and is induced by MYC. *Proc Natl Acad Sci USA*, 114(37):E7697–E7706, 2017.
- [213] de Martel, C., Georges, D., Bray, F., Ferlay, J., and Clifford, G. M. Global burden of cancer attributable to infections in 2018: a worldwide incidence analysis. *Lancet Glob Health*, 8(2):e180–e190, 2020.
- [214] Mittal, S. and Banks, L. Molecular mechanisms underlying human papillomavirus E6 and E7 oncoprotein-induced cell transformation. *Mutat Res Rev Mutat Res*, 772:23–35, 2017.
- [215] de Martel, C., Plummer, M., Vignat, J., and Franceschi, S. Worldwide burden of cancer attributable to HPV by site, country and HPV type. *Int J Cancer*, 141(4):664–670, 2017.
- [216] Martínez-Ramírez, I., Carrillo-García, A., Contreras-Paredes, A., Ortiz-Sánchez, E., Cruz-Gregorio, A., and Lizano, M. Regulation of Cellular Metabolism by High-Risk Human Papillomaviruses. *Int J Mol Sci*, 19(7):1839, 2018.
- [217] Schiffman, M., Castle, P. E., Jeronimo, J., Rodriguez, A. C., and Wacholder, S. Human papillomavirus and cervical cancer. *Lancet*, 370(9590):890–907, 2007.
- [218] Prigge, E. S., von Knebel Doeberitz, M., and Reuschenbach, M. Clinical relevance and implications of HPV-induced neoplasia in different anatomical locations. *Mutat Res Rev Mutat Res*, 772:51–66, 2017.
- [219] Doorbar, J., Quint, W., Banks, L., Bravo, I. G., Stoler, M., Broker, T. R., and Stanley, M. A. The biology and life-cycle of human papillomaviruses. *Vaccine*, 30:F55–F70, 2012.
- [220] Doorbar, J. Molecular biology of human papillomavirus infection and cervical cancer. *Clin Sci (Lond)*, 110(5):525–541, 2006.
- [221] von Knebel Doeberitz, M. and Vinokurova, S. Host factors in HPV-related carcinogenesis: cellular mechanisms controlling HPV infections. *Arch Med Res*, 40(6):435–442, 2009.
- [222] Doorbar, J. Latent papillomavirus infections and their regulation. *Curr Opin Virol*, 3(4):416–421, 2013.
- [223] Vinokurova, S. and von Knebel Doeberitz, M. Differential methylation of the HPV 16 upstream regulatory region during epithelial differentiation and neoplastic transformation. *PLoS one*, 6(9):e24451, 2011.
- [224] Moody, C. A. and Laimins, L. A. Human papillomavirus oncoproteins: pathways to transformation. *Nat Rev Cancer*, 10(8):550–560, 2010.
- [225] Thuesen, B., Andreasson, B., and Bock, J. E. Sexual function and somatopsychic reactions after local excision of vulvar intra-epithelial neoplasia. *Acta Obstet Gynecol Scand*, 71(2):126–128, 1992.
- [226] Green, M. S., Naumann, R. W., Elliot, M., Hall, J. B., Higgins, R. V., and Grigsby, J. H. Sexual dysfunction following vulvectomy. *Gynecol Oncol*, 77(1):73–77, 2000.

- [227] Kyrgiou, M., Koliopoulos, G., Martin-Hirsch, P., Arbyn, M., Prendiville, W., and Paraskevaïdis, E. Obstetric outcomes after conservative treatment for intraepithelial or early invasive cervical lesions: systematic review and meta-analysis. *Lancet*, 367(9509):489–498, 2006.
- [228] Turner, M. T., Byrd, J. K., and Ferris, R. L. Current role of surgery in the management of oropharyngeal cancer. *J Oncol Pract*, 12(11):1176–1183, 2016.
- [229] Wallbillich, J. J., Rhodes, H., Milbourne, A., Munsell, M., Frumovitz, M., Brown, J., Trimble, C. L., and Schmeler, K. Vulvar intraepithelial neoplasia (VIN 2/3): comparing clinical outcomes and evaluating risk factors for recurrence. *Gynecol Oncol*, 127(2):312–315, 2012.
- [230] Ang, K. K., Harris, J., Wheeler, R., Weber, R., Rosenthal, D. I., Nguyen-Tân, P. F., Westra, W. H., Chung, C. H., Jordan, R. C., Lu, C., Kim, H., Axelrod, R., Silverman, C. C., Redmond, K. P., and Gillison, M. L. Human papillomavirus and survival of patients with oropharyngeal cancer. *New Engl J Med*, 363(1):24–35, 2010.
- [231] Mirghani, H. and Blanchard, P. Treatment de-escalation for HPV-driven oropharyngeal cancer: where do we stand? *Clin Transl Radiat Oncol*, 8:4–11, 2018.
- [232] Seiwert, T. Y., Zuo, Z., Keck, M. K., Khattri, A., Pedomallu, C. S., Stricker, T., Brown, C., Pugh, T. J., Stojanov, P., Cho, J., Lawrence, M. S., Getz, G., Brägelmann, J., DeBoer, R., Weichselbaum, R. R., Langerman, A., Portugal, L., Blair, E., Stenson, K., Lingen, M. W., Cohen, E. E. W., Vokes, E. E., White, K. P., and Hammerman, P. S. Integrative and comparative genomic analysis of HPV-positive and HPV-negative head and neck squamous cell carcinomas. *Clin Cancer Res*, 21(3):632–641, 2015.
- [233] Chung, J., Sanford, E., Johnson, A., Klempner, S., Schrock, A., Palma, N., Erlich, R., Frampton, G., Chalmers, Z., Vergilio, J., Rubinson, D. A., Sun, J. X., Chmielecki, J., Yelensky, R., Suh, J. H., Lipson, D., George Jr, T. J., Elvin, J. A., Stephens, P. J., Miller, V. A., Ross, J. S., and Ali, S. M. Comprehensive genomic profiling of anal squamous cell carcinoma reveals distinct genomically defined classes. *Ann Oncol*, 27(7):1336–1341, 2016.
- [234] Krupar, R., Robold, K., Gaag, D., Spanier, G., Kreutz, M., Renner, K., Hellerbrand, C., Hofstaedter, F., and Bosserhoff, A. K. Immunologic and metabolic characteristics of HPV-negative and HPV-positive head and neck squamous cell carcinomas are strikingly different. *Virchows Arch*, 465(3):299–312, 2014.
- [235] Martinho, O., Silva-Oliveira, R., Cury, F. P., Barbosa, A. M., Granja, S., Evangelista, A. F., Marques, F., Miranda-Gonçalves, V., Cardoso-Carneiro, D., de Paula, F. E., Zanon, M., Scapulatempo-Neto, C., Moreira, M. A. R., Baltazar, F., Longatto-Filho, A., and Reis, R. M. HER family receptors are important theranostic biomarkers for cervical cancer: blocking glucose metabolism enhances the therapeutic effect of HER inhibitors. *Theranostics*, 7(3):717, 2017.

- [236] Coppock, J. D., Wieking, B. G., Molinolo, A. A., Gutkind, J. S., Miskimins, W. K., and Lee, J. H. Improved clearance during treatment of HPV-positive head and neck cancer through mTOR inhibition. *Neoplasia*, 15(6):620–IN10, 2013.
- [237] Hoppe-Seyler, K., Honegger, A., Bossler, F., Sponagel, J., Bulkescher, J., Lohrey, C., and Hoppe-Seyler, F. Viral E6/E7 oncogene and cellular hexokinase 2 expression in HPV-positive cancer cell lines. *Oncotarget*, 8(63):106342, 2017.
- [238] Hoppe-Seyler, K., Bossler, F., Braun, J. A., Herrmann, A. L., and Hoppe-Seyler, F. The HPV E6/E7 oncogenes: key factors for viral carcinogenesis and therapeutic targets. *Trends Microbiol*, 26(2):158–168, 2018.
- [239] Guo, Y., Meng, X., Ma, J., Zheng, Y., Wang, Q., Wang, Y., and Shang, H. Human papillomavirus 16 E6 contributes HIF-1 α induced Warburg effect by attenuating the VHL-HIF-1 α interaction. *Int J Mol Sci*, 15(5):7974–7986, 2014.
- [240] Leiker, A. J., DeGraff, W., Choudhuri, R., Sowers, A. L., Thetford, A., Cook, J. A., Van Waes, C., and Mitchell, J. B. Radiation enhancement of head and neck squamous cell carcinoma by the dual PI3K/mTOR inhibitor PF-05212384. *Clin Cancer Res*, 21(12):2792–2801, 2015.
- [241] Qin, S., Jiang, J., Lu, Y., Nice, E. C., Huang, C., Zhang, J., and He, W. Emerging role of tumor cell plasticity in modifying therapeutic response. *Signal Transduct Target Ther*, 5(1):1–36, 2020.
- [242] Jenkins, R. W., Barbie, D. A., and Flaherty, K. T. Mechanisms of resistance to immune checkpoint inhibitors. *Brit J Cancer*, 118(1):9–16, 2018.
- [243] Zugazagoitia, J., Guedes, C., Ponce, S., Ferrer, I., Molina-Pinelo, S., and Paz-Ares, L. Current challenges in cancer treatment. *Clin Ther*, 38(7):1551–1566, 2016.
- [244] Holohan, C., Van Schaeybroeck, S., Longley, D. B., and Johnston, P. G. Cancer drug resistance: an evolving paradigm. *Nat Rev Cancer*, 13(10):714–726, 2013.
- [245] Misale, S., Yaeger, R., Hobor, S., Scala, E., Janakiraman, M., Liska, D., Valtorta, E., Schiavo, R., Buscarino, M., Siravegna, G., Bencardino, K., Cercek, A., Chen, C.-T., Veronese, S., Zanon, C., Sartore-Bianchi, A., Gambacorta, M., Gallicchio, M., Vakiani, E., Boscaro, V., Medico, E., Weiser, M., Siena, S., Di Nicolantonio, F., Solit, D., and Bardelli, A. Emergence of KRAS mutations and acquired resistance to anti-EGFR therapy in colorectal cancer. *Nature*, 486(7404):532–536, 2012.
- [246] Zaretsky, J. M., Garcia-Diaz, A., Shin, D. S., Escuin-Ordinas, H., Hugo, W., Hu-Lieskovan, S., Torrejon, D. Y., Abril-Rodriguez, G., Sandoval, S., Barthly, L., Saco, J., Homet Moreno, B., Mezzadra, R., Chmielowski, B., Ruchalski, K., Shintaku, P., Sanchez, P. J., Puig-Saus, C., Cherry, G., Seja, E., Kong, X., Pang, J., Berent-Maoz, B., Comin-Anduix, B. n., Graeber, T. G., Tume, P. C., Schumacher, T. N. M., Lo, R. S., and Ribas, A. Mutations associated with acquired resistance to PD-1 blockade in melanoma. *New Engl J Med*, 375(9):819–829, 2016.

- [247] Sade-Feldman, M., Jiao, Y. J., Chen, J. H., Rooney, M. S., Barzily-Rokni, M., Eliane, J.-P., Bjorgaard, S. L., Hammond, M. R., Vitzthum, H., Blackmon, S. M., Frederick, D. T., Hazar-Rethinam, M., Nades, B. A., Van Seventer, E. E., Shukla, S. A., Yizhak, K., Ray, J. P., Rosebrock, D., Livitz, D., Adalsteinsson, V., Getz, G., Ducan, L. M., Li, B., Corcoran, R. B., Lawrence, D. P., Stemmer-Rachamimov, A., Boland, G. M., Landau, D. A., Flaherty, K. T., Sullivan, R. J., and Hacohen, N. Resistance to checkpoint blockade therapy through inactivation of antigen presentation. *Nat Commun*, 8(1):1–11, 2017.
- [248] Glasspool, R., Teodoridis, J. M., and Brown, R. Epigenetics as a mechanism driving polygenic clinical drug resistance. *Brit J Cancer*, 94(8):1087–1092, 2006.
- [249] Rando, O. J. and Verstrepen, K. J. Timescales of genetic and epigenetic inheritance. *Cell*, 128(4):655–668, 2007.
- [250] Pisco, A. O., Brock, A., Zhou, J., Moor, A., Mojtahedi, M., Jackson, D., and Huang, S. Non-Darwinian dynamics in therapy-induced cancer drug resistance. *Nat Commun*, 4(1):1–11, 2013.
- [251] Zhao, Y., Butler, E. B., and Tan, M. Targeting cellular metabolism to improve cancer therapeutics. *Cell Death Dis*, 4(3):e532, 2013.
- [252] Gu, X., Tohme, R., Tomlinson, B., Sakre, N., Hasipek, M., Durkin, L., Schuerger, C., Grabowski, D., Zidan, A. M., Radivoyevitch, T., Hong, C., Carraway, H., Hamilton, B., Sobecks, R., Patel, B., Jha, B. K., Hsi, E. D., Maciejewski, J., and Sauntharajah, Y. Decitabine-and 5-azacytidine resistance emerges from adaptive responses of the pyrimidine metabolism network. *Leukemia*, Epub:1–14, 2020.
- [253] Friesen, C., Kiess, Y., and Debatin, K.-M. A critical role of glutathione in determining apoptosis sensitivity and resistance in leukemia cells. *Cell Death Differ*, 11(1):S73–S85, 2004.
- [254] Estrela, J. M., Ortega, A., and Obrador, E. Glutathione in cancer biology and therapy. *Crit Rev Clin Lab Sci*, 43(2):143–181, 2006.
- [255] Hulleman, E., Kazemier, K. M., Holleman, A., VanderWeele, D. J., Rudin, C. M., Broekhuis, M. J., Evans, W. E., Pieters, R., and Den Boer, M. L. Inhibition of glycolysis modulates prednisolone resistance in acute lymphoblastic leukemia cells. *Blood*, 113(9):2014–2021, 2009.
- [256] Vasan, N., Baselga, J., and Hyman, D. M. A view on drug resistance in cancer. *Nature*, 575(7782):299–309, 2019.
- [257] Bankhead, P., Loughrey, M. B., Fernández, J. A., Dombrowski, Y., McArt, D. G., Dunne, P. D., McQuaid, S., Gray, R. T., Murray, L. J., Coleman, H. G., James, J. A., Salto-Tellez, M., and Hamilton, P. W. QuPath: Open source software for digital pathology image analysis. *Sci Rep-UK*, 7(1):1–7, 2017.
- [258] Brenner, J. C., Graham, M. P., Kumar, B., Saunders, L. M., Kupfer, R., Lyons, R. H., Bradford, C. R., and Carey, T. E. Genotyping of 73 UM-SCC head and neck squamous cell carcinoma cell lines. *Head Neck-J Sci Spec*, 32(4):417–426, 2010.

- [259] Tang, A. L., Hauff, S. J., Owen, J. H., Graham, M. P., Czerwinski, M. J., Park, J. J., Walline, H., Papagerakis, S., Stoerker, J., and McHugh, J. B. a. UM-SCC-104: A New human papillomavirus-16-positive cancer stem cell-containing head and neck squamous cell carcinoma cell line. *Head Neck*, 34(10):1480–1491, 2012.
- [260] Castro, F., Dirks, W. G., Fähnrich, S., Hotz-Wagenblatt, A., Pawlita, M., and Schmitt, M. High-throughput SNP-based authentication of human cell lines. *Int J Cancer*, 132(2):308–314, 2013.
- [261] Bürckstümmer, T., Banning, C., Hainzl, P., Schobesberger, R., Kerzendorfer, C., Pauler, F. M., Chen, D., Them, N., Schischlik, F., Rebsamen, M., Smida, M., Fece de la Cruz, F., Lapao, A., Liszt, M., Eizinger, B., Guenzl, P. M., Blumen, V. A., Konopka, T., Gapp, B., Parapatics, K., Maier, B., Stöckl, J., Fischl, W., Salic, S., Casari, M. R. T., Knapp, S., Bennett, K. L., Bock, C., Colinge, J., Kralovics, R., Ammerer, G., Casari, G., Brummelkamp, T. R., Superti-Furga, G., and Nijman, S. M. B. A reversible gene trap collection empowers haploid genetics in human cells. *Nat Methods*, 10(10):965–971, 2013.
- [262] Dunning, M. J., Smith, M. L., Ritchie, M. E., and Tavaré, S. beadarray: R classes and methods for Illumina bead-based data. *Bioinformatics*, 23(16):2183–2184, 2007.
- [263] Ritchie, M. E., Phipson, B., Wu, D., Hu, Y., Law, C. W., Shi, W., and Smyth, G. K. limma powers differential expression analyses for RNA-sequencing and microarray studies. *Nucleic Acids Res*, 43(7):e47–e47, 2015.
- [264] Benjamini, Y. and Hochberg, Y. Controlling the false discovery rate: a practical and powerful approach to multiple testing. *J R Stat Soc: series B (Methodological)*, 57(1):289–300, 1995.
- [265] Wickham, H., Averick, M., Bryan, J., Chang, W., McGowan, L. D., François, R., Grolemund, G., Hayes, A., Henry, L., Hester, J., Kuhn, M., Pedersen, T. L., Miller, E., Bache, S. M., Müller, K., Ooms, J., Robinson, D., Seidel, D. P., Spinu, V., Takahashi, K., Vaughan, D., Wilke, C., Woo, K., and Yutani, H. Welcome to the tidyverse. *Journal of Open Source Software*, 4(43):1686, 2019.
- [266] Wickham, H. and Bryan, J. *readxl: Read Excel Files*, 2019. R package version 1.3.1.
- [267] Ooms, J. *writexl: Export Data Frames to Excel 'xlsx' Format*, 2019. R package version 1.2.
- [268] Chen, H. *VennDiagram: Generate High-Resolution Venn and Euler Plots*, 2018. R package version 1.6.20.
- [269] Wickham, H., François, R., Henry, L., and Müller, K. *dplyr: A Grammar of Data Manipulation*, 2020. R package version 0.8.5.
- [270] Warnes, G. R., Bolker, B., Bonebakker, L., Gentleman, R., Huber, W., Liaw, A., Lumley, T., Maechler, M., Magnusson, A., Moeller, S., Schwartz, M., and Venables, B. *gplots: Various R Programming Tools for Plotting Data*, 2020. R package version 3.0.3.
- [271] Neuwirth, E. *RColorBrewer: ColorBrewer Palettes*, 2014. R package version 1.1-2.

- [272] Wickham, H. *ggplot2: Elegant Graphics for Data Analysis*. Springer-Verlag New York, 2016.
- [273] Wickham, H. and Seidel, D. *scales: Scale Functions for Visualization*, 2019. R package version 1.1.0.
- [274] Bollati, V., Baccarelli, A., Hou, L., Bonzini, M., Fustinoni, S., Cavallo, D., Byun, H.-M., Jiang, J., Marinelli, B., Pesatori, A. C., Bertazzi, P. A., and Yang, A. S. Changes in DNA methylation patterns in subjects exposed to low-dose benzene. *Cancer Res*, 67(3):876–880, 2007.
- [275] Kile, M. L., Baccarelli, A., Tarantini, L., Hoffman, E., Wright, R. O., and Christiani, D. C. Correlation of global and gene-specific DNA methylation in maternal-infant pairs. *PLoS one*, 5(10):e13730, 2010.
- [276] Yang, A. S., Estécio, M. R., Doshi, K., Kondo, Y., Tajara, E. H., and Issa, J.-P. J. A simple method for estimating global DNA methylation using bisulfite PCR of repetitive DNA elements. *Nucleic Acids Res*, 32(3):e38–e38, 2004.
- [277] Saiki, R. K., Gelfand, D. H., Stoffel, S., Scharf, S. J., Higuchi, R., Horn, G. T., Mullis, K. B., and Erlich, H. A. Primer-directed enzymatic amplification of DNA with a thermostable DNA polymerase. *Science*, 239(4839):487–491, 1988.
- [278] Nyrén, P., Pettersson, B., and Uhlén, M. Solid phase DNA minisequencing by an enzymatic luminometric inorganic pyrophosphate detection assay. *Anal Biochem*, 208(1):171–175, 1993.
- [279] Tost, J. and Gut, I. G. DNA methylation analysis by pyrosequencing. *Nat Protoc*, 2(9):2265, 2007.
- [280] Uhlmann, K., Brinckmann, A., Toliat, M. R., Ritter, H., and Nürnberg, P. Evaluation of a potential epigenetic biomarker by quantitative methyl-single nucleotide polymorphism analysis. *Electrophoresis*, 23(24):4072–4079, 2002.
- [281] Bradford, M. M. A rapid and sensitive method for the quantitation of microgram quantities of protein utilizing the principle of protein-dye binding. *Anal Biochem*, 72(1-2):248–254, 1976.
- [282] Laemmli, U. K. Cleavage of structural proteins during the assembly of the head of bacteriophage T4. *Nature*, 227(5259):680–685, 1970.
- [283] Towbin, H., Staehelin, T., and Gordon, J. Electrophoretic transfer of proteins from polyacrylamide gels to nitrocellulose sheets: procedure and some applications. *Proc Natl Acad Sci USA*, 76(9):4350–4354, 1979.
- [284] Faustino-Rocha, A., Oliveira, P. A., Pinho-Oliveira, J., Teixeira-Guedes, C., Soares-Maia, R., Da Costa, R. G., Colaço, B., Pires, M. J., Colaço, J., Ferreira, R., and Ginja, M. Estimation of rat mammary tumor volume using caliper and ultrasonography measurements. *Lab Anim (NY)*, 42(6):217–224, 2013.
- [285] GraphPad Software. GraphPad Knowledgebase - article #189, How to get "exact P values" from multiple comparisons tests that follow one-way or two-

- way ANOVA. <https://www.graphpad.com/support/faq/how-to-get-exact-p-values-from-multiple-comparisons-tests-that-follow-one-way-or-two-way-anova/>, 2021.01.27, 2015.
- [286] GraphPad Software. GraphPad Knowledgebase - Article #1655, Multiple comparisons of survival curves. <https://www.graphpad.com/support/faq/multiple-comparisons-of-survival-curves/>, 2021.01.31, 2010.
- [287] Sieber-Frank, J. Targeting glucose metabolism of cancer cells by novel anti-cancer agents (Master Thesis). Master's thesis, Ruprecht-Karls-University Heidelberg, 2017.
- [288] Ma, S., Jiang, B., Deng, W., Gu, Z.-K., Wu, F.-Z., Li, T., Xia, Y., Yang, H., Ye, D., Xiong, Y., and Guan, K.-L. D-2-hydroxyglutarate is essential for maintaining oncogenic property of mutant IDH-containing cancer cells but dispensable for cell growth. *Oncotarget*, 6(11):8606, 2015.
- [289] Ahmed, D., Eide, P., Eilertsen, I., Danielsen, S., Eknaes, M., Hektoen, M., Lind, G., and Lothe, R. Epigenetic and genetic features of 24 colon cancer cell lines. *Oncogenesis*, 2(9):e71–e71, 2013.
- [290] Siddik, Z. H. Cisplatin: mode of cytotoxic action and molecular basis of resistance. *Oncogene*, 22(47):7265–7279, 2003.
- [291] Li-Weber, M. Targeting apoptosis pathways in cancer by Chinese medicine. *Cancer Lett*, 332(2):304–312, 2013.
- [292] Hayflick, L. The limited *in vitro* lifetime of human diploid cell strains. *Exp Cell Res*, 37(3):614–636, 1965.
- [293] Chan, D. A., Sutphin, P. D., Nguyen, P., Turcotte, S., Lai, E. W., Banh, A., Reynolds, G. E., Chi, J.-T., Wu, J., Solow-Cordero, D. E., Bonnet, M., Flanagan, J. U., Bouley, D. M., Graves, E. E., Denny, W. A., Hay, M. P., and Giaccia, A. J. Targeting GLUT1 and the Warburg effect in renal cell carcinoma by chemical synthetic lethality. *Sci Transl Med*, 3(94):94ra70, 2011.
- [294] Kunkel, M., Reichert, T. E., Benz, P., Lehr, H.-A., Jeong, J.-H., Wieand, S., Bartenstein, P., Wagner, W., and Whiteside, T. L. Overexpression of Glut-1 and increased glucose metabolism in tumors are associated with a poor prognosis in patients with oral squamous cell carcinoma. *Cancer*, 97(4):1015–1024, 2003.
- [295] Sakashita, M., Aoyama, N., Minami, R., Maekawa, S., Kuroda, K., Shirasaka, D., Ichihara, T., Kuroda, Y., Maeda, S., , and Kasuga, M. Glut1 expression in T1 and T2 stage colorectal carcinomas: its relationship to clinicopathological features. *Eur J Cancer*, 37(2):204–209, 2001.
- [296] Kitagawa, T., Tsuruhara, Y., Hayashi, M., Endo, T., and Stanbridge, E. J. A tumor-associated glycosylation change in the glucose transporter GLUT1 controlled by tumor suppressor function in human cell hybrids. *J Cell Sci*, 108(12):3735–3743, 1995.
- [297] Asano, T., Katagiri, H., Takata, K., Lin, J.-L., Ishihara, H., Inukai, K., Tsukuda, K., Kikuchi, M., Hirano, H., and Yazaki, Y. The role of N-glycosylation of GLUT1 for glucose transport activity. *J Biol Chem*, 266(36):24632–24636, 1991.

- [298] Riley, P. Free radicals in biology: oxidative stress and the effects of ionizing radiation. *Int J Radiat Biol*, 65(1):27–33, 1994.
- [299] Parikh, H., Carlsson, E., Chutkow, W. A., Johansson, L. E., Storgaard, H., Poulsen, P., Saxena, R., Ladd, C., Schulze, P. C., Mazzini, M. J., Bjørn Jensen, C., Krook, A., Björnholm, M., Tornqvist, H., Zierath, J. R., Ridderstråle, M., Altshuler, D., Lee, R. T., Vaag, A., Groop, L. C., and Mootha, V. K. TXNIP regulates peripheral glucose metabolism in humans. *PLoS Med*, 4(5):868–879, 2007.
- [300] Pakos-Zebrucka, K., Koryga, I., Mnich, K., Ljubic, M., Samali, A., and Gorman, A. M. The integrated stress response. *EMBO Rep*, 17(10):1374–1395, 2016.
- [301] Teske, B. F., Fusakio, M. E., Zhou, D., Shan, J., McClintick, J. N., Kilberg, M. S., and Wek, R. C. CHOP induces activating transcription factor 5 (ATF5) to trigger apoptosis in response to perturbations in protein homeostasis. *Mol Biol Cell*, 24(15):2477–2490, 2013.
- [302] Duval, K., Grover, H., Han, L.-H., Mou, Y., Pegoraro, A. F., Fredberg, J., and Chen, Z. Modeling physiological events in 2D vs. 3D cell culture. *Physiology*, 32(4):266–277, 2017.
- [303] Beck, C. R., Collier, P., Macfarlane, C., Malig, M., Kidd, J. M., Eichler, E. E., Badge, R. M., and Moran, J. V. LINE-1 retrotransposition activity in human genomes. *Cell*, 141(7):1159–1170, 2010.
- [304] Chen, Q. and Ames, B. N. Senescence-like growth arrest induced by hydrogen peroxide in human diploid fibroblast F65 cells. *Proc Natl Acad Sci USA*, 91(10):4130–4134, 1994.
- [305] Macip, S., Kosoy, A., Lee, S., O’Connell, M., and Aaronson, S. Oxidative stress induces a prolonged but reversible arrest in p53-null cancer cells, involving a Chk1-dependent G2 checkpoint. *Oncogene*, 25(45):6037–6047, 2006.
- [306] Yamasaki, K., Chuang, V. T. G., Maruyama, T., and Otagiri, M. Albumin-drug interaction and its clinical implication. *Biochim Biophys Acta*, 1830(12):5435–5443, 2013.
- [307] Al Shoyaib, A., Archie, S. R., and Karamyan, V. T. Intraperitoneal Route of Drug Administration: Should it Be Used in Experimental Animal Studies? *Pharm Res*, 37(1):1–17, 2020.
- [308] Zaias, J., Mineau, M., Cray, C., Yoon, D., and Altman, N. H. Reference values for serum proteins of common laboratory rodent strains. *J Am Assoc Lab Anim Sci*, 48(4):387–390, 2009.
- [309] Ahadova, A. *Mechanisms of action of 2-Deoxy-D-Glucose in Cancer Cells and Evaluation of Novel Approaches of Application (PhD Thesis)*. PhD thesis, Ruprecht-Karls-University, Heidelberg, 2015.
- [310] Vilar, E., Scaltriti, M., Balmana, J., Saura, C., Guzman, M., Arribas, J., Baselga, J., and Tabernero, J. Microsatellite instability due to hMLH1 deficiency is associated with increased cytotoxicity to irinotecan in human colorectal cancer cell lines. *Brit J Cancer*, 99(10):1607–1612, 2008.

- [311] Bodo, S., Colas, C., Buhard, O., Collura, A., Tinat, J., Lavoine, N., Guilloux, A., Chalanstani, A., Lafitte, P., Coulet, F., Buisine, M.-P., Ilencikova, D., Ruiz-Ponte, C., Kinzel, M., Grandjouan, S., Brems, H., Lejeune, S., Blanché, H., Wang, W., Caron, O., Cabaret, O., Svrcek, M., Vidaud, D., Parfait, B., Verloes, A., Knappe, U. J., Soubrier, F., Mortemousque, I., Leis, A., Auclair-Perrossier, J., Frébourg, T., Fléjou, J.-F., Entz-Werle, N., Leclerc, J., Malka, D., Cohen-Haguénauer, O., Goldberg, Y., Gerdes, A.-M., Fedhila, F., Mathieu-Dramard, M., Hamelin, R., Wafaa, B., Gauthier-Villars, M., Bourdeaut, F., Sheridan, E., Vasen, H., Brugières, L., Wimmer, K., Muleris, M., and Duval, A. Diagnosis of constitutional mismatch repair-deficiency syndrome based on microsatellite instability and lymphocyte tolerance to methylating agents. *Gastroenterology*, 149(4):1017–1029, 2015.
- [312] Wheeler, J., Beck, N., Kim, H., Tomlinson, I., Mortensen, N. M., and Bodmer, W. Mechanisms of inactivation of mismatch repair genes in human colorectal cancer cell lines: the predominant role of hMLH1. *Proc Natl Acad Sci USA*, 96(18):10296–10301, 1999.
- [313] Wiseman, H. and Halliwell, B. Damage to DNA by reactive oxygen and nitrogen species: role in inflammatory disease and progression to cancer. *Biochem J*, 313(Pt 1):17, 1996.
- [314] Chung, H. W., Lee, S.-Y., Han, H. S., Park, H. S., Yang, J. H., Lee, H. H., and So, Y. Gastric cancers with microsatellite instability exhibit high fluorodeoxyglucose uptake on positron emission tomography. *Gastric Cancer*, 16(2):185–192, 2013.
- [315] Vilar, E., Mukherjee, B., Kuick, R., Raskin, L., Misek, D. E., Taylor, J. M., Giordano, T. J., Hanash, S. M., Fearon, E. R., Rennert, G., and Gruber, S. B. Gene expression patterns in mismatch repair-deficient colorectal cancers highlight the potential therapeutic role of inhibitors of the phosphatidylinositol 3-kinase-AKT-mammalian target of rapamycin pathway. *Clin Cancer Res*, 15(8):2829–2839, 2009.
- [316] Kalbasi, A. and Ribas, A. Tumour-intrinsic resistance to immune checkpoint blockade. *Nat Rev Immunol*, 20(1):25–39, 2020.
- [317] Zhu, J. Y., Lavrik, I. N., Mahlknecht, U., Giaisi, M., Proksch, P., Krammer, P. H., and Li-Weber, M. The traditional Chinese herbal compound rocaglamide preferentially induces apoptosis in leukemia cells by modulation of mitogen-activated protein kinase activities. *Int J Cancer*, 121(8):1839–1846, 2007.
- [318] Liu, Y., Cao, Y., Zhang, W., Bergmeier, S., Qian, Y., Akbar, H., Colvin, R., Ding, J., Tong, L., Wu, S., Hines, J., and Chen, X. A small-molecule inhibitor of glucose transporter 1 downregulates glycolysis, induces cell-cycle arrest, and inhibits cancer cell growth in vitro and in vivo. *Mol Cancer Ther*, 11(8):1672–1682, 2012.
- [319] Wells, S. I., Francis, D. A., Karpova, A. Y., Dowhanick, J. J., Benson, J. D., and Howley, P. M. Papillomavirus E2 induces senescence in HPV-positive cells via pRB- and p21CIP-dependent pathways. *EMBO J*, 19(21):5762–5771, 2000.
- [320] Li, Z.-Y., Shi, Y.-L., Liang, G.-X., Yang, J., Zhuang, S.-K., Lin, J.-B., Ghodbane, A., Tam, M.-S., Liang, Z.-J., Zha, Z.-G., and Zhang, H.-T. Visualization of GLUT1 Traf-

- ficking in Live Cancer Cells by the Use of a Dual-Fluorescence Reporter. *ACS Omega*, 5(26):15911–15921, 2020.
- [321] Wieman, H. L., Wofford, J. A., and Rathmell, J. C. Cytokine stimulation promotes glucose uptake via phosphatidylinositol-3 kinase/Akt regulation of Glut1 activity and trafficking. *Mol Biol Cell*, 18(4):1437–1446, 2007.
- [322] Wu, N., Zheng, B., Shaywitz, A., Dagon, Y., Tower, C., Bellinger, G., Shen, C.-H., Wen, J., Asara, J., McGraw, T. E., Kahn, B. B., and Cantley, L. C. AMPK-dependent degradation of TXNIP upon energy stress leads to enhanced glucose uptake via GLUT1. *Mol Cell*, 49(6):1167–1175, 2013.
- [323] Shalev, A. Minireview: Thioredoxin-interacting protein: regulation and function in the pancreatic β -cell. *Mol Endocrinol*, 28(8):1211–1220, 2014.
- [324] Wangpaichitr, M., Wu, C., Li, Y. Y., Nguyen, D. J., Kandemir, H., Shah, S., Chen, S., Feun, L. G., Prince, J. S., Kuo, M. T., and Savaraj, N. Exploiting ROS and metabolic differences to kill cisplatin resistant lung cancer. *Oncotarget*, 8(30):49275, 2017.
- [325] Duan, G., Shi, M., Xie, L., Xu, M., Wang, Y., Yan, H., Zhuge, Y., and Zou, X. Increased glutamine consumption in cisplatin-resistant cells has a negative impact on cell growth. *Sci Rep-UK*, 8(1):1–11, 2018.
- [326] Fitzgerald, K. A., Malhotra, M., Curtin, C. M., O’Brien, F. J., and O’Driscoll, C. M. Life in 3D is never flat: 3D models to optimise drug delivery. *J Control Release*, 215:39–54, 2015.
- [327] Gazel, A., Ramphal, P., Rosdy, M., De Wever, B., Tornier, C., Hosein, N., Lee, B., Tomic-Canic, M., and Blumenberg, M. Transcriptional profiling of epidermal keratinocytes: comparison of genes expressed in skin, cultured keratinocytes, and reconstituted epidermis, using large DNA microarrays. *J Invest Dermatol*, 121(6):1459–1468, 2003.
- [328] Forred, B. J., Neuharth, S., Kim, D. I., Amolins, M. W., Motamedchaboki, K., Roux, K. J., and Vitiello, P. F. Identification of redox and glucose-dependent Txnip protein interactions. *Oxid Med Cell Longev*, 2016, 2016.
- [329] Vattem, K. M. and Wek, R. C. Reinitiation involving upstream ORFs regulates ATF4 mRNA translation in mammalian cells. *Proc Natl Acad Sci USA*, 101(31):11269–11274, 2004.
- [330] Guo, L., Chen, R., Ma, N., Xiao, H., Chen, Y., Chen, F., Mei, J., Ding, F., and Zhong, H. Phosphorylation of eIF2 α suppresses cisplatin-induced A549 cell apoptosis via p38 inhibition. *Cancer Biother Radiopharm*, 28(4):268–273, 2013.
- [331] Fulda, S., Gorman, A. M., Hori, O., and Samali, A. Cellular stress responses: cell survival and cell death. *Int J Cell Biol*, 2010, 2010.
- [332] Gajate, C., Gonzalez-Camacho, F., and Mollinedo, F. Lipid raft connection between extrinsic and intrinsic apoptotic pathways. *Biochem Biophys Res Commun*, 380(4):780–784, 2009.

- [333] Montero, J., Morales, A., Llacuna, L., Lluís, J. M., Terrones, O., Basañez, G., Antonsson, B., Prieto, J., García-Ruiz, C., Colell, A., and Fernández-Checa, J. C. Mitochondrial cholesterol contributes to chemotherapy resistance in hepatocellular carcinoma. *Cancer Res*, 68(13):5246–5256, 2008.
- [334] Galvao, J., Davis, B., Tilley, M., Normando, E., Duchon, M. R., and Cordeiro, M. F. Unexpected low-dose toxicity of the universal solvent DMSO. *FASEB J*, 28(3):1317–1330, 2014.
- [335] Verheijen, M., Lienhard, M., Schrooders, Y., Clayton, O., Nudischer, R., Boerno, S., Timmermann, B., Selevsek, N., Schlapbach, R., Gmuender, H., et al. DMSO induces drastic changes in human cellular processes and epigenetic landscape in vitro. *Sci Rep-UK*, 9(1):1–12, 2019.
- [336] Savjani, K. T., Gajjar, A. K., and Savjani, J. K. Drug solubility: importance and enhancement techniques. *ISRN Pharm*, 2012, 2012.
- [337] Hoogenboezem, E. N. and Duvall, C. L. Harnessing albumin as a carrier for cancer therapies. *Adv Drug Deliv Rev*, 130:73–89, 2018.
- [338] Wunder, A., Muller-Ladner, U., Stelzer, E., Neumann, E., Sinn, H., Gay, S., and Fiehn, C. Albumin-based drug delivery as novel therapeutic approach for rheumatoid arthritis. *Arthritis Res Ther*, 5(3):1–54, 2003.
- [339] Andersson, C., Iresjö, B.-M., and Lundholm, K. Identification of tissue sites for increased albumin degradation in sarcoma-bearing mice. *J Surg Res*, 50(2):156–162, 1991.
- [340] Wunder, A., Stehle, G., Sinn, H., Schrenk, H., Hoffbiederbeck, D., Bader, F., Friedrich, E., Peschke, P., Maierborst, W., and Heene, D. Enhanced albumin uptake by rat tumors. *Int J Oncol*, 11(3):497–507, 1997.
- [341] Stehle, G., Sinn, H., Wunder, A., Schrenk, H. H., Stewart, J. C. M., Hartung, G., Maier-Borst, W., and Heene, D. L. Plasma protein (albumin) catabolism by the tumor itself - implications for tumor metabolism and the genesis of cachexia. *Crit Rev in Oncol Hematol*, 26(2):77–100, 1997.
- [342] Gradishar, W. J., Tjulandin, S., Davidson, N., Shaw, H., Desai, N., Bhar, P., Hawkins, M., and O’Shaughnessy, J. Phase III trial of nanoparticle albumin-bound paclitaxel compared with polyethylated castor oil-based paclitaxel in women with breast cancer. *J Clin Oncol*, 23(31):7794–7803, 2005.
- [343] Kratz, F. DOXO-EMCH (INNO-206): the first albumin-binding prodrug of doxorubicin to enter clinical trials. *Expert Opin Investig Drugs*, 16(6):855–866, 2007.
- [344] Kijanka, G., Prokopowicz, M., Schellekens, H., and Brinks, V. Influence of aggregation and route of injection on the biodistribution of mouse serum albumin. *PLoS One*, 9(1):e85281, 2014.
- [345] Domon, B. and Aebersold, R. Mass spectrometry and protein analysis. *Science*, 312(5771):212–217, 2006.

- [346] Banerjee, S. and Mazumdar, S. Electrospray ionization mass spectrometry: a technique to access the information beyond the molecular weight of the analyte. *Int J Anal Chem*, 2012, 2012.
- [347] Liu, T., Nair, S. J., Lescarbeau, A., Belani, J., Peluso, S., Conley, J., Tillotson, B., O'Hearn, P., Smith, S., Slocum, K., West, K., Helble, J., Douglas, M., Bahadoor, A., Ali, J., McGovern, K., Fritz, C., Palombella, V. J., Wylie, A., Castro, A. C., and Tremblay, M. R. Synthetic silvestrol analogues as potent and selective protein synthesis inhibitors. *J Med Chem*, 55(20):8859–8878, 2012.
- [348] Shimada, T., Nomura, M., Yokogawa, K., Endo, Y., Sasaki, T., Miyamoto, K.-i., and Yonemura, Y. Pharmacokinetic advantage of intraperitoneal injection of docetaxel in the treatment for peritoneal dissemination of cancer in mice. *J Pharm Pharmacol*, 57(2):177–181, 2005.
- [349] Nemes, K. B., Abermann, M., Bojti, E., Grézal, G., Al-Behaisi, S., and Klebovich, I. Oral, Intraperitoneal and Intravenous Pharmacokinetics of Deramciclane and its N-desmethyl Metabolite in the Rat. *J Pharm Pharmacol*, 52(1):47–51, 2000.
- [350] Kim, C., Kim, I. H., Kim, S.-i., Kim, Y. S., Kang, S. H., Moon, S. H., Kim, T.-S., and Kim, S.-k. Comparison of the intraperitoneal, retroorbital and per oral routes for F-18 FDG administration as effective alternatives to intravenous administration in mouse tumor models using small animal PET/CT Studies. *Nucl Med Mol Imaging*, 45(3):169–176, 2011.
- [351] Matzneller, P., Kussmann, M., Eberl, S., Maier-Salamon, A., Jäger, W., Bauer, M., Langer, O., Zeitlinger, M., and Poepl, W. Pharmacokinetics of the P-gp inhibitor Tariquidar in rats after intravenous, Oral, and Intraperitoneal administration. *Eur J Drug Metab Pharmacokinet*, 43(5):599–606, 2018.
- [352] Rozewski, D. M., Herman, S. E., Towns, W. H., Mahoney, E., Stefanovski, M. R., Shin, J. D., Yang, X., Gao, Y., Li, X., Jarjoura, D., et al. Pharmacokinetics and tissue disposition of lenalidomide in mice. *AAPS J*, 14(4):872–882, 2012.
- [353] Mouhid, L., Corzo-Martínez, M., Torres, C., Vázquez, L., Reglero, G., Fornari, T., and Ramírez de Molina, A. Improving in vivo efficacy of bioactive molecules: An overview of potentially antitumor phytochemicals and currently available lipid-based delivery systems. *J Oncol*, 2017, 2017.
- [354] Davidson, S. M., Papagiannakopoulos, T., Olenchock, B. A., Heyman, J. E., Keibler, M. A., Luengo, A., Bauer, M. R., Jha, A. K., O'Brien, J. P., Pierce, K. A., et al. Environment impacts the metabolic dependencies of Ras-driven non-small cell lung cancer. *Cell Metab*, 23(3):517–528, 2016.
- [355] Hensley, C. T., Faubert, B., Yuan, Q., Lev-Cohain, N., Jin, E., Kim, J., Jiang, L., Ko, B., Skelton, R., Loudat, L., et al. Metabolic heterogeneity in human lung tumors. *Cell*, 164(4):681–694, 2016.

- [356] Zhao, Y., Liu, H., Liu, Z., Ding, Y., LeDoux, S. P., Wilson, G. L., Voellmy, R., Lin, Y., Lin, W., Nahta, R., Liu, B., Fodstad, O., Chen, J., Wu, Y., Price, J. E., and Tan, M. Overcoming trastuzumab resistance in breast cancer by targeting dysregulated glucose metabolism. *Cancer Res*, 71(13):4585–4597, 2011.
- [357] Catanzaro, D., Gabbia, D., Cocetta, V., Biagi, M., Ragazzi, E., Montopoli, M., and Carrara, M. Silybin counteracts doxorubicin resistance by inhibiting GLUT1 expression. *Fitoterapia*, 124:42–48, 2018.
- [358] Saunders, N. A., Simpson, F., Thompson, E. W., Hill, M. M., Endo-Munoz, L., Leggatt, G., Minchin, R. F., and Guminski, A. Role of intratumoural heterogeneity in cancer drug resistance: molecular and clinical perspectives. *EMBO Mol Med*, 4(8):675–684, 2012.
- [359] Kreuzaler, P., Panina, Y., Segal, J., and Yuneva, M. Adapt and conquer: Metabolic flexibility in cancer growth, invasion and evasion. *Mol Metab*, 33:83–101, 2020.
- [360] Wolinsky, J. B., Colson, Y. L., and Grinstaff, M. W. Local drug delivery strategies for cancer treatment: gels, nanoparticles, polymeric films, rods, and wafers. *J Control Release*, 159(1):14–26, 2012.
- [361] Senapati, S., Mahanta, A. K., Kumar, S., and Maiti, P. Controlled drug delivery vehicles for cancer treatment and their performance. *Signal Transduct Target Ther*, 3(1):1–19, 2018.
- [362] Chen, C.-L., Hou, W.-H., Liu, I.-H., Hsiao, G., Huang, S. S., and San Huang, J. Inhibitors of clathrin-dependent endocytosis enhance TGF β signaling and responses. *J Cell Sci*, 122(11):1863–1871, 2009.

Supplement

Table S1: IC₅₀ concentrations of synthetic flavaglines alone and in combination with 2DG (1 mM). 1 mM 2DG only caused a reduction of cell viability below 50 % in the KM12 cell line. IMD-1 exhibits an average IC₅₀ ca. 176 nM (7 of 35 cell lines). IMD-1 combined with 2DG has an average IC₅₀ value of ca. 137 nM (13 of 35 cell lines). IMD-3 exhibits an average IC₅₀ ca. 65 nM (22 of 35 cell lines). IMD-3 combined with 2DG has an average IC₅₀ value of ca. 44 nM (30 of 35 cell lines). IC₅₀ values were determined using non-linear regression (Fig. 11, 12, 13, 14. S1).

	2DG (1 mM)	IMD-1	IMD-1 + 2DG (1 mM)	IMD-3	IMD-3 + 2DG (1 mM)
HCT116	-	-	-	45.0	18.0
HT29	-	-	-	-	-
Colo205	-	-	-	-	100.0
SW620	-	-	-	-	40.0
DLD-1	-	-	-	100.0	33.0
HCT15	-	-	-	-	65.0
KM12	*	-	-	10.0	0.0
Hap1 (wt)	-	150.0	80.0	13.0	5.0
Hap1 ΔMLH1 c11	-	175.0	115.0	13.0	8.0
Hap1 ΔMLH1 c29	-	180.0	122.0	15.0	7.0
Hap1 ΔMLH1 c30	-	170.0	125.0	16.0	8.0
Hap1 ΔMLH1 c44	-	158.0	113.0	13.0	6.0
C33A	-	200.0	175.0	30.0	20.0
CaSki	-	-	200.0	50.0	15.0
HeLa	-	-	-	-	145.0
SiHa	-	-	-	-	-
SW756	-	-	-	-	-
UM-SCC-47	-	-	200.0	130.0	30.0
UM-SCC-104	-	-	190.0	-	32.0
UPCI-SCC-90	-	-	70.0	70.0	7.0
UPCI-SCC-152	-	200.0	50.0	32.0	11.0
HaCaT	-	-	-	160.0	120.0
MCF7	-	-	-	70.0	45.0
T-47D	-	-	-	150.0	40.0
SW872	-	-	180.0	50.0	18.0
SW1353	-	-	-	50.0	15.0
HT-1080	-	-	160.0	50.0	13.0
U251	-	-	-	-	-
HL-60	-	-	-	-	-
RPMI-8226	-	-	-	80.0	68.0
A549	-	-	-	200.0	65.0
Dan-G	-	-	-	-	110.0
MIA PaCa-2	-	-	-	-	75.0
DU-145	-	-	-	-	165.0
PC-3	-	-	-	77.0	35.0


IMD concentration [nM] low  high

Table S2: Glucose uptake velocity of vehicle- and IMD-3-treated CaSki cells. For each medium glucose concentration, the average uptake of the vehicle-treated control cells was set to 100 % to calculate the percentage of glucose uptake velocity in IMD-3-treated cells.

Glucose concentration	Control		IMD-3		IMD-3		
	Average [ng/min]	Error [ng/min]	Average [ng/min]	Error [ng/min]	Incorporated glucose [%]	Error [%]	
0 g/l	0.0028	0.0002	0.0013	0.0001	47.34	4.79	
0.0625 g/l	44.4248	3.3099	22.1967	1.7967	49.96	5.50	
0.25 g/l	113.3068	10.3052	60.7972	4.9525	53.66	6.55	
1.0 g/l	118.7511	9.3231	79.9836	6.9639	67.35	7.90	
					Average incorporation:	54.58	3.15
					Average reduction by IMD-3 treatment:	45.42	

Table S3: z-scores and p-values of top 20 deregulated pathways in IMD-3-treated cell lines (sorted by z-score) identified by IPA comparison analysis (see Fig. 27A). For each pathway, the z-score (top) and p-value (bottom) are indicated for each cell line. z-scores predicting the activation (z-score ≥ 2) or inhibition (z-score ≤ -2) of the pathways are based on transcriptome data. If no direction could be predicted, the z-score is 0. Not calculable z-scores are indicated with N/A. Pathways with a p-value ≤ 0.05 are considered significant.

IPA Pathway	HCT116	HT29	CaSki	HeLa	SiHa	UPCI-SCC-90
Cell Cycle Control of Chromosomal Replication	-3.530 1.127*10 ⁻⁹	-4.382 9.628*10 ⁻⁸	-2.000 0.0026	-1.528 2.898*10 ⁻⁵	-3.530 2.482*10 ⁻⁹	-4.747 1.252*10 ⁻⁹
Stearate Biosynthesis I (Animals)	-2.646 0.1380	-3.153 0.0016	-2.828 0.1671	-3.000 0.1399	-2.887 0.0023	-1.897 0.0512
Glutathione-mediated Detoxification	-1.633 0.0365	-2.530 0.0086	-2.236 0.1151	-2.333 0.0078	-2.236 0.2437	-2.828 0.0225
Fatty Acid β -oxidation I	N/A 1.0000	-2.714 0.0373	-2.828 0.0433	-2.828 0.0686	-2.530 0.0046	-2.309 0.0034
Superpathway of Cholesterol Biosynthesis	-2.236 0.1495	-1.508 0.0221	-3.317 0.0001	-2.333 0.0173	-3.000 0.0092	-0.378 0.2141
Glutathione Redox Reactions I	-1.342 0.1502	-2.530 0.0092	-2.000 0.3523	-1.667 0.0029	-2.236 0.1677	-2.828 0.0290
Hypoxia Signalling in the Cardiovascular System	1.667 0.0100	1.897 0.0674	1.890 0.0311	2.530 0.0082	2.449 0.1012	1.414 0.1923
γ -linolenate Biosynthesis II (Animals)	N/A 0.3862	-2.449 0.1305	-2.236 0.0708	-2.000 0.2426	-2.121 0.0009	-2.828 0.0050
Pyrimidine Deoxyribonucleotides De Novo Biosynthesis I	-2.646 0.0183	-1.414 0.0742	-1.000 0.3523	-2.000 0.4225	-2.646 0.0221	-1.633 0.1798
Ethanol Degradation IV	N/A 0.4596	-3.162 0.0025	-2.236 0.1060	-1.667 0.0008	-1.890 0.0094	-2.121 0.0112

IPA Pathway	HCT116	HT29	CaSki	HeLa	SiHa	UPCI- SCC-90
Pyrimidine	-1.265	-1.291	-0.816	-2.714	-2.714	-2.111
Ribonucleotides	0.0404	0.0211	0.5186	0.0408	0.0212	0.1094
De Novo Biosynthesis						
Unfolded Protein	3.051	2.132	0.500	1.508	1.941	1.667
Response	0.0095	4.662*10 ⁻⁵	0.0002	0.0130	0.0052	0.2567
Pyrimidine	-1.265	-1.291	-0.816	-2.530	-2.530	-2.111
Ribonucleotides	0.0296	0.0132	0.4689	0.0659	0.0369	0.0822
Interconversion						
Serotonin	-1.667	-2.982	-0.632	-1.508	-1.414	-2.324
Degradation	0.2861	0.0150	0.2100	0.1911	0.4719	0.0507
Dopamine	-1.890	-3.207	-1.134	-1.000	-1.342	-1.667
Degradation	0.0235	4.033*10 ⁻⁵	0.0292	0.0041	0.1920	0.0125
Estrogen-mediated	-2.121	-2.333	-0.447	-2.236	-1.155	-1.941
S-phase Entry	0.0042	0.0332	0.2761	0.3470	0.0001	0.0002
Aldosterone Signalling	-1.291	-1.147	-0.577	-1.897	-2.121	-2.646
in Epithelial Cells	0.0260	0.2157	0.2018	1.0000	0.4274	1.0000
Cyclins and Cell	-3.051	-1.706	-0.632	-1.387	-0.853	-1.964
Cycle Regulation	0.0927	0.0029	0.1225	0.1345	1.070*10 ⁻⁵	0.0009
3-phosphoinositide	0.730	-1.155	-0.408	-2.117	-2.132	-2.694
Biosynthesis	0.0150	0.0030	0.2618	0.2777	0.4119	0.2469
Anti-proliferative	1.667	1.414	1.342	1.667	1.414	1.667
Role of TOB in	0.0223	0.3970	0.4748	0.0485	0.0687	0.1144
T Cell Signalling						

Table S4: z-scores and p-values of top 20 deregulated pathways in IMD-3-treated cell lines (sorted by p-value) identified by IPA comparison analysis (see Fig. 27B). For each pathway, the z-score (top) and p-value (bottom) are indicated for each cell line. z-scores predicting the activation (z-score ≥ 2) or inhibition (z-score ≤ -2) of the pathways are based on transcriptome data. If no direction could be predicted, the z-score is 0. Not calculable z-scores are indicated with N/A. Pathways with a p-value ≤ 0.05 are considered significant.

IPA Pathway	HCT116	HT29	CaSki	HeLa	SiHa	UPCI- SCC-90
Cell Cycle Control of Chromosomal Replication	-3.530 1.127*10 ⁻⁹	-4.382 9.628*10 ⁻⁸	-2.000 0.0026	-1.528 2.898*10 ⁻⁵	-3.530 2.482*10 ⁻⁹	-4.747 1.252*10 ⁻⁹
Aryl Hydrocarbon Receptor Signalling	-0.626 0.0007	-2.121 1.244*10 ⁻⁷	1.000 0.0003	0.218 8.704*10 ⁻⁷	0.192 3.287*10 ⁻⁶	-1.414 3.998*10 ⁻⁸
p53 Signalling	0.0 0.0003	0.0 7.813*10 ⁻⁶	0.688 0.0002	0.426 0.0004	0.0 2.586*10 ⁻⁵	0.577 1.479*10 ⁻⁵
Cell Cycle: G2/M DNA Damage Checkpoint Regulation	0.943 2.331*10 ⁻⁵	0.894 4.982*10 ⁻⁵	-0.775 0.0005	-1.291 0.0041	-0.243 3.828*10 ⁻⁵	1.606 0.0001
Molecular Mechanisms of Cancer	N/A 0.0319	N/A 4.327*10 ⁻⁵	N/A 0.0007	N/A 3.412*10 ⁻⁶	N/A 0.0001	N/A 0.0001
Senescence Pathway	2.100 0.0026	1.746 8.253*10 ⁻⁶	0.137 0.0040	0.630 1.523*10 ⁻⁵	0.132 0.0002	3.442 0.0003
NRF2-mediated Oxidative Stress Response	1.706 0.0002	2.535 9.033*10 ⁻⁶	0.853 0.0065	1.890 1.484*10 ⁻⁶	0.447 0.0033	1.091 0.0730
NER Pathway	-1.414 0.0056	-1.219 0.0003	-1.213 0.0182	-0.688 0.0763	-3.000 2.154*10 ⁻⁵	-1.414 2.014*10 ⁻⁶
Hereditary Breast Cancer Signalling	N/A 0.0308	N/A 0.0001	N/A 0.0174	N/A 0.0032	N/A 0.0048	N/A 1.121*10 ⁻⁷
Cell Cycle: G1/S Checkpoint Regulation	1.155 0.0433	1.886 0.0281	-0.688 0.0001	0.0 0.0152	0.218 2.542*10 ⁻⁶	1.706 2.595*10 ⁻⁵

Table S5: Fold changes (FC) and BH-corrected p-values for selected DEGs for relevance in metabolism and ISR in CRC and HPV-positive cell lines. For each gene, FC (top) and BH-corrected p-value (bottom) are indicated. Negative FC values indicate downregulation, while positive FC values indicate upregulation. FC of 1 or -1 indicate no deregulation of the gene compared to vehicle-treated cells. Genes with $FC \geq 2$ or $FC \leq -2$ and a BH-corrected p-value ≤ 0.05 are considered significantly deregulated. Genes with BH-corrected p-values > 0.05 are labelled non-significant (n.s.). All DEGs are listed in table ES11.

Gene	HCT116	HT29	CaSki	HeLa	SiHa	UPCI-SCC-90
<i>TXNIP</i>	n.s.	10.2 4.380*10 ⁻¹⁰	5.4 4.854*10 ⁻¹⁷	2.8 4.374*10 ⁻¹⁰	6.1 1.433*10 ⁻¹⁷	2.0 3.089*10 ⁻⁶
<i>AKT</i>	-1.4 0.0465	-5.7 3.700*10 ⁻⁹	-2.2 2.395*10 ⁻¹⁰	-2.2 1.684*10 ⁻⁹	-1.7 1.048*10 ⁻⁵	-2.3 1.815*10 ⁻⁸
<i>PIK3R1</i>	2.1 0.0014	-6.0 1.430*10 ⁻⁷	n.s.	3.2 4.715*10 ⁻⁸	1.7 0.0026	-2.9 9.961*10 ⁻⁷
<i>PIK3R2</i>	-5.4 2.680*10 ⁻⁸	-10.6 2.880*10 ⁻¹⁰	-3.0 1.477*10 ⁻⁷	-12.5 1.512*10 ⁻¹⁵	-2.9 4.769*10 ⁻⁷	-9.1 1.286*10 ⁻¹²
<i>PIK3CB</i>	-2.3 1.656*10 ⁻⁴	n.s.	-1.4 0.0270	-4.3 9.506*10 ⁻¹¹	-3.4 1.049*10 ⁻⁹	n.s.
<i>NDUFAF3</i>	-8.0 1.710*10 ⁻⁸	-4.8 2.780*10 ⁻⁸	-1.9 1.370*10 ⁻⁴	-6.5 8.032*10 ⁻¹⁴	-3.3 9.514*10 ⁻¹⁰	-5.6 8.016*10 ⁻¹²
<i>SDHC</i>	-2.4 2.077*10 ⁻⁴	-4.1 1.930*10 ⁻⁷	-2.6 6.029*10 ⁻⁹	-2.0 1.178*10 ⁻⁵	-2.1 1.385*10 ⁻⁶	-1.5 0.0346
<i>GLS</i>	2.1 7.790*10 ⁻⁵	9.4 4.630*10 ⁻⁸	n.s.	1.8 0.0408	2.2 0.0018	6.4 1.374*10 ⁻⁸
<i>DDIT3</i>	21.9 1.600*10 ⁻⁹	8.9 7.980*10 ⁻¹⁰	8.5 6.989*10 ⁻²³	3.8 2.302*10 ⁻¹⁵	16.5 9.146*10 ⁻²⁶	2.0 8.295*10 ⁻⁸
<i>ATF4</i>	1.7 0.0084	2.2 3.240*10 ⁻⁶	1.3 0.0494	1.6 0.0016	1.4 0.0028	1.5 0.0114
<i>ATF5</i>	-2.1 0.0005	-2.1 0.0001	3.5 2.271*10 ⁻¹¹	2.7 4.310*10 ⁻⁸	1.7 0.0006	3.0 3.799*10 ⁻⁸
<i>PMAIP1</i>	3.8 1.460*10 ⁻⁵	2.4 0.0005	2.7 4.291*10 ⁻¹⁰	3.8 3.546*10 ⁻¹²	5.1 2.061*10 ⁻¹⁵	1.8 0.0003

Table S6: Glucose uptake velocity of vehicle- and IMD-3-treated WT HGC178 and IMD-3-resistant HGC176 cells. For each medium glucose concentration, the average uptake of the vehicle-treated control cells was set to 100 % to calculate the percentage of glucose uptake velocity in IMD-3-treated cells.

Glucose concentration	Control		IMD-3		IMD-3	
	Average [ng/min]	Error [ng/min]	Average [ng/min]	Error [ng/min]	Incorporated glucose [%]	Error [%]
HGC178 (WT)						
0 g/l	0.005	0.0003	0.002	0.0002	40.51	5.06
0.0625 g/l	77.297	5.756	26.766	2.344	34.63	3.98
0.25 g/l	244.084	18.408	98.600	12.705	40.40	6.03
1.0 g/l	203.844	15.205	112.740	22.752	55.31	11.90
				Average incorporation:	42.71	3.70
				Average reduction by IMD-3 treatment:	57.29	
HGC176 (IMD-3-resistant)						
0 g/l	0.006	0.0009	0.005	0.0004	77.26	13.05
0.0625 g/l	96.430	9.560	77.616	6.485	80.49	10.44
0.25 g/l	262.772	22.094	217.465	23.959	82.76	11.47
1.0 g/l	186.128	15.026	154.956	17.518	83.25	11.57
				Average incorporation:	80.94	5.83
				Average reduction by IMD-3 treatment:	19.06	

Table S7: Fold changes (FC) and BH-corrected p-values for selected DEGs for relevance in metabolism and ISR in WT and IMD-3-resistant cell lines. Alterations in resistant HGC176 cell compared to WT HGC178 cells are listed on the left, while IMD-3-induced changes in gene expression for both cell lines are listed on the right. For each gene, FC (top) and BH-corrected p-value (bottom) are indicated. Negative FC values indicate downregulation, while positive FC values indicate upregulation. FC of 1 or -1 indicate no deregulation of the gene. Genes with $FC \geq 2$ or ≤ -2 and a BH-corrected p-value ≤ 0.05 are considered significantly deregulated. Genes with BH-corrected p-values > 0.05 are labelled non-significant (n.s.). All DEGs are listed in table ES15.

Gene	HGC176 vs. HGC178	Changes upon IMD-3 treatment	
		HGC178 (WT)	HGC176 (IMD-3-resistant)
<i>HSPA8</i>	-7.7 1.798*10 ⁻⁹	n.s. 2.4 6.902*10 ⁻⁷	3.0 2.012*10 ⁻⁵
<i>DDIT3</i>	n.s.	1.4 0.0382	1.5 0.0304
<i>ATF4</i>	-1.7 0.0013	-1.3 0.0300	n.s.
<i>ATF5</i>	n.s.	1.9 2.172*10 ⁻⁵	n.s.
<i>PMAIP1</i>	n.s.	-1.7 0.0002	-1.7 0.0006
<i>TXNIP</i>	-1.7 0.0002	n.s.	n.s.
<i>AKT</i>	n.s.	n.s.	n.s.
<i>PIK3R1</i>	n.s.	3.1 5.472*10 ⁻⁸	n.s.
<i>PIK3R2</i>	n.s.	-3.9 1.751*10 ⁻¹²	n.s.
<i>PIK3CB</i>	n.s.	-1.6 0.0326	n.s.
<i>NDUFAF3</i>	n.s.	-2.1 1.027*10 ⁻¹⁷	-1.3 0.0200
<i>SDHC</i>	-2.3 1.542*10 ⁻⁵	-2.2 4.073*10 ⁻⁸	-1.6 0.0007
<i>GLS</i>	n.s.	n.s.	n.s.

Table S8: z-scores and p-values of top 20 deregulated pathways in IMD-3-treated WT and IMD-3-resistant cells identified by IPA comparison analysis (see Fig. 44). For each pathway, the z-score (top) and p-value (bottom) are indicated for each cell line. z-scores predicting the activation (z-score ≥ 2) or inhibition (z-score ≤ -2) of the pathways are based on transcriptome data. If no direction could be predicted, the z-score is 0. Not calculable z-scores are indicated with N/A. Pathways with a p-value ≤ 0.05 are considered significant.

sorted by z-score			sorted by p-value		
IPA Pathway	HGC178 (WT)	HGC176 (resistant)	IPA Pathway	HGC178 (WT)	HGC176 (resistant)
Glutathione-mediated Detoxification	-2.646	N/A	Putrescine	-1.89	N/A
Huntington's Disease Signalling	2.5	N/A	Degradation III	0.0024	0.0010
Senescence Pathway	2.469	N/A	Colanic Acid Building Blocks Biosynthesis	6.090*10 ⁻⁶	1.0000
γ -linolenate Biosynthesis II (Animals)	-2.449	N/A	NRF2-mediated Oxidative Stress Response	2.357	N/A
Mitochondrial L-carnitine Shuttle Pathway	0.0117	1.0000	Oxidative Stress Response	4.010*10 ⁻⁵	0.4090
NRF2-mediated Oxidative Stress Response	2.357	N/A	Tryptophan Degradation X (Mammalian, via Tryptamine)	-1.633	N/A
Unfolded Protein Response	2.333	N/A	Dopamine Degradation	-1.89	N/A
Purine Nucleotides De Novo Biosynthesis II	-2.236	N/A	Docosahexaenoic Acid (DHA) Signalling	0.0158	0.0019
Glutaryl-CoA Degradation	-2.236	N/A	Virus Entry via Endocytic Pathways	N/A	N/A
Cell Cycle Control of Chromosomal Replication	-2.138	N/A	Aryl Hydrocarbon Receptor Signalling	0.0012	0.1015
	0.0057	0.1460	SAPK/JNK Signalling	1.46	N/A
			Noradrenaline and Adrenaline Degradation	0.0004	1.0000
				-1.633	N/A
				0.1461	0.0032

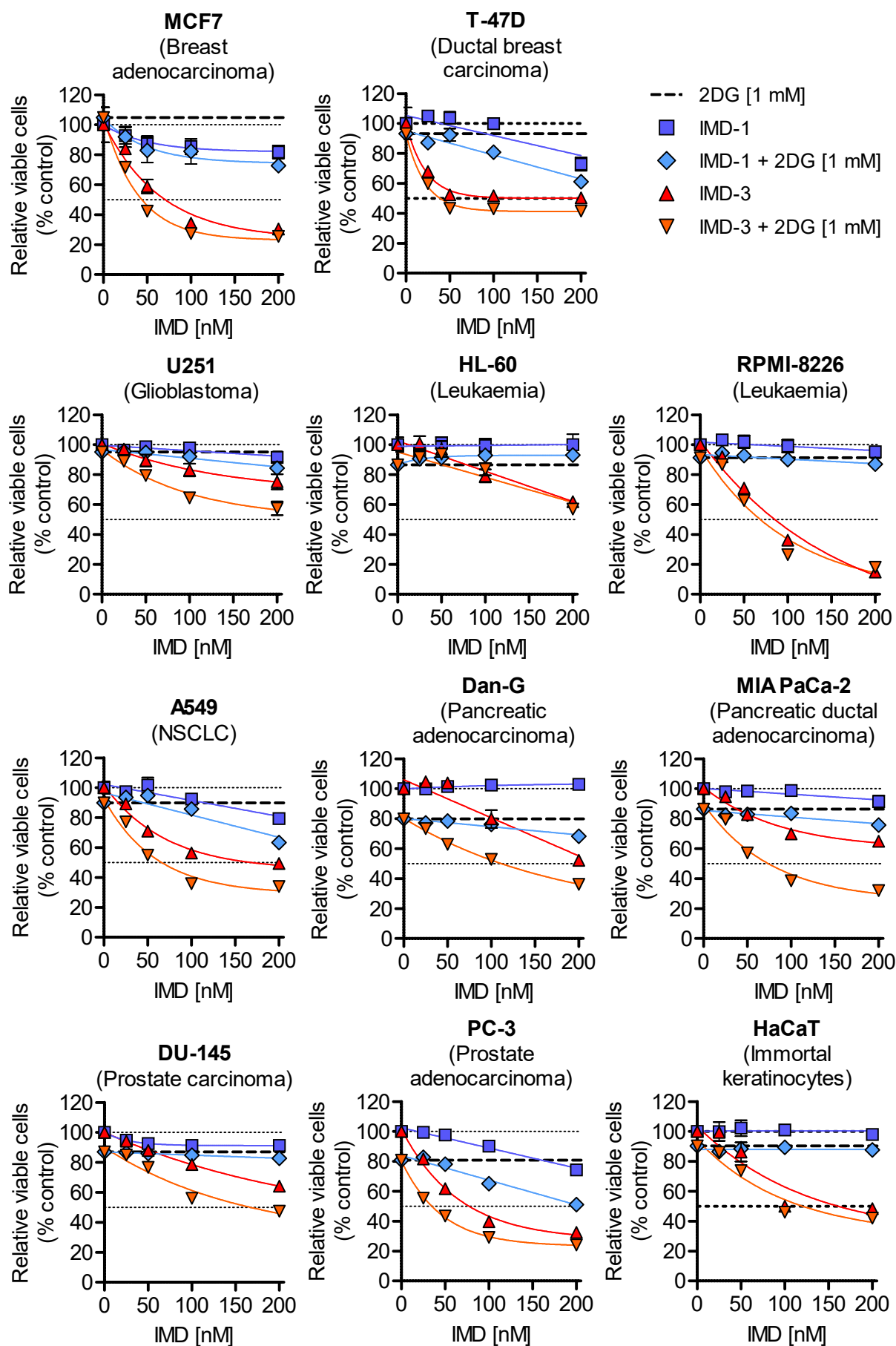


Figure S1: Sensitivity of different cancer entities, including breast, brain, blood, lung, pancreatic and prostate cancer cell lines, towards 48 h of synthetic flavagline treatment alone and in combination with 2DG (1 mM). Multiplicity-adjusted p-values are listed in table ES1.

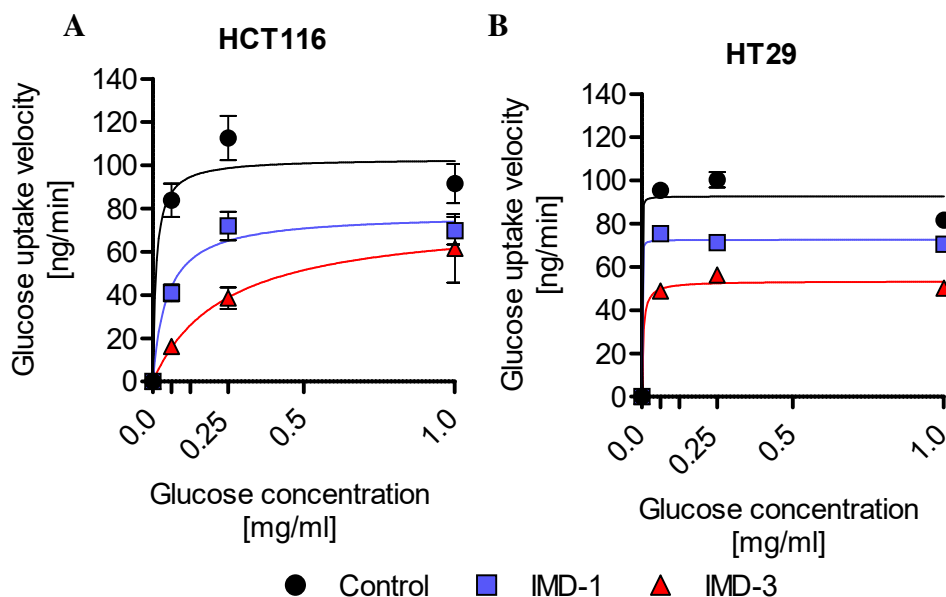


Figure S2: Glucose uptake velocity in CRC cell lines HCT116 (A) and HT29 (B). Glucose uptake velocity performed during my master thesis [287] were combined with the repetition of the experiment performed during my PhD thesis.

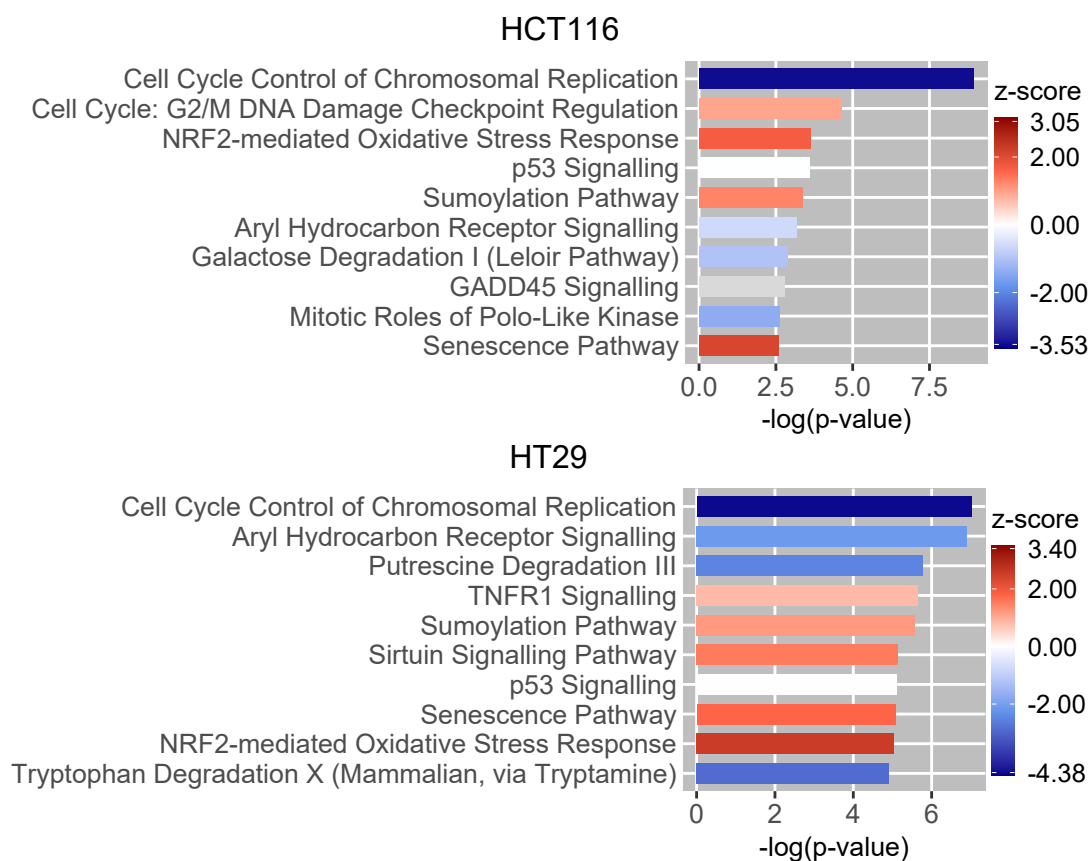


Figure S3: Top 10 deregulated pathways in IMD-3-treated CRC cell lines based on transcriptome data. Depicted z-scores indicate activation ($z\text{-score} \geq 2$; red) or inhibition ($z\text{-score} \leq -2$; blue) of the pathway. If no direction could be predicted, the z-score is 0 (white). If the z-score could not be calculated, pathways are displayed in grey. Pathway analysis was performed using IPA software.

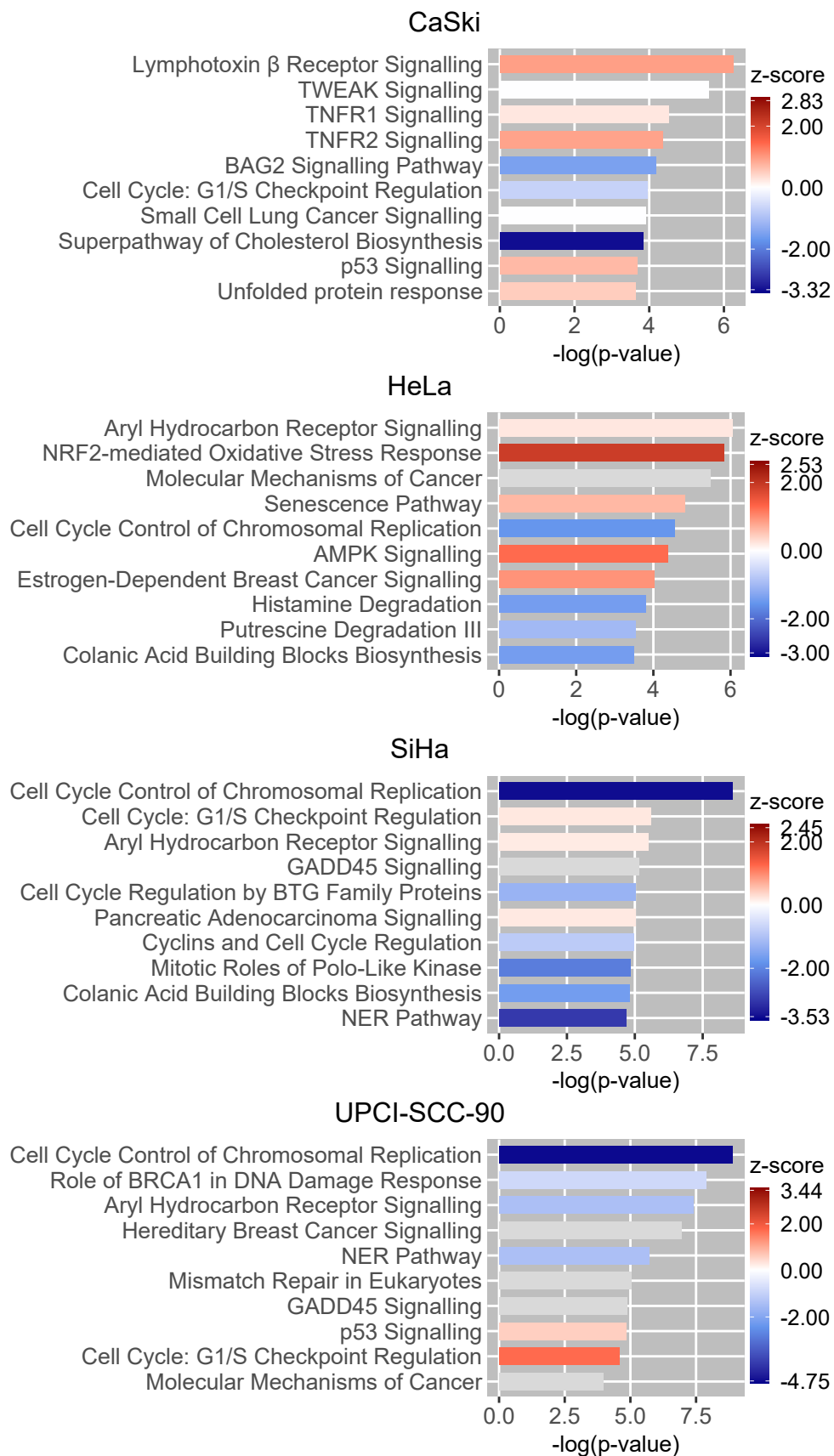


Figure S4: Top 10 deregulated pathways in IMD-3-treated HPV-positive cell lines based on transcriptome data. Depicted z-scores indicate activation ($z\text{-score} \geq 2$; red) or inhibition ($z\text{-score} \leq -2$; blue) of the pathway. If no direction could be predicted, the z-score is 0 (white). If the z-score could not be calculated, pathways are displayed in grey. Pathway analysis was performed using IPA software.

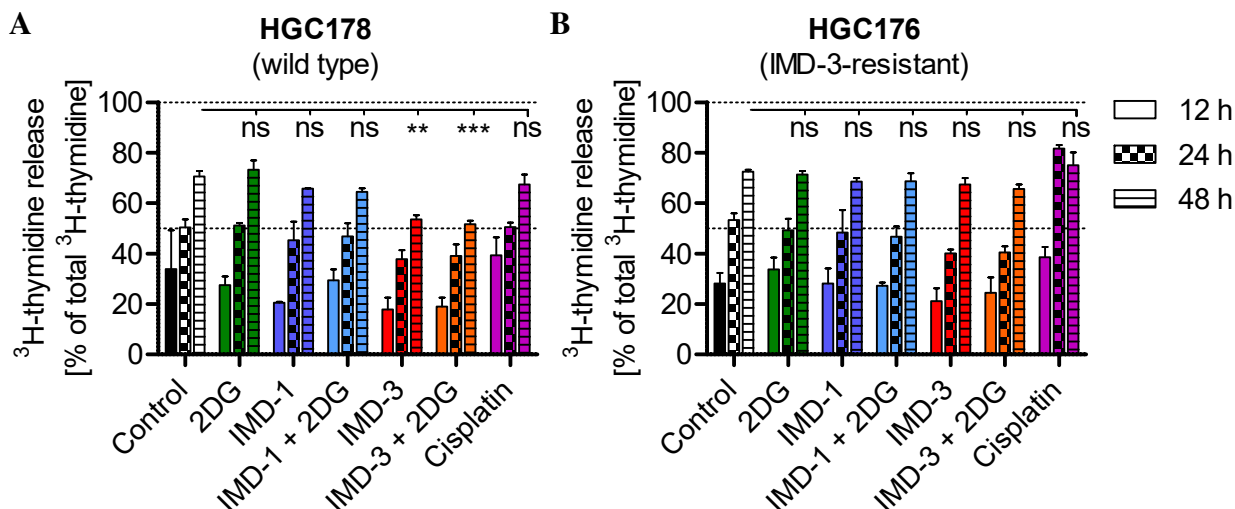


Figure S5: Release of ³H-thymidine from labelled WT HGC178 (A) and IMD-3-resistant HGC176 (B) cells upon treatment for 12, 24, or 48 h. Due to strong proliferation inhibition by IMD-3, release of ³H-thymidine is decreased in comparison to the control cells. Thus, it was not possible to calculate cytotoxic cell death. ³H-thymidine release also revealed high turnover rates of both cell lines, as the majority of the label was released into the medium after 48 h, although controls were approx. 95 % confluent. 2DG: 1 mM, IMD-1, IMD-3: 100 nM, Cisplatin: 75 μM. Only p-values for the 48 h time point are indicated in the graphs. All multiplicity-adjusted p-values are listed in table ES6.

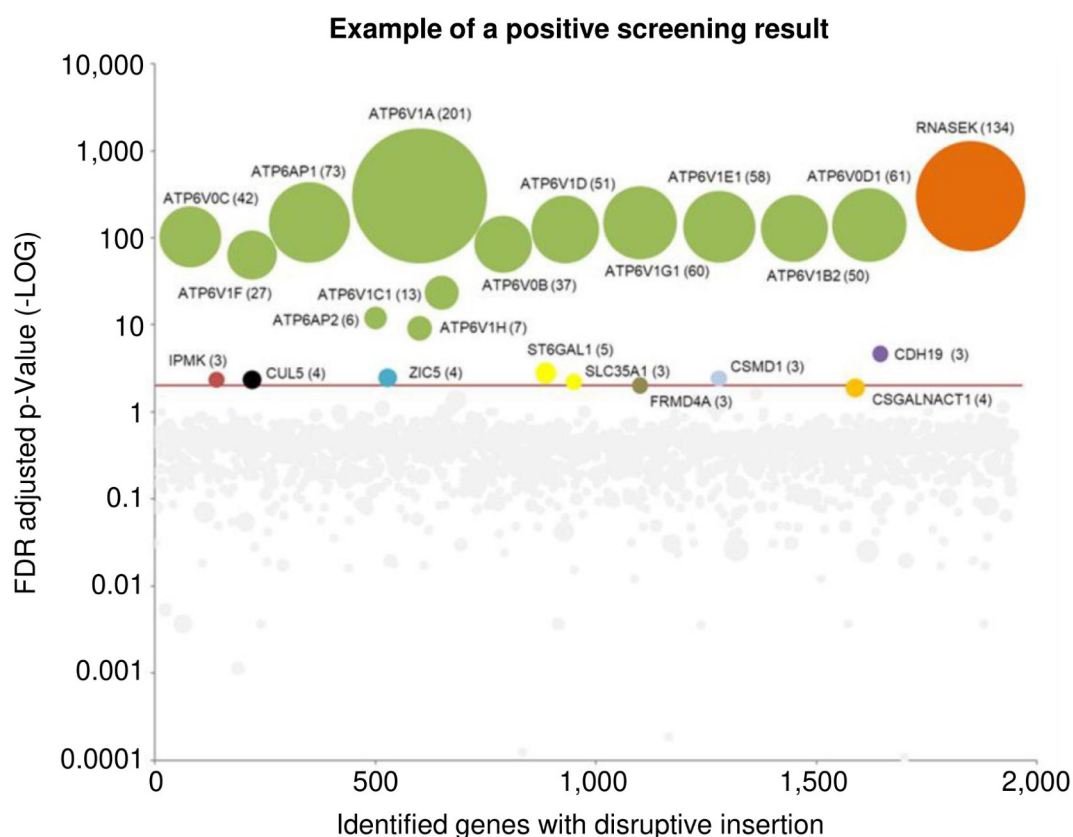


Figure S6: Positive NGS screening example provided by Haplogen GmbH (Vienna, Austria). Genes with multiple disruptive insertions and a FDR adjusted p-value ≤ 0.0001 (red line: -log₁₀ = 4) are considered relevant for the mechanism of action and resistance development towards the drug substance.

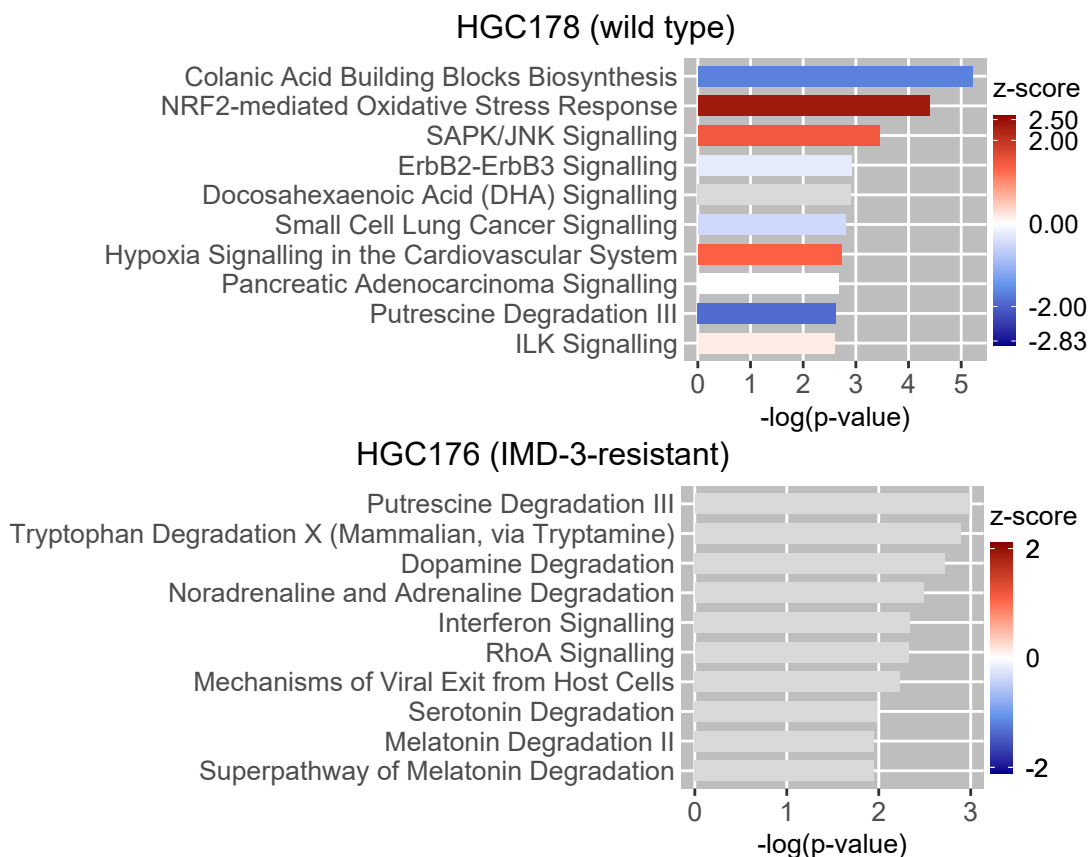


Figure S7: Top 10 deregulated pathways in IMD-3-treated WT and IMD-3-resistant cells. Displayed are z-scores for each pathway predicting the activation ($z\text{-score} \geq 2$; red) or inhibition ($z\text{-score} \leq -2$; blue) of the pathway based on the transcriptome data. If no direction of the pathway could be predicted, the z-score is 0 (white). If no z-score could be predicted, pathways are labelled in grey.

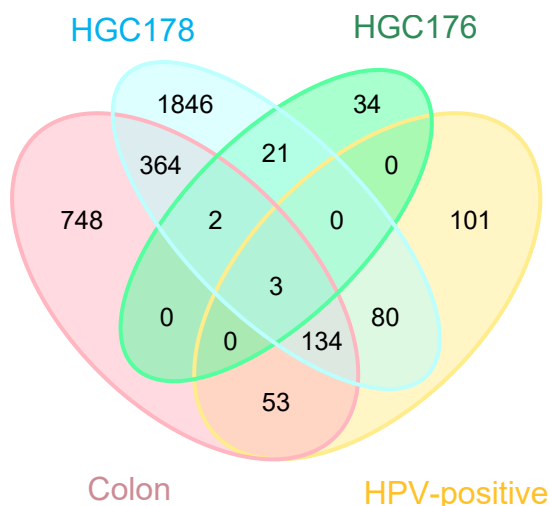
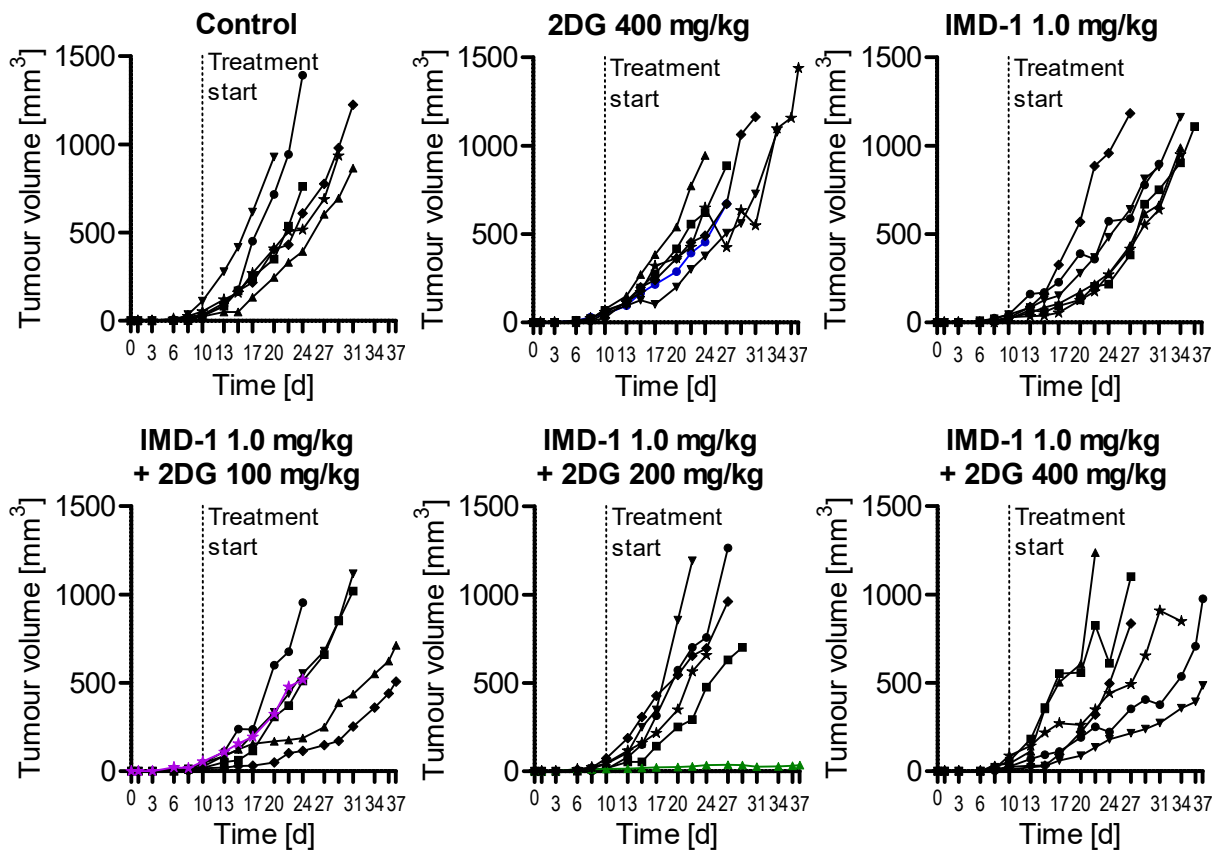
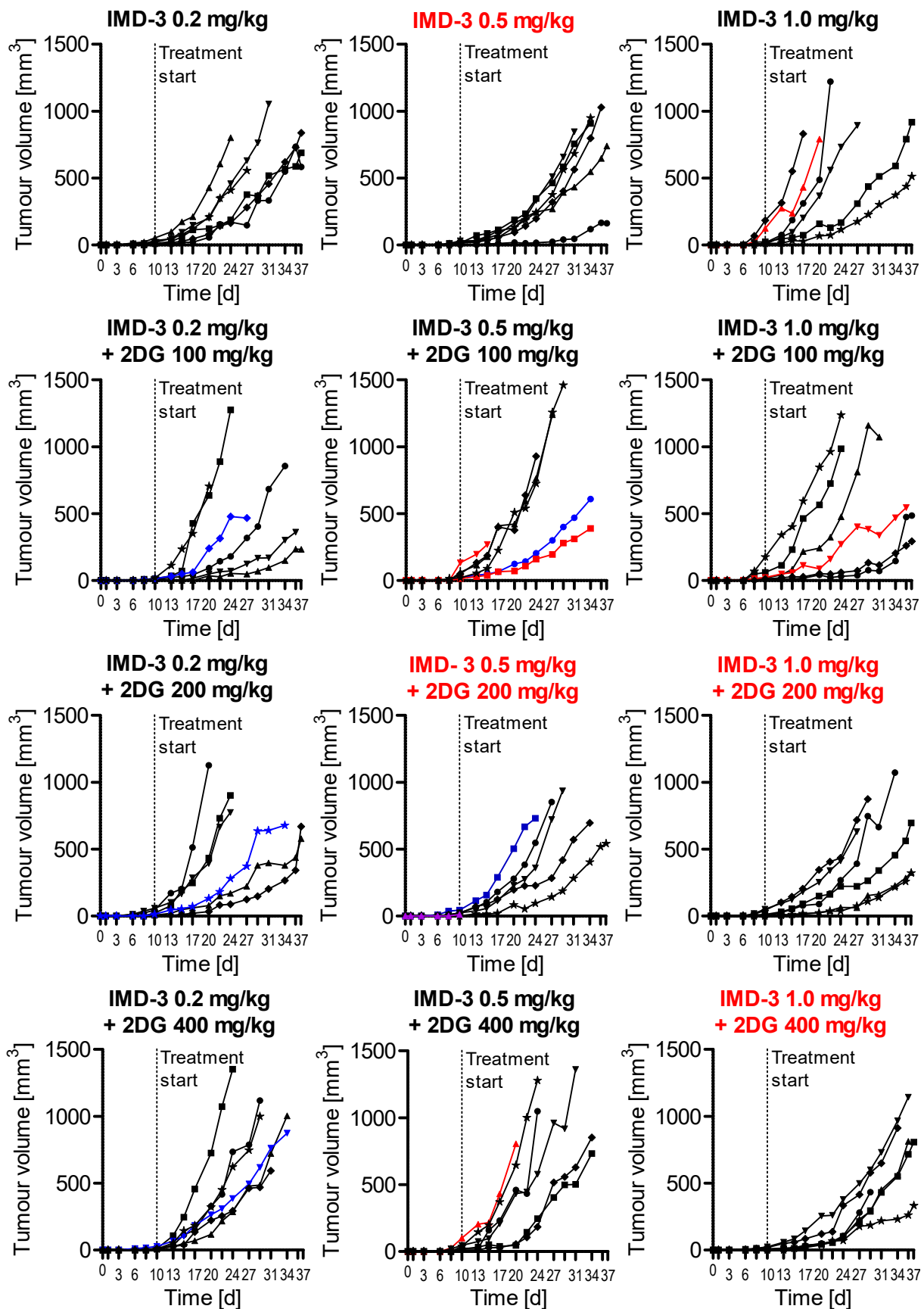


Figure S8: Comparison of shared DEGs upon IMD-3 treatment between CRC, HPV-positive, WT HGC178 and IMD-3-resistant HGC176 cells. Only significantly DEGs (BH-corrected $p\text{-value} \leq 0.05$, $\log_2FC \geq 1/ \leq -1$), which were regulated in the same direction upon IMD-3 treatment in different cell lines, were included. HCT116 and HT29 cell lines are grouped in ‘Colon’, while HPV-positive cell lines CaSki, HeLa, SiHa and UPCI-SCC-90 are grouped in ‘HPV-positive’.



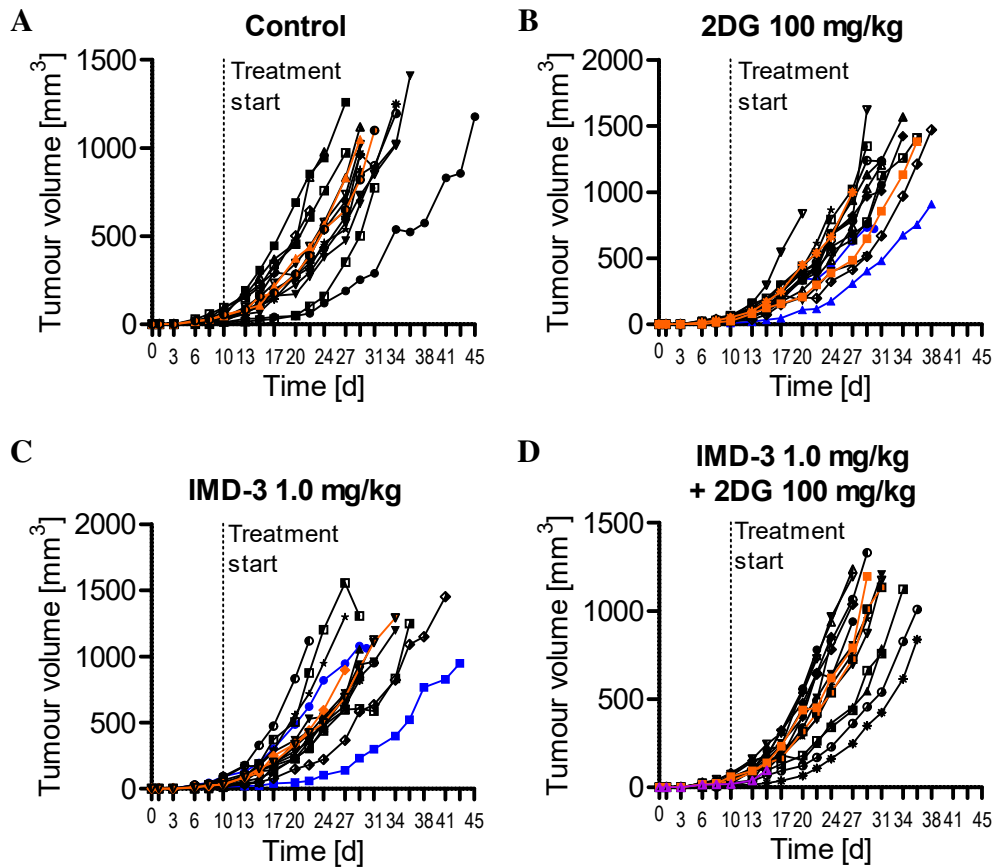
Blue: Skin injury at tumour site Violet: Spontaneous death Green: Tumour did not grow

Figure S9: Growth of HCT116 xenograft tumours in $Rag2^{-/-}Il2rg^{-/-}$ mice treated with vehicle, 2DG (400 mg/kg), and IMD-1 (1.0 mg/kg) alone and in combination with 2DG (100, 200, 400 mg/kg). Treatment was started at day 10 and mice were monitored to a maximum of 37 days (3 injections/week, max. 12 injections).



Red: Weight loss > 20 % **Blue:** Skin injury at tumour site **Violet:** Spontaneous death

Figure S10: Growth of HCT116 xenograft tumours in Rag2^{-/-}Il2rg^{-/-} mice treated with IMD-3 (0.2, 0.5, 1.0 mg/kg) alone and in combination with 2DG (100, 200, 400 mg/kg). Treatment was started at day 10 and mice were monitored to a maximum of 37 days (3 injections/week, max. 12 injections). Groups marked in red: Tumours grew slower compared to the other experiments already before treatment start.



Orange: Imaging mouse Blue: Skin injury at tumour site Violet: Spontaneous death

Figure S11: Growth of HCT116 xenograft tumours in $Rag2^{-/-}Il2rg^{-/-}$ mice treated with vehicle (A), 100 mg/kg 2DG (B), 1.0 mg/kg IMD-3 (C), or 1.0 mg/kg IMD-3 and 100 mg/kg 2DG (D). Mice received 3 *i.p.* injections per week (max. 12 injections) starting at day 10. Mice underwent MRI and PET/CT scans at day 14, 21 and 35. Vehicle-treated and IMD-3-treated groups consisted of 16 animals, while the 2DG and combination treatment groups comprised 17 animals.

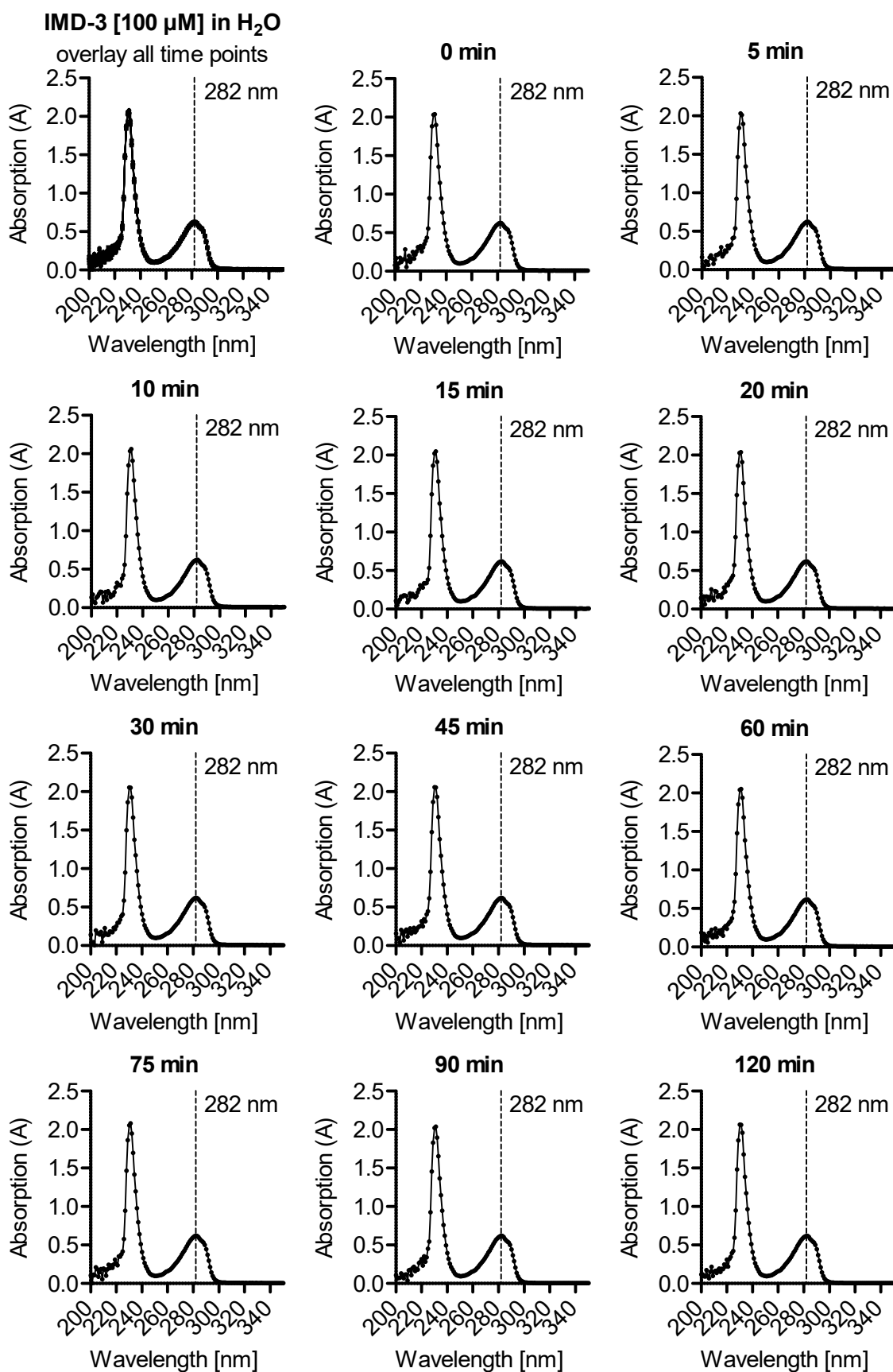


Figure S12: Stability of IMD-3 (100 μ M) in water at RT. Absorption spectrum of IMD-3 solution was measured repeatedly over 120 min. The band at 282 nm can be attributed to IMD-3 due to its aromatic absorption, whereas the band at 230 nm can be attributed to DMSO present in the solution.

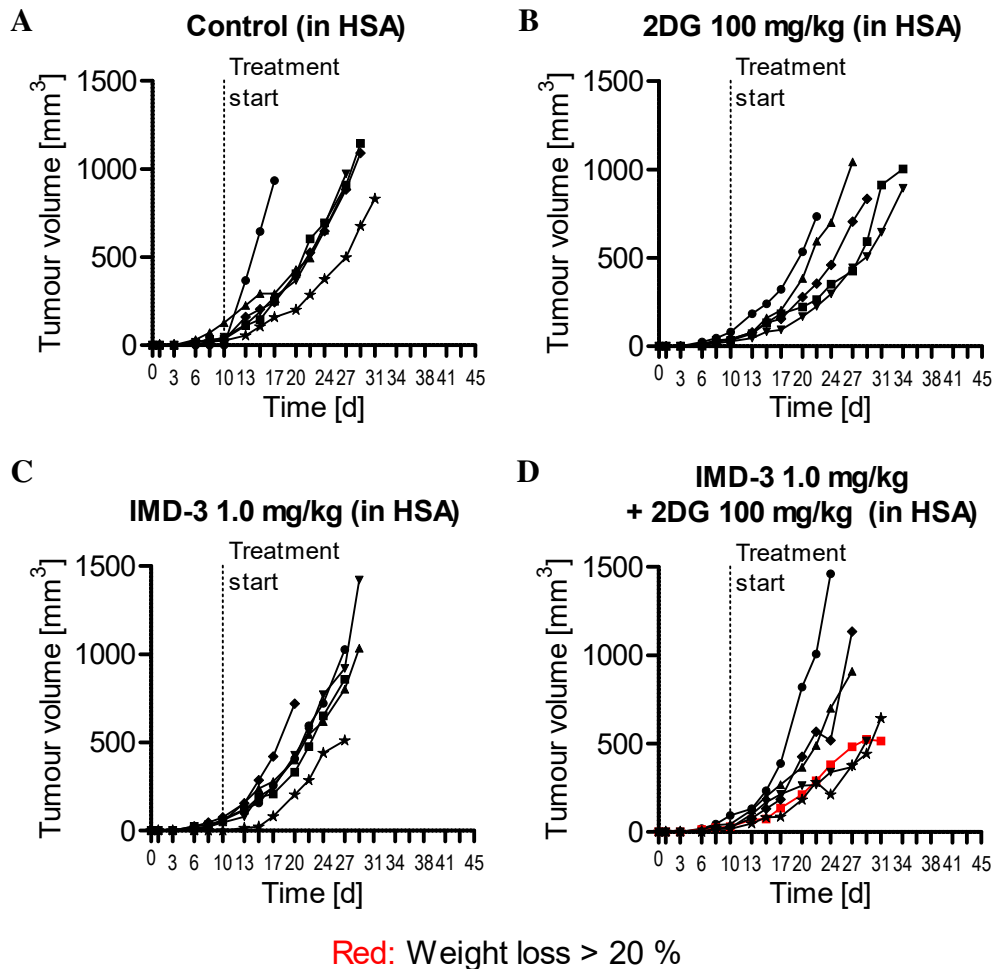


Figure S13: Growth of HCT116 xenograft tumours in Rag2^{-/-}Il2rg^{-/-} mice treated with vehicle (A), 100 mg/kg 2DG (B), 1.0 mg/kg IMD-3 (C), or 1.0 mg/kg IMD-3 and 100 mg/kg 2DG (D) solubilised in HSA solution (10 mg/kg). Mice received 3 *i.p.* injections per week (max. 12 injections) starting at day 10. All groups consisted of 6 mice except the 2DG-treated group as one mouse perished before starting the experiment.

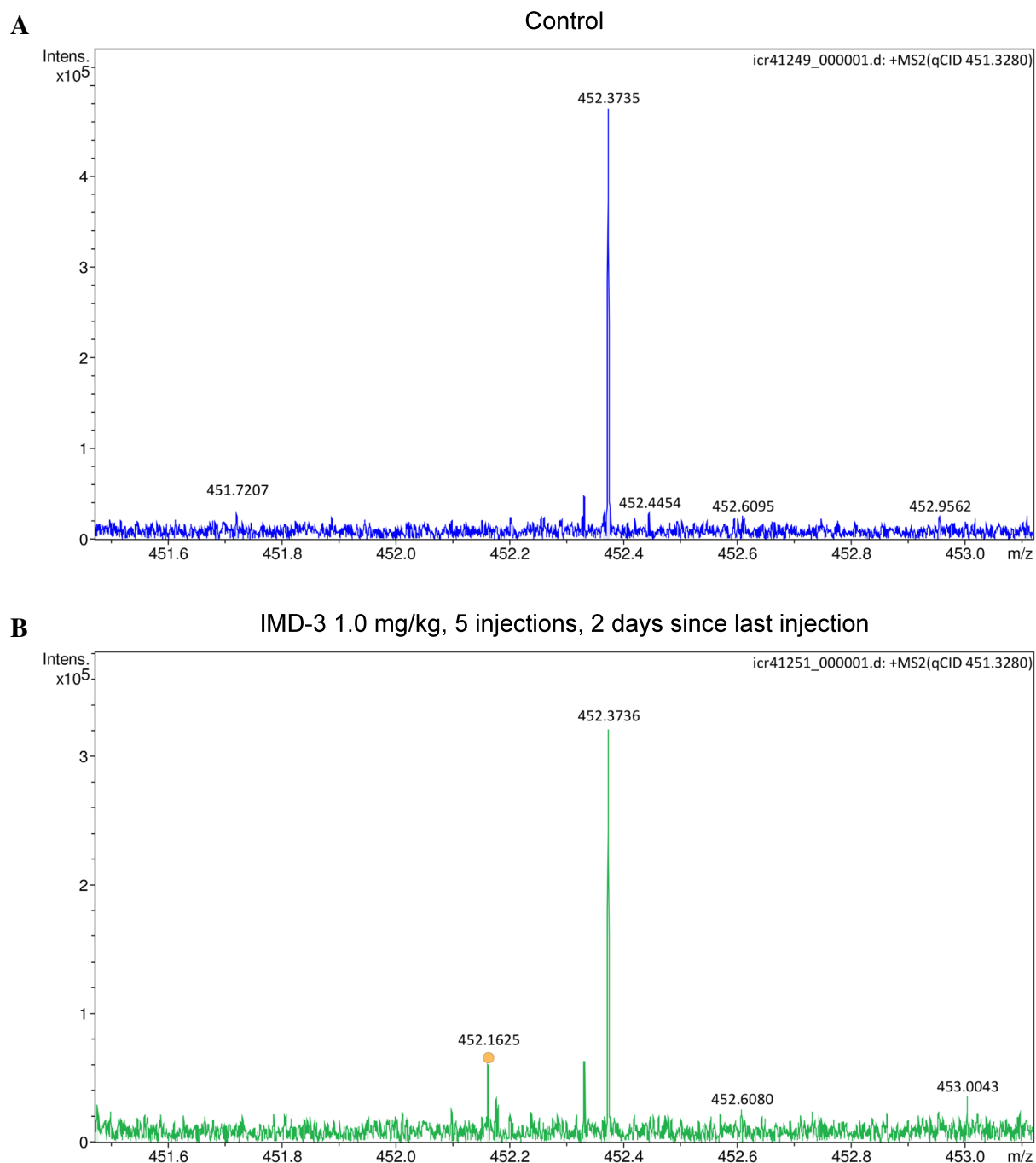


Figure S14: ESI-MS measurements of xenograft tumours from mice receiving IMD-3 solubilised in water and DMSO. IMD-3 + H⁺ exhibits a theoretical m/z value of 452.1623. Tumour lysates in acetonitrile with 0.01 % TFA were analysed with ESI-MS. (A) Tumour from vehicle-treated mouse receiving 8 *i.p.* injections. IMD-3 was not detected. (B) Tumour from IMD-3-treated mouse receiving 5 *i.p.* injections with 1.0 mg/kg IMD-3. IMD-3 was detected with a m/z value of 452.1625 (marked peak). The mouse received the last treatment injection 2 days before sacrificing.

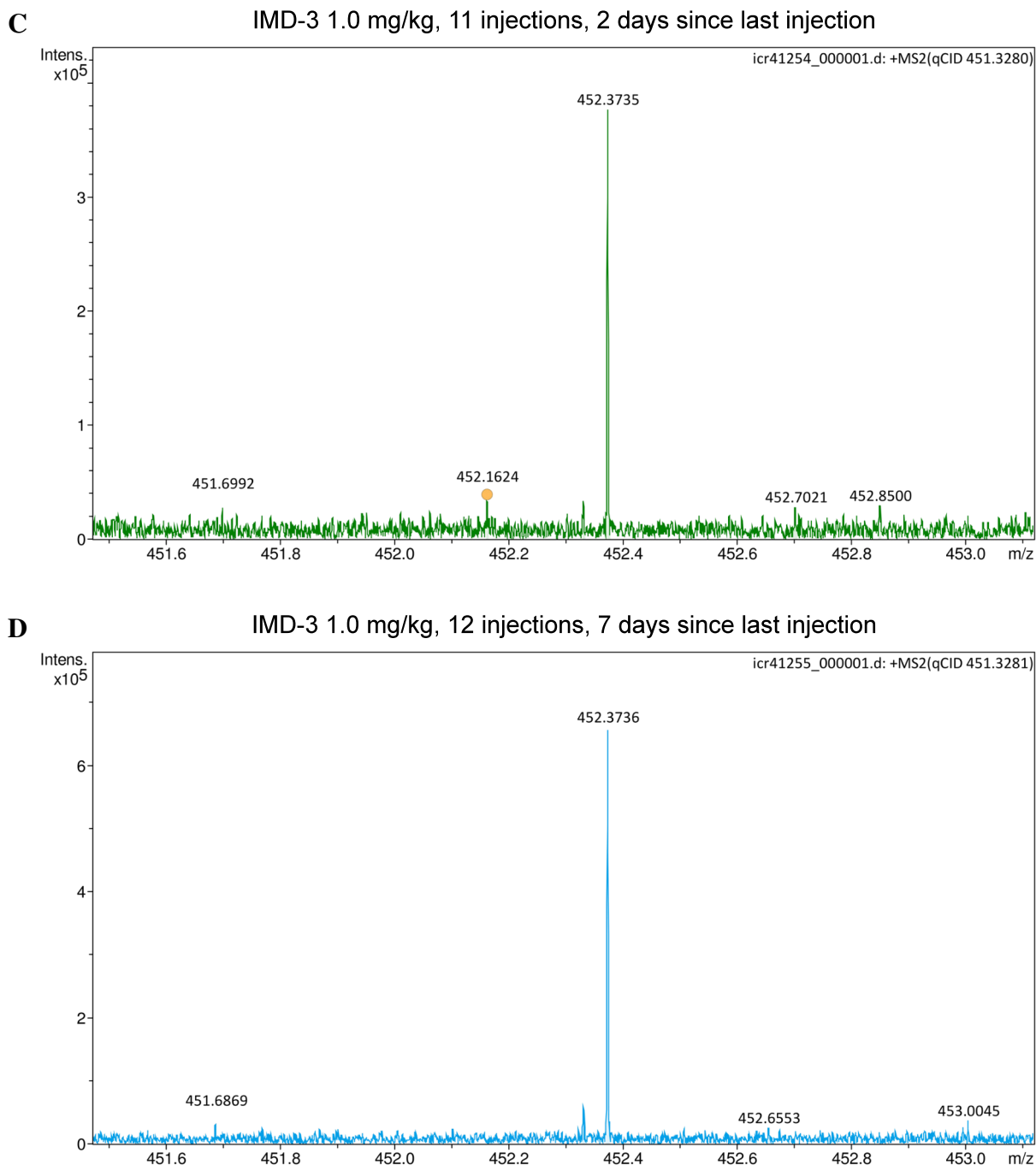


Figure S14: ESI-MS measurements of xenograft tumours from mice receiving IMD-3 solubilised in water and DMSO. IMD-3 ($C_{26}H_{26}ClNO_4$) + H^+ exhibits a theoretical m/z value of 452.1623. Tumour lysates in acetonitrile with 0.01 % TFA were analysed with ESI-MS. (C) Tumour from IMD-3-treated mouse receiving 11 *i.p.* injections with 1.0 mg/kg IMD-3. IMD-3 was detected with a m/z value of 452.1624 (marked peak). The mouse received the last treatment injection 2 days before sacrificing. (D) Tumour from IMD-3-treated mouse receiving the maximum of 12 *i.p.* injections with 1.0 mg/kg IMD-3. The mouse received the last treatment injection 7 days before sacrificing, thus, IMD-3 was not detected in the tumour lysate anymore.

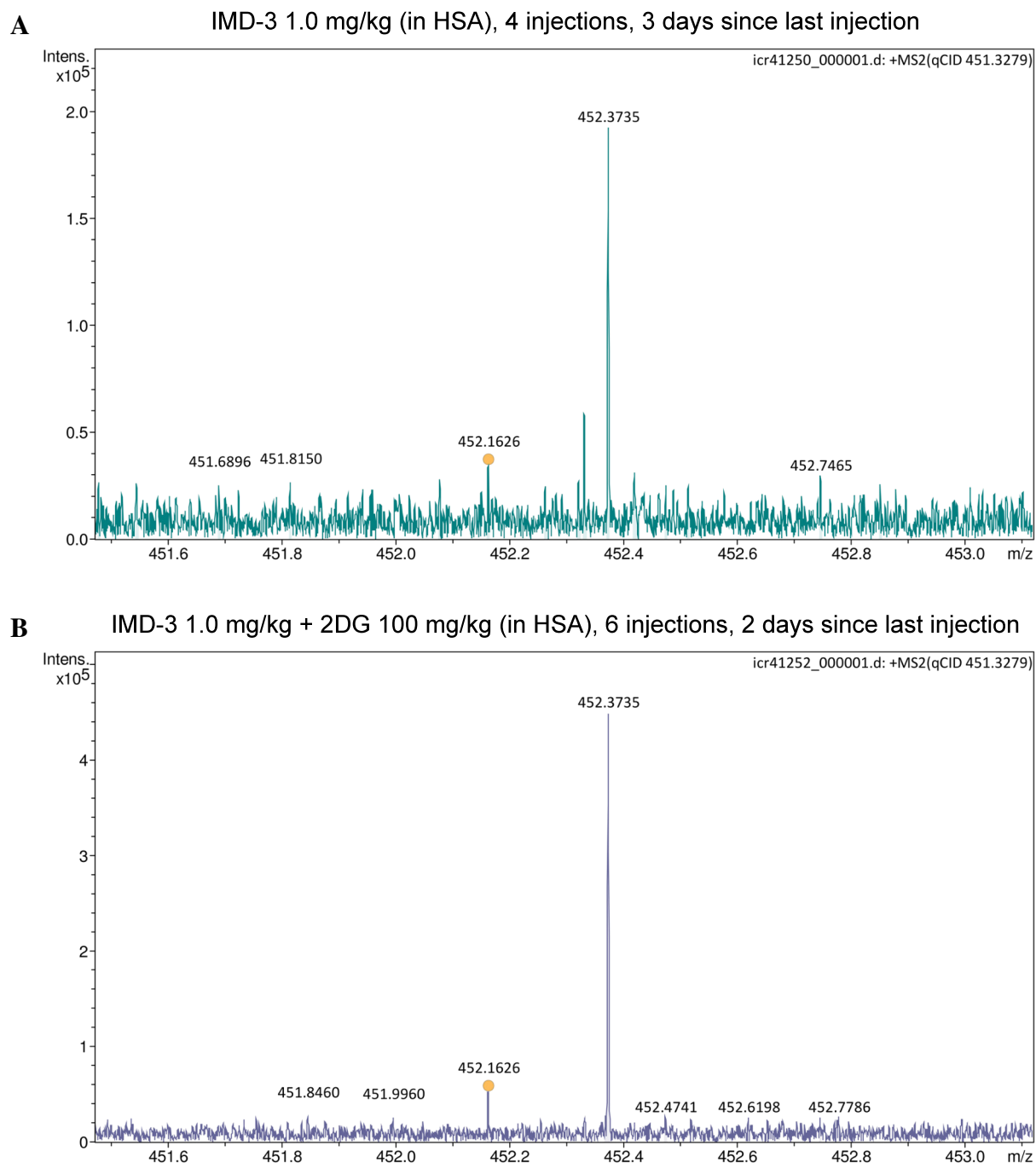


Figure S15: ESI-MS measurements of xenograft tumours from mice receiving IMD-3 solubilised in HSA solution and DMSO. IMD-3 ($C_{26}H_{26}ClNO_4$) + H^+ exhibits a theoretical m/z value of 452.1623. Tumour lysates in acetonitrile with 0.01 % TFA were analysed with ESI-MS. (A) IMD-3-treated mouse receiving 4 *i.p.* injections with 1.0 mg/kg IMD-3. IMD-3 was detected with a m/z value of 452.1626 (marked peak). The mouse received the last treatment injection 3 days before sacrificing. (B) IMD-3-treated mouse receiving 6 *i.p.* injections with 1.0 mg/kg IMD-3 and 100 mg/kg 2DG. IMD-3 was detected with a m/z value of 452.1626 (marked peak). The mouse received the last treatment injection 2 days before sacrificing.

Electronic supplements

- ES1 p-values: Treatment efficacy in different cancer entities
- ES2 p-values: Influence of IDH-mutation on treatment sensitivity
- ES3 p-values: Influence of MSS- and MSI-phenotype on treatment sensitivity
- ES4 p-values: Influence of MLH1 knockout on treatment sensitivity
- ES5 p-values: Influence of HPV on treatment sensitivity
- ES6 p-values: Treatment cytotoxicity
- ES7 p-values: Proliferation inhibition
- ES8 p-values: Glucose uptake
- ES9 p-values: Lactate production
- ES10 p-values: PPP activity
- ES11 Differentially expressed genes and IPA analysis of CRC and HPV-positive cells
- ES12 p-values: Treatment sensitivity of 3D spheroids
- ES13 p-values: Influence of IMD-3 resistance on treatment sensitivity
- ES14 p-values: Influence of DAC-pretreatment on treatment sensitivity
- ES15 Differentially expressed genes and IPA analysis of WT and IMD-3-resistant cells
- ES16 p-values: Influence of IMD-3 resistance on 2DG treatment sensitivity
- ES17 p-values: Survival of xenograft mice (dose escalation)
- ES18 p-values: GLUT-1 and Ki-67 expression in xenograft tumours (dose escalation)
- ES19 p-values: Survival of xenograft mice
- ES20 p-values: FDG uptake in xenograft tumours
- ES21 p-values: Treatment sensitivity of HCT116 cells after long term storage and medium preparation influence
- ES22 p-values: Influence of supplements on treatment sensitivity of HCT116 cells
- ES23 p-values: Influence of FBS, BSA and HSA on treatment sensitivity of HCT116 cells
- ES24 p-values: Influence of FBS and DMSO on treatment sensitivity of HCT116 cells
- ES25 p-values: Survival of xenograft mice treated with IMD-3 solubilised in HSA

Acknowledgements

First of all, I would like to thank Prof. Dr. med. Magnus von Knebel Doeberitz for providing me the opportunity to work in his department and on this exciting project. Your trust and encouragement motivated me during every step of my PhD.

My gratitude goes to my supervisors Dr. Aysel Ahadova and PD Dr. med. Matthias Kloor for their scientific guidance and encouragement during the project. I want to thank Aysel for reading my thesis and help with writing the manuscript.

I want to express my sincere appreciation and gratitude for Prof. Dr. Jürgen Kopitz for his scientific guidance and help with experimental setups. Your inspiring and valuable advice helped me to drive my project forward. Thank you for all the support and time given to me.

I would like to thank Thomas Henkel for kindly providing the flavagline substances and sharing his knowledge about them. Without your help, this project would not have been possible.

My gratitude also goes to Prof. Dr. Jürgen Gross for helping with the ESI-MS measurements getting as much as possible out of my data.

I also would like to thank all lab members of ATB for their support and great working atmosphere. A special thanks goes to Ricarda Mehr, Iris Martin, Nina Nelius, Laura Brandschwei, Jonathan Dörre, Lena Ehret-Maßholder and Vera Fuchs for their helping hands, whenever needed. Especially I want to thank Laura for her help with sectioning and staining of the xenograft tumours and Iris for setting up the organotypic co-cultures. I want to express my gratitude to Anja Rathgeb, Kerstin Musielak, Anette Berdel and Melina Fichtmüller for your ‘open ear’ and helpful advice with the animal experiments. As well, I want to thank the ‘Small Animal Imaging Centre’ for their helpful advice and execution of the imaging experiments. I also want to thank the ‘Genomics and Proteomics Core Facility’, especially Oliver Heil for his advice on transcriptome data analysis.

My special gratitude goes to Andrea Klingmann for her help with all organisational matters, her kindness and ‘open door’ in all situations.

I want to thank Angela Salnikov and Javier Ignacio Arriaza Gonzalez for their help for my project during their internship and medical thesis.

My deepest thanks goes to my friends and office members Lena Bohaumilitzky, Malwina Michalak, Lara Schlegel, Alejandro Hernandez Sanchez, Florian Seidler, Dr. Katharina Ur-

ban, Dr. Eva Katzenmaier, Dr. Fabia Fricke and Simon Kalteis for the unique atmosphere, their support and the unforgettable time. Thank you for amazing - scientific and non-scientific - 'kitchen talks', ice cream breaks, sharing joy and sorrow, and the great fun I had during my PhD.

I would like to thank my friends for their enormous support during my PhD. Thank you for long walks, book clubs, sporting activities, joyful and serious conversations, long horseback trips, cooking events and game nights.

Finally, I wish to express my great thankfulness to Thomas and my family. Thank you for your unconditional support, love and patients through all the ups and downs of my PhD.